

Translation of Novel Imaging Techniques into Clinical Use for Patients with Epilepsy

Dr Gavin Paul Winston

Thesis submitted for the degree of Doctor of Philosophy

Department of Clinical and Experimental Epilepsy

Institute of Neurology

University College London

DECLARATION

I, Gavin Paul Winston, confirm that the work presented in this thesis is my own. Where information has been derived from other sources, I confirm that this has been indicated in the thesis.

Signed:

Date: 8 January 2014

ABSTRACT

Temporal lobe epilepsy is the most common focal epilepsy. Up to 40% of patients are refractory to medication. Anterior temporal lobe resection (ATLR) is an effective treatment but damage to the optic radiation can result in a visual field deficit (VFD) that precludes driving, a key goal of surgery.

Diffusion tensor imaging tractography allows the *in vivo* delineation of white matter tracts such as the optic radiation. This thesis addresses the role of optic radiation tractography in planning and subsequently improving the safety of epilepsy surgery.

I show how tractography assists risk stratification and surgical planning in patients with lesions near the optic radiation and assess the utility of different tractography methods for surgical planning. To derive the greatest benefit, tractography information should be available during surgery which requires correction for intraoperative brain shift and other sources of image distortion.

I apply software developed at UCL in a clinical population underlying ATLR to show that postoperative imaging can predict the VFD and then use this software in real time during surgery in an intraoperative MRI suite. Updated anatomical scans can be acquired during surgery and tractography data accurately mapped on to these and displayed on the operating microscope display. I demonstrate that this image guidance allows the neurosurgeon to avoid significant VFD without affecting the seizure outcome.

Diffusion imaging can also probe tissue microstructure. I explore how structural changes within the frontoparietal working memory network and temporal lobes are related to working memory impairment in TLE. I describe the structural changes that occur following ATLR showing both Wallerian degeneration and structural plasticity. Finally, I show how a novel diffusion model (NODDI) could aid the clinical assessment of patients with focal cortical dysplasia.

The emphasis throughout this thesis is how diffusion imaging can be clinically useful and address clinically relevant outcomes.

TABLE OF CONTENTS

Declaration	2
Abstract	3
Table of Contents	4
List of Figures	15
List of Tables	17
List of Abbreviations.....	19
Acknowledgements	25
Funding Sources.....	26
Outline and Statement of Personal Contribution.....	27
Publications Associated with this Thesis	29
Conference Posters and Talks Related to this Thesis	33
Awards and Prizes.....	35
1 Epilepsy.....	36
1.1 Introduction	36
1.2 Epilepsy.....	36
1.2.1 Definition	36
1.2.2 Epidemiology	36
1.2.3 Classification.....	37
1.2.3.1 International Classification of Epileptic Seizures (1981)	37
1.2.3.2 International Classification of Epilepsies and Epileptic Syndromes (1989).....	37
1.2.3.3 Revised terminology and concepts for organization of seizures and epilepsies (2010)	37
1.3 Temporal Lobe Epilepsy	40
1.3.1 Introduction	40
1.3.2 Anatomy of the Temporal Lobe	40
1.3.3 Clinical Features of Mesial TLE	40
1.3.4 Clinical Features of Neocortical TLE.....	41
1.3.5 Medical Treatment	41
1.3.5.1 Anti-Epileptic Drugs.....	41
1.3.5.2 Medication-Refractory Epilepsy.....	42

1.3.6	Surgical Treatment	42
1.3.6.1	Rationale.....	42
1.3.6.2	Types of Surgery	43
1.3.6.3	Resective Surgery	43
1.3.6.4	Presurgical Evaluation	43
1.3.6.5	Neuroimaging in Presurgical Evaluation	44
1.3.6.6	Anterior Temporal Lobe Resection	45
1.3.6.6.1	Seizure Outcome	45
1.3.6.6.2	Neurological and Psychological Sequelae.....	47
1.4	Conclusions	47
2	Diffusion Magnetic Resonance Imaging: Principles	48
2.1	Introduction	48
2.2	Diffusion and its Measurement	48
2.2.1	Molecular Diffusion	48
2.2.2	Measurement of Diffusion: NMR	49
2.2.3	Measurement of Diffusion: MRI	50
2.3	Diffusion Weighted Imaging (DWI)	50
2.4	Diffusion Tensor Imaging (DTI)	51
2.4.1	Conceptual and Mathematical Formulation	51
2.4.2	Scalar Invariants from the Diffusion Tensor	54
2.4.2.1	Mean Diffusivity (MD)	54
2.4.2.2	Fractional Anisotropy (FA)	54
2.4.2.3	Axial and Radial Diffusivities	54
2.5	Biological Sources of Diffusion Anisotropy	55
2.5.1	Potential Sources of Anisotropy	55
2.5.1.1	Myelin	56
2.5.1.2	Axonal Membranes.....	56
2.5.1.3	Cytoskeleton	56
2.6	Clinical Studies of DTI parameters	57
2.6.1	Extraction of DTI parameters	57
2.6.2	Interpretation of DTI parameters	57
2.7	Fibre Orientation and Tractography	59

2.7.1	Basic Principles	59
2.7.2	Deterministic Tractography	60
2.7.3	Probabilistic Tractography	61
2.7.4	Tractography and Crossing Fibres.....	61
2.7.5	Improving the Spatial Resolution.....	62
2.7.6	Use of Tractography Data	62
2.8	Improving the Diffusion Model.....	62
2.8.1	Limitations of the Diffusion Tensor Model.....	62
2.8.2	Diffusion Profile.....	63
2.8.3	Tissue Models	63
2.8.4	Limitations of Tissue Models.....	64
2.9	Conclusions	64
3	Diffusion Magnetic Resonance Imaging: Clinical Studies.....	66
3.1	Introduction	66
3.2	Generic Studies in Epilepsy	66
3.2.1	Diffusion Imaging of the Hippocampus	66
3.2.2	Cross Sectional Diffusion Tensor Imaging in TLE	66
3.2.3	Longitudinal Diffusion Tensor Imaging in TLE	67
3.2.4	Malformations of Cortical Development.....	68
3.3	Tractography and Cognition in Epilepsy.....	75
3.3.1	Language	75
3.3.2	Memory	77
3.4	Tractography and Working Memory in Other Conditions	78
3.5	Conclusions	84
4	The Optic Radiation and Vision.....	85
4.1	Introduction	85
4.2	Gross Anatomy of the Visual Pathways	85
4.3	Initial Anatomical Studies of the Optic Radiation.....	85
4.4	Insights from Temporal Lobe Surgery for Epilepsy.....	89
4.4.1	Frequency of Deficits	89
4.4.2	Nature of Perimetry	89
4.4.3	Relationship of VFD to Resection Size.....	89

4.4.4	Relationship of Meyer's Loop to the Temporal Horn	90
4.4.5	Nature of the VFD	90
4.4.6	Retinotopic Organisation of the Optic Radiation	90
4.4.7	Left/Right Asymmetry of VFD	95
4.4.8	Relevance of the Deficit to Driving.....	96
4.4.9	Effect of the Surgical Technique	97
4.4.9.1	Lateral transsulcal/transcortical – access via the temporal gyri or sulci	97
4.4.9.2	Subtemporal – access via the fusiform or parahippocampal gyrus.....	98
4.4.9.3	Transsylvian – access via the Sylvian fissure	98
4.5	Anatomical Dissection Studies.....	99
4.6	Diffusion Tensor Imaging Tractography of the Optic Radiation	101
4.6.1	Choice of Acquisition and Algorithm	101
4.6.2	Choice of Seed Regions	101
4.6.3	Studies in Epilepsy	102
4.6.3.1	Postoperative diffusion changes	102
4.6.3.2	Tractography and postoperative visual outcome	106
4.6.3.3	Comparing deterministic and probabilistic tractography	107
4.6.3.4	Using tractography real-time during surgery	107
4.6.4	Studies in Other Conditions.....	107
4.7	Conclusions	110
5	Intraoperative Magnetic Resonance Imaging	111
5.1	Introduction	111
5.2	Image-Guided Surgery	111
5.2.1	Role of Image Guidance	111
5.2.2	Approaches to Intraoperative Imaging	111
5.3	Intraoperative MRI	113
5.3.1	Design Considerations.....	113
5.3.2	Safety and Anaesthetic Considerations	113
5.3.3	Clinical Utility.....	114
5.3.3.1	Tumour Surgery.....	114
5.3.3.2	Epilepsy Surgery.....	114
5.4	Technical Challenges	116

5.4.1	The Key Challenges	116
5.4.2	Brain Shift	116
5.4.2.1	The Nature of the Problem	116
5.4.2.2	The Extent of the Problem.....	117
5.4.2.3	The Correction of the Problem	117
5.4.3	Geometric Image Distortion	118
5.4.3.1	The Nature of the Problem	118
5.4.3.2	Gradient Field Non-Linearity	119
5.4.3.3	Magnetic Susceptibility Artefacts.....	119
5.5	Conclusions	121
6	Study Design And Generic Methods.....	122
6.1	Introduction	122
6.2	Aims of the Studies	122
6.3	Subjects and Recruitment	123
6.3.1	Source of Patients.....	123
6.3.2	Healthy Controls	123
6.3.3	Ethical Approval	124
6.4	Clinical and Demographic Characteristics	124
6.4.1	Patient Cohort.....	124
6.4.2	Control Cohort.....	125
6.5	Study Protocol.....	127
6.5.1	Clinical Assessment	127
6.5.2	Timing of Visits and Questionnaires	127
6.5.3	Magnetic Resonance Imaging	127
6.5.3.1	Structural Imaging	127
6.5.3.2	Diffusion Tensor Imaging.....	127
6.5.3.2.1	Acquisition	127
6.5.3.2.2	Preprocessing	128
6.5.3.2.3	Tractography of the Optic Radiation.....	129
6.5.3.3	Functional MRI	130
6.5.4	Neuropsychology	131
6.5.5	Visual Fields.....	132

6.5.5.1	Goldmann Kinetic Perimetry	132
6.5.5.2	Quantification of VFD	132
6.5.5.3	Determination of Driving Eligibility	134
6.6	Software for Image Registration	135
6.6.1	Introduction	135
6.6.2	Basics of Image Registration.....	135
6.6.3	NiftyReg Software.....	135
6.6.3.1	Global registration	135
6.6.3.2	Local registration	136
6.6.3.3	Extensions for Present Work	136
6.6.4	Gradient Non-Linearity Correction	137
6.6.5	Magnetic Susceptibility Artefact Correction.....	137
6.7	Conclusions	138
7	Diffusion Tensor Imaging Tractography to Visualise the Relationship of the Optic Radiation to Epileptogenic Lesions Prior to Neurosurgery	139
7.1	Introduction	139
7.2	Methods.....	139
7.2.1	Subjects	139
7.2.2	Tractography	141
7.2.3	Coregistration and Display of Tractography Data.....	141
7.2.4	Visual Fields.....	141
7.3	Results	143
7.3.1	Validation of tractography with post-operative outcome	143
7.3.2	Tractography assists the decision not to proceed to surgery	148
7.3.3	Tractography leads to a decision to defer surgery for now.....	149
7.4	Discussion	151
8	Diffusion Tensor Imaging Tractography of the Optic Radiation for Epilepsy Surgical Planning: a Comparison of Two Methods.....	153
8.1	Introduction	153
8.2	Methods.....	154
8.2.1	Subjects	154
8.2.2	Tractography	154

8.2.3	Volume of Optic Radiation and Degree of Overlap	156
8.2.4	Measurements of Meyer's Loop.....	156
8.3	Results	156
8.3.1	Visual Comparison	156
8.3.2	Volume of Optic Radiation and Degree of Overlap	157
8.3.3	Measurements of Meyer's Loop.....	160
8.4	Discussion	160
8.5	Conclusion.....	162
9	Optic Radiation Tractography and Vision in Anterior Temporal Lobe Resection.....	163
9.1	Introduction	163
9.2	Methods.....	163
9.2.1	Subjects	163
9.2.2	Tractography	165
9.2.3	Resection Size Estimates and Meyer's Loop Location	165
9.2.4	Propagation of Tractography and Measuring Damage	165
9.2.5	Visual Field Assessment	167
9.2.6	Statistical Analysis	168
9.3	Results	168
9.4	Discussion	170
9.4.1	Key Findings	170
9.4.2	Comparison with Previous Work	170
9.4.3	Implications for Driving.....	171
9.4.4	Strengths and Weaknesses.....	172
9.4.5	Implications of Results.....	173
9.5	Conclusion.....	173
10	Intraoperative Visualisation of the Optic Radiation Reduces Visual Field Deficits.....	174
10.1	Introduction	174
10.2	Methods.....	174
10.2.1	Subjects	174
10.2.2	Comparison Cohort	174
10.2.3	Preoperative Imaging	176
10.2.3.1	Optic Radiation Tractography	176

10.2.3.2	Preparing Preoperative Data	176
10.2.3.2.1	Cohort 1	176
10.2.3.2.2	Cohort 2	176
10.2.4	Intraoperative Imaging and Surgery	178
10.2.4.1	Overview	178
10.2.4.2	Imaging Protocol	178
10.2.4.3	Display of Imaging	178
10.2.4.4	Surgical and Imaging Approach	180
10.2.4.5	Cohort 1	183
10.2.4.6	Cohort 2	183
10.2.5	Outcome Data.....	185
10.2.5.1	Primary Outcome: Visual fields	185
10.2.5.2	Secondary Outcomes	185
10.2.6	Statistical Analysis	186
10.3	Results	186
10.3.1	Visual Field Deficits.....	186
10.3.2	Seizure Outcome	186
10.3.3	Hippocampal Resection.....	186
10.3.4	Surgeon's Feedback	187
10.3.5	Duration of Scanning.....	187
10.3.6	Degree of Brain Shift	188
10.4	Discussion	188
10.4.1	Key Findings	188
10.4.2	Vision and Driving	188
10.4.3	Importance of Brain Shift.....	188
10.4.4	Strengths and Limitations.....	189
10.5	Conclusion.....	189
11	Structural Correlates of Impaired Working Memory in Hippocampal Sclerosis.....	190
11.1	Introduction	190
11.2	Methods.....	190
11.2.1	Subjects	190
11.2.2	Magnetic Resonance Imaging	191

11.2.2.1	Working Memory fMRI	191
11.2.2.2	Voxel-Based Morphometry	191
11.2.2.3	DTI Processing and Analysis.....	192
11.2.3	Neuropsychological Measures of Working Memory.....	192
11.3	Results	193
11.3.1	Working Memory Performance.....	193
11.3.2	Working Memory fMRI	193
11.3.3	Voxel-Based Morphometry	193
11.3.4	Voxel-Based Analysis of DTI	196
11.3.5	Tract-Based Analysis of DTI.....	196
11.4	Discussion	199
11.4.1	Summary of Results	199
11.4.2	Impaired Working Memory in TLE	201
11.4.3	Frontoparietal Working Memory Network.....	201
11.4.4	Changes in Frontoparietal Grey Matter	201
11.4.5	Voxel-Based Changes in Frontoparietal White Matter.....	202
11.4.6	Tract-Based Changes in Frontoparietal White Matter.....	203
11.4.7	The Role of the Temporal Lobe	203
11.4.8	Strengths and Limitations.....	204
11.5	Conclusion.....	204
12	Longitudinal Changes in Diffusion Parameters Following Anterior Temporal Lobe Resection..	209
12.1	Introduction	209
12.2	Methods.....	210
12.2.1	Subjects	210
12.2.2	DTI Processing	210
12.2.3	Longitudinal Data.....	212
12.3	Results	212
12.3.1	Baseline Changes	212
12.3.1.1	Left TLE	212
12.3.1.2	Right TLE.....	213
12.3.1.3	Underlying Changes	213
12.3.2	Longitudinal Changes.....	213

12.3.2.1	Left TLE	213
12.3.2.2	Right TLE	213
12.3.2.3	Underlying Changes	220
12.4	Discussion	220
12.4.1	Summary of Findings	220
12.4.2	Biological Basis of Baseline Changes	221
12.4.3	Dichotomy of Longitudinal Changes	222
12.4.4	Biological Implications and Causes of Increased Postoperative FA	222
12.4.5	Time Course of Postoperative Change	223
12.4.6	Strengths and Limitations.....	223
12.5	Conclusion.....	224
13	Advanced Diffusion Models Could Aid Assessing Patients with Focal Cortical Dysplasia	231
13.1	Introduction	231
13.2	Methods.....	232
13.2.1	Subjects	232
13.2.2	Magnetic Resonance Imaging	232
13.2.3	NODDI Tissue Model	233
13.2.4	Model Fitting.....	233
13.2.5	Statistical Analysis	234
13.3	Results	234
13.3.1	Qualitative Results	234
13.3.2	Quantitative Results	238
13.4	Discussion	238
13.4.1	Key Findings	238
13.4.2	Interpretation	238
13.4.3	Limitations and Future Work	239
13.5	Conclusion.....	239
14	Overall Conclusion.....	240
14.1	Main Findings and Contribution	240
14.2	Limitations and Future Studies.....	242
14.2.1	Tractography	242
14.2.2	Sources of Image Distortion.....	244

14.2.3	Visual Outcomes	245
14.2.4	Intraoperative MRI	245
14.2.5	Working Memory	246
14.2.6	Longitudinal Study	246
14.2.7	NODDI	246
14.3	Possible Research Questions	247
14.4	Clinical Relevance and Final Conclusion.....	248
Appendices		249
Appendix A: Patient Information Sheet for the main study		250
Appendix B: Control Information Sheet for the main study		254
Appendix C: Consent form for the main study		258
Appendix D: Log form for patients in main study		260
Appendix E: Edinburgh handedness inventory for main study		261
Appendix F: Checklist for healthy volunteers for main study.....		263
Appendix G: Patient Information Sheet for intraoperative MRI study		265
Appendix H: Consent form for intraoperative MRI study.....		270
Appendix I: Checklist for processing of tractography data and transfer to intraoperative MRI.....		272
Appendix J: Log sheet for images acquired and displayed during surgery in intraoperative MRI.....		273
References		275

LIST OF FIGURES

Figure 2.1 - Spin echo NMR sequence.....	49
Figure 2.2 - Pulsed gradient spin echo NMR sequence.....	49
Figure 2.3 - Diffusion-weighted spin echo MRI sequence.....	50
Figure 2.4 - Diffusion-weighted imaging with different degrees of weighting.....	51
Figure 2.5 - Diffusion-weighted imaging with gradients applied along different axes	52
Figure 2.6 - Diffusion sphere and ellipsoid.....	52
Figure 2.7 - Diffusion tensor imaging	55
Figure 2.8 - Possible sources of diffusion anisotropy in a myelinated nerve axon	55
Figure 2.9 - Voxel-based techniques for analysing DTI parameters	58
Figure 2.10 - The problem with FA and crossing fibres	58
Figure 2.11 - Principle of tractography	60
Figure 3.1 - Anatomy of key language areas (Broca's and Wernicke's areas).....	75
Figure 3.2 - Anatomy of white matter tracts implicated in memory function	78
Figure 4.1 - Anatomy of the human visual system.....	86
Figure 4.2 - Anatomy of the optic radiation depicted from lateral and inferior aspect	88
Figure 4.3 - Two models for the retinotopic organisation of the optic radiation.....	95
Figure 4.4 - Anatomical variability of the optic radiation identified by dissection.....	100
Figure 5.1 - Intraoperative imaging during temporal lobe surgery for DNET	115
Figure 5.2 - Gradient non-linearity correction in a human subject.....	120
Figure 5.3 - Gradient non-linearity correction in a phantom.....	120
Figure 5.4 - Magnetic susceptibility artefact correction in intraoperative data	121
Figure 6.1 - Seed and way point for optic radiation tractography	130
Figure 6.2 - Quantification of visual field loss with Goldmann perimetry.....	133
Figure 6.3 - Assessing driving eligibility with Esterman binocular perimetry.....	134
Figure 7.1 - Seed and way points for optic radiation tractography	142
Figure 7.2 - Patient 1 with left parietal FCD.....	144
Figure 7.3 - Patient 2 with right inferior parietal DNET	145
Figure 7.4 - Patient 3 with tuberous sclerosis.....	146
Figure 7.5 - Patient 4 with otogenic left temporal lobe abscess	147
Figure 7.6 - Patient 5 with left fusiform gyrus DNET.....	148
Figure 7.7 - Patients 6 and 7 with focal damage	149
Figure 7.8 - Patient 9 with epidermoid tumour	150
Figure 7.9 - Patient 10 with left temporal lobe cavernoma	150
Figure 8.1 - Optic radiation tractography (method 2)	155
Figure 8.2 - Comparison of methods in a control subject	157
Figure 8.3 - Comparison of methods in patient 1 (right inferior parietal DNET)	158
Figure 8.4 - Comparison of methods in patient 2 (left temporal cavernoma).....	159

Figure 9.1 - Propagation of preoperative tractography on to postoperative imaging	166
Figure 9.2 - Measurement of the antero-posterior extent of resection of Meyer's loop	167
Figure 9.3 - Correlation between VFD and predicted damaged to Meyer's loop by image registration..	169
Figure 10.1 - Pipeline for processing of preoperative data.....	177
Figure 10.2 - Intraoperative MRI suite at NHNN (on next page)	178
Figure 10.3 - Pipeline for registration of pre- and intraoperative images for display during surgery	180
Figure 10.4 - BrainLab display of the first intraoperative image following initial dissection.....	181
Figure 10.5 - Operating microscope display of a patient undergoing right ATLRL.....	182
Figure 10.6 - Pipeline for intraoperative processing and display of images in cohort 2 (on prior page)..	185
Figure 10.7 - Distribution of postoperative VFD with and without iMRI-based image guidance	187
Figure 11.1 - Functional MRI findings with working memory task.....	194
Figure 11.2 - Voxel-based morphometry findings and working memory	195
Figure 11.3 - DTI findings (FA) in left HS and working memory	197
Figure 11.4 - DTI findings (FA) in right HS and working memory.....	198
Figure 11.5 - DTI findings (MD) in left HS and working memory.....	199
Figure 11.6 - Summary of changes observed in the working memory network in left and right HS.	200
Figure 12.1 - Whole brain TBSS analysis of changes in FA in left TLE compared to controls.....	214
Figure 12.2 - Whole brain TBSS analysis of changes in MD in left TLE compared to controls	214
Figure 12.3 - Whole brain TBSS analysis of changes in FA in right TLE compared to controls	215
Figure 12.4 - Whole brain TBSS analysis of changes in MD in right TLE compared to controls	215
Figure 12.5 - Whole brain TBSS analysis of changes in FA following left ATLRL.....	216
Figure 12.6 - Whole brain TBSS analysis of changes in MD following left ATLRL	217
Figure 12.7 - Whole brain TBSS analysis of changes in FA following right ATLRL	218
Figure 12.8 - Whole brain TBSS analysis of changes in MD following right ATLRL	219
Figure 13.1 - Residual FCD following a right middle frontal gyrus resection (patient 1).....	235
Figure 13.2 - Left inferior temporal gyrus FCD (patient 2)	235
Figure 13.3 - Left middle frontal gyrus MCD (patient 5)	235
Figure 13.4 - Summary of clinical, DTI and NODDI scans on subjects	237

LIST OF TABLES

Table 1.1 - International Classification of Epileptic Seizures (1981).....	38
Table 1.2 - International Classification of Epilepsies and Epileptic Syndromes (1989).....	39
Table 1.3 - Revised terminology and concepts for organization of seizures and epilepsies (2010).....	39
Table 1.4 - NICE guidelines on anti-epileptic drugs for focal seizures (2012).....	42
Table 1.5 - Minimum dataset for presurgical evaluation.....	44
Table 1.6 - Engel classification of seizure outcome following surgery.....	46
Table 1.7 - ILAE classification of seizure outcome following surgery.....	46
Table 3.1 - Summary of cross sectional DTI studies in epilepsy	72
Table 3.2 - Summary of longitudinal DTI studies in epilepsy	74
Table 3.3 - Anatomy of the two language pathways	76
Table 3.4 - Summary of DTI studies of memory in epilepsy	79
Table 3.5 - Summary of DTI studies of working memory function.....	83
Table 4.1 - Anatomical organisation of the three bundles of the optic radiation.....	87
Table 4.2 - Summary of literature on VFD following temporal lobe epilepsy surgery	94
Table 4.3 - Anatomical variability of the optic radiation by Klingler's fibre dissection	99
Table 4.4 - Summary of regions-of-interest and parameters used for optic radiation tractography	105
Table 4.5 - Anatomical variability of the optic radiation as shown by tractography.....	109
Table 5.1 - Approaches to intraoperative imaging	112
Table 5.2 - Measurements of brain shift during tumour surgery	117
Table 5.3 - Common sources of geometric image distortion.....	118
Table 6.1 - Outcome of patients in longitudinal study	125
Table 6.2 - Diagnoses of patients in longitudinal study based on structural MRI.....	125
Table 6.3 - Clinical and demographic characteristics of patients in longitudinal study	126
Table 6.4 - Epilepsy protocol for structural scans on 3T GE Signa Excite HDx scanner	128
Table 7.1 - Clinical and demographic characteristics of patients, management and visual outcomes	140
Table 8.1 - Demographics and imaging diagnoses of patients	154
Table 8.2 - Comparison of measurements from the two tractography methods.....	159
Table 9.1 - Clinical and demographic characteristics of patients, seizure and visual outcomes	164
Table 10.1 - Clinical and demographic characteristics of patients, seizure and visual outcomes	175
Table 11.1 - Clinical and demographic characteristics of patients and healthy controls.....	191
Table 11.2 - Working memory scores in each group - mean (sd)	193
Table 11.3 - Regions of GMV loss in patients compared to controls.....	205
Table 11.4 - Regions where GMV correlated with working memory performance	206
Table 11.5 - Regions where FA correlated with working memory performance	207
Table 11.6 - Regions where MD correlated with working memory performance.....	208
Table 12.1 - Clinical and demographic characteristics of patients	211

Table 12.2 - Summary of magnitude of longitudinal changes in diffusion parameters in the clusters of significantly altered FA in patients with TLE	221
Table 12.3 - Baseline changes in diffusion parameters in left TLE	225
Table 12.4 - Baseline changes in diffusion parameters in right TLE	227
Table 12.5 - Summary of longitudinal diffusion changes following left ATL	228
Table 12.6 - Summary of longitudinal diffusion changes following right ATL	230
Table 13.1 - Clinical and demographic characteristics of patients	232
Table 13.2 - Comparison of contrast-to-noise ratios for different diffusion contrasts	238

LIST OF ABBREVIATIONS

AC = anterior commissure

ACR = anterior corona radiata

AD = axial diffusivity

ADC = apparent diffusion coefficient

AED = anti-epileptic drug

AF = arcuate fasciculus

aFM = advanced fast marching tractography

ANOVA = analysis of variance

A-P = antero-posterior (distance)

ATLR = anterior temporal lobe resection

ATR = anterior thalamic radiation

AVM = arteriovenous malformation

BE = bending energy

CB = cingulum bundle

CC = corpus callosum (b = body, g = genu, s = splenium)

CHARMED = Composite Hindered And Restricted Model of Diffusion

CNR = contrast-to-noise ratio

CP = cerebral peduncle

CSF = cerebrospinal fluid

CST = cerebrospinal fluid

CT = computed tomography

CUDA = Compute Unified Device Architecture

DAI = diffuse axonal injury

DARTEL = Diffeomorphic Anatomical Registration using Exponentiated Lie algebra

DICOM = Digital Imaging and Communications in Medicine

DLPFC = dorsolateral prefrontal cortex

DNET = dysembryoplastic neuroepithelial tumour

DSB = digit span backwards

DSF = digit span forwards

DTI = diffusion tensor imaging

DVLA = Driver and Vehicle Licensing Agency

DWI = diffusion-weighted imaging

EC = external capsule

ECoG = electrocorticography

EEG = electroencephalogram

EFS = end folium sclerosis

EPI = echo-planar imaging

FA = fractional anisotropy

FACT = Fibre Assignment by Continuous Tracking

FCD = focal cortical dysplasia

FDG-PET = fluorodeoxyglucose positron emission tomography

FGRE = fast gradient echo

FL = frontal lobe

FLAIR = FLuid-Attenuated Inversion Recovery

FLASH = Fast Low Angle SHot

fMRI = functional magnetic resonance imaging

FMT = fast marching tractography

FRFSE = fast recovery fast spin echo

FSE = fast spin echo

FSPGR = fast spoiled gradient echo

FWE = family-wise error

FWHM = full-width at half-maximum

GMV = grey matter volume

GPU = graphical processing units

HARDI = high angular resolution diffusion imaging

HIP = hippocampus

HS = hippocampal sclerosis

IBE = International Bureau for Epilepsy

IC = internal capsule (a = anterior, g = genu, p = posterior)

ICVF = intracellular volume fraction

IFOF = inferior fronto-occipital fasciculus

ILAE = International League Against Epilepsy

ILF = inferior longitudinal fasciculus

iMRI = intraoperative magnetic resonance imaging

IQR = interquartile range

ITG = inferior temporal gyrus

JAC = Jacobian determinant

JICA = joint independent component analysis

LGN = lateral geniculate nucleus

LNS = letter number sequencing

MCD = malformations of cortical development

MD = mean diffusivity

MEG = magnetoencephalography

MEP = motor evoked potential

MFG = middle frontal gyrus

ML-TH = Meyer's loop to temporal horn (distance)

MNI = Montreal Neurological Institute (stereotactic space)

MRI = magnetic resonance imaging

MTG = middle temporal gyrus

NAA/Cr = N-acetylaspartate/creatine ratio

NMI = normalised mutual information

NMR = nuclear magnetic resonance

NODDI = Neurite Orientation Dispersion and Density Imaging

ODF = orientation distribution function

ODI = orientation dispersion index

ON = optic nerve

OR = optic radiation

PASAT = Paced Auditory Serial Addition Test

PCA = principal component analysis

PCR = posterior corona radiata

PD = proton density

PET = positron emission tomography

PFC = prefrontal cortex

PHC = parahippocampal cingulum

PHG = parahippocampal gyrus

PICo = probabilistic index of connectivity

PROPELLER = Periodically Rotated Overlapping Parallel Lines with Enhanced Reconstruction

PTR = posterior thalamic radiation

RD = radial diffusivity

ROI = region-of-interest

RRMS = relapsing-remitting multiple sclerosis

SAH = selective amygdalo-hippocampectomy

SDMT = Symbol Digit Modalities Test

SE = spin echo

SENSE = sensitivity encoding

SFG = superior frontal gyrus

SIRT = Sternberg Item Recognition Test

SLF = superior longitudinal fasciculus

SMA = supplementary motor area

SPECT = single positron emission computed tomography

SPL = superior parietal lobe

SPM = statistical parametric mapping

STEAM = stimulated-echo acquisition mode

STG = superior temporal gyrus

TBI = traumatic brain injury

TBSS = tract-based spatial statistics

TE = echo time

TEND = tensor deflection model

TFCE = Threshold-Free Cluster Enhancement

TL = temporal lobe

TLE = temporal lobe epilepsy

TP-ML = temporal pole to Meyer's loop (distance)

TP-OP = temporal pole to occipital pole (distance)

TR = repetition time

UF = uncinate fasciculus

VBA = voxel-based analysis

VEP = visual evoked potentials

VFD = visual field deficit

WAIS-III = Wechsler Adult Intelligence Scale Third Edition

ZOOM = zonally oblique multislice

ACKNOWLEDGEMENTS

I am deeply grateful to John Duncan, my principal supervisor, for excellent guidance and detailed feedback throughout my thesis and to Mark Symms, my secondary supervisor, for discussions on the acquisition and analysis of data.

I must greatly thank two key colleagues in Chalfont, Jason Stretton and Meneka Sidhu, with whom the recruitment of patients and acquisition of data for the longitudinal study was jointly performed and with whom I had many helpful discussions and brain storming sessions throughout. Numerous other colleagues in the Epilepsy Research Group provided input during and outside research meetings, including Mahinda Yogarajah, Christian Vollmar, Silvia Bonelli, Serge Vulliemoz, Umair Chaudhary and Anja Haag.

The radiographers in Chalfont - Philippa Bartlett, Elaine Williams and Jane Burdett - always provided excellent images and Peter Gilford resolved any IT issues promptly and responded to my many requests for an ever increasing amount of data storage capacity or the accidental overwriting of data.

I am very appreciative of all the software development performed in the UCL Centre for Medical Image Computing by Pankaj Daga, building on earlier work by Marc Modat, and supervised by Sebastien Ourselin. The ultimate goal of my research would not have been achieved without this hard work. I also thank Gary Zhang and Danny Alexander from the Microstructure Imaging Group who were very open to discussions about assessing novel microstructural models in a clinical cohort.

I would like to thank colleagues in the Neuroradiology Department at the National Hospital for Neurology and Neurosurgery - Mark White, Laura Mancini, Caroline Micallef and Tarek Yousry - for enabling the work to be implemented in a clinical environment and Andrew McEvoy and Anna Miserocchi from the Department of Neurosurgery for their surgical skills and willingness to assess new technologies.

Finally, this work could not have been undertaken without the patients and healthy controls who agreed to participate in the research and give up a significant amount of their time to do so. I hope that the results obtained will be able to help people in a similar situation in the future.

FUNDING SOURCES

The project was funded by a Wellcome Trust Programme Grant (083148) and supported by the National Institute for Health Research University College London Hospitals Biomedical Research Centre.

I was funded by a Clinical Research Training Fellowship from the Medical Research Council (G0802012) for 3 years and by a Wellcome Trust/Department of Health Innovation Challenge Fund Programme Grant (HICF-T4-275) for 1 year.

Software development by Pankaj Daga was funded by a joint Cancer Research United Kingdom/Engineering and Physical Sciences Research Council grant (C1519/A10331).

Development of the NODDI model by Daniel Alexander and Hui Zhang was supported by the Engineering and Physical Sciences Research Council (grant EP/E007748) and the EU CONNECT consortium.

The Wolfson Trust and the Epilepsy Society supported the Epilepsy Society MRI scanner.

OUTLINE AND STATEMENT OF PERSONAL CONTRIBUTION

In Chapters 1 to 5, I present an introduction and literature review.

- Chapter 1 provides an introduction to epilepsy including the definition, epidemiology and classification with an emphasis on temporal lobe epilepsy and surgical treatment of refractory patients
- Chapter 2 describes the underlying principles of diffusion imaging including the various parameters that can be derived for use in clinical studies and the basis of tractography
- Chapter 3 summarises the clinical diffusion imaging studies that have been undertaken in patients with epilepsy, including cross-sectional and longitudinal studies and those looking at cognitive skills such as language or memory. In addition, I describe how diffusion imaging contributes to understanding working memory in conditions other than epilepsy.
- Chapter 4 introduces the anatomy of the optic radiation and gives a detailed synopsis of the lessons learned from temporal lobe epilepsy surgery. Both dissection-based and imaging-based studies of this structure are summarised.
- Chapter 5 contrasts various approaches to intraoperative imaging, describes how intraoperative MRI has been used in tumour and epilepsy surgery and introduces the technical challenges to be addressed for its optimal use, principally brain shift and geometric image distortion.

Chapters 6 to 13 describe the experimental studies. I performed the data collection and analysis unless otherwise stated.

- In Chapter 6, I describe the generic methods employed concentrating on the longitudinal assessment of a cohort of patients with TLE undergoing surgery. Recruitment and scanning of these patients was conducted jointly by me, Jason Stretton and Meneka Sidhu. The software for image registration was written by Pankaj Daga and Marc Modat, supervised by Sebastien Ourselin.
- In Chapter 7, I describe the role of preoperative optic radiation tractography in patients undergoing surgery near the optic radiation and demonstrate its utility for planning surgery and counselling patients on the risk to vision from surgery. Some of the scans were acquired by Mahinda Yogarajah.
- In Chapter 8, I compare two methods for optic radiation tractography to show their relative advantages and disadvantages for different types of epilepsy surgery. The second method was developed by Jonathan Ashmore and applied by Laura Mancini. Measurements were performed by two raters – me and Laura Mancini – but I performed all subsequent statistical analysis.

- In Chapter 9, I show that preoperative tractography data can be accurately and rapidly propagated onto postoperative images to predict the visual outcome. The software used was developed as described in Chapter 6.
- In Chapter 10, I describe the use of optic radiation tractography in real-time during surgery showing that this enables the surgeon to reduce the risk of a significant visual deficit without adversely affecting the seizure outcome. I recruited the patients, performed the pre- and postoperative imaging and visual fields and prepared the optic radiation tractography. The subsequent use of these data during surgery relied on a large team of individuals including Pankaj Daga, Marc Modat, Sebastien Ourselin (software development); Mark White, Laura Mancini (integration of software with BrainLab neuronavigation system); Caroline Micallef (assessing images and outlining the ventricle during surgery); Andrew McEvoy, Anna Miserocchi (performing the surgery and providing feedback). I performed the quantitative analysis of brain shift and statistical analysis of the surgical outcomes.
- In Chapter 11, I demonstrate altered grey and white matter integrity within the frontoparietal working memory in TLE, that this correlates with working memory performance and that the temporal lobes also play a role. Analysis of the functional MRI scans and neuropsychological assessment of working memory performance was performed by Jason Stretton.
- In Chapter 12, I demonstrate longitudinal changes in diffusion parameters following temporal lobe resection including changes consistent with Wallerian degeneration in tracts adjacent to the resection and structural plasticity within the corona radiata, internal and external capsules.
- In Chapter 13, I demonstrate that a novel diffusion model (NODDI) may be of clinical benefit in detecting focal cortical dysplasia. The model and software were developed by Gary Zhang.

Chapter 14 summarises the main findings and conclusions, the limitations and future work and the clinical relevance of the studies.

PUBLICATIONS ASSOCIATED WITH THIS THESIS

Peer-reviewed papers as a first author:

Winston GP. The physical and biological basis of quantitative parameters derived from diffusion MRI. *Quant Imaging Med Surg* 2012;2(4):254-65. Based on Chapters 2 and 3.

Winston GP. Epilepsy surgery, vision and driving: what has surgery taught us and could modern imaging reduce the risk of visual deficits? *Epilepsia* 2013;54(11):1877-88. Based on Chapter 4.

Winston GP, Yogarajah M, Symms MR, McEvoy AW, Micallef C, Duncan JS. Diffusion tensor imaging tractography to visualize the relationship of the optic radiation to epileptogenic lesions prior to neurosurgery. *Epilepsia* 2011;52(8):1430-8. Based on Chapter 7.

Winston GP, Mancini L, Stretton J, Ashmore J, Symms MR, Duncan JS, Yousry TA. Diffusion tensor imaging tractography of the optic radiation for epilepsy surgical planning: a comparison of two methods. *Epilepsy Res* 2011;97(1-2):124-32. Based on Chapter 8.

Winston GP, Daga P, Stretton J, Modat M, Symms MR, McEvoy AW, Ourselin S, Duncan JS. Optic radiation tractography and vision in anterior temporal lobe resection. *Ann Neurol* 2012;71(3):334-41. Based on Chapter 9.

Winston GP, Stretton J, Sidhu MK, Symms MR, Thompson PJ, Duncan JS. Structural correlates of impaired working memory in hippocampal sclerosis. *Epilepsia* 2013;54(7):1143-53. Based on Chapter 11.

Winston GP, Stretton J, Sidhu MK, Symms MR, Duncan JS. Progressive white matter changes following anterior temporal lobe resection for epilepsy. *Neuroimage Clin* 2013; doi:10.1016/j.nicl.2013.12.004. Based on Chapter 12.

Winston GP, Micallef C, Symms MR, Alexander D, Duncan JS, Zhang H. Advanced diffusion imaging sequences could aid assessing patients with focal cortical dysplasia and epilepsy. *Epilepsy Res* 2013 doi:10.1016/j.epilepsyres.2013.11.004. Based on Chapter 13.

Peer-reviewed papers as a co-author:

Daga P, **Winston G**, Modat M, Cardoso MJ, White M, Mancini L, McEvoy AW, Thornton J, Micallef C, Yousry T, Hawkes D, Duncan JS, Ourselin S. Improved neuronavigation through integration of intraoperative anatomical and diffusion images in an interventional MRI suite. *Lecture Notes in Computer Science* 2011;6689:168-78.

Daga P, **Winston G**, Modat M, White M, Mancini L, Cardoso MJ, Symms M, Stretton J, McEvoy AW, Thornton J, Micallef C, Yousry T, Hawkes D, Duncan JS, Ourselin S. Accurate localization of optic radiation during neurosurgery in an interventional MRI suite. *IEEE Trans Med Imaging* 2012;31(4):882-91.

Stretton J, **Winston G**, Sidhu M, Centeno M, Vollmar C, Bonelli S, Symms M, Koepp M, Duncan JS, Thompson PJ. Neural correlates of working memory in Temporal Lobe Epilepsy - an fMRI study. *Neuroimage* 2012;60(3):1696-703.

Cardoso MJ, **Winston G**, Modat M, Keihaninejad S, Duncan J, Ourselin S. Geodesic shape-based averaging. *Med Image Comput Comput Assist Interv* 2012;15(Pt 3):26-33.

Stretton J, **Winston GP**, Sidhu M, Bonelli S, Centeno M, Vollmar C, Cleary RA, Williams E, Symms MR, Koepp MJ, Thompson PJ, Duncan JS. Disrupted segregation of working memory networks in temporal lobe epilepsy. *Neuroimage Clin* 2013;1(2):273-81.

Sidhu MK, Stretton J, **Winston GP**, Bonelli S, Centeno M, Vollmar C, Symms M, Thompson PJ, Koepp MJ, Duncan JS. A functional magnetic resonance imaging study mapping the episodic memory encoding network in temporal lobe epilepsy. *Brain* 2013;136(Pt 6):1868-88.

Conference abstracts as first author:

Winston GP, Yogarajah M, Symms MR, McEvoy A, Micallef C, Duncan JS. Tractography to visualise the relationship of the optic radiation to epileptogenic lesions prior to neurosurgery. Presented at Association of British Neurologists Meeting, London, September 2010. *J Neurol Neurosurg Psychiatry* 2010;82(e1):1 doi:10.1136/jnnp.2010.235572.

Winston GP, Daga P, Stretton J, Modat M, Symms MR, McEvoy AW, Ourselin S, Duncan JS. Developing optic radiation tractography to reduce visual field deficits following anterior temporal lobe resection. Presented at 21st Meeting of the European Neurological Society, Lisbon, May 2011. *J Neurol* 2011;258:54.

Winston G, Stretton J, Sidhu M, Symms MR, Duncan JS. Could laterality of diffusion measures prove useful in determining the lateralisation of non-lesional temporal lobe epilepsy? Presented at Association of British Neurologists Annual Meeting, Newcastle, October 2011. *J Neurol Neurosurg Psychiatry* 2012; 83(e1):9 doi:10.1136/jnnp-2011-301993.31

Winston GP, Stretton J, Sidhu MK, Vollmar C, Symms M, Thompson PJ, Duncan J. Functional and structural connectivity of working memory networks in temporal lobe epilepsy. Presented at 10th European Congress on Epileptology, London, October 2012. *Epilepsia* 2012;53(Suppl s5):127.

Winston GP, Symms MR, Alexander DC, Duncan JS, Zhang H. Clinical utility of NODDI in assessing patients with epilepsy due to focal cortical dysplasia. Presented at International Society for Magnetic Resonance in Medicine (ISMRM) 21st Scientific Meeting and Exhibition, Salt Lake City, April 2013. *Proc Intl Soc Mag Reson Med* 2013;21:0784.

Winston GP, Cardoso MJ, Williams EJ, Burdett JL, Bartlett PA, Espak M, Behr C, Duncan JS, Ourselin S. Online automated hippocampal segmentation in patients with epilepsy. Presented at 23rd Meeting of the European Neurological Society, Barcelona, June 2013. *J Neurol* 2013;260(Suppl1):S29.

Conference abstracts as co-author:

Daga P, **Winston G**, Modat M, Cardoso MJ, Stretton J, Symms M, McEvoy AW, Hawkes D, Duncan J, Ourselin S. Integrating structural and diffusion MR information for optic radiation localisation in focal epilepsy patients. *2011 IEEE International Symposium on Biomedical Imaging: From Nano to Macro* 2011;353-6. doi:10.1109/ISBI.2011.5872422.

Sidhu MK, Stretton J, **Winston G**, Bonelli S, Centeno M, Vollmar C, Thompson P, Symms M, Koepp M, Duncan JS. Frontal lobe activity during encoding in temporal lobe epilepsy. *Epilepsia* 2011(Suppl s6);52:175.

Sidhu MK, Stretton J, **Winston GP**, Bonelli S, Symms M, Thompson PJ, Koepp M, Duncan J. Imaging dynamic memory encoding network plasticity post anterior temporal lobe resection for refractory temporal lobe epilepsy. *Epilepsia* 2012;53(Suppl s5):127

Sidhu M, Stretton J, **Winston G**, Vollmar C, Bonelli S, Thompson P, Koepp M, Duncan JS. Effect of age of onset and duration of epilepsy on memory encoding in temporal lobe epilepsy. *J Neurol Neurosurg Psychiatry* 2012;83(e1) doi:10.1136/jnnp-2011-301993.4

Daga P, Modat M, **Winston G**, White M, Mancini L, McEvoy AW, Thornton J, Yousry T, Duncan JS, Ourselin S. Susceptibility artefact correction by combining B0 field maps and non-rigid registration using graph cuts. *Proc. SPIE* 2013;8669:86690B doi:10.1117/12.2006800

Cleary R, Stretton J, **Winston G**, Symms M, Thompson P, Koepp M, Duncan J, Foong J. Temporal lobe epilepsy & affective disorders: the role of the subgenual prefrontal cortex. *J Neurol Neurosurg Psychiatry* 2013;84(9):e1.

Sidhu MK, Stretton J, **Winston GP**, Centeno M, Bonelli S, Vollmar C, Symms M, Thompson PJ, Koepp MJ, Duncan JS. Extra-temporal memory encoding networks in temporal lobe epilepsy – an fMRI study. *Epilepsia* 2013;54(S3):213.

CONFERENCE POSTERS AND TALKS RELATED TO THIS THESIS

Tractography to delineate the relationship of the optic radiation to epileptogenic lesions prior to neurosurgery. Medical Research Society/Academy of Medical Sciences/Royal College of Physicians, Annual Meeting for Clinician Scientists in Training, February 2010, London. Poster presentation.

Tractography to visualise the relationship of the optic radiation to epileptogenic lesions prior to neurosurgery. Association of British Neurologists Autumn Meeting, September 2010, London. Platform presentation.

Validation of preoperative tractography of the optic radiation with intracranial electrode recording of visual evoked potentials. International League Against Epilepsy UK Chapter Annual Meeting, October 2010, Brighton. Platform presentation.

Application of tractography to delineate the relationship of the optic radiation to epileptogenic lesions prior to neurosurgery. 64th Annual Meeting of the American Epilepsy Society, December 2010, San Antonio. Poster presentation.

Tractography of the optic radiation and epilepsy surgery. Chinese University of Hong Kong, Department of Neurosurgery, March 2011, Hong Kong. Invited lecture.

Propagation of probabilistic tractography of the optic radiation for neuronavigation in epilepsy surgery. 19th Annual International Society for Magnetic Resonance in Medicine Meeting, May 2011, Montreal. Platform presentation.

Developing optic radiation tractography to reduce visual field deficits following anterior temporal lobe resection. 21st Meeting of the European Neurological Society, May 2011, Lisbon. Platform presentation.

Propagation of probabilistic tractography of the optic radiation for neuronavigation in epilepsy surgery. British Chapter International Society for Magnetic Resonance in Medicine Annual Meeting, September 2011, Manchester. Platform presentation.

Could laterality of diffusion measures prove useful in determining the lateralisation of non-lesional temporal lobe epilepsy? Association of British Neurologists Annual Meeting, October 2011, Newcastle. Platform presentation.

Structural correlates of impaired working memory in temporal lobe epilepsy. 65th Annual Meeting of the American Epilepsy Society, December 2011, Baltimore. Poster.

An Introduction to Epilepsy. Seizing Control: An Exploration of Artistic and Medical Representations of Epilepsy (HealthGovMatters.eu), January 2012, London. Invited speaker.

Structural correlates of impaired working memory in TLE using VBM and DTI. International League Against Epilepsy UK Chapter Scientific Meeting, April 2012, London. Platform presentation.

Structural correlates of impaired working memory in TLE using VBM and DTI. 18th Annual Meeting of the Organization for Human Brain Mapping, June 2012, Beijing. Poster presentation.

Tractography and interventional MRI for epilepsy surgery. Department of Neurosurgery, Chinese PLA General Hospital, June 2012, Beijing. Invited speaker.

Functional and structural connectivity of working memory networks in temporal lobe epilepsy. 10th European Congress on Epileptology, October 2012, London. Poster presentation.

Tractography and display of critical tracts. 10th European Congress on Epileptology, October 2012, London. Invited speaker.

Clinical utility of NODDI in assessing patients with epilepsy due to focal cortical dysplasia. 22nd Postgraduate Symposium of the British Chapter of ISMRM, March 2013, London. Platform presentation.

Clinical utility of NODDI in assessing patients with epilepsy due to focal cortical dysplasia. 21st Annual Meeting of the International Society for Magnetic Resonance in Medicine, April 2013, Salt Lake City. Platform presentation.

Online automated hippocampal segmentation in patients with epilepsy. 23rd Meeting of the European Neurological Society, June 2013, Barcelona. Platform presentation.

Poster Highlight Session on Epilepsy. 23rd Meeting of the European Neurological Society, June 2013, Barcelona. Chair.

Utility of image guidance with intraoperative MRI to avoid visual field deficits from epilepsy surgery. Up and coming techniques in Medical Physics translated into clinical practice, Institute of Physics Medical Physics Group, November 2013, London. Poster presentation.

AWARDS AND PRIZES

Best 10% poster award, 64th Annual Meeting of the American Epilepsy Society, December 2010.

First Prize for PhD students, Queen Square Symposium, March 2011.

Queen Square Prize in Neurology (for essay Developing Optic Radiation Tractography to Reduce Visual Field Deficits following Anterior Temporal Lobe Resection), August 2011.

Sir Peter Mansfield Prize for best presentation on innovative technical developments in the field of magnetic resonance in medicine and biology, British Chapter International Society for Magnetic Resonance in Medicine Annual Meeting, September 2011.

Best 10% poster award, 65th Annual Meeting of the American Epilepsy Society, December 2011.

Editor's choice, Seizure, June 2012.

Best poster award, 10th European Congress on Epileptology, October 2012.

Merit Award (Magna Cum Laude), 21st Annual Meeting of the International Society for Magnetic Resonance in Medicine, April 2013.

1 EPILEPSY

1.1 Introduction

This chapter introduces epilepsy by reviewing the definition, epidemiology and classification. The syndrome of temporal lobe epilepsy (TLE) is discussed emphasising the anatomy of the temporal lobe, clinical features, medical and surgical treatment. The concept of refractory epilepsy is defined along with the necessary evaluation to consider surgical treatment. The outcome measures for seizure frequency following surgery and the potential adverse consequences that are studied in this thesis are introduced.

1.2 Epilepsy

1.2.1 Definition

Epilepsy is one of the most common and serious neurological disorders. It does not represent a single disease or syndrome. The term is used to refer to a group of disorders with a variety of symptomatic presentations reflecting underlying brain dysfunction from different pathological causes. The consensus definitions from the International League Against Epilepsy (ILAE) and International Bureau for Epilepsy (IBE) are (Fisher et al. 2005):

*“An **epileptic seizure** is a transient occurrence of signs and/or symptoms due to abnormal excessive or synchronous neuronal activity in the brain.”*

*“**Epilepsy** is a disorder of the brain characterized by an enduring predisposition to generate epileptic seizures and by the neurobiologic, cognitive, psychological, and social consequences of this condition. The definition of epilepsy requires the occurrence of at least one epileptic seizure.”*

1.2.2 Epidemiology

Epilepsy is common. In the developed world, the incidence is 40-70/100000/year with a prevalence of active epilepsy of 4-10/1000 (Sander & Shorvon 1996). A UK community-based study suggested an age- and sex-adjusted incidence rate of 46/100000/year (MacDonald et al. 2000) whilst a large study conducted over 50 years in Rochester, Minnesota (1935-1984) gave an age-adjusted incidence of 44/100000/year (Hauser et al. 1993).

The age-specific incidence is highest in the young, especially the first few months of life, and in later life. In a UK General Practice survey, 37% of newly identified seizures occurred before the age of 20 years with the onset in a further quarter after the age of 60 years (Sander et al. 1990). In this study 52% of seizures were partial, 39% generalised and 9% unclassified. The findings in Minnesota were similar with half of seizures beginning in childhood or adolescence with 57% partial, 40% generalised and 3% unclassified (Hauser et al. 1993).

The most recent data from the General Practice Research Database presented by the Joint Epilepsy Council suggest an incidence of 51/100000/year and prevalence of 0.97% in the UK (Joint Epilepsy Council of the UK and Ireland 2011). Epilepsy thus affects around 600,000 people in the UK based on 2010 population estimates.

Mortality is raised to 2-3 times the general population. In a UK General Practice study, the standardised mortality ratio was 2.1 despite 70% of patients achieving seizure freedom (Lhatoo et al. 2001). Deaths may be directly related to epilepsy (e.g. SUDEP, status epilepticus), indirectly related (e.g. accidents, aspiration pneumonia), related to the underlying disease (e.g. cerebrovascular) or unrelated (e.g. cardiovascular). The rate of SUDEP is approximately 0.09 per 1000 person-years (Lhatoo et al. 2001) but varies greatly according to type and severity of epilepsy.

1.2.3 Classification

The classification of epileptic seizures and epilepsy has evolved over the years from purely clinical observation and expert opinion to an era where modern neuroimaging and genetic findings play a key part. The 1981 International Classification of Epileptic Seizures (International League Against Epilepsy 1981) and 1989 International Classification of Epilepsies and Epileptic Syndromes (International League Against Epilepsy 1989) have recently been superseded by the proposed 2010 classification (Berg et al. 2010), but both are presented as terms from the former are still in common clinical usage.

1.2.3.1 International Classification of Epileptic Seizures (1981)

This classification utilises clinical and electroencephalographic features. The key distinction is between partial seizures, where the *“first clinical and electroencephalographic changes indicate activation of a system of neurons limited to part of one cerebral hemisphere”* and generalised seizures where the *“first clinical changes indicate initial involvement of both hemispheres”*. Partial seizures are further subdivided into simple partial seizures where consciousness is not impaired and complex partial seizures in which consciousness is impaired. A simplified summary is presented in Table 1.1.

1.2.3.2 International Classification of Epilepsies and Epileptic Syndromes (1989)

This classification proposes two main divisions. The first is between epilepsies with generalised seizures and those with partial seizures. The second is on the basis of aetiology between symptomatic (secondary) (*“the consequence of a known or suspected disorder of the central nervous system”*), idiopathic (primary) (*“no underlying cause”*) and cryptogenic (*“presumed to be symptomatic, but the etiology is not yet known”*). A simplified summary is presented in Table 1.2.

1.2.3.3 Revised terminology and concepts for organization of seizures and epilepsies (2010)

The classification of seizures remains between partial and generalised although the definition of these terms has changed and the term focal is used in place of partial (Table 1.3). Generalised seizures are those *“originating at some point within, and rapidly engaging, bilaterally distributed networks”* and focal

seizures are those “*originating within networks limited to one hemisphere ... discretely localized or more widely distributed*”. The distinction between simple and complex focal seizures has been abandoned.

The terms idiopathic, symptomatic and cryptogenic for the underlying type of cause have been replaced by genetic, structural/metabolic and unknown cause. Further diseases, syndromes and epilepsies have been replaced by:

- Electroclinical syndromes (e.g. Lennox-Gastaut syndrome)
- Distinctive constellations (e.g. mesial TLE with hippocampal sclerosis)
- Epilepsies associated with structural or metabolic conditions (e.g. malformations of cortical development)
- Epilepsies of unknown cause

I. PARTIAL (FOCAL, LOCAL) SEIZURES

- A. Simple partial seizures
- B. Complex partial seizures
- C. Partial seizures evolving to generalised tonic-clonic convulsions

II. GENERALISED SEIZURES (convulsive or non-convulsive)

- A. Absence seizures
- B. Myoclonic seizures
- C. Clonic seizures
- D. Tonic seizures
- E. Tonic-clonic seizures
- F. Atonic seizures

III. UNCLASSIFIED EPILEPTIC SYNDROMES

Table 1.1 - International Classification of Epileptic Seizures (1981)

Adapted from International League Against Epilepsy 1981.

1. Localisation-related (focal, local, partial) epilepsies and syndromes

- 1.1. Idiopathic (with age-related onset)
- 1.2. Symptomatic
- 1.3. Cryptogenic

2. Generalised epilepsies and syndromes

- 2.1. Idiopathic (with age-related onset)
- 2.2. Cryptogenic or symptomatic
- 2.3. Symptomatic

3. Epilepsies and syndromes undetermined whether focal or generalised

- 3.1. With both generalised and focal seizures
- 3.2. Without unequivocal generalised or focal features

4. Special syndromes

- 4.1. Situation-related seizures
-

Table 1.2 - International Classification of Epilepsies and Epileptic Syndromes (1989)

Adapted from International League Against Epilepsy 1989.

Generalised seizures

- Tonic-clonic (in any combination)
- Absence
- Myoclonic
- Clonic
- Tonic
- Atonic

Focal seizures**Unknown**

Table 1.3 - Revised terminology and concepts for organization of seizures and epilepsies (2010)

From Berg et al. 2010.

1.3 Temporal Lobe Epilepsy

1.3.1 Introduction

Around 60% of the adult population with epilepsy have focal seizures. The majority of focal seizures arise from the temporal lobe, particularly the mesial structures, and this comprises the majority of referrals for epilepsy surgery (Engel, Jr. et al. 2003). Of those undergoing resective neurosurgery, the most frequent pathological finding is hippocampal sclerosis, either in isolation or in association with a second pathology (“dual pathology”).

1.3.2 Anatomy of the Temporal Lobe

The mesial structures of the temporal lobe comprise a network including the hippocampus, entorhinal and perirhinal cortices and amygdala. The intrinsic properties and high degree of local connectivity of these structures render them particularly prone to seizure activity. Seizures most commonly arise here, particularly from the hippocampus, rather than the lateral neocortical structures. The original concept by Papez and a limbic circuit involving the hypothalamus, anterior thalamus, cingulate cortex and hippocampus and modulating emotional behaviour has thus been expanded by MacLean to include the amygdala and parahippocampal structures.

The hippocampus is implicated in learning, memory and plasticity and involved in a variety of diseases including epilepsy, Alzheimer’s disease and psychiatric disorders. The major cortical input is via neocortical projections to the entorhinal cortex then on to the dentate gyrus via the perforant path. Subcortical input to the hypothalamus is predominantly cholinergic from the medial septal nucleus via the fimbria/fornix and is critical for learning and cognitive function.

The classic trisynaptic pathway comprises perforant path input to the dentate gyrus from the entorhinal cortex which then connects to CA3 and in turn to CA1 via Schaffer collaterals. There is also separate direct input from the entorhinal cortex to CA1 (temporoammonic pathway) and also CA3.

Information from CA1 passes to the subiculum and cortical projections from both these structures feed back to the entorhinal, perirhinal and prefrontal cortices whilst subcortical projections pass to the lateral septal nucleus, thalamus, amygdala and hypothalamus.

The adjacent amygdala is important in learning, but in addition plays in a role in emotion including fear and aggression.

1.3.3 Clinical Features of Mesial TLE

A typical mesial temporal lobe seizure comprises an aura followed by behavioural manifestations. The aura is most commonly a rising epigastric sensation, but may also include olfactory or gustatory sensations, psychic phenomena such as perceptual hallucinations, déjà or jamais vu and autonomic or emotional changes. The behavioural seizure lasting 1-2 minutes commences with impaired consciousness and a fixed stare with dilated pupils followed by oro-alimentary automatisms (such as lip smacking or chewing), limited interaction with the environment or stereotyped repetitive motor behaviour. Other

features such as dystonic posturing, head or eye deviation or unilateral automatisms or hemiparesis may help lateralise the seizure onset. Postictally the patient may be disorientated and amnesic for the event. Postictal aphasia suggests onset in the speech-dominant hemisphere.

Patients with hippocampal sclerosis often have a classical clinical picture. A history of febrile convulsions or early neurological insults in a genetically susceptible individual is followed by complex partial seizures beginning in the first or second decade of life. These often remit initially with treatment but subsequently have a high risk of becoming refractory to medical treatment. Structural changes in the hippocampus, amygdala and limbic cortex are associated with more widespread functional changes including hypometabolism of the whole temporal lobe and ipsilateral thalamus or basal ganglia (Henry et al. 1993).

The syndrome of mesial TLE is associated with widespread cognitive impairment (Hermann et al. 1997). Left TLE is associated with impaired verbal learning and memory, particularly delayed recall (Helmstaedter et al. 1997a) whilst right TLE is associated with impaired performance on visual (non-verbal) tasks (Gleissner et al. 1998). These impairments and imaging findings are discussed further in Chapter 3.

1.3.4 Clinical Features of Neocortical TLE

Neocortical TLE arising from the lateral structures is much less common than mesial TLE and may be associated with lesions such as focal cortical dysplasia, tumours or cavernoma. Seizures often propagate to the mesial structures making neocortical and mesial TLE clinically indistinguishable. However, there are some features that are supportive of a lateral onset (Foldvary et al. 1997, Gil-Nagel & Risinger 1997, Maillard et al. 2004).

A history of febrile convulsions or early insults such as head injury is less common and age of onset is usually later than mesial TLE. The aura is typically experiential including auditory, vertiginous or complex visual hallucinations rather than an epigastric aura. The seizures are shorter, more frequently generalise and lack the typical automatisms of MTLE whilst involving early contralateral dystonic posturing and early loss of contact.

1.3.5 Medical Treatment

1.3.5.1 Anti-Epileptic Drugs

Since the discovery of the efficacy of phenobarbital in treating seizures by Hauptmann in 1912, a multitude of anti-epileptic drugs (AEDs) have been licensed as monotherapy or adjunctive therapy for partial seizures. The recommendations given by NICE guidelines (National Institute of Health and Clinical Excellence 2012) are illustrated in Table 1.4.

Gabapentin, phenobarbital, phenytoin and topiramate are also licensed for monotherapy and more recently perampanel and retigabine have been licensed for adjunctive therapy although retigabine may now lose favour due to recent reports of side effects with long term usage. Despite this vast choice, 20-30% of patients do not achieve seizure freedom (Sander 1993). Patients not responding to the first medication are less likely to respond to subsequent medications and the remission rate is lower for those

with symptomatic or cryptogenic epilepsy than idiopathic epilepsy (60% vs. 74%) (Kwan & Brodie 2000). Patients with only complex partial seizures respond poorly compared to those with secondary generalised seizures, with only 23-26% seizure-free at 12 months in an observational study (Mattson et al. 1996).

First-line AEDs (monotherapy)	Adjunctive AEDs	Other AEDs that may be considered on referral to tertiary care
Carbamazepine	Carbamazepine	Eslicarbazepine acetate
Lamotrigine	Clobazam	Lacosamide
Levetiracetam	Gabapentin	Phenobarbital
Oxcarbazepine	Lamotrigine	Phenytoin
Sodium valproate	Levetiracetam	Pregabalin
	Oxcarbazepine	Tiagabine
	Sodium valproate	Vigabatrin
	Topiramate	Zonisamide

Table 1.4 - NICE guidelines on anti-epileptic drugs for focal seizures (2012)

Adapted from National Institute of Health and Clinical Excellence 2012.

1.3.5.2 Medication-Refractory Epilepsy

It is important to be able to identify and define those patients who are refractory to anti-epileptic medications. The trend has been to defining refractory epilepsy earlier in the disease progression with a consensus proposal from the ILAE suggesting that only two AED trials are necessary (Kwan et al. 2010):

“Drug resistant epilepsy may be defined as failure of adequate trials of two tolerated and appropriately chosen and used AED schedules (whether as monotherapies or in combination) to achieve sustained seizure freedom.”

Factors predictive of refractory epilepsy include symptomatic or cryptogenic epilepsies, a documented aetiology, neurological dysfunction, a high initial seizure frequency and focal EEG slowing. It is these patients who should be considered for surgical treatment.

1.3.6 Surgical Treatment

1.3.6.1 Rationale

Patients who fail to respond to medication and have ongoing seizures are at significant risk of both morbidity and mortality. Aside from sustaining seizure-related injuries, there are negative social, cognitive and psychiatric consequences. Ongoing seizures preclude holding a driving licence with the consequent loss of independence and have implications for employment and educational attainment.

In medically refractory TLE, a progressive decline in memory is reported by patients (Hendriks et al. 2002) and a higher proportion of patients with TLE undergoing medical treatment have significant memory decline at 2-10 years of neuropsychological testing compared to those undergoing surgery (Helmstaedter et al. 2003). TLE is a network disease and the changes are more widespread than just being confined to the temporal lobe. Interictal FDG-PET (fluorodeoxyglucose positron emission tomography) studies showing unilateral temporal lobe hypometabolism often show involvement of the ipsilateral thalamus and basal ganglia (Henry et al. 1993) whilst diffusion MRI shows widespread changes that may not be fully reversible if seizures are controlled (see Chapter 3).

1.3.6.2 Types of Surgery

Surgical approaches may be broadly divided into two categories:

- **Resective surgery** - aims to eliminate seizures by removal of the epileptogenic area (lesionectomy, lobectomy)
- **Palliative surgery** - aims to stop the most disabling seizures and/or reduce the seizure burden (corpus callosotomy, multiple subpial transections, vagal nerve stimulation)

1.3.6.3 Resective Surgery

In the late 19th century, Hughlings Jackson suggested removal the lesion as a treatment for epilepsy and early surgery by MacEwan (Glasgow) and Horsley (London) relied solely on clinical localisation. However the development of EEG greatly aided surgical approaches with the recognition of spikes over the anterior temporal lobe in psychomotor epilepsy leading to the concept of anterior temporal lobe resection (ATLR) (Bailey & Gibbs 1951).

TLE remains particularly amenable to surgical resection and ATLR is the most common surgical procedure. The benefits of ATLR were established in a randomised controlled trial in which 58% achieved freedom from seizures impairing awareness compared to 8% in the control group of medication only (Wiebe et al. 2001). It is cost effective but remains underutilised with patients being referred for surgical evaluation of refractory complex partial seizures at an average of 22.1 years after seizure onset (Berg et al. 2003). This is despite a practice parameter from the American Academy of Neurology, American Epilepsy Society and the American Association of Neurological Surgeons recommending consideration of surgical referral for refractory TLE (Engel, Jr. et al. 2003).

1.3.6.4 Presurgical Evaluation

Presurgical evaluation aims to identify those patients who are suitable for surgical intervention, the chances of seizure freedom and the potential risks inherent in surgery so the patient can make an informed choice. Between a quarter and a half of patients with medically intractable seizures could undergo surgical treatment following solely non-invasive techniques, and this is particularly true of temporal lobe seizures (Table 1.5). A further proportion requires further invasive investigations.

Neuroimaging aims to identify the underlying structural substrate for seizures. As a minimum a high resolution structural MRI is required, but this may be supplemented by further techniques if no lesion is

identified (see section 1.3.6.5 below). Video-telemetry aims to identify the electroencephalographic site of seizure onset and characterise the seizure semiology, whilst neuropsychological evaluation may help lateralise and localise any deficit. Neuropsychiatric evaluation is critical to identify factors such as interictal psychosis or mood disorders and to assess the degree of family support and dynamics.

Intracranial EEG recordings may be necessary if, following all appropriate non-invasive tests including multiple neuroimaging modalities, there are insufficient concordant data to accurately localise the seizure onset zone, discordant findings or seizure onset is near eloquent cortex. Patients with TLE typically have bilateral depth electrodes in the mesial temporal structures and subdural strip and grid electrodes over the neocortical surface.

The available data are synthesised and discussed by a multidisciplinary team, including neurology, neurosurgery, neurophysiology, neuroradiology, neuropsychology, neuropsychiatry and epilepsy nurses. The discussion determines the best way to proceed and estimates the chance of seizure freedom and potential risks.

Clinical assessment (detailed history and examination)

Neuroimaging (high resolution structural MRI at a minimum)

Neurophysiology (interictal and ictal video-EEG telemetry)

Neuropsychology

Neuropsychiatry

Table 1.5 - Minimum dataset for presurgical evaluation

1.3.6.5 Neuroimaging in Presurgical Evaluation

A dedicated high resolution epilepsy-protocol MRI series that uses a tilted “hippocampal axis” is necessary to ensure the whole of the hippocampus is seen in a single axial slice and to minimise partial volume effects in the coronal plane (Jackson et al. 1993). This should at least include T1-weighted volumetric, T2-weighted and FLAIR images. Good spatial resolution, signal-to-noise ratio and contrast are required to identify subtle temporal lobe pathologies.

Hippocampal sclerosis is characterised by hippocampal atrophy, a loss of the internal microarchitecture and signal change (high T2 and low T1 signal). Quantitative measurements can help support the diagnosis, with manual or semi-automated hippocampal volume measurements on T1 volumetric sequences to identify atrophy, and T2 relaxometry to demonstrate the abnormal signal characteristics (Malmgren & Thom 2012).

Malformations of cortical development, in particular focal cortical dysplasia (FCD), may be difficult to identify on neuroimaging and it is particularly important for high quality images to be obtained and reviewed by an experienced neuroradiologist. Diffusion imaging may assist in this area (Chapter 13). Tumours, including astrocytic tumours which often affect the amygdala and parahippocampal gyrus and dysembryoplastic neuroepithelial tumours (DNET) involving both gray and white matter are more readily identified. Other less common pathologies include vascular malformations and traumatic damage.

Despite advances in magnetic resonance technology, in around 30% of patients with focal epilepsy no structural correlate is identified (Duncan 2010) so structural MR imaging is increasingly complemented by other imaging modalities. Interictal FDG-PET may assist in the localisation of epilepsies, particularly those of extratemporal origin (Henry et al. 1991) whilst ictal SPECT (single photon emission computed tomography) can be compared to interictal studies to identify the transient focal hyperperfusion associated with the seizure onset zone (O'Brien et al. 1998).

Functional MRI for language-lateralisation is now routine in many centres replacing the invasive Wada test (Woermann et al. 2003) and is being investigated for predicting memory outcome from surgery. Diffusion tensor imaging is being used to aid surgical planning and to understand the effects of epilepsy and surgery on white matter networks. Further work in this area is the topic of this thesis.

1.3.6.6 Anterior Temporal Lobe Resection

The most common surgical procedure for TLE is ATLR. An alternative approach is selective amygdalo-hippocampectomy and these approaches are compared in detail in Chapter 4. There are two key outcomes to consider following surgery; firstly, whether the patient attains seizure freedom (or a significant reduction in seizures); second, whether there are any adverse neurological and psychological sequelae.

1.3.6.6.1 Seizure Outcome

There are two main rating scales for seizure outcome following surgery. The earlier and more established classification is that described by Engel (Engel et al. 1993). This divides outcome into four classes, which are further subdivided (Table 1.6). It does however include poorly defined terms such as “worthwhile improvement” and “disabling seizures” that involve subjective opinion.

The second approach is that adopted by ILAE Commission on Neurosurgery (Wieser et al. 2001). This is designed to assess seizure outcome on an annual basis following surgery and avoids the subjective terms in the Engel classification and makes a clear distinction between completely seizure free (Class 1) and those still having auras (Class 2), which are both group I in the Engel classification. This classification is employed in this thesis (Table 1.7).

Following ATLR, studies have shown that 53-84% of patients with hippocampal sclerosis are seizure free at 1 year (Spencer & Huh 2008). Predictors of good outcome include prolonged febrile convulsions or hippocampal sclerosis, unilateral anterior temporal localisation of interictal and ictal EEG, an absence of preoperative generalised seizures and an absence of seizures in the immediate postoperative period (McIntosh et al. 2001). Around 55% of all patients remain in ILAE outcome groups 1 or 2 at 5 years following ATLR (de Tisi et al. 2011).

Class I: Free of disabling seizures

A: Completely seizure free since surgery

B: Non disabling simple partial seizures only since surgery

C: Some disabling seizures after surgery, but free of disabling seizures for at least 2 years

D: Generalised convulsions with AED discontinuation only

Class II: Rare disabling seizures (“almost seizure free”)

A: Initially free of disabling seizures but has rare seizures now

B: Rare disabling seizures since surgery

C: More than rare disabling seizures since surgery, but rare seizures for the last 2 years

D: Nocturnal seizures only

Class III: Worthwhile improvement

A: Worthwhile seizure reduction

B: Prolonged seizure-free intervals amounting to greater than half the followed-up period, but not <2 years

Class IV: No worthwhile improvement

A: Significant seizure reduction

B: No appreciable change

C: Seizures worse

Table 1.6 - Engel classification of seizure outcome following surgery

From Engel et al. 1993.

Outcome classification	Definition
1	Completely seizure free; no auras
2	Only auras; no other seizures
3	One to three seizure days per year; ± auras
4	Four seizure days per year to 50% reduction of baseline seizure days; ± auras
5	Less than 50% reduction of baseline seizure days to 100% increase in baseline seizure days; ± auras
6	More than 100% increase of baseline seizure days; ± auras

Table 1.7 - ILAE classification of seizure outcome following surgery

From Wieser et al. 2001.

1.3.6.6.2 Neurological and Psychological Sequelae

Memory decline may be seen following ATLR. Left ATLR is associated with a decline in verbal memory, particularly immediate, with possible improvement in non-verbal memory (Lee et al. 2002). Factors predicting the decline include intact preoperative memory, intact memory functions with a Wada test on the contralateral hemisphere or other data suggesting preserved function in the lobe to resected, pathologies other than non-hippocampal sclerosis or an absence of hippocampal atrophy (Spencer & Huh 2008). Right ATLR may affect non-verbal memory although the effects are less consistent (Lee et al. 2002, Vaz 2004). A dominant TLE focus is associated with impaired language and dominant ATLR impairs naming ability in one in four (Langfitt & Rausch 1996). The imaging correlates of such changes are discussed in Chapter 3. A proportion of patients also develop a visual field deficit, which is discussed further in Chapter 4.

1.4 Conclusions

Epilepsy forms a common group of neurological disorders affecting around 1% of the population. Around 60% of people with epilepsy suffer from focal seizures which most commonly arise from the temporal lobe. Mesial temporal lobe seizures have a typical semiology consisting of an aura followed by behaviour manifestations. Many anti-epileptic drugs are available but around a third of patients with TLE are refractory to treatment. Surgery, particularly ATLR, plays a key role in the treatment of such patients. Detailed presurgical evaluation is required including neuroimaging. Around 60-70% of patients become seizure free but the possible sequelae of the operation include language or memory decline or visual field deficits. Diffusion tensor imaging may help understand, predict or avoid some of these deficits.

2 DIFFUSION MAGNETIC RESONANCE IMAGING: PRINCIPLES

2.1 Introduction

Magnetic resonance imaging (MRI) is an imaging modality based on the principles of nuclear magnetic resonance (NMR). Nuclei with unpaired protons or neutrons possess a fundamental property known as spin. When placed in an external magnetic field, B_0 , the nuclear spins align with this field producing a net magnetization vector. The net magnetization vector can be perturbed from its equilibrium state by a radiofrequency (RF) pulse matching the resonant frequency of the nuclei (“resonance”) and then returns to its equilibrium state (“relaxation”) emitting an NMR signal that can be measured. The combination of additional magnetic field gradients - slice select gradient to selectively excite a single slice; frequency and phase encoding gradients to encode the signal from different parts of the slice in two dimensions - and a two-dimensional Fourier transform yields an image.

Conventional MR images include proton-density, T1-weighted and T2-weighted images but the signal may also be sensitised to the effects of molecular diffusion. Diffusion MRI non-invasively measures a single phenomenon - the dephasing of proton spins in the presence of a spatially-varying magnetic field (“gradient”) (Jones et al. 2013). Mathematical models of the underlying tissue enable the determination of parameters describing the tissue microstructure whilst consideration of the predominant direction of diffusion within each voxel allows *in vivo* tracing of white matter pathways (“tractography”).

In this chapter, I introduce the concept of molecular diffusion, how it may be measured using diffusion MRI and the metrics that can be derived from diffusion-weighted and diffusion tensor imaging. I discuss the biological sources of anisotropic diffusion, how to extract and interpret these parameters in clinical studies and how tractography may be used to delineate white matter tracts. Its application to the optic radiation is discussed in Chapter 4. Finally more complex tissue models that may be employed to quantify microstructural parameters are introduced. The next chapter summarises how these techniques have been used to study patients with epilepsy.

2.2 Diffusion and its Measurement

2.2.1 Molecular Diffusion

Any particle at a temperature above absolute zero possesses thermal energy that manifests as random movement (“molecular diffusion”). In the presence of a concentration gradient, there is a net flux of particles from high to lower concentration. Einstein recognised that diffusive mixing also occurs in the absence of a concentration gradient (“self diffusion”). By considering the conditional probability distribution of a group of particles after a time t , the mean squared displacement after a given time is proportional to the diffusion coefficient (Einstein’s relationship) (Einstein 1905).

2.2.2 Measurement of Diffusion: NMR

A standard spin echo sequence is shown in Figure 2.1 (Hahn 1950). The 90 degree RF pulse rotates the magnetization vector into the horizontal plane. Spins precess at the Larmor frequency but begin to dephase due to magnetic field inhomogeneities leading to signal decay. The 180 degree pulse reverses the phase dispersal enabling the spins to rephase and produce an echo.

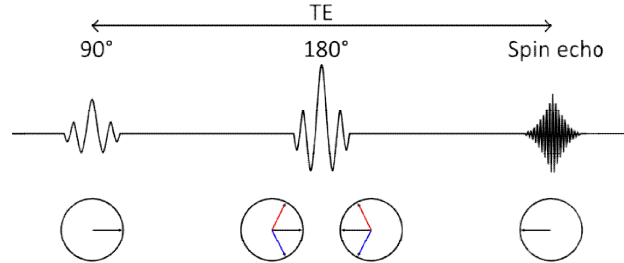


Figure 2.1 - Spin echo NMR sequence

The 90 degree RF pulse produces coherent transverse magnetization (first circle). The spins begin to dephase due to magnetic field inhomogeneities (red, blue and black arrows in the second circle). The 180 degree pulse reverses the phase dispersal (third circle). The spins then rephase and produce an echo (fourth circle).

The addition of two gradient pulses that induce a spatially dependent phase shift makes this sequence sensitive to the effects of diffusion (Figure 2.2) (Stejskal & Tanner 1965). For static (non-diffusing) spins, the phase shifts induced by two opposing gradients cancel. However for moving (diffusing) spins, the cancellation is incomplete leading to residual phase dispersal and further signal attenuation. The degree of signal attenuation is given by the Stejskal-Tanner equation:

$$\ln\left(\frac{S_{G,\Delta,\delta}}{S_0}\right) = -\gamma^2 G^2 \delta^2 \left(\Delta - \frac{\delta}{3}\right) D = -bD \quad \text{where } b = \gamma^2 G^2 \delta^2 \left(\Delta - \frac{\delta}{3}\right) \quad (1)$$

where $S_{G,\Delta,\delta}$ and S_0 are the echo signal in the presence and absence of the diffusion gradients, γ is the gyromagnetic ratio, G is the gradient amplitude, Δ is the pulse separation, δ is the pulse duration and D the diffusion coefficient.

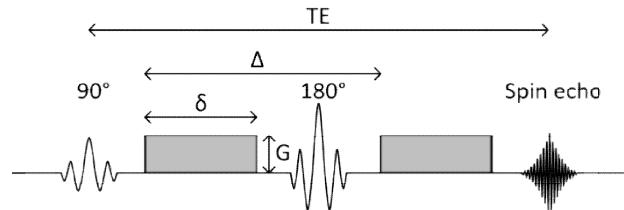


Figure 2.2 - Pulsed gradient spin echo NMR sequence

The spin echo sequence is modified by the addition of two gradient pulses (grey blocks) that induce and then reverse a spatially-dependent phase shift.

2.2.3 Measurement of Diffusion: MRI

Diffusion NMR experiments can be extended to three dimensions by applying diffusion-weighting gradients in any direction (Figure 2.3). Clinical scans are typically acquired using echo-planar imaging (EPI) in which all the data points necessary to reconstruct the image are sampled after a single 90-180 pair of RF pulses (Turner et al. 1991). However, due to the low bandwidth in the phase encode direction this sequence is very susceptible to off-resonance effects such as magnetic field inhomogeneity, local susceptibility gradients and chemical shift. Subject motion and eddy currents induce further artefacts. These artefacts cause distortions that are deleterious for the accurate neurosurgical use of diffusion imaging and are discussed further in Chapter 5.

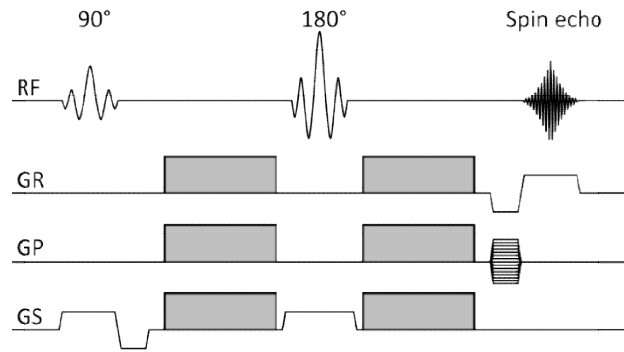


Figure 2.3 - Diffusion-weighted spin echo MRI sequence

RF shows the 90 and 180 degree pulses, GR is the readout gradient (typically x-direction, left-right), GP is the phase-encoding gradient (typically y-direction, anterior-posterior) and GS is the slice-select gradient (typically z-direction, superior-inferior). The diffusion gradients (grey blocks) can be applied as any combination of these directions.

2.3 Diffusion Weighted Imaging (DWI)

The echo signal in a typical spin echo sequence (Figure 2.3) combines T_2 and diffusion-weighting. However by measuring the signal with two different b -values (Figure 2.4) but the same TE the effects of T_2 decay can be removed leaving just the diffusion-weighted attenuation. The diffusion coefficient D can be determined in each voxel using a diffusion-weighted scan and a non-diffusion weighted scan by:

$$\ln\left(\frac{S_b}{S_0}\right) = -bD \quad (2)$$

where S_b is the signal in the presence of the diffusion gradients described by the b -value b and S_0 is the signal in the absence of diffusion-weighting.

With typical diffusion times of 30ms and the diffusion coefficient of water at 37°C of $3.0 \times 10^{-3} \text{ mm}^2 \text{ s}^{-1}$, the diffusion distance of around 20μm exceeds the size of structures such as cells. Thus barriers such as cell membranes hinder free diffusion and the signal attenuation is also modulated by other factors including

perfusion. The diffusion coefficient term D is therefore replaced by the apparent diffusion coefficient ADC (Le Bihan et al. 1986), typically around $0.8 \times 10^{-3} \text{ mm}^2 \text{ s}^{-1}$ in white matter.

ADC was initially shown to be a sensitive early indicator for ischemic stroke in cats (Moseley et al. 1990b) and subsequently in humans (Warach et al. 1995). Whilst largely independent of the direction of the diffusion gradients in grey matter, the same was not true in white matter (Moseley et al. 1990a). The ADC was higher when the diffusion gradients were aligned with the predominant fibre direction, reflecting water diffusing more freely along the length of an axon than perpendicular to it (Figure 2.5). This finding led to the development of diffusion tensor imaging.

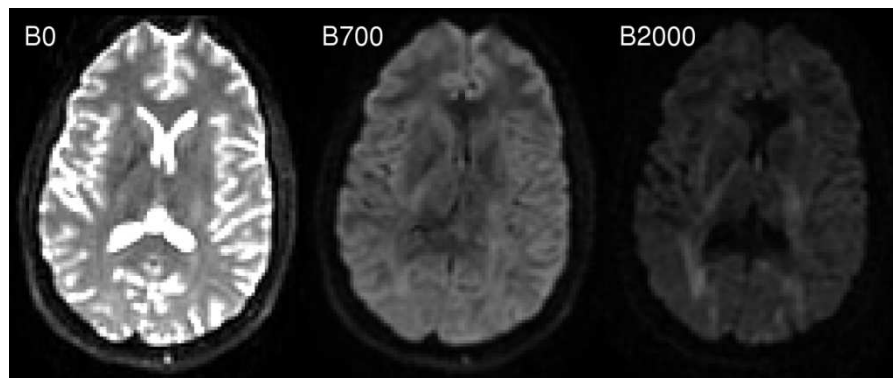


Figure 2.4 - Diffusion-weighted imaging with different degrees of weighting

The image on the left is a T2-weighted EPI image with no diffusion-weighting ($b=0 \text{ s mm}^{-2}$), the middle image has a modest degree of diffusion-weighting ($b=700 \text{ s mm}^{-2}$) and the right hand image has a high degree of diffusion-weighting ($b=2000 \text{ s mm}^{-2}$). The diffusion gradients have been applied in the x-direction (left-right). Note the high attenuation in cerebrospinal fluid (CSF) where the diffusion coefficient is high and the lower attenuation in white matter structures such as the internal capsule running perpendicular to the diffusion gradient direction.

2.4 Diffusion Tensor Imaging (DTI)

2.4.1 Conceptual and Mathematical Formulation

Imagine a droplet of ink diffusing freely in water. Diffusion is *isotropic* as it occurs equally in all directions and a surface of constant mean-squared displacement can be represented by a *diffusion sphere* (Figure 2.6). In contrast, in many biological tissues including white matter, skeletal and cardiac muscle diffusion is *anisotropic* as the observed magnitude of diffusion depends on the direction. The surface of constant mean-squared displacement is then represented by a *diffusion ellipsoid* (Figure 2.6).

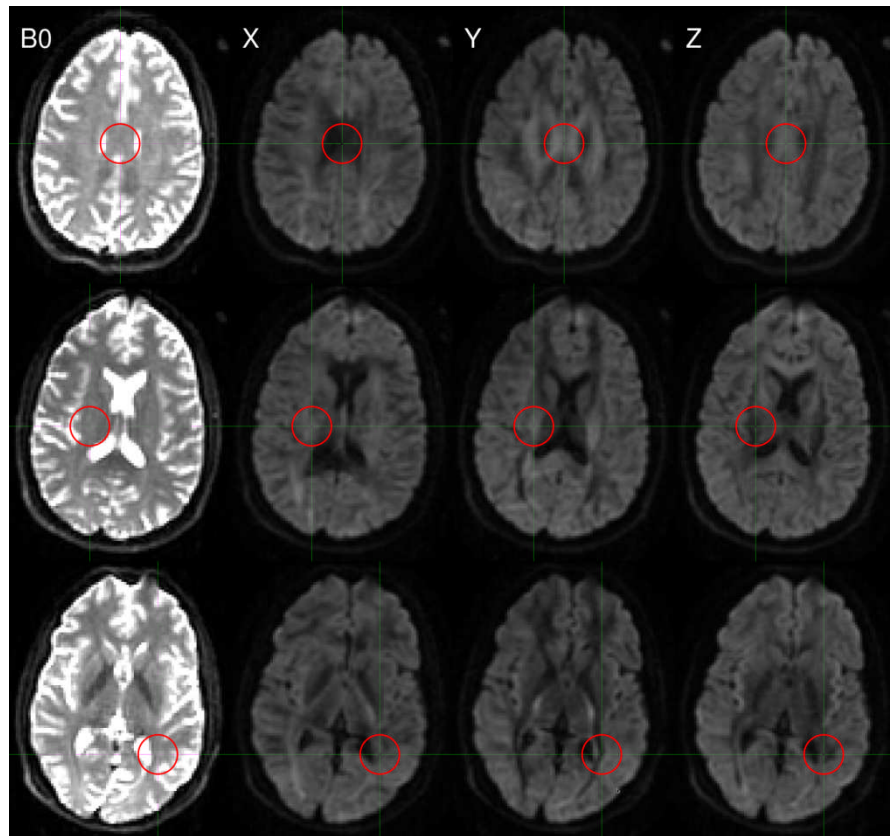


Figure 2.5 - Diffusion-weighted imaging with gradients applied along different axes

The first column shows the non-diffusion weighted scan, the second column shows diffusion weighting applied predominantly in the x-direction (left-right), the third column the y-direction (anterior-posterior) and the final column the z-direction (superior-inferior). The red circles on the first row show that signal attenuation in the corpus callosum (running left-right) is greatest with diffusion gradients in the x-direction, on the second row show the internal capsule (running superior-inferior) has greatest attenuation in the z-direction and on the third row show the optic radiation (running anterior-posterior) has greatest attenuation in the y-direction.

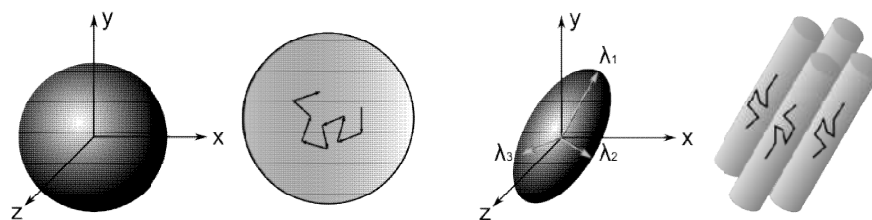


Figure 2.6 - Diffusion sphere and ellipsoid

With isotropic diffusion, diffusion is equal in all directions and can be represented as a sphere (left) whilst anisotropic diffusion can be visualised as an ellipsoid (right).

Anisotropic diffusion cannot be adequately represented by a single scalar ADC but can instead be represented by an effective (or apparent) diffusion tensor (Basser et al. 1994):

$$\mathbf{D} = \begin{bmatrix} D_{xx} & D_{xy} & D_{xz} \\ D_{xy} & D_{yy} & D_{yz} \\ D_{xz} & D_{yz} & D_{zz} \end{bmatrix} \quad (3)$$

The diffusion tensor is a matrix of variances and covariances that quantifies diffusion along the orthogonal axes (diagonal elements) and the correlations between these (off-diagonal elements). It is symmetric so has six independent parameters. Just as the ADC can be derived using simple linear regression and 2 DWIs, the diffusion tensor can be derived through multivariate linear regression with at least 7 DWIs along non-collinear, non-coplanar directions (Basser & Pierpaoli 1998). Typically, at least one of the DWIs has negligible diffusion-weighting ($b=0$ image).

Equation (2) can now be generalised to incorporate the diffusion tensor \mathbf{D} . The b -factor is replaced by the b -matrix which performs the same role for anisotropic diffusion as the scalar b -factor does for isotropic diffusion in representing the interactions between diffusion and imaging gradients:

$$\ln \left(\frac{S(\mathbf{b})}{S(\mathbf{0})} \right) = (-b_{xx}D_{xx} + 2b_{xy}D_{xy} + 2b_{xz}D_{xz} + b_{yy}D_{yy} + 2b_{yz}D_{yz} + b_{zz}D_{zz}) \quad (4)$$

where $S(\mathbf{b})$ is the signal in the presence of the diffusion gradients described by the symmetric b -matrix \mathbf{b} with components b_{ij} and $S(\mathbf{0})$ is the signal in the absence of diffusion-weighting.

In Figure 2.6, the laboratory frame of reference is $[x,y,z]$. However by using a frame of reference $[x',y',z']$ with an axis coincident with the principal axis of the diffusion ellipsoid, the off-diagonal terms become zero so the signal attenuation is:

$$\ln \left(\frac{S(\mathbf{b})}{S(\mathbf{0})} \right) = (-b_{x'x'}D_{x'x'} + b_{y'y'}D_{y'y'} + b_{z'z'}D_{z'z'}) \quad (5)$$

This frame of reference and diffusivities can be found by diagonalising the matrix \mathbf{D} and determining three eigenvectors and three eigenvalues. The eigenvectors give the unique local orthogonal coordinate system $[\epsilon_1, \epsilon_2, \epsilon_3]$ in which displacements along orthogonal directions appear uncorrelated and whose directions correspond to the internal tissue structure. In white matter the principal eigenvector ϵ_1 is inferred to represent the predominant fibre orientation. The degree of diffusion along these three principal axes is given by the three eigenvalues $\lambda_1, \lambda_2, \lambda_3$ (principal diffusivities). The diffusion ellipsoid representation (Figure 2.6) has axes aligned with the eigenvectors with magnitude proportional to the square roots of the corresponding eigenvalues.

2.4.2 Scalar Invariants from the Diffusion Tensor

Scalar quantities can be derived from the eigenvalues on a voxelwise basis that are independent of the laboratory frame of reference, the direction of the applied imaging and diffusion-sensitising gradients, the position of the patient and the orientation of structures contributing to the anisotropy.

2.4.2.1 Mean Diffusivity (MD)

The trace of the diffusion tensor is proportional to the orientationally averaged apparent diffusivity so removes the orientational dependence of the ADC. In clinical studies, it is divided by three to yield the mean diffusivity (MD). The values of MD are remarkable similar across grey and white matter, between different subjects and across mammalian species at $0.7 \times 10^{-3} \text{ mm}^2 \text{ s}^{-1}$ (Figure 2.7).

$$\text{Trace}(\mathbf{D}) = \lambda_1 + \lambda_2 + \lambda_3, \text{MD}(\mathbf{D}) = \frac{\lambda_1 + \lambda_2 + \lambda_3}{3} \quad (6)$$

2.4.2.2 Fractional Anisotropy (FA)

Fractional anisotropy (FA) quantifies the degree to which the diffusion tensor deviates from isotropy by measuring the fraction of the whole “magnitude” of the diffusion tensor that can be ascribed to anisotropic diffusion (Figure 2.7). It includes a scaling coefficient to give values between 0 (isotropic diffusion) and 1 (diffusion along one axis).

$$\begin{aligned} \text{FA}(\mathbf{D}) &= \sqrt{\frac{3}{2} \frac{\sqrt{(\lambda_1 - \langle D \rangle)^2 + (\lambda_2 - \langle D \rangle)^2 + (\lambda_3 - \langle D \rangle)^2}}{\sqrt{\lambda_1^2 + \lambda_2^2 + \lambda_3^2}}} \\ &= \sqrt{\frac{1}{2} \frac{\sqrt{(\lambda_1 - \lambda_2)^2 + (\lambda_1 - \lambda_3)^2 + (\lambda_2 - \lambda_3)^2}}{\sqrt{\lambda_1^2 + \lambda_2^2 + \lambda_3^2}}} \end{aligned}$$

$$\text{where } \langle D \rangle = \frac{\lambda_1 + \lambda_2 + \lambda_3}{3} \quad (7)$$

2.4.2.3 Axial and Radial Diffusivities

Mean diffusivity (MD), the mean of the three eigenvalues, can be decomposed into two components, the axial diffusivity (AD, also known as parallel or longitudinal diffusivity), $\lambda_{\parallel} = \lambda_1$, and the radial diffusivity (RD, also known as perpendicular or transverse diffusivity), $\lambda_{\perp} = \frac{\lambda_2 + \lambda_3}{2}$ which have been considered to represent axonal and myelin integrity respectively (see Section 2.6.2).

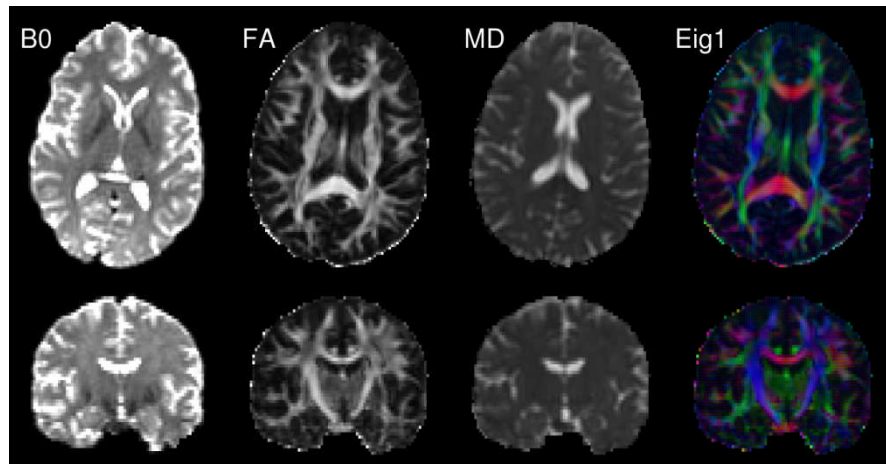


Figure 2.7 - Diffusion tensor imaging

The non-diffusion weighted scan (B0) is shown on the left, followed by the fractional anisotropy (FA) image demonstrating higher values in white matter tracts then the mean diffusivity (MD) image with elevated values in the CSF. The final column shows the direction of principal eigenvector (Eig1) both in colour-coded form (red = left/right, green=anterior/posterior, blue=superior/inferior) and in vector form (line segments).

2.5 Biological Sources of Diffusion Anisotropy

2.5.1 Potential Sources of Anisotropy

Following the observation that diffusion is predominantly isotropic in gray matter but anisotropic in white matter (Moseley et al. 1990a) occurring parallel to the direction of white matter tracts (Moseley et al. 1991), a key question has been the source of such anisotropy and whether it relates to a specific microstructural component or combination thereof. Potential contributors include the cytoskeleton (neurofilaments and microtubules), the axonal membranes and the myelin sheath (Figure 2.8). The relevant data summarised here are discussed in more detail elsewhere (Beaulieu 2002).

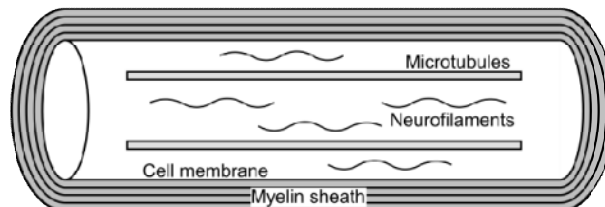


Figure 2.8 - Possible sources of diffusion anisotropy in a myelinated nerve axon

The cytoskeleton (microtubules and neurofilaments), cell membrane and myelin sheath are all longitudinally orientated.

2.5.1.1 Myelin

The initial assumption that the relatively water impermeable lipid bilayers of the myelin sheath were the main source of diffusion anisotropy seems unlikely as myelin is not essential for anisotropy. The garfish has both myelinated and unmyelinated nerves with similar anisotropy in each (Beaulieu & Allen 1994a) and diffusion anisotropy persists in genetic models of dysmyelination (Gulani et al. 2001).

Myelin, although not essential, is likely to contribute to anisotropy. It is hard to study since the myelin encasing cannot be removed experimentally and a direct comparison of myelinated and unmyelinated axons is hampered by differing axonal diameters. Nevertheless, in genetic models of dysmyelination anisotropy is slightly reduced due to an increase in perpendicular diffusivity (Gulani et al. 2001).

2.5.1.2 Axonal Membranes

Anisotropy is present in myelinated and unmyelinated axons in the peripheral and central nervous systems in both mammalian and non-mammalian species so axonal membranes appear sufficient for anisotropy and are likely to play the primary role. In unmyelinated axons of lamprey spinal cord, anisotropy is higher in regions with more axons per cross-sectional area and thus an increased higher packing density and number of axonal membranes (Takahashi et al. 2002).

2.5.1.3 Cytoskeleton

Axons possess a complex internal cytoskeleton of longitudinally orientated microtubules (25nm diameter) and neurofilaments (10nm diameter) cross-linked with microfilaments that may present physical barriers to hinder perpendicular diffusion. Microtubules are also responsible for fast axonal transport along the length the axon that may enhance parallel diffusion.

Treatment of myelinated and unmyelinated garfish neurons with vinblastine to depolymerise and eliminate microtubules and fast axonal transport leads to a fall in both parallel and perpendicular diffusivity (which may be partly an effect of time) and preservation of anisotropy (Beaulieu & Allen 1994a). Similarly degradation of the microtubules (and to a lesser extent the neurofilaments) of rat optic nerve with subcutaneous methylmercury leads to an increase in parallel diffusivity but no change in perpendicular diffusivity again preserving anisotropy (Kinoshita et al. 1999).

The contribution of the more numerous neurofilaments has been assessed with the isolated giant squid axon whose large diameter (200-1000µm) means the effect of the axonal membrane is insignificant with typical diffusion times. Parallel diffusivity was only around slightly greater than perpendicular diffusivity (Beaulieu & Allen 1994b) and isotropic diffusion is seen in the giant reticulospinal axons of the sea lamprey spinal cord (diameter 20-40µm) (Takahashi et al. 2002). The cytoskeleton does not thus appear to be a significant contributor to diffusion anisotropy.

2.6 Clinical Studies of DTI parameters

2.6.1 Extraction of DTI parameters

For clinical studies involving DTI parameters, a suitable parameter must be extracted, compared between groups and interpreted. Two common techniques are employed to extract the parameter (Snook et al. 2007, Chanraud et al. 2010) with the first being predominantly employed in this thesis.

Voxel-based analyses take quantitative maps (e.g. FA) and spatially normalise them to a template using non-linear registration. Following smoothing, a voxel-based comparison is undertaken between groups using software such as SPM. The main advantages of this technique are that it is automated and performs a whole brain analysis without any *a priori* hypothesis. However, sensitivity is limited by the accuracy of spatial normalization (Snook et al. 2007) and results may vary depending on the degree of smoothing (Jones et al. 2005). Statistical correction is also required for the multiple comparisons.

A variant of this technique known as Tract-Based Spatial Statistics (TBSS) determines a white matter skeleton representing the ‘core’ of the tracts from the group and projects each subject’s FA map onto this skeleton (Figure 2.9) (Smith et al. 2006). This aims to alleviate the problems of inaccurate image registration and requires no smoothing and is widely used. It does however limit the analysis to the core of white matter so cannot detect changes occurring in the periphery of white matter tracts (or in grey matter).

The second main approach is region-of-interest (ROI) based analysis. The structure(s) of interest are delineated either manually by an operator or automatically from an atlas and the mean of a diffusion parameter (e.g. FA) is determined in each structure in each subject. This requires an *a priori* hypothesis of which structures to assess but the single number derived per subject allows correlational analyses with clinical variables, such as cognitive scores. It cannot detect localised changes within structures, and the delineation of the structure can be time consuming and inaccurate. In particular due to the relatively large voxel size of DTI, it can be hard to delineate a structure accurately whilst avoiding partial volume effects.

2.6.2 Interpretation of DTI parameters

Having extracted a parameter and performed a group comparison, any differences must be interpreted. Since FA is higher in ordered white matter and typically falls in disease processes, it is often considered a direct marker of white matter integrity but this is an over-simplification (Jones et al. 2013). FA is related to many factors including axonal count and density, degree of myelination and fibre organization including the presence of crossing fibres. Whilst changes are frequently attributed to one or more of these factors, DTI alone cannot distinguish them and is thus non-specific. In post-mortem multiple sclerosis brains, FA positively correlated with axonal count and myelin content and negatively with degree of gliosis (Schmierer et al. 2008). In temporal lobe epilepsy surgery, FA of the fimbria-fornix correlated mostly strongly with the total axon membrane circumference on electron microscopy but also to a lesser extent with axonal density and myelin thickness (Concha et al. 2010).

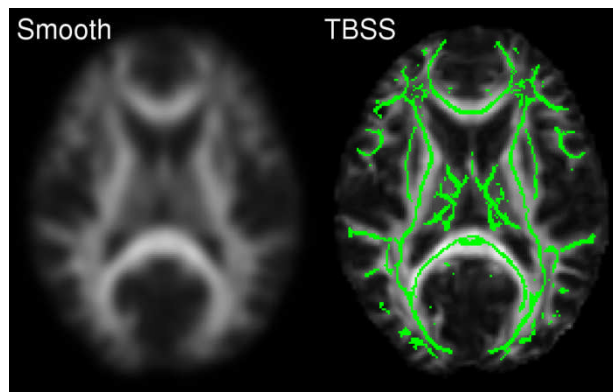


Figure 2.9 - Voxel-based techniques for analysing DTI parameters

In conventional voxel-based analyses the FA map is non-linearly registered to a template and smoothed (left). In Tract-Based Spatial Statistics following normalisation the FA map is projected onto a white matter skeleton (right, in green).

Another critical factor is crossing fibres as two obliquely orientated fibre populations will have a lower FA than a single coherent fibre population (Figure 2.10) and thus selective loss of one of these populations will lead to a paradoxical increase in FA. This has been postulated in mild cognitive impairment with an increased FA in the centrum semiovale being related to a relative preservation of motor-related projection fibres crossing association fibres of the superior longitudinal fasciculus (Douaud et al. 2011).

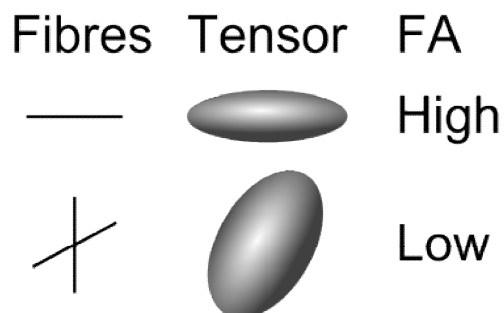


Figure 2.10 - The problem with FA and crossing fibres

With a single fibre population, the diffusion tensor is prolate so FA is high. With two fibre populations crossing at 60 degrees, the diffusion tensor becomes more oblate so the FA is reduced.

MD may rise in pathology but is studied less often. In the same two studies as above, opposite correlations to FA were seen in post-mortem multiple sclerosis brains (Schmierer et al. 2008) with no correlations seen in the fimbriae-fornix in epilepsy surgery (Concha et al. 2010). It is however useful to consider the separate components of diffusivity as a reduction in anisotropy may result from increased perpendicular diffusivity, decreased parallel diffusivity or a combination of the two, each of which has a different structural interpretation. In particular it may be helpful to know the specific relationship between myelin loss, axonal damage and diffusivities in conditions such as multiple sclerosis.

This was first addressed in animal studies. In the shiverer mouse, a genetic model of dysmyelination, perpendicular diffusivity is increased with no change in parallel diffusivity (Song et al. 2002). In a mouse model of retinal ischaemia, an early reduced parallel diffusivity with axonal degeneration on immunohistochemistry was followed by a later increased perpendicular diffusivity with myelin degradation (Song et al. 2003). Similarly in cuprizone-induced corpus callosal damage in mice, the initial axonal damage is accompanied by reduced parallel diffusivity with later demyelination associated with increased perpendicular diffusivity (Sun et al. 2006).

Taken together these animal studies have led to the suggestion that parallel diffusivity is a marker of axonal damage whilst perpendicular diffusivity reflects myelin damage. Such an interpretation has been extended to human studies. In a study of patients with epilepsy undergoing corpus callosotomy, an early reduction in parallel diffusivity (at 1 week) was inferred to reflect axonal fragmentation with the later increase in perpendicular diffusivity (at 2-4 months) consistent with myelin degradation (Concha et al. 2006). However, these parameters may not portray an accurate reflection of demyelination especially in areas of low anisotropy due to complex tissue architecture such as crossing fibres (Wheeler-Kingshott & Cercignani 2009).

2.7 Fibre Orientation and Tractography

2.7.1 Basic Principles

The diffusion tensor model assumes that the direction of the principal eigenvector ε_1 in each voxel is aligned with the predominant direction of local fibres. The eigenvectors can be displayed either as a vector field or through colour coding (Figure 2.7). The Directionally Encoded Colour scheme represents the x, y and z components in red, green and blue respectively (Pajevic & Pierpaoli 1999) so fibres running left-right are red, anterior-posterior green and superior-inferior blue.

Standard techniques for studying white matter pathways including macroscopic dissection, microscopic histology and the use of anatomical tracers such as horseradish peroxidase are invasive and can only be applied post-mortem. Tractography, the process by which white matter connections are inferred by tracing through the vector fields (Figure 2.11), is non-invasive and can be applied *in vivo*. Tractography algorithms can be divided into two broad groups - deterministic and probabilistic.

2.7.2 Deterministic Tractography

A unique trajectory (streamline) is propagated from a defined starting point (seed) in both directions until specified stopping criteria are met. The direction of propagation is defined by the direction of the underlying principle eigenvectors. One common algorithm is FACT (Fibre Assignment by Continuous Tracking) (Mori et al. 1999) in which tractography precedes similarly to Figure 2.11. In areas of low FA, such as CSF or grey matter, there is likely to be a large error in the direction of the principle eigenvector so an FA threshold is commonly used as a stopping criterion (e.g. $FA < 0.2$). In addition, a curvature threshold may be specified as the radius of curvature of a white matter tract is usually significantly greater than an imaging voxel. Additional constraints such as retaining only streamlines passing through a waypoint or excluding those passing through an exclusion zone can be used to delineate tracts correlating with known anatomy – virtual in vivo dissection (Catani et al. 2002).

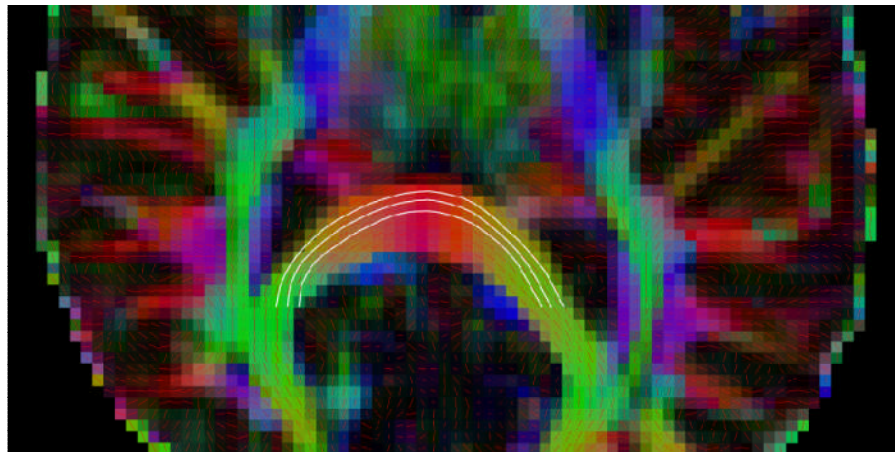


Figure 2.11 - Principle of tractography

Close up of the corpus callosum with the vector field from the principal eigenvectors and white lines indicating how tractography algorithms follow the vector field.

Deterministic streamlines are however subject to important limitations. They are particularly susceptible to errors due to imaging noise and limitations of the underlying model (e.g. crossing fibres in the diffusion tensor model). These errors compound as the streamline passes further from the initial seed. If a voxel is noisy, the streamline may be diverted along a false pathway or terminate prematurely depending on the stopping criteria chosen. The use of all the information in the tensor, rather than just the principle eigenvector, can render the technique less sensitive to noise, but the limitations remain. This is implemented in the TEND (tensor deflection) model (Lazar et al. 2003).

2.7.3 Probabilistic Tractography

Probabilistic techniques address some of the issues inherent in deterministic algorithms including the ability to track through areas of high uncertainty. Rather than an all-or-none output where streamlines either pass via a voxel or not, the technique aims to assign a confidence level that connections from a seed pass through each voxel. Whilst deterministic tractography always has a set direction of propagation at each location, probabilistic tractography provides an additional estimate of the uncertainty in the measurement of the principle diffusion direction.

Tracts are propagated by sampling from the orientation distribution function at each step of the tractography using Monte Carlo analysis (Parker & Alexander 2003, Behrens et al. 2003b) thus enabling passage beyond noisy voxels, and assigning low probability values to erroneous tracts which tend to disperse. There is less need for stopping criteria such as a FA threshold, which is used in the deterministic techniques to prevent streamlines from entering areas of high uncertainty and being incorrectly diverted.

Probabilistic tractography has two main disadvantages. Firstly, it is much more time consuming computationally than deterministic tractography so cannot be performed in real time. Secondly, the connectivity distribution obtained is not the distribution of connections from a seed point, but rather the confidence bounds on the location of the most probable single connection. When counting streamlines, the value in each voxel represents the probability that the dominant streamline from the seed passes through this particular voxel and tends to fall with increasing distance from the seed. For displaying the results, or performing tract-based analyses, the choice of threshold is arbitrary.

2.7.4 Tractography and Crossing Fibres

The diameter of an axon (e.g. $1\mu\text{m}$) is tiny in comparison to a voxel (e.g. 2mm isotropic) so each voxel contains hundreds of thousands of axons. If a voxel contains two crossing fibre populations, the diffusion tensor represents an average between these directions and thus reflects neither of the two populations. The assumption of Gaussian diffusion in a single compartment, a key part of the diffusion tensor model, is violated and misleading information is obtained.

The multitensor model assumes that each voxel contains n populations of fibres and that each molecule remains in one of these compartments without exchange. The Gaussian model is thus replaced by a mixture of n Gaussian densities. The proportion of fibres in each population is estimated along with a diffusion tensor for each population. The principle eigenvectors of each tensor reflect the direction of that population of fibres. In this thesis, the spherical-harmonic voxel-classification algorithm of Alexander is used to classify voxels into isotropic, anisotropic Gaussian or non-Gaussian (Alexander et al. 2002) with two tensors fitted in the latter but a single tensor in the other two cases. There are other approaches now available that better deal with crossing fibres, particularly constrained spherical deconvolution (Tournier et al. 2004, Tournier et al. 2007) (discussed in section 14.2.1).

2.7.5 Improving the Spatial Resolution

A typical resolution for DTI (2mm isotropic) limits the accuracy of tractography. However increasing the resolution to 1mm isotropic reduces the signal from each voxel by a factor of eight. If retaining whole-brain coverage, this signal loss cannot be recovered on clinical scanners by repeating and averaging given the need to acquire images with diffusion-weighting applied in multiple different directions.

Attempts have been made to increase in-plane resolution by acquisition of a reduced field-of-view. ZOOM (zonally oblique multislice) DTI has been used to image the hippocampus with 1.4x1.4mm in-plane resolution (Salmenpera et al. 2006). The limitation is the partial brain coverage with only five non-contiguous 5mm-thick slices. This can be improved with modern scanners but limitations still remain.

Alternatively, the loss of signal with smaller voxels can be partially compensated by an increased field strength (signal is proportional to the square of field strength) and stronger magnetic field gradients (enabling shorter diffusion-weighted pulses and thus signal readout at a shorter TE with reduced T2 decay). However even using a specially engineered scanner for the Human Connectome Project with a field strength of 7T, a maximum gradient strength of 300mT/m (typically 40mT/m on clinical scanners) and a 64 channel coil, only a 1.5mm isotropic resolution was obtained (Setsompop et al. 2013). Thus retaining the spatial resolution whilst increasing the angular resolution and employing better models of the underlying diffusion is likely to be of greater utility (Section 2.8).

2.7.6 Use of Tractography Data

The resulting tracts may be used qualitatively for surgical planning, or to extract quantitative parameters. These include the volume of connections and fibre counts which have significant limitations (Jones et al. 2013) or an assessment of the degree of connectivity or connection strength between different regions. The delineated tract can also provide a region-of-interest for the DTI parameters discussed above. Clinical studies are discussed in Chapter 3 and the application to optic radiation tractography for surgical planning in Chapters 4 and 5.

2.8 Improving the Diffusion Model

2.8.1 Limitations of the Diffusion Tensor Model

Whilst the diffusion tensor model provides helpful quantitative parameters, it is based on the fundamental assumption that within each voxel there is a single diffusing process that follows a Gaussian distribution. Studies have shown that with higher b -values the measured diffusion signal deviates from the linear relationship predicted by equation 2 so the assumption of Gaussian diffusion is not valid (Niendorf et al. 1996).

The diffusion signal from a single voxel reflects the contribution of several tissue compartments with differing diffusion profiles. Further the large voxel size in diffusion imaging (typically 2mm isotropic) in comparison to underlying microstructure means that a single voxel may contain a mixture of grey matter, white matter and cerebrospinal fluid (partial voluming effect) and even within white matter, a voxel may contain a variety of fibre populations with different orientations. Thus in white matter with complex fibre architectures such as crossing or diverging fibres or in grey matter where diffusion is relatively isotropic this model fits poorly (Tuch et al. 2002).

2.8.2 Diffusion Profile

The diffusion profile within a voxel can be more accurately measured by acquiring data with increased angular resolution (HARDI, high angular resolution diffusion imaging) (Frank 2002), with varying b -values to assess the deviation from Gaussian diffusion or a combination of the two. The spatial diffusion profile obtained, the diffusion orientation distribution function (dODF), reflects the relative amount of diffusion in different directions.

These data may be acquired and assessed using model-free approaches such as Q-ball imaging (Tuch 2004) or diffusion spectrum imaging (Wedeen et al. 2005) which make no assumptions on the underlying diffusion profile but these do not give immediate quantitative values. A second approach is to design a biological plausible model of the tissue and relate parameters of this model such as axonal density to the measured diffusion signal (Panagiotaki et al. 2012). If the model is valid, by fitting the model to the measured diffusion data these quantitative parameters may be extracted. Some examples of such models are now given.

2.8.3 Tissue Models

The bi-exponential model addresses the discrepancy with higher b -values by considering two different diffusing pools (fast and slow) with separate diffusion coefficients and volume fractions (Niendorf et al. 1996). Whilst this model fits well, the fast and slow decaying components are not equivalent to the extra- and intracellular components as originally hypothesised as the fitted volume fractions are significantly different. This model does not allow for exchange between the compartments and with increasing b -values, the fit requires higher order exponentials (Assaf & Cohen 1998).

The ball-and-stick model consists of an intra-axonal fraction modelled as a “stick” (idealised cylinder with zero radius) and an extra-axonal fraction modelled as a “ball” (isotropic diffusion) (Behrens et al. 2003b). This formulation allows an estimate of fibre orientation, the relative volume fraction of the two components and their associated diffusion coefficients. The model can be extended to multiple fibres and is implemented in FSL for tractography (Behrens et al. 2007).

The CHARMED (Composite Hindered and Restricted Model of Diffusion) model encompasses the different forms of diffusion in biological systems (Assaf & Basser 2005). Intra-axonal diffusion is *restricted* due to barriers such as the cell membrane resulting in non-Gaussian diffusion with increasing diffusion time. It is modelled as impermeable parallel cylinders of a given diameter and can be extended to cover multiple fibre orientations. Extra-axonal diffusion is *hindered* due to obstacles increasing the

mean path length between positions, characterised by the degree of tortuosity and is modelled by a diffusion tensor (anisotropic Gaussian diffusion). Fitted parameters give estimates of the diffusivity in the extra-axonal matrix (diffusivity of hindered part), the axonal density (volume fraction of the restricted part) and fibre orientations (ODF of the restricted part).

AxCaliber extends this framework to replace the fixed axon diameter by a gamma distribution to allow the axon diameter distribution to be estimated (Assaf et al. 2008). However to achieve a realistic scan time, diffusion was only measured perpendicular to the long axis of the nerve so must be known in advance (for example the corpus callosum) and the estimates obtained deviate from histological findings.

More recently two key factors that affect FA, neurite density and fibre orientation dispersion, have been estimated within a clinically feasible scan duration (20 minutes) using NODDI (neurite orientation dispersion and density imaging) (Zhang et al. 2012). This relaxes the constraint of the above models which assume parallel cylinders and allows dispersion of fibre orientation. It employs a three-compartment model with the intra-cellular compartment modelled by “sticks” (cylinders of zero radius) with orientation dispersion represented by a Watson distribution, the extra-cellular compartment as Gaussian anisotropic diffusion and the CSF compartment as Gaussian isotropic diffusion.

2.8.4 Limitations of Tissue Models

Models with additional parameters require a longer acquisition to provide the necessary data to perform the fitting so there is always a balance between the accuracy of the model and the acquisition time. By incorporating various assumptions to reduce the number of free parameters scan time is reduced at the expense of the accuracy of the model. In general a combination of the low spatial resolution, poor signal-to-noise with higher b -values and the necessary length of acquisition limit their clinical utility (Panagiotaki et al. 2012) although NODDI does represent a clinically feasible scan which is assessed further in Chapter 13.

2.9 Conclusions

Diffusion is a fundamental physical process characterised by the diffusion coefficient that can be quantified with diffusion MRI. Diffusion-weighted imaging measures the apparent diffusion coefficient which is useful in detecting early ischemia. However diffusion in biological tissues is fundamentally anisotropic which is better represented mathematically by a diffusion tensor.

Diagonalisation of this diffusion tensor provides eigenvectors, the orthogonal axes of diffusion used for tractography, and eigenvalues, a measure of diffusivity along these axes. Scalar invariants derived from the eigenvalues including FA and MD provide sensitive but non-specific measures of pathology that may be affected by a numerous factors. Tractography may be performed using either deterministic or probabilistic algorithms, which have contrasting advantages and disadvantages.

The diffusion tensor remains widely used but increasingly its limitations are being recognised. The assumption of a single compartment with Gaussian diffusion does not adequately model biological systems. By fitting biologically plausible models of white matter to the diffusion profile, additional parameters such as axonal density, axonal diameter distributions and fibre orientations may be derived. These techniques hold promise to provide more quantitative parameters via diffusion MRI but are not yet in widespread clinical use due in part to lengthy acquisition times.

3 DIFFUSION MAGNETIC RESONANCE IMAGING: CLINICAL STUDIES

3.1 Introduction

The previous chapter has introduced the principles of diffusion imaging and shown how these can be applied for clinical studies. In this chapter, previous studies using diffusion imaging in epilepsy are summarised including both cross sectional and longitudinal studies. The role of diffusion imaging in detecting malformations of cortical development and the use of tractography to study cognition (language and memory) in epilepsy is reviewed. Finally, the application of diffusion imaging to study working memory in conditions other than epilepsy is discussed with the application to epilepsy forming the subject of Chapter 11.

3.2 Generic Studies in Epilepsy

3.2.1 Diffusion Imaging of the Hippocampus

Animal models of status epilepticus demonstrate an acute postictal fall in ADC within the hippocampus (due to cytotoxic oedema) followed by interictal normalization then chronic elevation (Zhong et al. 1993). It was therefore suggested that the neuronal loss and gliosis of chronic mesial TLE might be detectable via an increase in ADC in humans. Initial DWI studies showed an interictal increase in ADC in the sclerotic hippocampus could reliably lateralise seizures (Hugg et al. 1999, Yoo et al. 2002, Lee et al. 2004a), correlated with memory dysfunction (Lui et al. 2005) and duration of epilepsy (Goncalves Pereira et al. 2006) but was less reliable when other pathologies were considered (Londono et al. 2003). These findings were replicated by subsequent DTI studies showing reduced FA and increased MD in sclerotic hippocampi (Assaf et al. 2003, Salmenpera et al. 2006) and similar but less consistent findings in non-lesional hippocampi (Wehner et al. 2007).

3.2.2 Cross Sectional Diffusion Tensor Imaging in TLE

Attention then turned to demonstrating more widespread alterations in white matter structure in patients with TLE. Arfanakis reported altered diffusion parameters within the external capsule and corpus callosum using region-of-interest based analysis (Arfanakis et al. 2002) whilst Concha showed bilateral changes within the fornix and cingulum, two key tracts from the temporal lobe, using tractography (Concha et al. 2005). Many further studies have been published using either these region-of-interest based analyses (manual or via tractography) or whole brain voxel-based analyses (SPM or TBSS) (Table 3.1).

The major themes are of widespread changes in diffusion parameters encompassing both temporal and extratemporal white matter bilaterally, but with an emphasis on the ipsilateral hemisphere. The changes

are typically more widespread in left TLE than right TLE (Focke et al. 2008, Ahmadi et al. 2009, Shon et al. 2010, Kemmotsu et al. 2011, Keller et al. 2012) and in hippocampal sclerosis than non-lesional cases (Concha et al. 2009, Shon et al. 2010).

A comparison of the two voxel-based approaches (SPM and TBSS) in patients with hippocampal sclerosis showed that TBSS was more sensitive to changes in white matter, whilst SPM was more sensitive to the increased MD in the ipsilateral hippocampus (Focke et al. 2008). The findings of non-voxel based approaches have been summarised in a recent meta-analysis (Otte et al. 2012). The degree of changes may be related to age of onset (Arfanakis et al. 2002), the duration of epilepsy (Lin et al. 2008, Govindan et al. 2008) or modulated by gender (Oguz et al. 2013).

The observed changes in diffusion parameters correlate with the cognitive profile of patients with TLE. Temporal white matter integrity has been shown to be related to memory performance (Riley et al. 2010) whilst that of the frontal lobe is related to verbal fluency (Wang et al. 2010a). Frontal and temporal regions are also implicated in clinical features such as the presence of interictal psychosis (Flugel et al. 2006). Diffusion measures within specific tracts are related to language and memory performance (McDonald et al. 2008) (see section 3.3).

Little data are available on the histological changes underlying the observed changes in diffusion parameters. In excised fimbria-fornix tissue following surgery, patients with hippocampal sclerosis were found to have a larger extra-axonal fraction, reduced myelin fraction and also looser packing with greater variability in axon size (Concha et al. 2010). Preoperative FA of this tract positively correlated with axonal membrane circumference, but there was also a trend to a positive correlation with axonal density and a negative correlation with myelin thickness. This highlights the non-specificity of measures such as FA, which may in part be addressed by better models (Chapter 13).

3.2.3 Longitudinal Diffusion Tensor Imaging in TLE

Following surgery (or injury), transected white matter tracts undergo Wallerian degeneration. An acute phase (hours-days) of fragmentation and axonal dying back is followed by a chronic phase (weeks-months) in which myelin is slowly degraded and phagocytosed. Reduced FA and increased MD occurs in the optic radiation following temporal lobe surgery resulting in a hemianopia consistent with Wallerian degeneration (Wieshmann et al. 1999).

There is also the potential for recovery of diffusion abnormalities, reflecting either neuronal plasticity or perhaps the cessation of seizures not longer causing ictal fluid shift. Detection requires longitudinal DTI studies with scans before and after surgery (Table 3.2). By studying patients undergoing corpus callosotomy, Concha demonstrated an early fall in FA and AD consistent with axonal degradation at 1 week followed by normalization of AD and increased MD and RD consistent with myelin degradation at 2-4 months (Concha et al. 2006). This was consistent with previous findings in animal models of axonal injury (Song et al. 2003, Sun et al. 2006). However more recent data suggest that the time course in humans followed ATLR may differ from the mouse retinal ischaemia model (Liu et al. 2013). Using multiple imaging timepoints, an acute reduction in MD, RD and AD of the fornix was observed in the

first week following ATLR that was more suggestive of axonal swelling. This is followed by a more chronic reduction of FA (due to reduced AD and increased RD) consistent with myelin degradation and gliosis.

The majority of longitudinal studies have considered temporal lobe resection. Initial data suggested that the preoperative DTI abnormalities may persist after surgery. In HS, preoperative diffusion abnormalities within the ipsilateral fornix and cingulum increase by 1 year following surgery reflecting Wallerian degeneration of damaged tracts whilst contralateral abnormalities in the fornix, cingulum and external capsule do not resolve despite seizure freedom (Concha et al. 2007). This argues for underlying structural changes (axonal or myelin degradation) rather than functional fluid shifts from seizures. Schoene-Bake showed widespread reductions in FA bilaterally in both left and right HS at a variable time period of 3-11 years following surgery, but comparison was only made to healthy controls as no preoperative DTI data for the patients were available (Schoene-Bake et al. 2009).

Several further studies have showed progression of diffusion abnormalities following surgery. In patients undergoing ATLR, FA decreased in ipsilateral tracts by 2 months with the change in the inferior longitudinal fasciculus correlating with the postoperative visual field deficit (McDonald et al. 2010). No further changes were seen between 2 and 12 months. In contrast, Faber et al demonstrated a reduction in FA in the left cingulum and fornix by 3-6 months following SAH with additional changes in the uncinate fasciculus by 1 year (Faber et al. 2013). It is important to note that the patients for the two operative timepoints only partially overlapped. Finally Nguyen showed no changes in FA following ATLR with increases in MD in the ipsilateral anterior temporal region, but the group size was small (10 subjects) so left and right HS were combined by flipping which will significantly reduce sensitivity (Nguyen et al. 2011).

There is also some evidence for resolution of diffusion abnormalities following surgery. This first report was post-operative resolution of diffusion abnormalities in the contralateral hippocampus (Thivard et al. 2007). In a more detailed study of a large cohort undergoing ATLR, bilateral widespread reductions in FA were seen (Yogarajah et al. 2010). However, there was also an increase in the FA of the corona radiata, internal and external capsules following left ATLR and the increase correlated with post-operative language performance. Post-hoc tractography suggested this cluster formed part of the ventro-medial language area (Saur et al. 2008).

3.2.4 Malformations of Cortical Development

Diffusion measures evolve with brain maturation so may assist the detection of malformations of cortical development (MCD). Widespread diffusion changes comprising reduced FA and increased MD extending beyond the visible abnormality have been identified in MCD (Eriksson et al. 2001) and in other focal lesions (Dumas de la Roque et al. 2005). In tuberous sclerosis, ADC is elevated in both epileptic and non-epileptic tubers, but more so in the former (Jansen et al. 2003). In focal cortical dysplasia (FCD), fibre connectivity assessed by FA is reduced in subcortical white matter adjacent to the abnormality (Lee et al. 2004b) and is accompanied by a rise in MD although this may not extend to FCD without white matter hyperintensities (Gross et al. 2005).

Paper	Patients/ Controls	Pathology	Laterality	Analysis	Regions	Positive findings
Arfanakis et al. 2002	15 / 15	TLE (HS or MRI-negative)	-	ROI	EC/CC/IC	EC/CC (FA, RD)
Concha et al. 2005	8 / 9	MTLE (HS)	6L, 2R	Tractography	Fornix, cingulum	Bilateral fornix (FA, RD), cingulum (FA, MD, RD)
Thivard et al. 2005	35 / 36	MTLE (any)	18L, 17R	ROI	Hippocampus	Contralateral MD
				SPM	Whole brain	Ipsilateral hippocampus, temporal, posterior extratemporal (FA and/or MD); contralateral hippocampus, amygdala, temporal pole (MD)
Kimiwada et al. 2006	14 / 14 (children)	TLE (any)	11L, 3R	ROI	Hippocampus, thalamus, lentiform	Bilateral hippocampus (FA), ipsilateral hippocampus (MD)
Gross et al. 2006	11 / 14	MTLE (HS)	7L, 4R	ROI	Hippocampus, EC/CC/IC	EC/CC (FA, MD)
Yu et al. 2006	14 / 14	MTLE (HS or MRI-negative)	5L, 9R	ROI	Hippocampus	Bilateral MD (ipsilateral greater)
Rodrigo et al. 2007	10 / 10	MTLE (HS)	All right	Tractography	Uncinate	Reduced FA on right (loss of asymmetry)

Focke et al. 2008	33 / 37	MTLE (HS)	21L, 12R	SPM	Whole brain	LHS: Ipsilateral TL/FL, bilateral thalamus/cingulate (FA); ipsilateral TL/cingulum, bilateral FL (MD) RHS: Ipsilateral TL (FA); ipsilateral hippocampus/TL (MD)
				TBSS	Whole brain	LHS: Ipsilateral TL/fornix, bilateral thalamus/cingulate, bilateral FL (FA); ipsilateral TL/thalamus, bilateral cingulum/CC/EC (MD) RHS: Ipsilateral TL/PHG/fornix, bilateral cingulum/CC (FA); ipsilateral TL/FL, bilateral parietal (MD)
Govindan et al. 2008	13 / 12 (children)	TLE (MRI-negative)	All left	Tractography	UF, ILF, AF, CST	Bilaterally in all (FA) - reversed asymmetry of AF
Gong et al. 2008	17 / 26	TLE (HS)	11L, 6R	ROI	Thalamus	Reduced FA, increased MD bilaterally
	10 / same	TLE (no HS)	4L, 2R, 4 bilateral			No significant differences
Kim et al. 2008	10 / 10	TLE (any)	4L, 6R	ROI	Corpus callosum	Reduced FA/AD, increased RD in splenium
Nilsson et al. 2008	8 / 10 (children)	TLE (any)	7L, 1R	Tractography	Temporal, cingulate	Bilateral changes (MD, AD, RD)
Concha et al. 2009	17 / 25	TLE (HS)	-	ROI	EC/CC	EC/CC (FA, MD, RD) (both except MD in CC HS only)
	13 / same	TLE (MRI-negative)	6L, 2R, 5 bilateral	Tractography	Fornix, cingulum, CC	Bilateral cingulum (FA, MD, RD; both groups), bilateral fornix (FA, RD; HS only)

Knake et al. 2009	12 / 12	MTLE (HS)	All left	ROI	Hippocampus, PHG, TL, FL, CC	Ipsilateral hippocampus, PHG, CC (FA)
				VBA (unspecified)	Whole brain	Bilateral TL, CC, ipsilateral frontal (FA)
Ahmadi et al. 2009	21 / 21	TLE (any)	10L, 11R	Tractography	Cingulum, PHG, SLF, ILF, UF, fornix, ATR, IFOF	LTLE : reduced ipsilateral (6 tracts) and contralateral (4 tracts) RTLE : reduced ipsilateral (4 tracts)
Shon et al. 2010	19 / 20	TLE (HS)	12L, 7R	SPM	Whole brain	LHS : Ipsilateral hippocampus, TL, FL, cingulate RHS : Medial temporal/frontoparietal
	18 / same	TLE (non-HS)	10L, 8R			LTLE : Ipsilateral posterior limbic (PHG/cingulate) RTLE : No changes
Bonilha et al. 2010	23 / 34	MTLE (HS)	8L, 15R	NPM	Whole brain	Medial TL, frontotemporal, orbitofrontal ipsi>contra (FA); FL, TL (MD in RHS)
Kim et al. 2010	9 / 16	TLE (HS)	5L, 4R	ROI	Thalamus	Asymmetrical reduced FA Bilateral increased MD
	9 / same	TLE (dysplasia)	5L, 4R			Asymmetrical reduced FA Bilateral increased MD
Meng et al. 2010	8 / 8 (children)	TLE (any)	6L, 2R	ROI	CC/EC/IC	Bilateral IC/splenium (FA) Bilateral IC/EC (MD)
Kemmotsu et al. 2011	36 / 36	TLE (any)	18L, 18R	ROI (atlas)	Fornix, PHG, UF, ILF, IFOF, AF	Bilateral changes (FA), more marked ipsilateral and LTLE (especially UF, ILF)

Afzali et al. 2011	19 / 12	TLE (any)	11L, 8R	SPM/TBSS	Whole brain	TL/PHG/FL/EC/fornix/CC (FA)
Keller et al. 2013	10 / 81	TLE (MRI- negative)	All left	SPM	Whole brain	Bilateral TL/CC/EC/thalamus (FA), CC/thalamus (MD)
Keller et al. 2012	62 / 68	TLE (HS)	41L, 21R	ROI	TL, FL, CC, IC, brainstem, hippocampus, PHG, putamen, thalamus	LHS: bilateral hippocampus, PHG, TL, CC, FL, IC, brainstem (FA) RHS: right PHG, bilateral thalamus/CC (FA)
Liacu et al. 2012	9 / 10	TLE (HS)	7L, 2R	Tractography	Cingulum, fornix	Bilateral changes (FA, RD)
	9 / same	TLE (MRI- negative)	8L, 1R			Ipsilateral all (FA), cingulum (RD), no contralateral changes
Oguz et al. 2013	44 / 44	MTLE (HS)	22L, 22R	TBSS	Whole brain	Temporal/extra-temporal especially ipsilateral (FA, MD); FA changes greatest in male/left, MD in female/right

Table 3.1 - Summary of cross sectional DTI studies in epilepsy

Pathology: HS = hippocampal sclerosis; *Analysis:* ROI = region-of-interest based, SPM = statistical parameter mapping, TBSS = tract-based spatial statistics, VBA = voxel-based analysis; *Regions and Tracts:* AF = arcuate fasciculus, ATR = anterior thalamic radiation, CC = corpus callosum, CST = corticospinal tract, EC = external capsule, FL = frontal lobe, IC = internal capsule, IFOF = inferior fronto-occipital fasciculus, ILF = inferior longitudinal fasciculus, PHG = parahippocampal gyrus, SLF = superior longitudinal fasciculus, TL = temporal lobe, UF = uncinate fasciculus; *Positive findings:* refers to reduced FA or increased MD/AD/RD unless otherwise stated

Paper		Patients/ Controls	Pathology	Laterality	Surgery	Timepoints	Analysis	Regions	Positive findings
Concha et al. 2006		3 / 1	Various	-	Corpus callosotomy	0w/1w/2-4m	Tractography	Corpus callosum	1w: decreased FA/AD (axonal degradation) 2-4m: decreased FA, increased MD/RD (myelin degradation)
Concha et al. 2007		8 / 22	HS	6L, 2R	ATLR (3) or SAH (5)	0y/1y	Tractography ROI	Fornix, cingulum EC/genu/splenium	0: reduced FA, increased MD/RD bilateral fornix, cingulum, EC 1y: ipsilateral fornix/cingulum reduced FA/increased MD/RD; contralateral fornix, cingulum, EC did not normalise
Thivard et al. 2007		24 / 36	HS	12L, 12R	ATLR (20) or SAH (4)	0m/8m	ROI	Hippocampus	0: Increased MD ipsilateral, decreased MD contralateral 8m: contralateral MD normalised
Schoene-Bake et al. 2009		40 / 28	HS	19L, 21R	ATLR (3) or SAH (37)	No pre-op 3-11y	TBSS	Whole brain	LHS: reduced FA ipsilateral SLF, cingulum, CC, forceps minor, UF, IFOF, ILF, CST, contralateral ILF RHS: reduced FA ipsilateral SLF, cingulum, CC, UF, ATR, IFOF, ILF, CST, contralateral posterior cingulum

McDonald et al. 2010	7 / none	TLE	3L, 4R	ATLR	0m/2m/12m	ROI (atlas)	Fornix, UF, PHC, ATR, SLF, IFOF, ILF, CST, cingulum	2m: decreased FA ipsilateral ILF, PHC, UF, IFOF, CC, bilateral fornix 12m: no further change
Yogarajah et al. 2010	46 / none	TLE	26L, 20R	ATLR	0m/4m	TBSS	Whole brain	LHS: reduced FA ipsilateral OR, PHG, SLF, UF; bilateral ILF, fornix, AC; increased FA corona radiata, IC, EC; increased MD ipsilateral ILF, UF, AC, EC RHS: reduced FA ipsilateral OR, PHG, SLF, UF, IFOF; bilateral ILF, fornix, AC; increased FA corona radiata; increased MD ipsilateral UF, AC, EC, bilateral fornix
Nguyen et al. 2011	22 / none (only 10 in post-op)	HS	11L, 11R	ATLR	0m/2-7m	TBSS (left flipped)	Whole brain	0: reduced FA ipsilateral HIP/fornix/UF/CC, widespread increased MD 2-7m: increased MD ipsilateral anterior temporal
Faber et al. 2013	20 / none	HS	All left	SAH	0m/3-6m/12m	TBSS	Whole brain	3-6m: reduced FA left cingulum, fornix 12m: in addition, reduced FA UF
Liu et al. 2013	6 / 3	TLE	3L, 3R	ATLR (4) or SAH (2)	Many e.g. 0, 1/2/3/6d, 2m	Tractography	Fornix	Ipsilateral MD/AD/RD reduced by 2 days FA reduced/MD/RD rises by 1-4m

Table 3.2 - Summary of longitudinal DTI studies in epilepsy

Pathology and Analysis: as Table 3.1; *Surgery:* ATLR = anterior temporal lobe resection, SAH = selective amygdalohippocampectomy; *Region and Tracts:* AC = anterior commissure, ATR = anterior thalamic radiation, CC = corpus callosum, CST = corticospinal tract, EC = external capsule, HIP = hippocampus, IC = internal capsule, IFOF = inferior fronto-occipital fasciculus, ILF = inferior longitudinal fasciculus, OR = optic radiation, PHC = parahippocampal cingulum, SLF = superior longitudinal fasciculus, UF = uncinate fasciculus

The reduced FA could be a result of increased or abnormally located grey matter or pathological white matter with abnormal myelination or ectopic neurons whilst the increase in MD could reflect defective neurogenesis or cellular loss increasing the extracellular space (Eriksson et al. 2001). Improved diffusion models to study the extracellular volume could help disentangle these possibilities (Chapter 13).

3.3 Tractography and Cognition in Epilepsy

3.3.1 Language

A dominant temporal lobe focus is associated with impaired language performance and up to 40% of patients show decline in naming following surgery (Davies et al. 1998). Earlier age of onset appears protective suggesting language reorganisation (Hermann et al. 1994, Saykin et al. 1995), which is supported by the higher incidence of atypical right hemisphere or bihemispheric language representation seen in patients with epilepsy (Helmstaedter et al. 1997b). Those with hippocampal sclerosis decline less because they start from a lower baseline (Seidenberg et al. 1998, Davies et al. 1998).

Language laterality has traditionally been determined using the Wada test but this is now being replaced by non-invasive functional MRI (fMRI) with verbal fluency and verb generation paradigms yielding reliable activation of expressive language areas in the frontal lobe (Arora et al. 2009). Functional MRI demonstrates reorganisation to the contralateral hemisphere in early onset lesions (Liegeois et al. 2004) and following surgery (Bonelli et al. 2012).

The classical anatomy of language pathways from the nineteenth century consists of Broca's area (expressive language) in the inferior and middle frontal gyrus and Wernicke's area (receptive language) in the superior temporal gyrus (Figure 3.1). These are linked by the arcuate fasciculus (AF), a subcomponent of the superior longitudinal fasciculus (SLF), passing from the dorsal premotor cortex to the superior temporal gyrus.

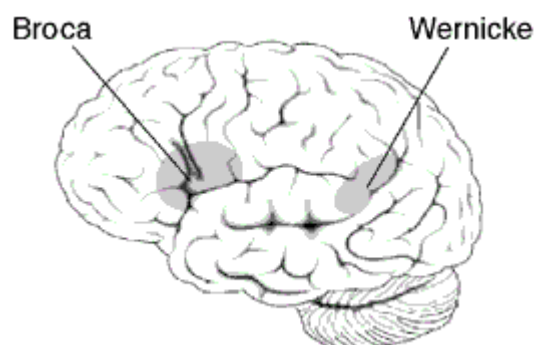


Figure 3.1 - Anatomy of key language areas (Broca's and Wernicke's areas)

Source: Wikimedia Commons.

In right-handed controls, these frontotemporal connections are left-lateralised and the degree of functional and structural lateralisation is correlated (Powell et al. 2006). In left TLE but not right TLE, there is reversal or loss of this asymmetry suggesting reorganisation (Powell et al. 2007). Reorganisation is more common in those with earlier onset of seizures and persistent lateralisation to the dominant hemisphere, and thus a failure to reorganise, is associated with greater postoperative decline in naming following dominant ATLR (Powell et al. 2008a).

Attempts have been made to use asymmetry of the AF to determine language laterality akin to fMRI. Asymmetry indices of AF volume correlate with language dominance on Wada testing (Matsumoto et al. 2008) and in children a combination of parameters including FA and volume predicts Wada-defined laterality (Tiwari et al. 2011). The best predictor comes from combining laterality indices from language fMRI and AF tractography with handedness (Ellmore et al. 2010).

Cortical stimulation in left-language dominant patients undergoing surgery generally identifies sites near to the AF as defined by tractography as critical for language (Ellmore et al. 2009, Diehl et al. 2010) and children undergoing resection of the left AF show a compensatory increase in FA of the contralateral AF (Goradia et al. 2011). However, it is increasingly recognised that the AF is not the only language pathway.

Dorsal and ventral language pathways have been described with the dorsal pathway (AF) necessary for mapping of sound to articulation and repetition (Table 3.3). In contrast the ventral pathway, passing from the middle temporal lobe to the ventrolateral premotor cortex via the extreme capsule, is important for semantic processing (Saur et al. 2008).

Pathway	Purpose	From	Via	To
Dorsal	Sound to articulation (sublexical repetition)	Superior temporal	Arcuate (part of superior longitudinal) fasciculus	Premotor
Ventral	Sound to meaning (language comprehension)	Middle temporal	Extreme capsule	Ventrolateral prefrontal cortex

Table 3.3 - Anatomy of the two language pathways

The distributed nature of language function is supported by a study showing the diffusion parameters of several atlas-defined white tracts, including the uncinate fasciculus (UF), AF and inferior fronto-occipital fasciculus (IFOF) particularly on the left correlate with naming performance in patients with epilepsy (McDonald et al. 2008). As already mentioned in section 3.2.3, a postoperative increase in the FA in the ventral pathway (external capsule) was found to correlate with postoperative verbal fluency following left temporal lobe surgery (Yogarajah et al. 2010).

3.3.2 Memory

The concept of material specific memory suggests that left hippocampal sclerosis is associated with impaired verbal memory (Baxendale et al. 1998b) whilst right hippocampal sclerosis is associated with impaired spatial memory (Baxendale et al. 1998a) although in reality the distinction is not so clear cut (Saling 2009). Left ATL R is associated with a decline in verbal memory, particularly immediate, with possible improvement in non-verbal memory (Lee et al. 2002). Factors predicting greater decline include intact preoperative memory, intact memory functions with a Wada test on the contralateral hemisphere or other data suggesting preserved function in the lobe to be resected (functional adequacy) and pathologies other than hippocampal sclerosis with the absence of hippocampal atrophy (Spencer & Huh 2008). Right ATL R may affect non-verbal memory although the effects are less consistent (Lee et al. 2002, Vaz 2004). It is important however to recognise that there is considerable variation in the extent and direction of any postoperative memory change. A significant minority of patients show an improvement in memory function after ATL R, especially in the contralateral function (i.e. verbal memory after right ATL R, visual memory after left ATL R) (Baxendale et al. 2008). This could in part relate to a reduction in seizure and medication burden.

The involvement of memory with epilepsy has primarily been addressed with fMRI. Verbal memory encoding activates the left hippocampus in healthy controls whilst in left TLE reorganisation to the right hippocampus is seen (Richardson et al. 2003) with greater reorganisation predictive of a lower decline in verbal memory following left ATL R (Richardson et al. 2004). The concept of asymmetry on fMRI has been extended to non-verbal memory decline following non-dominant ATL R (Powell et al. 2008b). Asymmetry during encoding tasks toward the lesional side of anterior hippocampal activation predicts decline whilst asymmetry to the lesional side of posterior hippocampal activation predicts a better outcome (Bonelli et al. 2010) although other groups argue that language lateralisation per se, rather than asymmetry of episodic memory encoding processes is more important for predicting verbal memory outcome after dominant ATL R (Binder et al. 2010).

The hippocampus and adjacent parahippocampal structures are essential for declarative memory (Eichenbaum 2000) and three main white matter tracts have been implicated in memory function - the uncinate fasciculus connects the anterior temporal and inferior frontal lobes (Ebeling & von Cramon 1992), the two key areas identified by fMRI; the fornix projects from the hippocampus to the septal region and mammillary bodies and the cingulum projects from the parahippocampal gyrus around the cingulate gyrus.

Diffusion changes in these tracts have been reported in TLE (Section 3.2.3) and several studies have shown how these correlate with memory function (Table 3.4). The main findings are that verbal memory correlates with diffusion parameters of left-sided structures such as the hippocampus, parahippocampal cingulum and uncinate fasciculus whilst non-verbal memory correlates with right-sided structures although the findings are not this clear cut. Changes in post-operative diffusion parameters of the non-resected hippocampi correlate with memory outcome (Pfeuty et al. 2011).

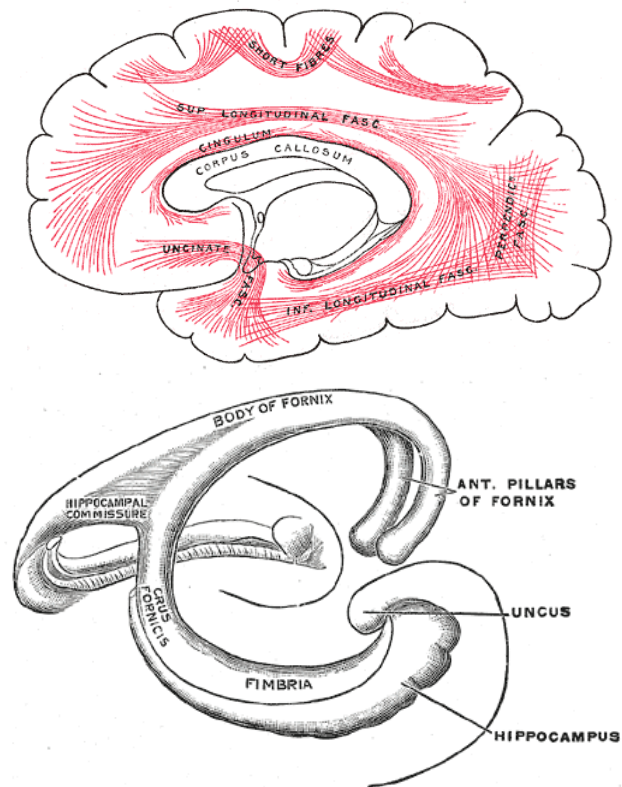


Figure 3.2 - Anatomy of white matter tracts implicated in memory function

Uncinate fasciculus and cingulum (top), fornix (bottom). *Source:* Wikimedia Commons (from Gray's Anatomy of the Human Body, 1918).

3.4 Tractography and Working Memory in Other Conditions

Working memory requires the maintenance and manipulation of information over short periods of time. It is an active process requiring executive regulation and controlled attention that involves a complex neural network in which interconnecting white matter is critical. Aging and disease processes are hypothesised to disrupt working memory through cortico-cortical and cortico-subcortical disconnection. TLE has previously been considered to impair formation and storage of long-term memories (Squire 1992), whilst not affecting working memory (Cave & Squire 1992). However, recent evidence suggests that working memory is compromised (reviewed in Stretton & Thompson 2012).

The working memory network has been explored using multiple imaging modalities, including fMRI, DTI and voxel-based morphometry. “n-back” paradigms employing progressively increasing working memory load (Braver et al. 1997) can delineate the task-positive network with fMRI demonstrating activation in the frontal and parietal regions bilaterally (reviewed in Owen et al. 2005) that is reduced in subjects with epilepsy (Vlooswijk et al. 2011, Stretton et al. 2012). Studies that have shown a correlation between DTI measures and working memory performance are summarised in Table 3.5 but have not been undertaken in epilepsy.

Paper	Subjects	Measurements	Group differences	Memory correlations
Lui et al. 2005	20 nonlesional TLE (9 left, 11 right) 20 controls	ROI hippocampi and PHG – ADC	Raised ADC compared to controls with ipsilateral > contralateral in HIP/PHG	Left HIP (-) - verbal delayed recall, recognition; visual (Ray-Osterreith) Right HIP (-) - verbal recall Right PHG (+) - delayed recall visuospatial
Yogarajah et al. 2008	18 unilateral TLE (8 left, 10 right) 10 controls	Tractography from PHG - mean FA and volume	Reduced left-sided connectivity in LTLE (volume, FA) Trend in RTLE	LTLE: left FA correlates with verbal (list learning), right FA correlates with non-verbal (design learning) RTLE: none
Diehl et al. 2008	28 unilateral TLE (18 left, 10 right) 10 controls	Tractography of UF - mean FA and MD	Reduced FA left UF, increased MD bilaterally in LTLE and RTLE	LTLE: Left UF MD (-) auditory immediate/delayed LTLE: Left UF FA (+) auditory delayed LTLE: Right UF FA (+) visual delayed memory RTLE: None
McDonald et al. 2008	17 unilateral TLE (9 left, 8 right) 17 controls	FA/MD of atlas-derived tracts (UF, AF, fornix, PHC, IFOF, CST)	Multiple changes in FA/MD within these tracts reported	Verbal memory: Left UF/PHC/IFOF MD, bilateral AF MD (-), right AF FA (+) Non-verbal memory: None
Riley et al. 2010	12 unilateral TLE (10 left, 2 right) 10 controls	Whole brain (TBSS), then these regions used for cognitive correlation	Reduced FA ipsilateral anterior, mesial temporal, cerebellum, contralateral frontoparietal	Delayed memory: FA anterior temporal Immediate memory: FA mesial temporal
Pfeuty et al. 2011	23 unilateral TLE (12 left, 11 right) before/after surgery	ROI of hippocampi (MD)	Contralateral MD increases after surgery	LTLE: contralateral recovery correlated with non-verbal memory RTLE: contralateral recovery correlated with verbal memory

Table 3.4 - Summary of DTI studies of memory in epilepsy

Measurements: ROI = region-of-interest, TBSS = tract-based spatial statistics; *Regions and tracts:* AF = arcuate fasciculus, CST = corticospinal tract, HIP = hippocampus, IFOF = inferior fronto-occipital fasciculus, PHC = parahippocampal cingulum, PHG = parahippocampal gyrus, UF = uncinate fasciculus; *Memory correlations:* direction of correlation indicated by + or -.

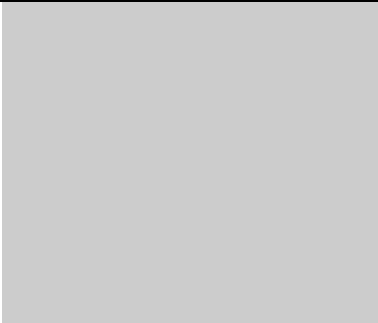


Maturation of the gray and white matter of this frontoparietal network is seen in healthy children (Olesen et al. 2003) and is related to working memory performance (Nagy et al. 2004, Ostby et al. 2011). In healthy controls, white matter volumes of left frontoparietal regions correlate with verbal working memory (Takeuchi et al. 2010) and both the volume and cortical thickness of frontoparietal regions are related to verbal working memory in children following traumatic brain injury (Wilde et al. 2011).

Maturation of the right SLF, a tract connecting the frontal and parietal regions, alongside cortical thinning of the frontal and parietal lobes is key in the maturation of working memory in adolescence (Ostby et al. 2011), and the integrity of this tract mediates the increased brain responsivity observed during working memory fMRI that correlates with better performance (Burzynska et al. 2011) in healthy controls. Diffusion parameters of tracts connecting the frontal and parietal lobes, including the SLF, cingulum and corpus callosum, account for a significant degree of variations in working memory capacity seen in infants (Short et al. 2013).

Similarly diffusion changes in the SLF and cingulum correlate with working memory decline in normal aging (Kennedy & Raz 2009, Charlton et al. 2010), multiple sclerosis (Dineen et al. 2009), schizophrenia (Karlsgodt et al. 2008), and traumatic brain injury (Palacios et al. 2011). Connections from the thalamus (Piras et al. 2010) and cerebellum (Law et al. 2011) may also play a role. Further, white matter changes in the parietal lobe consistent with plasticity have been observed following working memory training (Takeuchi et al. 2010).

The evidence for hippocampal involvement in working memory is mixed, as fMRI studies have shown both task-dependent hippocampal activation (Axmacher et al. 2009) and deactivation (Cousijn et al. 2012). In patients with HS, reduced activation of the right superior parietal lobe is observed and deactivation of the ipsilateral hippocampus with increasing working memory load is disrupted and associated with impaired working memory performance (Stretton et al. 2012). However, no studies have addressed the structural correlates of impaired working memory in patients with epilepsy or the structural integrity of the temporal lobe itself in working memory.

Paper	Subjects	DTI analysis	Working memory measure	Group findings	Working memory correlations
Nagy et al. 2004	Children (23)	Voxel-based (SPM)	Non-verbal (dot locations)		FA/+ L superior frontoparietal, inferior frontal, anterior CC, temporo-occipital
Charlton et al. 2006	Elderly (99)	Whole brain (histogram), ROI (centrum semiovale)	Verbal (DSB + LNS)	Age-related ↓FA, ↑MD	FA/+, MD/- (whole brain, ROI)
Karlsgodt et al. 2008	Schizophrenia (12), controls (17)	Voxel-based (TBSS) ROI (SLF)	Verbal (SIRT)	↓FA posterior SLF ↓FA bilaterally	None FA/+ L SLF
Dineen et al. 2009	RRMS (37), controls (25)	Voxel-based (TBSS)	Attention/verbal (PASAT)	↓FA in CC, ILF, IFOF, fornix, PCR, left CP	FA/+ CC, forceps major, L CB, R ILF, L SLF, bilateral parietal AF
Kennedy & Raz 2009	Healthy aging (52; aged 19-81yr)	ROI (CCg/CCs, ICa/ICg/ICp, subcortical association white matter in each lobe)	Non-verbal (size judgement span) Non-verbal (n-back) Verbal (listening span) Verbal (n-back)	Age-related ↓FA (most)	FA/+ PFC/CCg/ICp/temporal FA/+ PFC/CCg/ICa/temporal FA/+ CCg/temporal None
Zahr et al. 2009	Healthy aging (12 young; 12 old)	Tractography from ROI (CCg/CCs, fornix, ILF, CB, UF)	Verbal (SIRT) Non-verbal (blocks forward)	Age-related ↓FA, ↑MD in many	FA/+ CCg, fornix MD/- CCg, fornix, superior CB, UF
Takahashi et al. 2010	Adults (38)	Voxel-based (SPM) Post-hoc ROI cerebellar peduncles	Verbal (n-back)		FA/+ R anterior cingulate, R occipital, cerebellar peduncles

Piras et al. 2010	Adults (181)	ROI (caudate, putamen, pallidum, thalamus, hippocampus, amygdala) Voxel-based (thalamus only)	Non-verbal (n-back)		MD/- thalami (especially prefrontal and posterior parietal projections)
Palacios et al. 2011	TBI (15), controls (16)	Voxel-based (TBSS) with ROI (CC, SLF, ILF, IFOF, UF, CB, fornix)	Non-verbal (n-back)	Widespread ↓FA	FA/+ SLF, fornix, CC bilaterally
Vestergaard et al. 2011	Children (76)	ROI (SLF, DLPFC, posterior parietal)	Non-verbal (CANTAB)		FA/+ L SLF AD/- L SLF
Wilde et al. 2011	Children with TBI (40), controls (41)	ROI (IFOF, ILF, frontal white matter, UF, ICa/p, CB)	Verbal (SIRT)	↑MD in L IFOF, UF, frontal, ICa	MD/- L frontal, L CB
Burzynska et al. 2011	Young adults (27)	ROI (SLF)	Verbal (n-back)		FA/+ SLF (especially left)
Ostby et al. 2011	Children (108)	Voxel-based (TBSS) ROI (SLF)	Verbal (DSF, DSB)		DSF and DSB: RD/- L SLF DSF: RD/- L ILF, L inf parietal/supramarginal/temporal DSB: RD/- L PHG, L supramarginal/temporal

Palacios et al. 2012)	TBI (19), controls (19)	Voxel-based (TBSS)	Non-verbal (n-back)	Not reported	FA/+ R SLF, bilateral ILF, IFOF, CCg/CCs
Yu et al. 2012)	RRMS (37), controls (20)	Voxel-based (TBSS)	Attention/verbal (PASAT) Cognitive speed/non-verbal (SDMT)	Widespread ↓FA, ↑MD	FA/+ PTR/CC/EC FA/+ in all tracts (non-specific)
Sugranyes et al. 2012)	Schizophrenia (25), controls (19)	JICA (of fMRI and FA)	Verbal (n-back)	↓FA L IFOF, bil UF, L CB, R ILF, bil fornix/PHG, R CC	FA CCg/posterior CB
Short et al. 2013)	12-month infants (73)	ROI (CCg/s/b, ant CB, ATR, STR, AF, ON, ILF, spinothalamic)	Non-verbal (recall toy location)		FA/+, RD/- in CCg/ATR/STR/ant CB/AF
Gu et al. 2013)	Early DAI (15), controls (15)	ROI (ICp, UF, ACR, SLF, ILF, CCg/s, CB)	Verbal (DSB)	Widespread ↓FA, ↑MD	FA/+ CB/UF/SLF/ILF MD/- SLF/ILF AD/+ UF RD/- CB/SLF/ILF

Table 3.5 - Summary of DTI studies of working memory function

Subjects: DAI = diffuse axonal injury, RRMS = relapsing-remitting multiple sclerosis, TBI = traumatic brain injury; *DTI Analysis:* JICA = joint independent component analysis, ROI = region-of-interest, SPM = statistical parametric mapping, TBSS = tract-based spatial statistics; *Regions:* ACR = anterior corona radiata, AF = arcuate fasciculus, ATR = anterior thalamic radiation, CB = cingulum bundle, CC = corpus callosum (CCb = body, CCg = genu, CCs = splenium), CP = cerebral peduncle, CST = corticospinal tract, DLPFC = dorsolateral prefrontal cortex, EC = external capsule, IC = internal capsule (ICa = anterior, ICg = genu, ICp = posterior), IFOF = inferior fronto-occipital fasciculus, ILF = inferior longitudinal fasciculus, ON = optic nerve, PCR = posterior corona radiata, PFC = prefrontal cortex, PHG = parahippocampal gyrus, PTR = posterior thalamic radiation, SLF = superior longitudinal fasciculus, STR = superior thalamic radiation, UF = uncinate fasciculus; *Measures:* DSB = Digit Span Backwards, DSF = Digit Span Forwards, LNS = Letter Number Sequencing, PASAT = Paced Auditory Serial Addition Test, SDMT = Symbol Digit Modalities Test, SIRT = Sternberg Item Recognition Test; *Correlations:* Direction of correlation indicated by + or - (e.g. FA/+ = positive correlation with fractional anisotropy)

3.5 Conclusions

Initial diffusion imaging studies showing changes within the lesional hippocampus were followed by cross-sectional DTI studies demonstrating widespread alterations in white matter encompassing bilateral temporal and extra-temporal regions in TLE. Longitudinal studies have shown changes consistent with Wallerian degeneration occur early after surgery in ipsilateral tracts whilst changes in contralateral tracts persist. There is also evidence for improvement (plasticity) within the corona radiata, internal and external capsules following left ATLRL that is related to improved language performance.

Diffusion imaging has been used to study the cognitive effects of epilepsy. Language laterality can be studied by both fMRI and DTI which can be used to demonstrate reorganisation and predict language outcome following surgery. Verbal memory impairment is related to diffusion parameters of left-sided temporal structures whilst non-verbal memory correlating with right-sided structures. The role of frontoparietal pathways, in particular the SLF and cingulum, in working memory has been demonstrated in conditions other than epilepsy but not yet explored in patients with epilepsy.

4 THE OPTIC RADIATION AND VISION

4.1 Introduction

Meyer's loop, the most anterior portion of the optic radiation, passes through the temporal lobe. It is at risk during ATLR so the majority of patients experience a post-operative contralateral partial superior quadrantanopia. Whilst minor for many, it is significant enough to preclude driving in between 4 and 50% even if seizure-free (Manji & Plant 2000, Pathak-Ray et al. 2002, Jeelani et al. 2010). The optic radiation is thus of considerable interest in epilepsy surgery.

First, the gross anatomy of the visual pathways is summarised with a review of the initial anatomical studies of the optic radiation. Second, the advent of temporal lobe surgery for epilepsy and the information gained from this is considered. Then, more recent dissection-based studies that concentrate on the relationship of the optic radiation to anatomical landmarks during surgery are summarised. Finally, the extensive literature on the use of diffusion tensor imaging tractography of the optic radiation both in epilepsy surgery and for other conditions is discussed. The role of these, and other, data in surgical planning with intraoperative imaging is discussed in Chapter 5.

4.2 Gross Anatomy of the Visual Pathways

The human visual pathway is well characterised (Figure 4.1). Following signal transduction in the retina, visual information passes posteriorly along the optic nerves to the optic chiasm. Here information from the nasal retina (temporal visual field) crosses over so that all parts of the visual system posterior to this represent the contralateral visual hemifield from both eyes. The optic tract leads from the optic chiasm to the lateral geniculate nucleus (LGN), a thalamic nucleus. The optic radiation is the final part of the pathway comprising a major white matter tract connecting the LGN to primary visual cortex in the occipital lobe.

4.3 Initial Anatomical Studies of the Optic Radiation

Careful dissection of the preserved optic radiation by Adolf Meyer in two patients with temporo-occipital cortical degeneration allowed the description of the three bundles of the optic radiation and the “*peculiar detour of the ventral portion of the geniculocalcarine path [optic radiation]*” (Meyer 1907):

1. **Anterior bundle (ventral)** – fibres pass anteriorly over the roof of the temporal horn of the lateral ventricle, then turn backwards (known as Meyer's loop, or the temporal knee) passing back along the inferolateral aspect of the temporal horn before turning to run underneath the ventricle and pass into the lower lip of the calcarine fissure

2. **Central bundle (lateral)** – fibres pass laterally across the roof of the temporal horn then posteriorly along the lateral wall and roof of the trigone and occipital horn to the occipital pole
3. **Posterior bundle (dorsal)** – fibres pass directly posteriorly along the roof of the trigone and occipital horn radiating into the upper lip of the calcarine fissure

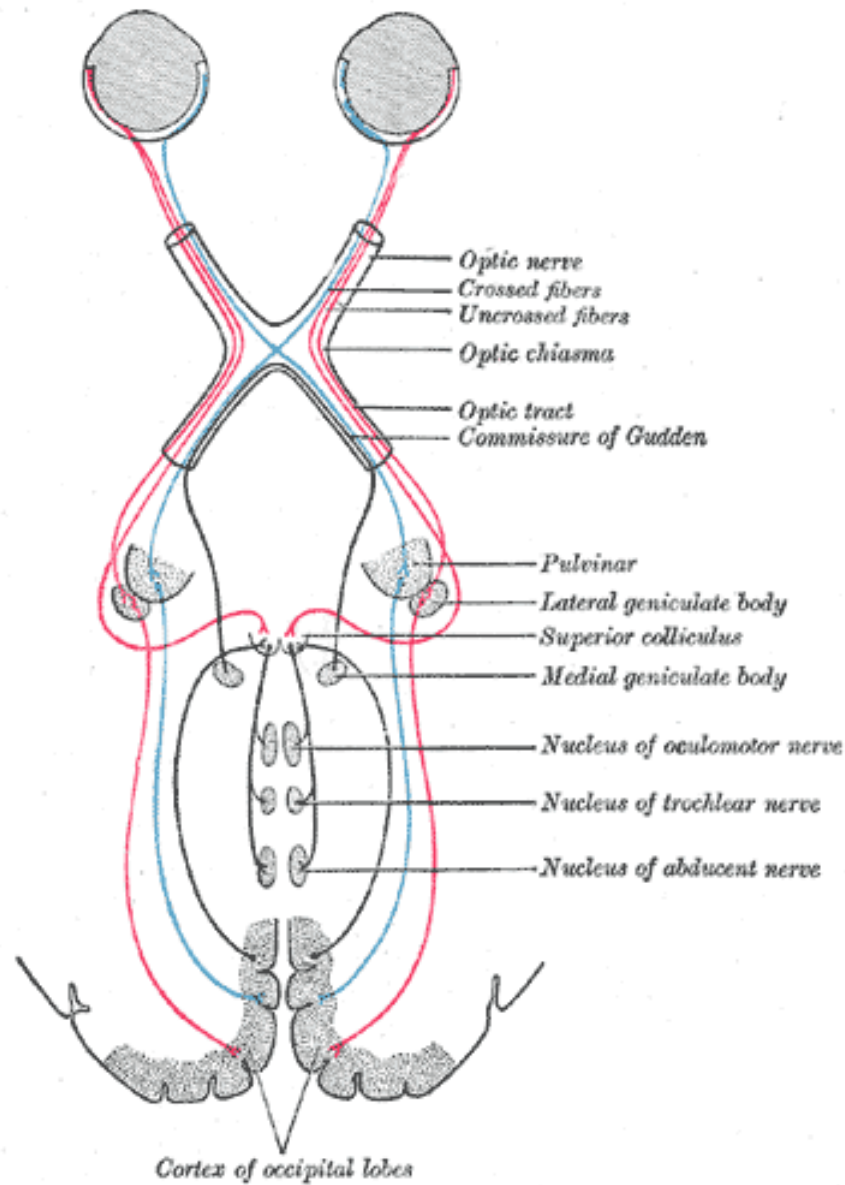


Figure 4.1 - Anatomy of the human visual system

Source: Wikimedia Commons (from Gray's Anatomy of the Human Body, 1918).

Meyer recognised the important functional distinction between the anterior and posterior bundles (Meyer 1907), and subsequent work showed that the central bundle represented macula vision (Harrington 1961):

"Cases of quadrant hemianopsia tend to point to the dorsal parts of the optic radiation and cortex for defect of the lower quadrant (that is, blindness of the upper quadrant of the retina); affection of the ventral parts to defect in the upper quadrant of the visual field." (Meyer 1907)

Such a functional division was supported by later work by Gordon Holmes looking at the visual deficits resulting from gunshot wounds in World War I (Holmes 1918), and a series of patients with temporal lobe tumours described by Harvey Cushing in whom over three-quarters suffered from a visual deficit (Cushing 1921). It was confirmed by a large series of 62 patients with visual deficits from damage to the optic radiation from penetrating head injuries (Spalding 1952). This paper also suggested that the central bundle represented macula vision, giving the following anatomical organisation (Table 4.1):

Bundle	Location in optic radiation	Target in visual cortex	Visual representation
Anterior	Ventral	Lower lip of calcarine fissure	Upper quadrant
Central	Lateral (central)	Occipital pole	Macula (central)
Posterior	Dorsal	Upper lip of calcarine fissure	Lower quadrant

Table 4.1 - Anatomical organisation of the three bundles of the optic radiation

A key fact not addressed in Meyer's original description of the loop was its anterior extent. Cushing's later figures based on Meyer's description depict the optic radiation entirely clothing the anterior extent of the temporal horn (Figure 4.2). Rasmussen debated the anterior extent of Meyer's loop and suggested that it reached virtually as far the as far as the tip of the temporal horn noting that "*some geniculo-calcarine fibers may proceed fully 2cm forward before turning back*" (Rasmussen 1943).

The organisation of fibres within the optic radiation has also been debated. Early suggestions were that fibres from the ipsilateral eye ran more laterally than those from the contralateral eye since damage to the more anterior portions of the optic radiation seemed to lead to an incongruous deficit, greater on the ipsilateral side (Harrington 1961). The incongruity of deficits has however remained on a matter of debate. The advent of anterior temporal lobe surgery however began to address these and other questions.

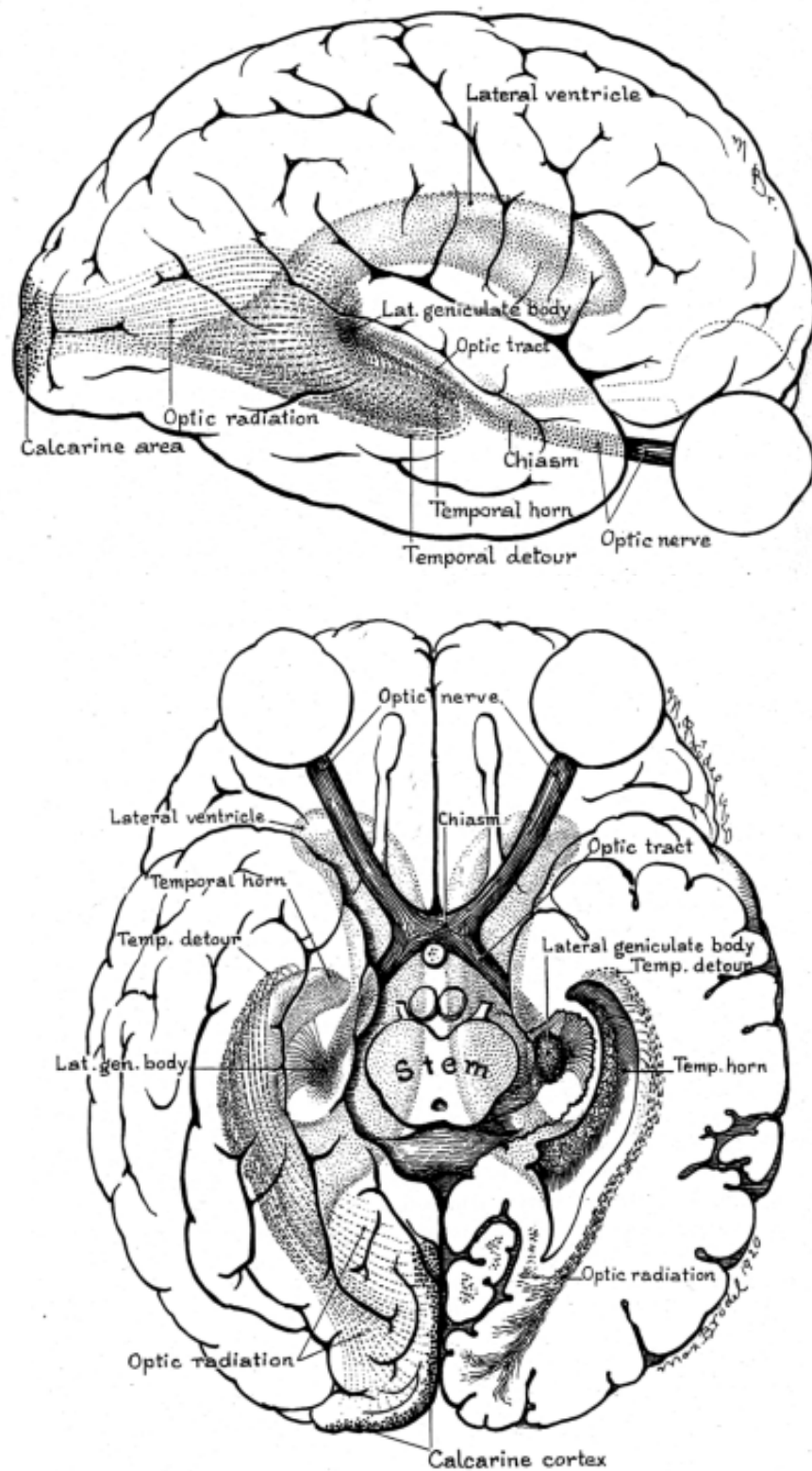


Figure 4.2 - Anatomy of the optic radiation depicted from lateral and inferior aspect

Source: Cushing 1921

4.4 Insights from Temporal Lobe Surgery for Epilepsy

The use of ATLR as a treatment for epilepsy was pioneered by Wilder Penfield from the Montreal Neurological Institute and Murray Falconer from the Guy's-Maudsley Neurosurgical Unit, London from the late 1940s onwards. It was soon recognised that surgery often resulted in a visual field deficit (VFD), thus providing an ideal opportunity to study vision with a well-defined and reproducible insult both temporally and spatially. Penfield observed:

“When the line of removal is less than 6cm posterior to the tip, it is apt to result in no post-operative visual field defect. If the removal includes 6cm and more, it is apt to produce contralateral upper quadrantic homonymous hemianopia. When the line is pushed back to 8cm, there is apt to be a complete homonymous hemianopic defect.” (Penfield 1954)

However Falconer noted intersubject variability as a 6cm resection caused hemianopia in one patient, but an 8cm resection resulted in virtually no visual field loss in another (Falconer et al. 1955). Many subsequent studies have been published which have further refined this risk (Table 4.2) and from which the following conclusions can be drawn.

4.4.1 Frequency of Deficits

VFD are common with a reported frequency ranging from 48% to 100%. Deficits are typically a partial superior quadrantanopia and only rarely extend into the inferior quadrant. There is single outlying study showing only a 15% risk of VFD (Jeelani et al. 2010), but this is likely to be related to the method of perimetry employed (binocular Esterman) and bias by only recording significant VFD.

4.4.2 Nature of Perimetry

Early studies tended to use manual kinetic perimetry (Goldmann perimeter or Haimark), which allows a detailed mapping of the visual fields. It is however affected by subject and observer variability (Parrish et al. 1984) and there is more limited ability for quantification of the deficit although this is possible (Barton et al. 2005). More recent studies use automated static perimetry, either monocular (Humphrey, or Metrovision) or binocular (Esterman). These are more reproducible and easier to analysis quantitatively but the binocular Esterman test is less sensitive (Manji & Plant 2000). Whatever method is employed, it is far superior to visual confrontation (Hughes et al. 1999, Manji & Plant 2000).

4.4.3 Relationship of VFD to Resection Size

Numerous studies show a relationship between the size of resection and either the risk of a VFD, or the severity of a VFD. A key finding is substantial variability between subjects, reflecting the anatomical variability in the location of Meyer's loop. The original 6cm safety margin proposed by Penfield (Penfield 1954) is clearly an overestimate, and the following studies by Bjork (Bjork & Kugelberg 1957) and Falconer (Falconer & Wilson 1958) suggested margins of 30-40mm and 45mm from the temporal pole to avoid a VFD. Over time, estimates have gradually reduced further. Despite the anatomical variability, a linear relationship between the severity of a VFD and the degree of resection (antero-

posterior distance on postoperative MRI) has been shown (Barton et al. 2005). This model predicts that the ipsilateral nasal field is involved with resections 24mm or more from the temporal pole, and the contralateral temporal field in resections 28mm or more from the temporal pole.

4.4.4 Relationship of Meyer's Loop to the Temporal Horn

Bjork (Bjork & Kugelberg 1957) and earlier diagrams by Cushing (Cushing 1921) suggest that the optic radiation clothes the temporal horn and lies anterior to it. However, Van Buren (Van Buren & Baldwin 1958) and Marino (Marino, Jr. & Rasmussen 1968) depict the optic radiation ending just posterior to the temporal horn. Recent studies suggest that the optic radiation is anterior to the temporal horn, at least in the majority of cases. In Barton, the average distance from temporal pole to temporal horn was 32mm, with the optic radiation predicted to be 24mm on average from the temporal pole (Barton et al. 2005). This hypothesis is supported by dissection studies. It is of importance as the temporal horn is entered during the standard neurosurgical approach for ATLR.

4.4.5 Nature of the VFD

The medial border of the deficit is generally sharp and superimposed on the vertical meridian, whilst the inferior border slopes towards the point of fixation and the isopters are separated. Early papers describe a "wedge"-shaped deficit, and some refer to the inferior border being radial. Close observation of the published field deficits however suggests that the inferior border whilst sloping does not point towards the central point of fixation, and that the deficits are more of a "pseudowedge".

No consensus on the congruity of deficits exists. Some studies report that most or all of deficits are congruous, whilst others report incongruous deficits which are typically larger on the ipsilateral side. Barton found a consistent 15% greater VFD on the ipsilateral side regardless of the extent of resection and laterality (Barton et al. 2005). Many authors have used this as evidence that fibres from the ipsilateral eye are more laterally located (Van Buren & Baldwin 1958, Hughes et al. 1999).

Similar disagreement exists as to the degree of macular involvement. The majority of studies report macula involvement only for VFD greater than a quadrantanopia (Falconer & Wilson 1958, Marino, Jr. & Rasmussen 1968, Jensen & Seedorff 1976, Babb et al. 1982) or macular sparing in studies where only partial quadrantanopias are seen (Bjork & Kugelberg 1957, Egan et al. 2000). However some studies do suggest that the macula may be involved in significant quadrantanopias (Hughes et al. 1999, Krolak-Salmon et al. 2000, Barton et al. 2005).

4.4.6 Retinotopic Organisation of the Optic Radiation

Van Buren suggested a retinotopy in which the visual field adjacent to the vertical meridian is represented most anteriorly in the optic radiation, with radial degrees from vertical to horizontal represented going more posteriorly (Van Buren & Baldwin 1958). This was used to explain the range of deficits from the small paravertical deficits, through wedge-shaped deficits with a sloping inferior border to a complete quadrantanopia. This converts rapidly to a hemianopia with larger resections, with deficits between a quadrantanopia and hemianopia only rarely seen.

Paper Centre (Surgery Years)	Surgical technique (degree of resection)	Cases	VF	Prevalence/size of postoperative VFD	Relationship between VFD and resection size	Proposed anterior limit of Meyer's loop
Bjork & Kugelberg 1957 Stockholm	Temporal lobectomy (4-6.5cm)	26	G ± B	25/26 (96%) <q	Yes, greater loss with larger resection	30-40mm, anterior to temporal horn
Falconer & Wilson 1958 Guy's-Maudsley	Temporal lobectomy (4.5-9cm)	50	G + B or C	50/50 (100%) <q/q/>q/h	Variable, >q more likely if 8-9cm	<45mm, no comment on temporal horn
Van Buren & Baldwin 1958 NINDS, NIH, USA	Temporal lobectomy (unknown)	44	G + B	33/41 (80%) <q/q	-	Posterior to temporal horn
Wendland & Nerenberg 1960 Minnesota (1952-60)	Temporal lobectomy (5-10cm)	24	*	24/24 (100%) [9<q, 7q, 2>q, 6h]	Yes, related but marked variability	-
French 1962 Minnesota (1948-61)	Temporal lobectomy (5-9cm)	30	*	30/30 (100%) [13<q, 9q, 2>q, 6h]	Yes, greater loss with larger resection	-
Marino, Jr. & Rasmussen 1968 Montreal (1962-67)	Temporal lobectomy (4-8cm)	50	**	33/50 (66%) [26<q, 3q, 3>q, 1h]	Yes, related but marked variability	<40mm, posterior to temporal horn
Jensen & Seedorff 1976 Copenhagen (1960-69)	Temporal lobectomy (5.5-6cm D, 5.5- 7cm)	74	B	51/69 (74%) [38<q/q, 7>q, 6h]	No, but greater VFD in R-sided resection (larger resections)	May or may not involve temporal horn
Babb et al. 1982 Los Angeles, UCLA	Temporal lobectomy (5-7.5cm)	22	G	13/22 (59%) [3<q, 7q/>q, 3h]	No, but correlates with parahippocampal VEP	-

Spencer et al. 1984	Standard temporal lobectomy (6.0-6.5cm	17	-	14/15 (93%)	-	-
Yale	ND, less by ECoG D)			[1<q, 9q, 4>q]		
	Modified temporal lobectomy (4.5cm, or	19	-	15/16 (94%)	-	-
	3cm in D STG)			[5<q, 9q, 1>q]		
Wieser 1986	SAH (Yasargil)	13	O	0/13 (0%)	-	-
Zurich (1983-)						
Katz et al. 1989	Temporal lobectomy (unknown)	45	G	27/39 (69%) <q/q	No, but resections larger in those with	-
Cleveland					VFD (MRI)	
Tecoma et al. 1993	Temporal lobectomy (3.5-5cm D, 4-	33	G	17/33 (52%)	-	-
San Francisco (1986-91)	6.5cm ND)					
Renowden et al. 1995	Transcortical SAH (Niemeyer)	7	-	4/7 (57%) <q	-	-
Oxford (1989-92)	Transsylvian SAH (Yasargil)	10		5/10 (50%) <q		
Vajkoczy et al. 1998	Transsylvian-transcisternal SAH	32	G	1/32 (3%) q	-	-
Munich/Heidelberg (1990-96)						
Hughes et al. 1999	Temporal lobectomy (4-7cm)	32	H	31/32 (97%)	Yes, contralateral deficit worse in	-
Vanderbilt (1990-95)					resections >6cm than <5cm	

Manji & Plant 2000 Queen Square (1986-95)	Temporal lobectomy (unknown)	24	C	5/24 (21%)	-	-
			G	13/24 (54%) [10/24 (42%) fail DVLA]		
			E	11/24 (46%) [6/24 (25%) fail DVLA]		
Krolak-Salmon et al. 2000 Lyon (1994-98)	Temporal lobectomy (2-6cm D, 2-7cm ND)	18	M	15/18 (83%) <q/q	Yes, more likely with larger resection (based on MRI)	20-30mm, anterior to temporal horn
Egan et al. 2000 Portland, USA	Modified temporal lobectomy (3.5-4cm)	15	G	11/15 (73%) <q	-	-
	Transcortical SAH (Niemeyer)	14		11/14 (79%) <q	-	-
Hervas-Navidad et al. 2002 Granada, Spain (1995-98)	Temporal lobectomy (unknown)	30	H	27/30 (90%) [15<q, 3q, 8>q, 1h]	Yes, greater loss with larger resection (based on MRI), variable	-
Pathak-Ray et al. 2002 Cardiff (10 years)	Temporal lobectomy (unknown)	14	H	9/14 (64%) [8<q, 1q, 2 vigabatrin]	-	-
			E	7/14 (50%) fail DVLA [4<q, 1q, 2 vigabatrin]		

Nilsson et al. 2004 Gothenburg (1987-99)	Standard temporal lobectomy (5-5.5cm D, 6cm ND)	33	G	16/33 (48%) [9<q, 6q, 1h]	Yes, correlated with anterior STG resection (based on MRI)	Involvement of STG at 18-36mm
	Modified temporal lobectomy (3cm D/less STG, 3.5-4.5cm ND)	17		9/17 (53%) [5<q, 4q]		
Barton et al. 2005 Boston (9 months)	Temporal lobectomy	29	G	29/29 (100%)	Yes, linear regression with size of resection (based on MRI)	24mm nasal, 28mm temporal, 32mm temporal horn
Yeni et al. 2008 Istanbul	Transsylvian SAH (Yasargil)	30	H	11/30 (37%) <q/q	-	-
Mengesha et al. 2009 Vanderbilt (2001-06)	Transcortical SAH (Niemeyer)	18	H	16/18 (89%) [13 <q/q, 3 >q]	-	-
<i>Ditto</i> Vanderbilt (1990-95)	Standard temporal lobectomy (4-7cm)	33	H	30/33 (91%) [<q/q]	-	-
Jeelani et al. 2010 Queen Square (1984-2004)	Modified temporal lobectomy (4-4.5cm)	105	E	16/105 (15%) [4/105 (4%) fail DVLA]	No, but resections all stereotyped at 4- 4.5cm (based on MRI)	<45mm, but cannot assess further

Table 4.2 - Summary of literature on VFD following temporal lobe epilepsy surgery

Surgical technique: D = dominant, ND = non-dominant, ECoG = electrocorticography. *Visual field technique (VF):* B = Bjerrum campimetry, C = confrontation, E = Esterman (binocular), G = Goldmann, H = Haimark, M = Metrovision, O = Octopus, * = mixture of central fields + perimetry (unspecified), ** = Haimark perimetry + tangent; *Visual field deficits (VFD):* <q = partial quadrantanopia, q = complete quadrantanopia, >q = greater than quadrantanopia, h = hemianopia, DVLA = Driving and Vehicle Licensing Agency guidelines for driving, VEP = visual evoked potentials.

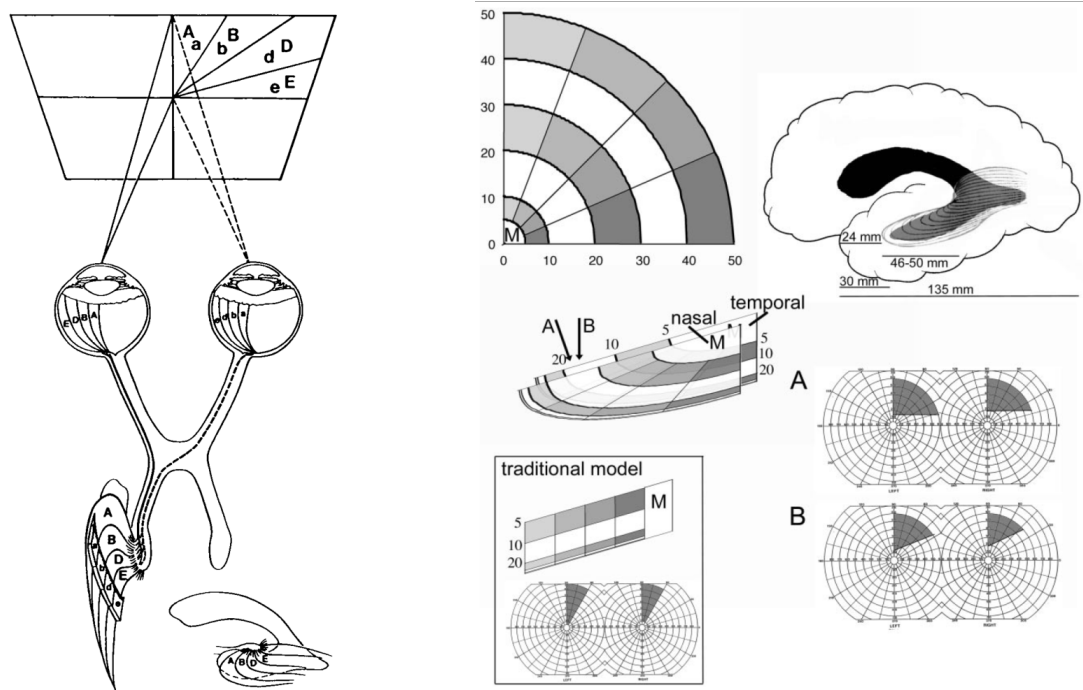


Figure 4.3 - Two models for the retinotopic organisation of the optic radiation

Left: Van Buren suggested radial degrees from vertical to horizontal going more posteriorly (from Egan et al. 2000 with permission; promotional and commercial use of the material in print, digital or mobile device format is prohibited without the permission from the publisher Lippincott Williams & Wilkins; please contact journalpermissions@lww.com for further information). *Right:* Barton instead suggests a 90 degree rotation of this scheme thus going from superior to inferior field more posteriorly (from Barton et al. 2005 by permission of Oxford University Press).

Barton suggests a revised model in which the superior field (rather than that by the vertical meridian) is represented most anteriorly, with more inferior portions being represented more posteriorly (Barton et al. 2005). Further, the macula is represented most posteriorly and ipsilateral fibres are slightly more anterior than the contralateral fibres (rather than more lateral as previously suggested). This 90-degree rotation coupled with the principle of central magnification better explains the observed pseudowedge deficits and could explain the linear relationship seen between resection size and severity of VFD.

4.4.7 Left/Right Asymmetry of VFD

An early study showed the frequency of a VFD was similar for left- and right-sided resections but that the severity of the VFD was greater in right-sided resections (Jensen & Seedorff 1976). This was postulated to be a result of larger resections in the non-dominant hemisphere. Whilst the findings were replicated in one study (Hervas-Navidad et al. 2002), another found that right-sided resections did not lead to greater VFD despite larger resections (Hughes et al. 1999). Further, in a study which assessed resection size with postoperative MRI, the average VFD did not differ between left- and right-sided resections for any given size of resection (Barton et al. 2005).

There is however mounting recent evidence however that the left optic radiation may be more anterior, which is supported by imaging data (Table 4.5). Data from hippocampal visual evoked potentials suggest that the anterior extent of the optic radiations may differ by as much as 1.5cm (Babb et al. 1982). In a cohort undergoing selective amygdalo-hippocampectomy, VFD were seen in 10/21 (left-sided resection) but only 1/9 (right-sided resection) (Yeni et al. 2008). Further, in a large cohort of patients undergoing ATLR the odds ratio for a VFD was 3.51 for a left-sided versus a right-sided resection, with no significant difference in the extent of resection between the two sides (Jeelani et al. 2010).

4.4.8 Relevance of the Deficit to Driving

Patients are typically unaware of the deficit (0-9% aware in the published studies) but intact vision is essential for a driving licence, one of the key aims for patients having epilepsy surgery (Taylor et al. 2001). Current Driving and Vehicle Licensing Agency (DVLA) regulations are based on European Union Commission Directive 2009/112/EC and require a binocular Esterman assessment demonstrating:

“a field of at least 120° on the horizontal measured using a target equivalent to the white Goldmann III4e settings; the extension should be at least 50° left and right. In addition, there should be no significant defect in the binocular field which encroaches within 20° of fixation above or below the horizontal meridian”
(Driver and Vehicle Licensing Agency 2013)

Relatively few studies have looked at vision and driving following epilepsy surgery. In 24 patients who had undergone temporal lobe resection, 13 had a deficit detected by Goldmann perimetry with 10 failing to meet driving criteria (42%) but using the more lenient Esterman test, deficits were only shown in 11 with 6 failing driving criteria (25%) (Manji & Plant 2000). In a study in a more homogenous group undergoing ATLR for hippocampal sclerosis alone, 7 of 14 (50%) failed DVLA criteria (Pathak-Ray et al. 2002). However, this included two patients with a pre-existing VFD from vigabatrin usage. The most recent study suggested that only 4% of a consecutive series of 105 patients failed to meet DVLA criteria (Jeelani et al. 2010). The reasons for the discrepant figures are unclear, but it may partly be related to a change in surgical practice.

Assessment for driving in the UK uses automated binocular Esterman perimetry, which has been shown to be less sensitive for VFD and more lenient than monocular Goldmann perimetry (Manji & Plant 2000) and the European Union Eyesight Working Group has recommended against its use within Europe (Eyesight Working Group 2005). Further all these studies concentrate on historical series in patients with predominantly hippocampal sclerosis. Improved imaging techniques and changes in surgical practice have enabled surgery in patients where it was not previously possible, including neocortical or non-lesional epilepsy (Duncan 2010). The risk to vision in such patients may be greater if the epileptogenic cortex is more posterior.

4.4.9 Effect of the Surgical Technique

The surgical technique has changed over the years in two major ways – the modification of the technique for temporal lobectomy, and the introduction of groups of techniques known as selective amygdalo-hippocampectomy (SAH).

Penfield working at the Montreal Neurological Institute was the first to recognise that removal of the temporal lobe including the hippocampus and amygdala could be both safe and effective (Penfield & Baldwin 1952). The standard ATLR, comprising en bloc resection of both medial temporal (amygdala, anterior hippocampus) and lateral temporal neocortical structures was subsequently described by Falconer from the Maudsley Hospital (Falconer et al. 1955). Morris described that a standard temporal lobectomy should include 6.5cm of lateral temporal cortex, the uncus, the amygdala and 2-4cm of anterior hippocampus (Morris 1956). However, such extensive resections are prone to post-operative neuropsychological and visual deficits.

In the late 1970s, modifications to the standard procedure were made. Spencer described a technique whereby removal of the medial structures could be achieved with only a more limited temporal pole resection thus preserving the remaining lateral temporal neocortex (Spencer et al. 1984). Resections were limited to 4.5cm of the superior, middle and inferior temporal gyri in the non-dominant hemisphere, with a further reduction to 3cm of the superior temporal gyrus in the dominant hemisphere. The two studies which have compared the visual outcome in standard and modified temporal lobectomy (Spencer et al. 1984, Nilsson et al. 2004) both found that whilst the frequency of a VFD was unchanged, the VFD were less severe.

The second approach was to perform a more selective resection of mesial structures. Wieser and Yasargil first described the SAH in which the amygdala, uncus and hippocampus posteriorly to the level of the superior colliculus are removed with complete preservation of the lateral temporal neocortex (Wieser & Yasargil 1982). A variety of surgical approaches to the temporal lobe exist for this procedure which can broadly be divided into three groups (Sincoff et al. 2004). However large studies of visual outcomes are lacking.

4.4.9.1 Lateral transsulcal/transcortical – access via the temporal gyri or sulci

This includes the modified temporal lobectomy and the original transcortical-transventricular SAH introduced by Niemeyer in 1958 (Niemeyer 1958) which enters via the middle temporal gyrus and puts the optic radiation at risk as the lateral aspect of the temporal horn is deep to the superior and middle temporal gyri. Two studies comparing temporal lobectomy and transcortical SAH reveals that the frequency of VFD does not differ between these operations (Egan et al. 2000, Mengesha et al. 2009). However, Mengesha note that the lateral part of the vision field is less severely affected with transcortical SAH.

More inferior approaches have been proposed, including through the inferior temporal sulcus (Miyagi et al. 2003) or the inferior temporal gyrus via a zygomatic osteotomy (Shimizu et al. 1989) to reduce the risk of VFD. Miyagi *et al.* describe no VFD in a small series of 7 patients whilst Shimizu *et al.* did not assess this outcome.

4.4.9.2 Subtemporal – access via the fusiform or parahippocampal gyrus

These approaches should avoid the optic radiation as they do not involve the floor of the temporal horn, but do risk damage to the vein of Labbe by retraction and the fusiform gyrus is important for language. Entry via the fusiform gyrus did not cause a VFD in 4 patients (Hori et al. 1993) whilst entry via the parahippocampal gyrus resulted in a single case of quadrantanopia in 7 patients (Park et al. 1996).

4.4.9.3 Transsylvian – access via the Sylvian fissure

Yasargil describes a transsylvian-transventricular approach, with access to temporal horn via an incision in the superior temporal gyrus at the level of limen. This operation is designed to spare lateral temporal cortex in mesial temporal lobe epilepsy to improve the neuropsychological outcome whilst maintaining a good seizure outcome. Avoiding the lateral temporal cortex makes this a technically demanding operation and entry via the temporal stem passes through the uncinate fasciculus and may put the optic radiation at risk, although Yasargil believes that it may be avoided.

This operation has a very low risk of VFD in the hands of the pioneer (2 of 173 patients affected) (Yasargil et al. 2004) but the only peer-reviewed study includes only 13 patients (Wieser 1986) and this success has not been reproduced by other surgeons applying this technique (Renowden et al. 1995, Yeni et al. 2008). Further, cortical damage in the superior, middle and inferior temporal gyri is seen on postoperative MRI in both the transcortical and transsylvian approaches for SAH consistent with downstream Wallerian degeneration (Renowden et al. 1995). A modification of this technique (transsylvian-transcisternal approach) led to only a single VFD in a series of 32 patients, but no other studies using this technique have been published.

Overall whilst there is a suggestion that alternative surgical approaches reduce the risk or severity of a VFD, these findings are not always replicated and need validation in larger series. At my centre, the surgeon performs a Spencer modified temporal lobectomy.

4.5 Anatomical Dissection Studies

The introduction of the Klingler's fibre dissection technique (Ludwig & Klingler 1956) allowed careful study of the location and variability of the optic radiation in post-mortem specimens. In a landmark study of the optic radiation in 25 hemispheres, the key finding was that of anatomical variability between subjects (Figure 4.4) (Ebeling & Reulen 1988).

The distance from the temporal pole to Meyer's loop of the optic radiation was 22-37mm (mean 27mm), whilst Meyer's loop lay between 10mm in front and 5mm behind the tip of the temporal horn (mean 5mm in front). They noted that whilst the ventricle might prove a useful landmark for the preservation of the optic radiation, a safety zone of 10mm anterior to the tip of the temporal horn was required.

Subsequent studies confirm these findings (Table 4.3) and have been used to postulate safe approaches to the temporal lobe avoiding the optic radiation. Noting that traditional lateral approaches via the superior or middle temporal gyri will traverse the optic radiation, but transsylvian or subtemporal (e.g. fusiform gyrus) approaches do not place the optic radiation at risk (Sincoff et al. 2004), a modified transsylvian approach based on anatomical criteria has been proposed but not clinically validated (Coppens et al. 2005). Likewise, dissectional studies have been used to define a safe triangle with low risk to the optic radiation at the anterior extent of the limen via a transsylvian approach (Choi et al. 2006), the route already pioneered by Yasargil. However these studies require further validation.

Paper	Hemispheres	TP-ML distance (mean)	ML-TH distance (mean)
Ebeling & Reulen 1988	25	22 to 37mm (27mm)	-5 to 10mm (5mm)
Sincoff et al. 2004	10	Not specified	>0mm in all
Peuskens et al. 2004	17	15 to 30mm	-4 to 6mm
Rubino et al. 2005	20	22 to 30mm (25mm)	1 to 3mm (2mm)
Choi et al. 2006	10	28 to 34mm (31.4mm)	>0mm in all
Pujari et al. 2008	5	22 to 30mm (25mm)	Not specified

Table 4.3 - Anatomical variability of the optic radiation by Klingler's fibre dissection

TP-ML distance: temporal pole to Meyer's loop distance. *ML-TH distance*: Meyer's loop to temporal horn distance (+ = ML anterior to TH, - = ML posterior to TH)

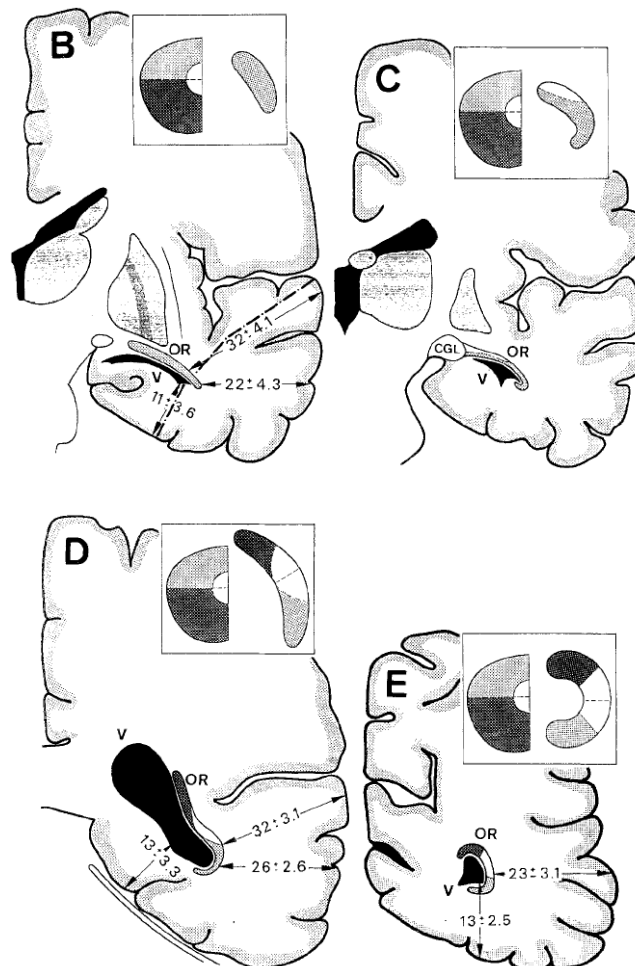
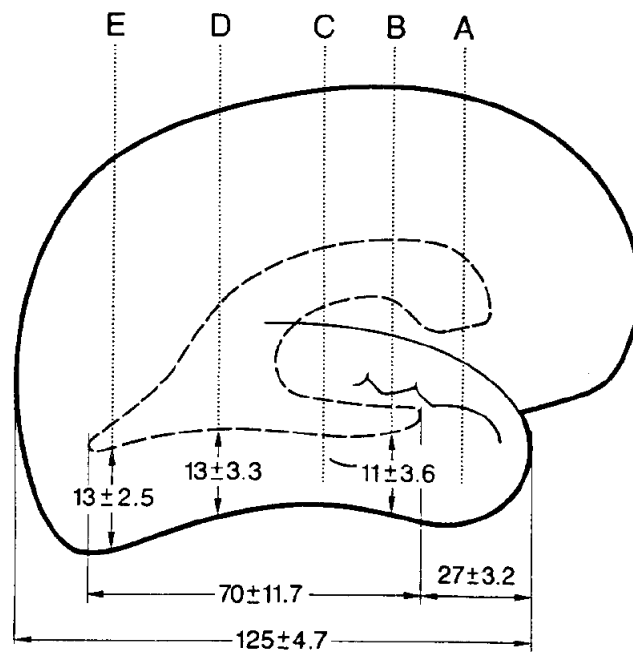


Figure 4.4 - Anatomical variability of the optic radiation identified by dissection

From Ebeling & Reulen 1988 with permission of Springer.

4.6 Diffusion Tensor Imaging Tractography of the Optic Radiation

4.6.1 Choice of Acquisition and Algorithm

Whilst anatomical dissection studies are informative, application in clinical practice requires an *in vivo* technique such as tractography. The optic radiation may be delineated using either *deterministic* or *probabilistic* algorithms (Section 2.7). Deterministic algorithms are simple and fast to implement, but lose accuracy in regions of crossing fibres and high curvature such as Meyer's loop (Nilsson et al. 2010). Probabilistic algorithms are more robust but require lengthy processing.

The optic radiation was first delineated using a *deterministic* approach, fast marching tractography (Parker et al. 2002), by seeding from Meyer's loop (Ciccarelli et al. 2003a). Other deterministic techniques have been used to separate the optic radiation from the inferior longitudinal fasciculus (ILF) (Catani et al. 2003) and to depict the three separate parts of the optic radiation in healthy volunteers (Yamamoto et al. 2005). However, deterministic algorithms do not demonstrate the most anterior portions of Meyer's loop even if increasing from 6 to 12, 40 or 81 gradient directions (Yamamoto et al. 2007).

An adapted algorithm taking into account the whole diffusion tensor to better cope with crossing fibres delineates the entire visual system from the optic nerve to visual cortex, but the published images do not include Meyer's loop (Staempfli et al. 2007). Using smaller voxels and a STEAM (stimulated-echo acquisition mode) acquisition to avoid the distortions inherent in EPI-based diffusion sequences (see section 5.4.3.3) the whole visual system can be delineated (Hofer et al. 2010) but although Meyer's loop was depicted, no measurements were given to verify the accuracy.

Probabilistic algorithms were first used by seeding from lateral to the LGN (Behrens et al. 2003a). Modifying the technique to include prior anatomical information gives results comparable to dissection studies with Meyer's loop more anterior (24-34mm, mean 28mm) than previous deterministic studies (Sherbondy et al. 2008). However probabilistic tractography is time consuming both for the operator and computationally so automation to reduce the observer variability in seed point and threshold selection has been proposed (Clatworthy et al. 2010).

4.6.2 Choice of Seed Regions

Reliable optic radiation tractography is challenging and the choice of the seed point and other restrictions and parameters is key (Table 4.4). Whilst it is possible to seed only from the LGN (Romano et al. 2007, Romano et al. 2009), this tends to poorly depict Meyer's loop and may identify other false tracts. Moving the seed slightly laterally avoids depicting the brachium of the superior colliculus (Behrens et al. 2003a) which led to an approach of placing the seed anterolateral to the LGN or in Meyer's loop.

Ciccarelli described a procedure of choosing a single voxel at the apex of Meyer's loop with principle eigenvector located in an anteromedial-posterolateral direction on the axial slice on which the transition from posterior limb of internal capsule to the cerebral peduncle occurs (Ciccarelli et al. 2003a) that was employed in subsequent studies for both deterministic and probabilistic tractography (Ciccarelli et al. 2003b, Ciccarelli et al. 2005, Kamada et al. 2005, Powell et al. 2005, Bassi et al. 2008).

Seeding from Meyer's loop risks depicting only more inferior part of the optic radiation since additional fibres pass directly posteriorly from the LGN (Section 4.3). Therefore others have seeded from two regions around the LGN and in Meyer's loop (Govindan et al. 2008, White & Zhang 2010) and this approach is utilised in Chapter 0 where depiction of the entire optic radiation is key.

Better results can be obtained by providing further restrictions on the paths. The first and commonest approach is to define two seeds retaining only tracts that pass between these two, typically the LGN and occipital cortex (Catani et al. 2003, Yamamoto et al. 2005, Yu et al. 2005, Kikuta et al. 2006, Yamamoto et al. 2007, Wang et al. 2008, Sherbondy et al. 2008, Chen et al. 2009, Thudium et al. 2010, Wang et al. 2010b, Sun et al. 2011) or Meyer's loop and occipital cortex (Okada et al. 2007, Maruyama et al. 2007). This may be extended further by the occipital region-of-interest being split to obtain the three different parts of the optic radiation with different targets (Yamamoto et al. 2005, Chen et al. 2009, Hofer et al. 2010). The LGN can be identified visually or by tractography from the optic chiasm (Catani et al. 2003, Sherbondy et al. 2008).

The second approach is to use a seed near the LGN and a coronal waypoint in the stratum sagittale posterior to the splenium of the corpus callosum, retaining only tracts that pass via this (Nilsson et al. 2007, Taoka et al. 2008, Yogarajah et al. 2009, Benjamin et al. 2012) or in one case using this as a target and thus only delineating a subset of the optic radiation (Henze et al. 2012). Common additional constraints are a midline exclusion zone and a frontal exclusion zone to remove other tracts such as the uncinate fasciculus and fronto-occipital fasciculus (Yogarajah et al. 2009, Clatworthy et al. 2010, Benjamin et al. 2012). This approach is used for the majority of this thesis.

It may be possible to automate the selection of seed points (Clatworthy et al. 2010) and careful attention to the seed regions improves results (Benjamin et al. 2012). The effect of different seed regions is considered further in Chapter 8. Stopping criteria, including FA and angular thresholds also vary widely between studies (Table 4.4) but have not been formally evaluated.

4.6.3 Studies in Epilepsy

4.6.3.1 Postoperative diffusion changes

Initial studies in epilepsy used DTI as a marker for Wallerian degeneration or plasticity. Following surgery resulting in a VFD, diffusion parameters of the optic radiation alter consistent with Wallerian degeneration (reduced FA, increased MD) (Wieshmann et al. 1999). Region-of-interest analysis of the sagittal stratum (comprising optic radiation and ILF) in 14 patients shows significantly lowered FA on the operated side by 4 weeks with a greater difference in those with more severe deficits (Taoka et al. 2005). Similarly change in FA of the ipsilateral ILF at 2 months post-surgery correlates with the VFD (McDonald et al. 2010).

Paper	Subjects	Aim	Algorithm, Software, Parameters	Regions-of-interest
Ciccarelli et al. 2003a,	11 controls	Reproducibility assessment	D (FMT)	Seed voxel at apex of Meyer's loop, restrict to
Ciccarelli et al. 2003b	21 controls	Producing group maps		hemisphere posterior to third ventricle
Behrens et al. 2003a	8 controls	Thalamo-cortical connections	P (FSL - Bayesian)	Seed voxel lateral to LGN
Catani et al. 2003	11 controls	Occipito-temporal connections	D (custom), FA 0.2	Seeds in LGN + occipital white matter
Kamada et al. 2005	2 patients undergoing surgery	Surgical monitoring with VEP	D (dTV), FA 0.15	Seed voxel at apex of Meyer's loop
Ciccarelli et al. 2005	10 controls 7 optic neuritis	Group maps after optic neuritis	D (FMT), FA 0.1, ADC 0.002	Single voxel at apex of Meyer's loop with FA>0.5, restricted to hemisphere posterior to genu
Powell et al. 2005	2 patients undergoing ATLR	Predicting visual outcome	P (Camino - PICO)	Single voxel anterior to LGN (eigenvector in anteromedial-posterolateral direction)
Yu et al. 2005	16 patients (3 with tumours)	Surgical planning	D (Siemens Leonardo), FA 0.2, angle 20	Seeds in LGN (sagittal) and occipital
Yamamoto et al. 2005	5 controls	Depicting 3 layers of optic radiation	D (Philips PRIDE)	Seeds in LGN (sagittal) and near visual cortex (upper, between, lower calcarine fissure)
Kikuta et al. 2006	10 patients with AVM	Correlation with visual outcome	D (DTIStudio - FACT), FA 0.2, angle 41	Seeds in LGN and occipital
Yamamoto et al. 2007	12 controls	Comparison of acquisition schemes	D (DTIStudio - FACT), FA 0.25, angle 70	Seeds in LGN (sagittal) and occipital (coronal)
Okada et al. 2007	34 patients with AVM	Quantitative analysis by lesion	D (DTIStudio - FACT), FA 0.2, angle 70	Seeds in temporal stem including Meyer's loop (sagittal), calcarine cortex (coronal), exclusion zones medial and lateral to Meyer's loop (coronal)
Romano et al. 2007	25 patients with tumours	Integration into neuronavigation	D (BrainLab), FA 0.2, angle 35	Seed in LGN
Maruyama et al. 2007	10 patients with AVM	Integration into gamma knife planning	D (dTV), FA 0.18	Seed voxels in apex of Meyer's loop, with target in calcarine fissure
Staempfli et al. 2007	8 controls	Delineation of whole visual system	D (aFM)	Seeds in optic chiasm (axial) and optic nerves

Nilsson et al. 2007	7 controls, 2 patients undergoing ATLR	Assess variability in Meyer's loop	D (Philips PRIDE), FA 0.25	Seeds anterior to LGN (coronal) and stratum sagittale (coronal)
Govindan et al. 2008	10 patients with occipital lobe epilepsy	Plasticity following occipital lobectomy	D (FACT), FA 0.2, angle 60	Seeds posterior thalamus (coronal) and medial Meyer's loop (sagittal), exclusion zones to remove artefactual connections
Bassi et al. 2008	37 preterm infants	Correlation with visual function	P (FSL - Bayesian), threshold 10%	Seed white matter lateral to LGN (9 voxels), restrict to hemisphere posterior to third ventricle
Wang et al. 2008	10 controls	Define landmarks for tracts	D (dTV), FA 0.18, 160 steps	Seed occipital (coronal), target LGN (sagittal)
Taoka et al. 2008	14 patients undergoing ATLR/SAH	Correlation between Meyer's loop damage and VFD	D (dTV), FA 0.18, no angular threshold	Seed anterior to LGN (coronal), target stratum sagittale (coronal)
Sherbondy et al. 2008	8 controls	Apply ConTrack algorithm	P (ConTrack), angle 130, length <300mm	Seeds 4mm sphere in LGN (determined by streamline from optic chiasm) + calcarine sulcus
Chen et al. 2009	48 patients undergoing ATLR	Correlate Meyer's loop damage to VFD	D (BrainLab), FA 0.15, length >50mm	Seeds in LGN and occipital (lower, mid, upper)
Yogarajah et al. 2009	20 controls, 21 patients undergoing ATLR	Correlate Meyer's loop location and VFD	P (Camino - PICO), FA 0.1, no angular threshold	Seed anterolateral to LGN (15 voxels), way stratum sagittale posterior to splenium (coronal), exclusion midline + iterative frontal exclusion mask
Romano et al. 2009	28 patients undergoing tumour surgery	Presurgical planning	D (BrainLab), FA 0.15, angle 55	Seed in LGN
Clatworthy et al. 2010	20 controls	Automation of seed point selection	P (FSL - Bayesian)	Seed encompassing anterior optic radiation (coronal) + target in primary visual cortex, exclusion masks in midline + frontal
Hofer et al. 2010	6 controls	Reconstruct entire visual pathway	D (custom), FA 0.1, angle 30-70	Seed in LGN, target in white matter near visual cortex
White & Zhang 2010	10 controls	Evaluate Meyer's loop	D (GE Functool), FA 0.01, ADC 0.01, steps 160	Two seeds in LGN + anterior of Meyer's loop

Thudium et al. 2010	12 patients undergoing SAH	Preoperative planning, intraoperative guidance	D (BrainLab), FA 0.2, length >50mm	Seeds in roof of temporal horn and primary visual cortex
Wang et al. 2010b	16 controls	Compare measurements with different software	D (BrainLab), FA 0.2, angle 70, length >50mm D (Philips FiberTrak), FA 0.15, angle 90, length >50mm	Seeds in LGN/adjacent temporal lobe and occipital lobe
Sun et al. 2011	44 patients with lesions near OR	Intraoperative guidance	D (BrainLab), FA 0.15, angle 20, length >50mm	Seeds in LGN and occipital (lower, mid, upper)
Henze et al. 2012	13 controls, 13 schizophrenia	Determine if visual pathways affected in disease	D (NeuroQLab - TEND), FA 0.02, angle 107, length <400mm	Seed in LGN and Meyer's loop (coronal), target stratum sagittale posterior to splenium (coronal)
Wu et al. 2012	10 controls	Characterise relationship to other tracts	D (Slicer)	Multiple slices of optic tract near LGN
Benjamin et al. 2012	13 controls	Investigate optimal seed region	D (CRKit), FA 0.1, angle 30 (6 steps per voxel)	Optimum is broad seed next to LGN, way point in stratum sagittale (coronal), exclusion midline + frontal

Table 4.4 - Summary of regions-of-interest and parameters used for optic radiation tractography

Algorithm: D = deterministic, P = probabilistic, aFM = advanced fast marching tractography, FACT = fibre assignment by continuous tracking, FMT = fast marching tractography, PICO = probabilistic index of connectivity

4.6.3.2 Tractography and postoperative visual outcome

Determining the location of the optic radiation by tractography for surgery is critical for three reasons. Firstly, the optic radiation shows high anatomical variability (Ebeling & Reulen 1988). Secondly, the optic radiation cannot be delineated on conventional MRI sequences, and finally it cannot be identified visually during surgery.

Tractography can be used to measure the distance from the temporal pole to Meyer's loop (TP-ML). Using deterministic tractography in healthy controls a range of 34-51mm (mean 44mm) was found but Meyer's loop appeared posterior to the temporal horn in all cases, which does not agree with dissectional studies (Nilsson et al. 2007). Nevertheless, preoperative tractography superimposed on postoperative imaging showed disruption in the patient with a VFD, but an intact Meyer's loop in the unaffected patient (Powell et al. 2005).

Preoperative tractography measurements were related to outcome in 14 patients undergoing ATLR or SAH (Taoka et al. 2008). In those without a postoperative VFD, Meyer's loop was on average 5.0mm behind the resection margin whilst in those developing a complete quadrantanopia the resection involved on average 7.5mm of Meyer's loop. However in the 3 patients with the most minor deficits, tractography placed Meyer's loop posterior to the resection margin in all cases, possibly as a result of the deterministic algorithm used.

Further work established that tractography was indeed predictive of the visual deficit. 48 patients undergoing ATLR were studied with pre- and intraoperative imaging including DTI (Chen et al. 2009). Damage to Meyer's loop and postoperative VFD were each classified into 5 groups on the basis of preoperative/intraoperative tractography and Goldmann perimetry respectively. A significant correlation between the two was found.

This study was notable in that tractography was performed using intraoperative imaging, but Meyer's loop could not always be delineated due to the damage (using a deterministic algorithm). Further, rigid registration of the pre- and intraoperative tractography confirmed significant brain shift during surgery (horizontal shift 0.0-11.1mm, mean 3.75mm, either inward or outward; vertical shift 0.0-7.8mm, mean 2.46mm, either up or down) such that preoperative tractography would no longer be valid without compensation.

In view of the limitations of *deterministic* tractography, preoperative *probabilistic* tractography and postoperative Goldmann perimetry were used in 21 patients undergoing ATLR (Yogarajah et al. 2009). Linear regression showed that both TP-ML distance and resection size were predictive of the postoperative VFD, with the former having a greater effect.

4.6.3.3 Comparing deterministic and probabilistic tractography

The difference between deterministic and probabilistic algorithms is critical. Studies that place Meyer's loop significantly more posterior than dissection-derived data use deterministic tractography (Table 4.5). Whilst anatomical dissections may provide a small underestimate due to the difficulties in distinguishing the optic radiation from other adjacent fibres, it is more likely that deterministic tractography techniques are giving an overestimate. A direct comparison of deterministic and probabilistic approaches in 11 controls and 7 patients gave a TP-ML distance of 32-51mm (mean 41mm) for the deterministic algorithm and 17-42mm (mean 30mm) for the probabilistic algorithm (Nilsson et al. 2010). It is noteworthy that all but one study employing deterministic tractography places Meyer's loop posterior to the temporal horn in all subjects, whereas all studies employing probabilistic tractography place Meyer's loop either anterior or posterior to the temporal horn (Table 4.5).

4.6.3.4 Using tractography real-time during surgery

The next step is to use these data for intraoperative guidance. The first study in epilepsy surgery superimposed preoperative deterministic tractography of Meyer's loop on the head-up surgical display to guide entry in the temporal horn in patients undergoing transcortical or subtemporal SAH (Thudium et al. 2010). On entry to the temporal horn, CSF leakage led to unacceptable brain shift so image guidance was no longer possible. Three out of 12 (25%) developed a post-operative VFD (two out of ten using the subtemporal approach), which is no better than a series of subtemporal SAH performed without image guidance (Hori et al. 2007). Preoperative tractography has also been used to guide extratemporal epilepsy surgery in an intraoperative MRI environment (Sommer et al. 2013). This is discussed in detail in the next chapter.

4.6.4 Studies in Other Conditions

Several studies have examined the use of tractography in patients with arteriovenous malformations (AVM). Preoperative DTI in 10 patients with AVM near the optic radiation showed a disrupted optic radiation in the three patients with significant preoperative visual loss (Kikuta et al. 2006). Similar findings were seen with post-operative DTI and visual fields, although one patient with an intact optic radiation on imaging had developed a quadrantanopia. A subsequent study of 34 patients confirmed that the optic radiation and pyramidal tract were less well visualised in patients when the nidus was close to the lesion or with associated neurological symptoms (Okada et al. 2007). Incorporation of tractography into the planning stage for gamma knife surgery for AVM to ensure the dose to the optic radiation does not exceed a safe limit has been suggested (Maruyama et al. 2007). However, findings were based on retrospective analysis of 10 patients, only one of whom developed a VFD.

Paper	Subjects	Tractography method	TP-ML distance (mean)	ML-TH distance (mean)	ML/TH relationship
Yamamoto et al. 2005	5 controls	D (Philips PRIDE)	33.1-40.0mm (37.3mm)	-4.3mm to -3.7mm (-4.0mm)	ML posterior
Nilsson et al. 2007	7 controls	D (Philips PRIDE)	34-51mm (44mm)	-21mm to -8mm (-16mm)	ML posterior
Taoka et al. 2008	14 patients	D (dTV II)	30.0-43.2mm (36.6mm)		
Sherbondy et al. 2008	8 controls	P (ConTrack)	24-34mm (28mm)	-1mm to +8mm (3mm)	ML anterior or posterior
Chen et al. 2009	48 patients	D (BrainLab iPlan)	20.9-51.5mm (32.1mm)		
Yogarajah et al. 2009	20 controls	P (Camino)	24-47mm (35mm)	-11 to +9mm (0mm)	ML anterior or posterior
	21 patients		24-43mm (34mm)	-15 to +9mm (0mm)	
Mori et al. 2009	10 controls	D (DTI Studio)	26.1-58.0mm (40.3mm)		
Wang et al. 2010b	16 controls	D (BrainLab iPlan) (Operator A)	26.6-48.9mm (36.3mm)		
		D (BrainLab iPlan) (Operator B)	26.8-48.2mm (36.3mm)		
		D (Philips FiberTrak) (Operator B)	20.8-48.4mm (35.9mm)		

Nilsson et al. 2010	11 controls	D (Philips)	32-51mm (41mm)	-21mm to -8mm (-14mm)	ML posterior
	7 patients	P (FSL)	17-42mm (30mm)	-15mm to +10mm (-2mm)	ML anterior or posterior
White & Zhang 2010	10 controls	D (GE Functool)	<i>Left</i> 26.3-33.5mm (30.5mm)	-2.6mm to +3.8mm (+0.6mm)	ML anterior or posterior
			<i>Right</i> 28.8-34.0mm (31.1mm)	-4.5mm to +2.1mm (-1.0mm)	
Wu et al. 2012	10 controls	D (Slicer)	<i>Left</i> 34.8-49.5mm (39.9mm)	-11.1mm to -7.0mm	ML posterior
			<i>Right</i> 34.6-53.6mm (40.7mm)	-14.7mm to -6.2mm	
Benjamin et al. 2012	7 controls measured	P (CRKit)		<i>Left</i> -1mm to +5mm (+1.1mm)	ML anterior or posterior
				<i>Right</i> -4mm to +3mm (-0.7mm)	

Table 4.5 - Anatomical variability of the optic radiation as shown by tractography

Tractography method: D = deterministic, P = probabilistic; *TP-ML distance:* temporal pole to Meyer's loop distance. *ML-TH distance:* Meyer's loop to temporal horn distance (+ = ML anterior to TH, - = ML posterior to TH)

Nevertheless tractography aids surgical planning. In a study of two patients with lesions near the optic radiation, preoperative deterministic tractography was used to delineate the optic radiation and resective surgery was undertaken with continuous VEP monitoring (Kamada et al. 2005). In the first patient, the resection was achieved with stable intraoperative VEP and no post-operative VFD. In the second patient, surgery resulted in hemianopia. Tractography data were incorporated into the neuronavigation system and the intraoperative VEP remained stable until the resection reached the optic radiation according to the neuronavigation. The authors were however fortunate that minimal brain shift occurred intraoperatively, so that the simple affine registration used remained accurate.

In 16 patients undergoing surgery near the pyramidal tract or optic radiation (only two of the latter), a three-dimensional object in anatomical space could be created within 15 minutes, including DTI acquisition time (Nimsky et al. 2006b). A further anatomical MRI acquisition after head fixation but prior to any surgical intervention allowed the object to be displayed on the operating display. However, diffusion and anatomical data were rigidly registered thus not allowing for the distortion in diffusion images and the two anatomical scans were rigidly registered without further intraoperative scans so no allowance for brain shift was made limiting the application.

Despite these shortcomings, tractography data do lead to a change in the neurosurgery performed in the majority of cases (Romano et al. 2007). Twenty-five patients undergoing tumour resection underwent preoperative tractography to delineate the pyramidal tract, arcuate fasciculus and optic radiation for preoperative planning. Images first without and then with tractography were displayed to the surgeon, resulting in a changed surgical approach in 4 (16%). The data were then used for neuronavigation updated by a preoperative anatomical scan. The surgeons reported retrospectively that extent of resection was affected in 17 (68%), so overall surgery was altered in 20 (80%) of patients. It is unclear how much benefit this conferred, but only a single patient developed a new neurological deficit (dysphasia).

4.7 Conclusions

Meyer's loop of the optic radiation is at risk during temporal lobe surgery with many patients experiencing a postoperative VFD and a lesser proportion not meeting visual criteria for driving. Epilepsy surgery has yielded much information about the nature and extent of these deficits and anatomical dissection has characterised the variability in the location of Meyer's loop. Meyer's loop frequently passes anterior to the temporal horn and the degree of the characteristically pseudowedge-shaped partial superior quadrantanopia is related to the degree of damage to this structure. Alternative approaches to surgery, including several techniques for SAH, may pose a lesser risk to vision but have not been systematically studied.

Diffusion tensor imaging tractography has the potential to delineate the optic radiation but probabilistic tractography is necessary to accurately delineate Meyer's loop. Most studies have concentrated on preoperative planning but tractography also has the potential for real-time guidance of neurosurgery. However, numerous challenges including brain shift must be addressed to maximise utility. Intraoperative MRI may provide a means of doing so using the techniques described in this thesis.

5 INTRAOPERATIVE MAGNETIC RESONANCE IMAGING

5.1 Introduction

Image-guidance has the potential to improve the outcome of surgery by increasing the extent of resection of the lesion whilst minimising the surgical morbidity from damage to critical white matter tracts and eloquent cortex. In this chapter, I summarise the approaches to intraoperative imaging and then discuss the design, safety and clinical utility of intraoperative MRI (iMRI) systems. Two key technical challenges of iMRI are compensation for brain shift and geometric image distortion. Previous approaches to these problems are summarised and a novel approach is employed in this thesis (Chapters 6 and 10).

5.2 Image-Guided Surgery

5.2.1 Role of Image Guidance

Image guidance during surgery is helpful due to limited direct visualisation of anatomy, including the optic radiation. It assists the localisation and targeting of abnormalities, defining lesion margins, achieving a safe surgical approach and may be used to monitor the changing anatomy during surgery or potential complications, such as haemorrhage. Image-guidance may be either *frame-based* or *frameless*. In the latter, fiducial markers are combined with optical (or other) sensors to detect the position of surgical instruments in relation to the anatomical structures.

Conventional image-guidance presents static images that were acquired preoperatively and does not therefore respond to dynamic changes. During surgery, significant brain shift occurs (Nabavi et al. 2001) and whilst modelling of the deformation to correct images is possible to a limited extent, beyond this updated intraoperative imaging are required.

5.2.2 Approaches to Intraoperative Imaging

Fluoroscopy, ultrasound and computed tomography (CT) have been employed and whilst these techniques have some advantages, there are also significant disadvantages (Table 5.1) (Jolesz 1995). Magnetic resonance imaging is particularly attractive due to its relatively high spatial and temporal resolution, excellent soft tissue contrast, directly acquired multi-planar scans for planning surgical trajectories and absence of radiation exposure. However, it is more prone to geometric distortions from gradient non-linearity or magnetic susceptibility artefacts (Section 5.4.3).

Imaging Modality	Benefits	Limitations
Fluoroscopy	Real-time imaging Bone imaging	Radiation exposure Not multiplanar (projection views) Poor soft tissue contrast
Ultrasound	Readily available Real-time imaging (fast) Multiplanar views No radiation Inexpensive Good patient access	Poor spatial and contrast resolution Cannot image bone/air-filled space Restricted field of view Challenging to integrate into neuronavigation
Computed tomography	Bone imaging No geometric distortions Suitable for stereotactic guidance	Radiation exposure Limited multiplanar views (fixed slice orientation) Low soft tissue contrast Limited access to patient
MRI (open system)	Good access to patient Full multiplanar imaging Near real-time imaging Good soft tissue contrast No radiation	Expensive Limited availability Limited field strength (image quality)
MRI (closed system)	Full multiplanar imaging Excellent soft tissue contrast High temporal and spatial resolution No radiation	Expensive Limited availability No access to patient during imaging Necessity to move patient for imaging

Table 5.1 - Approaches to intraoperative imaging

5.3 Intraoperative MRI

5.3.1 Design Considerations

The first iMRI system was a General Electric 0.5T Signa SP installed at the Brigham and Women's Hospital in March 1994 (Black et al. 1997). This was a "double doughnut" design with two vertically orientated magnets allowing direct operating access to the patient in the small 56cm gap between these. Such an "open" configuration permits real-time imaging during surgery but requires the use of appropriate MRI compatible surgical instrumentation. Magnetic field strength and patient access are also limited (Table 5.1).

Another approach is to move to patient to and from a conventional scanner during surgery. The first implementations were identical low-field 0.2T Siemens Magnetom Open scanners in Heidelberg (Wirtz et al. 1997) and Erlangen (Steinmeier et al. 1998) installed in May 1996. The advantages of this approach are the use of a conventional MRI scanner and as surgery is undertaken outside the fringe field of the scanner, patient access is unrestricted and conventional surgical instruments may be employed (Rubino et al. 2000). Subsequent higher field (1.5T or more recently 3T) closed scanners yield vastly superior image quality. However, the necessity to move the patient imposes safety and time considerations (Table 5.1).

Whilst the scanner may be installed in the same room as the operating theatre, a common design is the twin-operating room concept where the scanner is an adjacent room with air lock and pressure controlled air flow and may be utilised for other patients whilst not needed for the patient in the operating theatre (Wirtz et al. 1997, Steinmeier et al. 1998). An adaptation of this is the IMRIS system installed in Alberta in December 1997 in which the magnet is mounted with an overhead crane system so that it may be moved to and from the operating room rather than moving the patient (Hoult et al. 2001). Any chosen design is a compromise between image quality, patient access, expense and time.

5.3.2 Safety and Anaesthetic Considerations

Surgery in an iMRI environment must be subject to the same standards of sterility and patient monitoring as in a conventional operating theatre. In designs where the magnet is located in the operating theatre, MRI-compatible anaesthetic equipment and surgical implements are required. If the patient is transferred to the magnet (or vice versa), safety checks must be undertaken before the transfer to ensure all ferromagnetic materials are removed. Safety protocols and checklists have thus been developed (Kettenbach et al. 2006, Rahmathulla et al. 2012).

A comparison of craniotomy in an interventional MRI suite with matched cases in a conventional theatre showed that whilst the duration of surgery was significantly increased by around 2 hours, there was no increase in anaesthetic complications (Archer et al. 2002). This was confirmed in subsequent studies (Schmitz et al. 2003, Cox et al. 2011).

5.3.3 Clinical Utility

5.3.3.1 Tumour Surgery

The main role of iMRI has been in the resection of brain tumours, particularly gliomas. Numerous benefits have been described including the ability to precisely define tumour margins, providing accurate information to allow the extent of resection to be balanced against risk of damage to eloquent cortex and verifying the presence and position of any residual tumour with sequential imaging (Oh & Black 2005). A systematic review identified increased extent of resection, quality of life and survival from glioblastoma multiforme as key benefits of intraoperative imaging (Kubben et al. 2011) with similar findings of increased extent of resection in glioma surgery (Liang & Schulder 2012).

Limiting surgical morbidity is a key outcome. By combining multimodality data (functional MRI, magnetic resonance spectroscopy, DTI, positron emission tomography, magnetoencephalography) with intraoperative imaging, the proportion of complete glioma resections was increased, with only 4 of 137 patients suffering from a permanent neurological deficit (Nimsky et al. 2006a). Tractography of critical white matter tracts plays a particularly important role.

The most common tract of interest is the corticospinal tract and this may be combined with monitoring with motor evoked potentials (MEP). However data have shown the importance of correcting for brain shift (Section 5.4.2). In 9 patients with tumours, tractography performed on intraoperative images showed a shift from the preoperative tractography and co-localised with MEP from direct subcortical stimulation (Bozzao et al. 2010).

In patients with glioma near the arcuate fasciculus (language pathway), tractography can be displayed to guide resection and updated using intraoperative tractography (Zhao et al. 2012). And in patients with tumours adjacent to the optic radiation, use of tractography and intraoperative MRI allowed the extent of resection to be increased without significant impairment of visual fields (Sun et al. 2011). The mean tumour residual was 5% in glioma patients and 0% in non-glioma patients whilst visual fields were mostly improved (11%) or unchanged (82%) with only a few declining (7%).

5.3.3.2 Epilepsy Surgery

The first application of iMRI for epilepsy surgery employed intraoperative scans following resection (Buchfelder et al. 2000, Buchfelder et al. 2002). In 32 non-lesional patients undergoing predominantly temporal lobe resection, the extent of resection or callosotomy could be documented whilst in the 29 lesional patients, further resection following imaging increased the rate of complete resection from 23 (79%) to 26 (90%), with full resection not possible in the remainder due to involvement of eloquent cortex (Buchfelder et al. 2000). Assessment of postoperative scans revealed an identical resection size to intraoperative imaging in the majority of patients, although in some there were small changes in either direction (Buchfelder et al. 2002) (Figure 5.1).

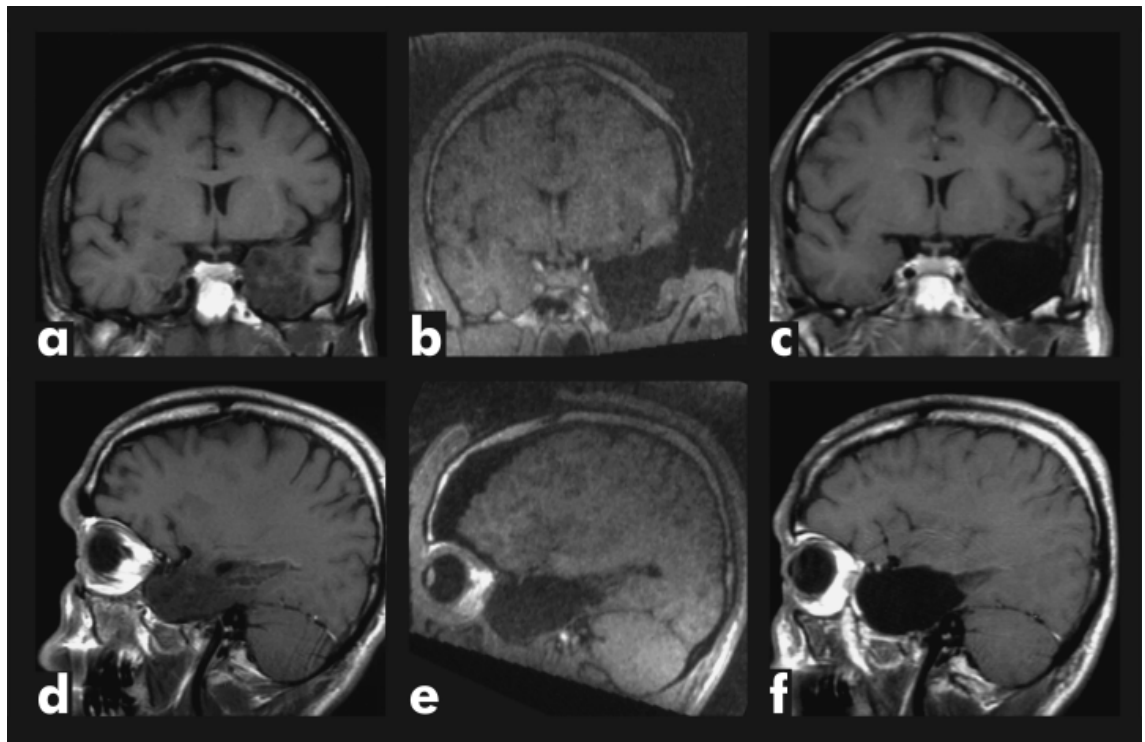


Figure 5.1 - Intraoperative imaging during temporal lobe surgery for DNET

Preoperative (a, d), intraoperative (b, e) and postoperative (c, f) images. Reproduced from Buchfelder et al. 2002 by permission of Wiley (© International League Against Epilepsy).

The extent of medial temporal lobe resection is a key determinant of seizure outcome (Wyler et al. 1995) with incomplete resection being the commonest cause of surgical failure (Wyler et al. 1989). In patients undergoing ATLR or SAH for refractory temporal lobe epilepsy, intraoperative scans following resection revealed incomplete hippocampal or amygdala resection leading to further resection in 50% and seizure freedom was attained in all but one at a mean follow up of 17 months (Kaibara et al. 2002). This finding has been replicated - 5 patients undergoing SAH all required further resection following intraoperative imaging (Schwartz et al. 2002) and 5 of 13 patients with lesions required further resection with complete radiological resection achieved in all (Walker et al. 2002).

The aim to limit surgical morbidity is equally applicable to epilepsy surgery. Image guidance can be used to localise critical landmarks for temporal lobe resection such as the temporal horn of the lateral ventricle and white matter tracts including the optic radiation. Display of preoperative tractography was used to guide entry in the temporal horn (Thudium et al. 2010) but in the absence of intraoperative imaging, entry to the temporal horn causing CSF leakage resulted in significant brain shift precluding further guidance.

Preoperative tractography (corticospinal tract, optic radiation or arcuate fasciculus) and fMRI data (motor or language) have been superimposed on intraoperative images of 25 patients undergoing extratemporal resections (Sommer et al. 2013). Although complete resection and good seizure outcomes were achieved, the optic radiation was only shown in 6 patients, with two developing a quadrantanopia. Further, the

preoperative imaging was rigidly registered to the intraoperative imaging thus not taking account of any brain deformation.

Tractography has been performed on intraoperatively acquired DTI data in patients undergoing ATR (Chen et al. 2009). However the limitations imposed by data quality and the available processing time mean that only deterministic algorithms are possible. These result in a poor depiction of Meyer's loop and in some cases, damage to this region prevented the successful delineation of Meyer's loop. Rigid registration of the pre- and intraoperative tractography confirmed significant brain shift during surgery (horizontal shift 0.0-11.1mm, mean 3.75mm, either inward or outward; vertical shift 0.0-7.8mm, mean 2.46mm, either up or down) demonstrating that preoperative tractography would no longer be valid without compensation.

A potential approach would therefore be to acquire and process tractography preoperatively and then map this on to intraoperative imaging using more accurate, but fast, non-linear registration (Section 5.4.2.3). Given the extensive computational and hardware requirements of this approach, an alternative method of acquiring a two-dimensional intraoperative photograph with a conventional digital camera and back projecting this on to the three-dimensional preoperative model has also been suggested (Wang et al. 2011). However this was only applied in a single patient undergoing temporal lobe surgery. The former approach is used in this thesis (Chapter 6).

5.4 Technical Challenges

5.4.1 The Key Challenges

Use of intraoperative MRI is technically challenging for many reasons. Two key issues are *brain shift* and *geometric image distortion*. Brain shift occurring during surgery renders any preoperative imaging inaccurate and geometric image distortion from sources such as the EPI sequences used for functional MRI or DTI limits the accuracy of imaging data derived from these modalities. Corrections for both limitations are implemented in the methods employed in this thesis (Chapter 6).

5.4.2 Brain Shift

5.4.2.1 The Nature of the Problem

Brain shift collectively refers to changes in brain position or shape following imaging ("post-imaging brain distortion"). Potential sources include gravity, cerebrospinal fluid leakage, tissue swelling or oedema, tissue resection, brain retraction and the effects of drugs such as osmotic diuretics. The degree of brain shift depends on the histology and location of the lesion, the internal brain structure (vessels, white matter), patient positioning, the surgical strategy, fluid/electrolyte balance and the choice of anaesthetic agents.

5.4.2.2 The Extent of the Problem

The degree of brain shift can be assessed by a comparison of preoperative and intraoperative imaging. In 64 patients undergoing tumour surgery, rigid registration between the pre- and intraoperative images allowed the maximal displacement at various sites to be measured and showed shifts of up to 3cm (Table 5.2) (Nimsky et al. 2000). Patient positioning affected the direction but not the degree of brain shift whilst entering the ventricular system (as in epilepsy surgery) increased ventricular and cortical shift. Although the authors concluded that “*experienced neurosurgeons with surgical common sense can use various techniques to minimize the effects of brain shift on surgical procedures*” much more can be done to accurately compensate for brain shift.

Serial acquisitions at a minimum of four timepoints (baseline, following dural opening and CSF drainage, following tumour resection and at dural closure) in patients with supratentorial lesions revealed two differing types of shift (Nabavi et al. 2001). The high number of intraoperative scans relied on performing scans *in situ* with an open scanner. Whilst the brain surface sinks under gravity following craniotomy and this continues throughout resection, deeper structures sink in the same direction but may rebound following tissue removal which is less predictable.

Anatomical site	Minimum	Maximum	Mean \pm SD	Direction
Cortex	-23.8mm	0.0mm	-8.4 \pm 5.6mm	83% inward, 17% none
Deep tumour margin	-7.9mm	30.9mm	4.4mm \pm 6.8mm	14% inward, 17% none, 69% outward
Midline	-4.0mm	5.9mm	-0.1mm \pm 1.7mm	
Ventricular system	0.0mm	8.0mm	2.1mm \pm 1.6mm	

Table 5.2 - Measurements of brain shift during tumour surgery

Negative values depict inward movements (sinking) and positive values depict outward movements (swelling).
Source: Adapted from Nimsky et al. 2000.

5.4.2.3 The Correction of the Problem

There are two broad approaches to updating anatomical and tractography information during surgery. The first is to perform intraoperative imaging following significant brain shift and to update the navigation with these images. DTI can also be acquired during surgery and used to perform tractography. However, the necessary time constraints of neurosurgery mean that lower quality data (lower resolution, fewer directions, lower signal-to-noise ratio) is available and only less accurate deterministic algorithms can be applied. This has however successfully been applied for the corticospinal tract (Bozzao et al. 2010), arcuate fasciculus (Zhao et al. 2012) and optic radiation (Chen et al. 2009, Sun et al. 2011).

The second approach is to acquire intraoperative anatomical data and then to perform image registration from the preoperative anatomical data to this. The same registration can be then be applied to update other preoperative modalities, including functional MRI and DTI. Commercially available software in neuronavigation systems including those from Medtronic and BrainLab only performs rigid registration (rotation and translation only) so makes no allowance for any deformation.

Non-linear registration that encompasses both an affine transformation (translation, rotation, scaling, shearing) and local deformation is required but such higher order transformation models are computationally expensive. In order to satisfy the constraints of a neurosurgical procedure, fast, robust and accurate registration is necessary. By calculating a patient-specific biomechanical finite element model from the preoperative imaging to enforce realistic deformations, accurate non-rigid registration between preoperative and intraoperative images can be achieved (Clatz et al. 2005) and applied prospectively in patients undergoing tumour resection (Archip et al. 2007). The computational time of 15-40 minutes on a standard workstation with 4 processors was reduced to 3 minutes by parallel processing with 240 processors. Moreover, the same transformations can be applied to fMRI and DTI data for display.

In this thesis, a non-rigid image registration algorithm is employed to correct for intraoperative brain shift (Section 6.6). This employs the complementary information from anatomical and diffusion data to improve registration accuracy and is implemented on a graphical processing unit (GPU) to reduce computational time. No biomechanical modelling is performed.

5.4.3 Geometric Image Distortion

5.4.3.1 The Nature of the Problem

Geometric image distortion results from any artefacts that violate the assumption of linear encoding of position in space with the frequency and phase encoding gradients in MR imaging (Table 5.3). Soft tissue distortion (brain shift) discussed above (Section 5.4.2) occurs in addition to this.

Equipment-induced	Patient-induced
Static field inhomogeneity	Magnetic susceptibility artefacts
Gradient field non-linearity	Chemical shift artefact
Eddy currents from gradient switching	Flow effects

Table 5.3 - Common sources of geometric image distortion

5.4.3.2 Gradient Field Non-Linearity

Gradient field non-linearity represents a technical imperfection in the gradient that leads to both geometric and intensity distortions. The distortion is specific to the scanner and independent of the patient's position within the scanner. It is particularly important when different scanners are used, for example when combining preoperative imaging from one scanner with intraoperative imaging from another scanner.

Manufacturer-supplied software may only correct in-plane (in two-dimensions) so distortions remain through plane. For example, in a coronally acquired T1-weighted volumetric scan distortions remain in the antero-posterior direction (Figure 5.2) whilst in an axially acquired scan distortions remain in the supero-inferior direction (Figure 5.3).

The displacements can be calculated and applied from the non-linear terms of the magnetic field generated by each of the gradient coils. The fields can be supplied by the vendor as a truncated series of spherical harmonic coefficients (Janke et al. 2004). Corrections are applied to pre- and intraoperative data used for neurosurgical guidance in iMRI using custom written software in this thesis (Chapters 6 and 10).

5.4.3.3 Magnetic Susceptibility Artefacts

A patient in a scanner induces microscopic variations in the magnetic field strength. At interfaces with large magnetic susceptibility differences, such as air/tissue or bone/tissue boundaries, this results in significant geometric (and intensity) distortions. It thus particularly affects the anterior temporal lobe and in the context of neurosurgery, the resection cavity introduces air and thus susceptibility differences and distortions around the area of resection.

Echo-planar imaging (EPI) is used for functional MRI and DTI sequences due to its high temporal resolution. However since it samples the entire frequency space of a single slice with fast gradient blipping following a single excitation pulse, this results in a very low bandwidth in the phase encoding direction. Thus EPI sequences are particularly susceptible to magnetic susceptibility artefacts. As the phase encoding direction is typically anterior-posterior, this is critical when considering the anterior extent of a structure such as the optic radiation.

Correction of susceptibility induced distortion may be performed either by field map estimation or non-linear image registration. Field maps are acquired at the same time as the EPI data to estimate the magnetic field inhomogeneity from two phase images acquired at different echo times (Jezzard & Balaban 1995). Non-linear image registration is performed between the distorted EPI image and a high resolution undistorted T1-weighted anatomical image (Merhof et al. 2007). EPI images acquired intraoperatively have low signal-to-noise ratio and artefacts which make this approach challenging. The former approach with field maps and custom written software is used in this thesis (Figure 5.4).

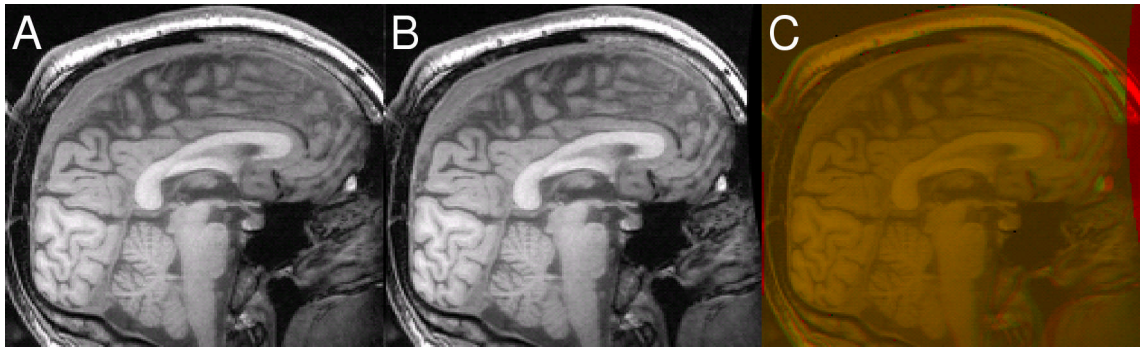


Figure 5.2 - Gradient non-linearity correction in a human subject

T1-weighted volumetric image from scanner with on scanner in-plane (coronal) correction (A), image after post acquisition correction in third (anterior-posterior) dimension (B), and comparison of images (red and green respectively).

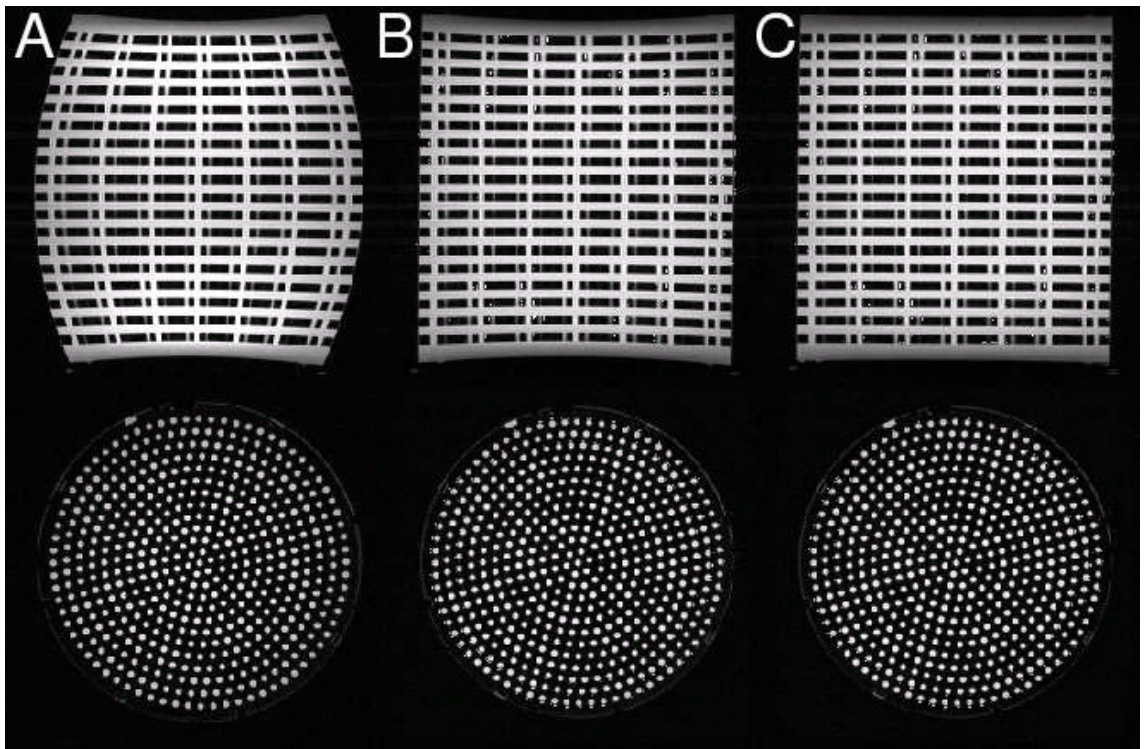


Figure 5.3 - Gradient non-linearity correction in a phantom

Axial acquisition with top row showing coronal plane, and bottom row showing axial plane. Uncorrected scan (A), scan with on-scanner in-plane (axial) correction (B), and image after post acquisition correction in third (superior-inferior) dimension (C).

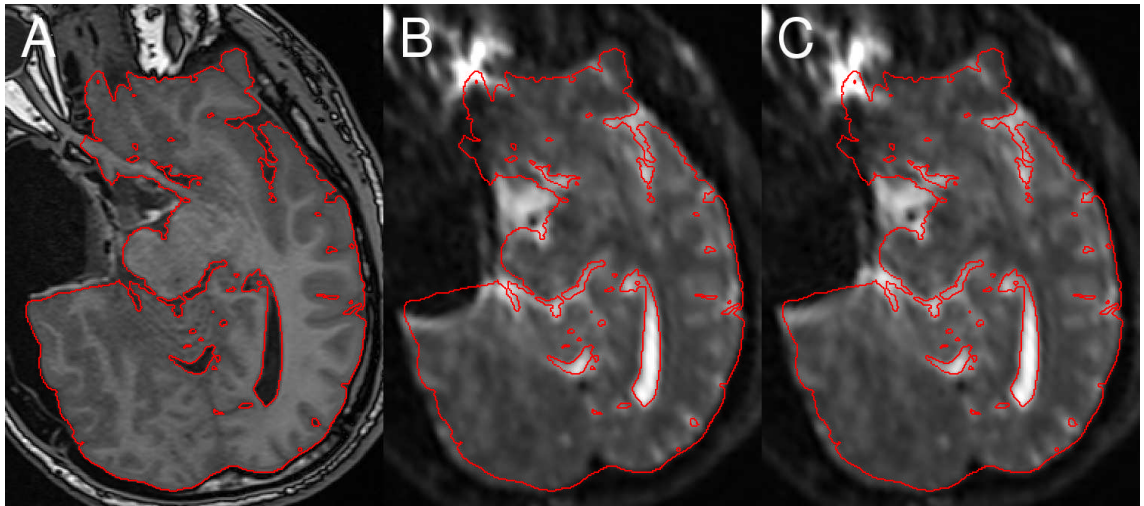


Figure 5.4 - Magnetic susceptibility artefact correction in intraoperative data

Intraoperative T1-weighted scan (A), non-diffusion weighted image from DTI sequence acquired with EPI uncorrected (B) and field-map corrected (C). Image courtesy of Pankaj Daga.

5.5 Conclusions

There are several approaches to intraoperative imaging but intraoperative MRI has the advantages of high temporal and spatial resolution, good soft tissue contrast and full multiplanar imaging without any radiation exposure. It is safe and can be used to maximise the degree of resection whilst minimising the associated morbidity in both tumour and epilepsy surgery. Technical challenges including correction for brain shift and geometric image distortion must be addressed in order to use the data optimally.

6 STUDY DESIGN AND GENERIC METHODS

6.1 Introduction

The studies described in this thesis predominantly involve a cohort of patients with refractory TLE undergoing surgery who were prospectively recruited and followed up longitudinally. This chapter introduces the cohort, their clinical and demographic features and the main assessments undertaken including MRI, neuropsychology and visual fields. Specific features of the methods for each study are included in the relevant chapters.

6.2 Aims of the Studies

In Chapter 0, I assess the utility of preoperative tractography for planning surgery in and counselling patients with lesions lying near the presumed course of the optic radiation. The aims are to optimise the technique for tractography to delineate the entire optic radiation and to subsequently visualise the results on anatomical images and in 3D renderings so aiding the consideration of the risk of surgery and the planning of the surgical approach. The tractography results are validated against visual outcomes following surgery.

In Chapter 8, I compare two different methods for tractography of the optic radiation in both healthy controls and patients with lesions by the optic radiation. The first method was designed to accurately delineate Meyer's loop and is used in the rest of this thesis whilst the second was designed to provide some more automation to the technique and so save operator time. The use of the same datasets and parameters allows a direct comparison of the effect of differing seed regions. The aims are to determine the level of agreement between the methods and to identify the method that more reliably identifies different components of the optic radiation for use in different types of epilepsy surgery.

In Chapter 9, I assess the feasibility of a rapid novel image processing technique to propagate preoperative tractography data on to postoperative structural images by showing that the extent of damage to Meyer's loop as assessed by this technique is more highly predictive of visual field outcome following surgery than assessment using the combination of the degree of resection and location of Meyer's loop. Confirming that the technique is both fast and accurately predicts visual outcome enables the technique to be extended for use on intraoperative images in real time for surgical guidance.

In Chapter 10, I apply this technique in real-time in an iMRI suite for image-guided surgery of patients undergoing anterior temporal lobe resection. The hypothesis is that display of tractography will reduce the severity of visual field deficits and increase the proportion of patients that can drive following surgery with adversely affecting the secondary outcomes of seizure outcome and degree of hippocampal resection. I also assess the incremental benefit of correction for brain shift on outcome.

In Chapter 11, I assess the structural correlates of impaired working memory in patients with hippocampal sclerosis. I test the hypotheses that structural changes exist in the grey matter of the bilateral frontoparietal working memory identified by functional MRI and in the white matter tracts connecting these regions, and that working memory performance correlates with these structural changes. In addition, I seek evidence that working memory involves and is affected by the structural integrity of the temporal lobes given the impairment of working memory in this population.

In Chapter 12, I assess the longitudinal changes in diffusion parameters at two timepoints following temporal lobe surgery. I show changes consistent with Wallerian degeneration in adjacent tracts and changes compatible with structural plasticity in the corona radiata, internal and external capsules. I assess the time course of these changes and whether it differs between left and right-sided surgery.

In Chapter 13, I perform a preliminary study of a novel advanced diffusion model (NODDI) in patients with focal cortical dysplasia. The aims are to determine whether this technique can detect changes compatible with the underlying disrupted tissue microstructure and whether it may provide useful additional clinical information, by being a more sensitive marker for pathology than other diffusion indices or conventional structural imaging.

6.3 Subjects and Recruitment

6.3.1 Source of Patients

Patients with medically refractory TLE being investigated for consideration of surgery (ATLR or lesionectomy) at the National Hospital for Neurology and Neurosurgery (NHNN) were invited to participate in the study. They were identified using the following sources:

- The weekly epilepsy surgery multidisciplinary meeting at NHNN
- Referrals to a tertiary referral epilepsy clinic at NHNN for consideration of surgery
- Patients undergoing inpatient presurgical assessment at the Williams Gowers Centre, Epilepsy Society
- Referrals for day case investigations that include MRI at the Epilepsy Society MRI Unit

For the study on patients with lesions near to the optic radiation, some additional patients were recruited with lesions outside the temporal lobe and some additional previously scanned patients with TLE were also included (Chapter 0).

6.3.2 Healthy Controls

A group of native English speaking age-matched healthy controls were also studied for comparison. They were recruited as friends or relatives of patients, by word-of-mouth or advertising on the Epilepsy Society website and in a local supermarket. Healthy controls completed a proforma (Appendix F) to exclude those with history of neurological or psychiatric disorder or with a contraindication to MRI scanning. Questions

included history of seizures, serious head injury, stroke, brain haemorrhage, depression or other psychiatric problems, inflammation/infection of the nervous system, alcohol/drug intake and current medication.

6.3.3 Ethical Approval

The study was approved by the National Hospital for Neurology and Neurosurgery and the Institute of Neurology Joint Research Ethics Committee, and informed written consent was obtained from all subjects. The information sheet for patients is shown in Appendix A, the information sheet for healthy controls in Appendix B and the consent form in Appendix C.

6.4 Clinical and Demographic Characteristics

6.4.1 Patient Cohort

A total of 146 patients were recruited into the study predominantly from December 2008 to March 2012, with an additional three patients recruited in November-December 2012 for the interventional MRI study. The outcomes of these patients are illustrated in Table 6.1. Over half (84 patients) underwent surgery of which 78 were seen at 3-4 months following surgery and 47 were seen again at 12 months. Two patients declined research follow up, three patients were not seen again following surgery as the original fMRI acquisition was altered after the first few patients and the final patient was not seen as the study follow-up period had ended.

The clinical and demographic features of the cohort are shown in Table 6.3 split into groups on the basis of the structural imaging findings - hippocampal sclerosis (HS), dual pathology (HS + another lesion), another pathology or MRI-negative. Hippocampal sclerosis was defined on the basis of the clinical neuroradiology report that includes manual hippocampal volumes and T2 relaxation times. All patients with hippocampal sclerosis had a normal contralateral hippocampus based on qualitative and quantitative MRI criteria (Woermann et al. 1998). The breakdown of pathology in the non-HS or dual pathology groups is shown in Table 6.2.

A few patients had undergone previous surgery and were excluded from some studies. In the left dual pathology group, one patient had previous treatment for an AVM; in the right HS group, one patient had a previous ATLR and in the right dual pathology group, one patient had a previous selective amygdalo-hippocampectomy for DNET with residual HS. In the right other pathology group, three patients had undergone surgery (lesionectomy for tumour, previous ATLR for gliosis with residual heterotopia, previous cavernoma resection).

There were 12 patients not suitable for inclusion in studies ("other" group) - 6 patients had bitemporal discharges (4 MRI negative, 1 tuberous sclerosis, 1 hypothalamic hamartoma), a single MRI negative patient declined intracranial EEG and another patient with an incidental cavernoma is awaiting intracranial EEG. A further 4 patients were found to have epileptic foci outside the temporal lobe.

6.4.2 Control Cohort

A total of 31 healthy controls were recruited, but one was unable to tolerate MRI scanning due to claustrophobia. For the remaining 30 subjects, the gender split was 13 male, 17 female, the age range was 19-64 years (median 37 years) and 26 were right-handed with the remaining 4 left-handed. Structural MRI was normal with normal hippocampal volumes except in a single patient who had some periventricular white matter signal change and was thus not included in analyses of white matter or followed up.

Follow-up data were available for 17 controls at 3-4 months and 16 controls at 12 months. Two controls seen at 12 months did not have DTI scans at 3-4 months due to scanner failure and time constraints respectively so there were 14 controls with a complete DTI dataset at all three timepoints.

Outcome	Number of patients (%)
Surgical treatment	84 (57.5%)
Gamma knife surgery	3 (2.1%)
Unsuitable for surgery	24 (16.4%)
Declined surgery or intracranial EEG	31 (21.2%)
Awaiting surgery, intracranial EEG or other investigation	3 (2.1%)
Deceased	1 (0.7%)

Table 6.1 - Outcome of patients in longitudinal study

Pathology	Left TLE (dual)	Left TLE (other)	Right TLE (dual)	Right TLE (other)
Focal cortical dysplasia	0	0	1	1
Other dysplasia	0	4	1	0
Heterotopia	0	0	0	1
Polymicrogyria	0	0	0	1
Dysembryoplastic neuroepithelial tumour	1	6	1	5
Other tumour	1	1	0	1
Amygdala lesion	1	2	0	4
Parahippocampal gyrus signal change	0	0	0	3
Cavernoma	0	6	1	6
Arteriovenous malformation	1	0	0	0
Ischaemia/damage	3	0	1	0

Table 6.2 - Diagnoses of patients in longitudinal study based on structural MRI

Group	Total	3-4m scan	12m scan	Gender (M/F)	Handedness (right/left)	Age at scan (yr)	Age of onset (yr)	Duration (years)
Left TLE								
HS	32	17	11	15/17	27/5	18-54 (39)	0.25-35 (13)	3-51 (18.5)
Dual	7	4	4	4/3	6/1	18-47 (38)	0.4-25 (2)	9-46 (25)
Other	19	14	6	8/11	19/0	26-63 (38)	1-44 (23)	1-46 (10)
Negative	7	2	2	4/3	6/1	25-49 (31)	10-37 (21)	4-23 (11)
Right TLE								
HS	29	15	10	7/22	24/5	22-56 (42)	1-39 (11)	3-54 (29)
Dual	5	4	3	1/4	5/0	21-51 (41)	5-31 (9)	7-46 (22)
Other	22	14	8	5/17	11/3	17-66 (36)	0.25-44 (19)	1-30 (15)
Negative	13	8	3	6/7	12/1	19-44 (36.5)	7-34 (18)	4-34 (12)
Other								
See text	12	0	0	9/3	11/1	18-48 (29.5)	2-42 (13)	5-35 (12.5)

Table 6.3 - Clinical and demographic characteristics of patients in longitudinal study

Range and median values given for age at scan, age of onset and duration of epilepsy.

6.5 Study Protocol

6.5.1 Clinical Assessment

All patients had structural MRI scans performed at 3T, video EEG telemetry, neuropsychology, neuropsychiatry and if necessary intracranial EEG recordings in order to confirm suitability for surgery. Some patients had additional investigations including PET or ictal SPECT. All these investigations were performed as part of standard clinical practice.

6.5.2 Timing of Visits and Questionnaires

Patients (and controls) underwent the same research assessment prior to surgery, 3-4 months following surgery and 12 months following surgery. A proforma was completed at each visit for patients (Appendix D) recording clinical details including age of onset, seizure type(s) and frequency, the date of the last seizure and any medications. Seizure outcome was assessed using the ILAE classification (Section 1.3.6.6.1).

At baseline, patients and controls completed the Edinburgh Handedness Inventory (Oldfield 1971) using a proforma with 17 items (Appendix E). This was converted to a number ranging from -100 (completely left-handed) to +100 (completely right-handed) using the formula:

$$\text{Handedness} = \frac{(\text{Crosses in right} - \text{Crosses in left})}{(\text{Crosses in right} + \text{Crosses in left})} \times 100$$

6.5.3 Magnetic Resonance Imaging

MRI studies were performed on a 3T GE Signa Excite HDx scanner (General Electric, Waukesha, Milwaukee, WI, USA). Standard imaging gradients with a maximum strength of 40mT m⁻¹ and slew rate 150T m⁻¹s⁻¹ were used. All data were acquired using a body coil for transmission, and eight channel phased array coil for reception.

6.5.3.1 Structural Imaging

Standard clinical scans were performed with the sequences listed in Table 6.4.

6.5.3.2 Diffusion Tensor Imaging

6.5.3.2.1 Acquisition

DTI data were acquired using a cardiac-triggered single-shot spin-echo planar imaging (EPI) sequence (Wheeler-Kingshott et al. 2002) with echo time (TE) of 73 ms. Sets of 60 contiguous 2.4mm thick axial slices were obtained covering the whole brain, with diffusion sensitising gradients applied in each of 52 non-collinear directions [*b* value of 1200 mm² s⁻¹ ($\delta = 21$ ms, $\Delta = 29$ ms, using full gradient strength of 40 mT m⁻¹)] along with six non-diffusion weighted scans. The gradient directions were calculated and ordered as described elsewhere (Cook et al. 2007). The field of view was 24x24cm, and the acquisition matrix size was 96x96, zero filled to 128x128 during reconstruction giving a reconstructed voxel size of

1.875x1.875x2.4mm. The DTI acquisition time for a total of 3480 image slices was approximately 25 minutes (depending on subject heart rate).

Accompanying field maps were acquired from December 2011 until the end of the project. A 3D fast spoiled gradient echo sequence (FSPGR) sequence with 64 contiguous 2.4mm thick axial slices was performed covering the same region as the DTI and ensuring no table movement between the two acquisitions. Two slices were discarded at each end and the sequence was performed twice using a repetition time (TR) of 7.6ms and a TE of 5.46ms and 3.00ms respectively. The field of view was 24x24cm and the acquisition matrix size was 128x128, zero filled to 256x256 giving a reconstructed voxel size of 0.9375x0.9375x2.4mm. Real and imaginary images were acquired and used to calculate phase maps.

Sequence	Plane	Acquisition time (m:ss)	Slice thickness / spacing (mm)	Number of slices	Matrix size	Field of view (cm)
T1 FLAIR	Sagittal obl	1:28	5 / 2	17	320x224	24x24
FSPGR 3D	Coronal obl	7:30	1.1 / 0	170	256x256	18x24
T2 FLAIR	Coronal obl	2:56	5 / 0	32	224x256	18x24
PD/T2 FRFSE	Coronal obl	2:01	5 / 0	32	256x256	18x24
FGRE T2*	Coronal obl	2:12	5 / 0	32	192x192	18x24
FSE T2	Axial obl	1:23	5 / 0	30	256x512	18x24
PROPELLER	Coronal obl	3:20	2 / 0	32	416x416	22x22
(selected patients)						

Table 6.4 - Epilepsy protocol for structural scans on 3T GE Signa Excite HDx scanner

Key: FGRE = fast gradient echo, FLAIR = fluid-attenuated inversion recovery, FRFSE = fast recovery fast spin echo, FSE = fast spin echo, FSPGR = fast spoiled gradient recalled, PD = proton density, PROPELLER = periodically rotated overlapping parallel lines with enhanced reconstruction, SE = spin echo, obl = oblique

6.5.3.2.2 Preprocessing

The scans were transferred to a Linux-based Sun Ultra workstation in DICOM format and converted to a single multivolume Analyze 7.5 format file using locally written software. Eddy current correction of the DTI data was performed using the eddy_correct tool in FSL (Smith et al. 2004).

A multi-tensor model was fitted to the eddy corrected diffusion data using the Camino toolkit (version 2 release 767) (Cook et al. 2006). Voxels in which a single tensor fitted the data poorly were identified using a spherical-harmonic voxel-classification algorithm (Alexander et al. 2002). In such voxels a two tensor model was fitted, with the principal diffusion directions of the two diffusion tensors providing estimates of the orientations of the crossing fibres. In all other voxels, a single tensor model was fitted.

6.5.3.2.3 Tractography of the Optic Radiation

Tractography was carried out using the Probabilistic Index of Connectivity (PICO) algorithm (Parker et al. 2003) as implemented in Camino and extended to deal with multiple fibres (Parker & Alexander 2003, Cook et al. 2004). Seed, way and exclusion masks were defined using MRICro (<http://www.psychology.nottingham.ac.uk>) based on previous work (Yogarajah et al. 2009).

Fractional anisotropy and principal diffusion direction maps were used to identify the lateral geniculate nucleus (LGN) by selecting the axial slice at the level of the transition from the posterior limb of the internal capsule to the cerebral peduncle. Voxels antero-lateral to the LGN across the base of Meyer's loop, with principle eigenvectors orientated in an antero-medial to postero-lateral orientation, were identified and used to define a seed point in a coronal plane (Figure 6.1a-c). Contiguous voxels, with principal directions in an anterior-posterior direction, were also selected in order to cover the entire coronal cross-section of Meyer's loop, using a standardised seed point volume of 15 voxels (127 mm³).

Tracking from the seed was performed using 50000 Monte Carlo iterations, an angular threshold of 180° and a fractional anisotropy threshold of 0.1, in order to ensure that the paths detected would not erroneously enter areas of cerebrospinal fluid, and yet had sufficient angular flexibility to allow tracking of Meyer's loop.

In order to restrict the pathway to anatomically valid tracts, a way point was defined in the lateral wall of the occipital horn of the lateral ventricle at the posterior extent of the corpus callosum (Figure 6.1d). Two exclusion masks were applied. Firstly, a midline exclusion mask and then a coronal exclusion mask to remove artefactual connections to adjacent white matter tracts, such as the fronto-occipital fasciculus, anterior commissure and uncinate fasciculus. An objective, iterative process was performed to determine the optimum location for this mask whereby the exclusion mask was moved posteriorly until it began to coincide with Meyer's loop, identified by a visible thinning of the estimated trajectory of the optic radiation, typically associated with a reduction in tract volume greater than 10% (Yogarajah et al., 2009).

A connectivity distribution was generated from each voxel in the seed region and combined into an overall connectivity map representing the maximum observed connection probability to each voxel within the brain from all the voxels within the seed region. For display purposes, the connectivity distributions were thresholded at 5%, representing a compromise between retaining anatomically valid tracts and removing obviously artefactual connections.

The above approach to tractography was slightly modified for surgical planning outside the temporal lobe in Chapter 7 and two different methods were compared in Chapter 8.

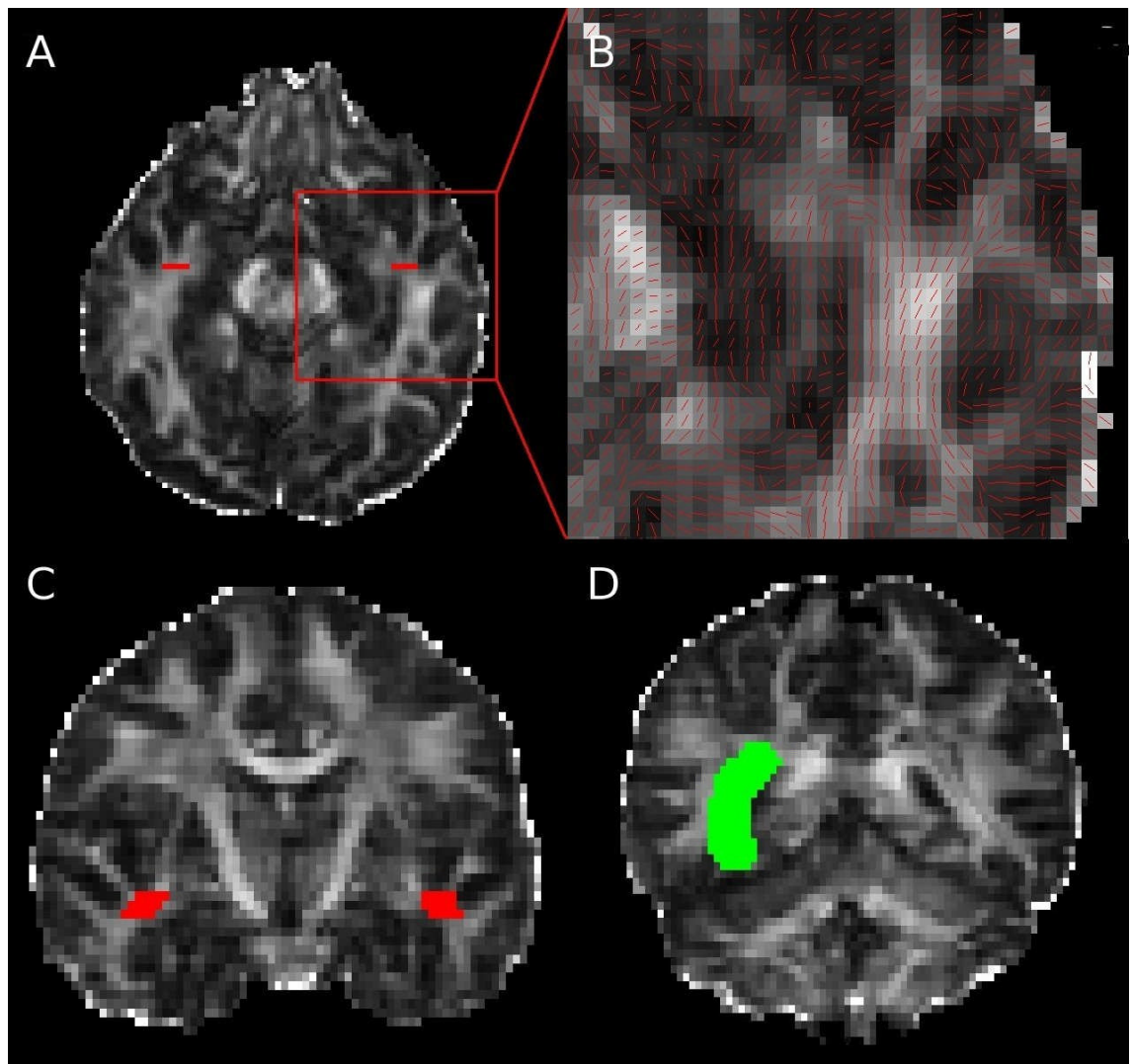


Figure 6.1 - Seed and way point for optic radiation tractography

The seed point was across Meyer's loop, red (A – axial slice, B – close up of axial slice with principle diffusion directions showing the high curvature of the loop, C – coronal slice) and the way point, green, was in the stratum sagittale (lateral wall of the lateral ventricle) (D). Displayed on the FA map.

6.5.3.3 Functional MRI

Subjects also underwent five fMRI paradigms:

- Working memory (visuospatial n-back)
- Working memory (verbal n-back)
- Language (verbal fluency)
- Language (verb generation)
- Episodic memory (memory encoding)

For the working memory fMRI task, gradient-echo planar T2*-weighted images were obtained with 50 non-contiguous 2.4mm thick oblique axial slices (0.1mm gap) covering the whole brain. The field of view was 24x24cm and the acquisition matrix size was 64x64 giving in-plane resolution of 3.75x3.75mm. TE was 25ms, TR was 2.5s and a SENSE factor of 2 was used.

The working memory network was identified using a modified version of the '*n*-back' task (Callicott et al. 1999, Kumari et al. 2003) in which subjects were required to monitor the location of dots (presentation time 440ms, inter-stimulus interval 1500 ms) within a diamond shaped box on the screen at a given delay with the original occurrence (0-, 1- or 2-back). There were three 30 second active conditions in total (0-, 1-, and 2-back) presented to subjects five times in pseudorandom order, controlling for any order effect. In total, 15 stimuli were presented in each 30 second active block. Each active condition started with a 15 second resting baseline (the word "Rest" appeared on the screen during this period). Subjects were required to move the joystick corresponding to the correct location of the current (0-back) or previously presented (1-back = previous presentation; 2-back = previous presentation but one) stimulus. On-line accuracy data were determined by joystick movement on every trial with output stating either a correct response, wrong response or no response. The percentage of correct 2 dot-back trials was used as a measure of performance.

The other functional MRI paradigms were not used in this thesis.

6.5.4 Neuropsychology

Patients underwent a full clinical neuropsychology assessment, including measures of language and episodic memory performance and the Wechsler Adult Intelligence Scale Third Edition (WAIS-III) (Wechsler 1997) to establish full scale IQ.

The WAIS-III includes a Digit Span subtest in which subjects have to repeat digit strings of increasing length in original or reverse order. The digit sequences range in length from 2 to 8 with two trials per sequence. Span size was calculated as the highest digit sequence where both trials were successful. Digit span backwards was used as a measure of working memory and two further assessments of working memory capacity were undertaken for use in Chapter 11.

In the Gesture Span task (Canavan et al. 1989), subjects repeat sequences of hand gestures of increasing length up to 5 gestures. The test ends following two consecutive errors at any given gesture span or when the maximum of 5 gestures is reached. The task was repeated a second time and the mean span across the two trials was used as the measure of working memory.

In the Motor Sequences task (Canavan et al. 1989), subjects repeat a sequence of 3 hand gestures in the same order. Ten alternating sequences were administered and the total number of successful trials was used as the measure of working memory.

6.5.5 Visual Fields

6.5.5.1 Goldmann Kinetic Perimetry

Visual fields were primarily assessed using Goldmann kinetic perimetry (Haag Streit, UK) as the interaction between operator and individuals with poor fixation, attention or cognition (common in subjects with epilepsy) enables a more reliable determination of the visual field (Beck et al. 1985). Each eye was examined using three isopters (V4e, I4e and I2e in that order) with measurements made every 15 degrees to allow reliable detection of minor postoperative VFD. The Goldmann perimeter was regularly calibrated to the specified target and background luminance in the manufacturers' instructions. Assessment was performed at each of the three timepoints, except in the initial patients where no preoperative perimetry was performed as the equipment was not yet available.

6.5.5.2 Quantification of VFD

In order to determine the post-operative visual deficit, the post-operative visual fields were scanned and the total area within the V4e and I4e isopters in each quadrant (in pixels) was determined by locally-written MatLAB scripts (Mathworks, Cambridge, UK) (Figure 6.2). The I2e isopter was not assessed as some subjects were unable to reliably detect this stimulus.

Due to the high variability observed between Goldmann perimetry sessions (Parrish et al. 1984) and the lack of preoperative data in some patients, postoperative visual field loss was determined using only the postoperative data. Since following temporal lobe surgery the contralateral upper quadrant (UQ) may be affected whereas the ipsilateral upper quadrant should be unaffected, the following formula was employed:

$$\text{Visual field loss} = 1 - \frac{[\text{Area contralateral UQ (sum of both eyes)}]}{[\text{Area ipsilateral UQ (sum of both eyes)}]}$$

In the event of a negative visual field loss reflecting minor asymmetry between the upper quadrants, a figure of zero was used. By using the unaffected upper quadrant ipsilateral to the side of surgery as the reference for each patient, this allowed the use of post-operative data alone and eliminated inter-session variability. No significant asymmetry in the upper quadrants was observed on preoperative Goldmann perimetry, and no deficits within the ipsilateral upper quadrants were observed in post-operative fields.

In the initial proof of concept, just the outer V4e isopter was measured (Chapter 9) but when extended for use in the intraoperative studies the average of the V4e and I4e isopters was calculated as this is more sensitive to minor VFD (Chapter 10).

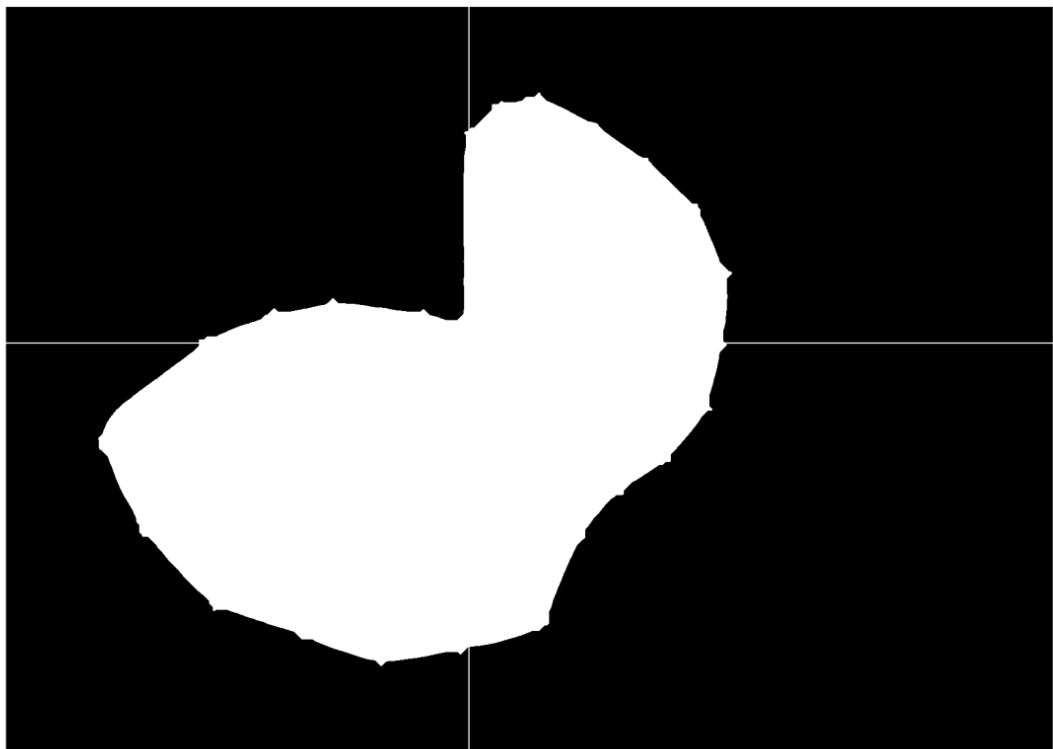
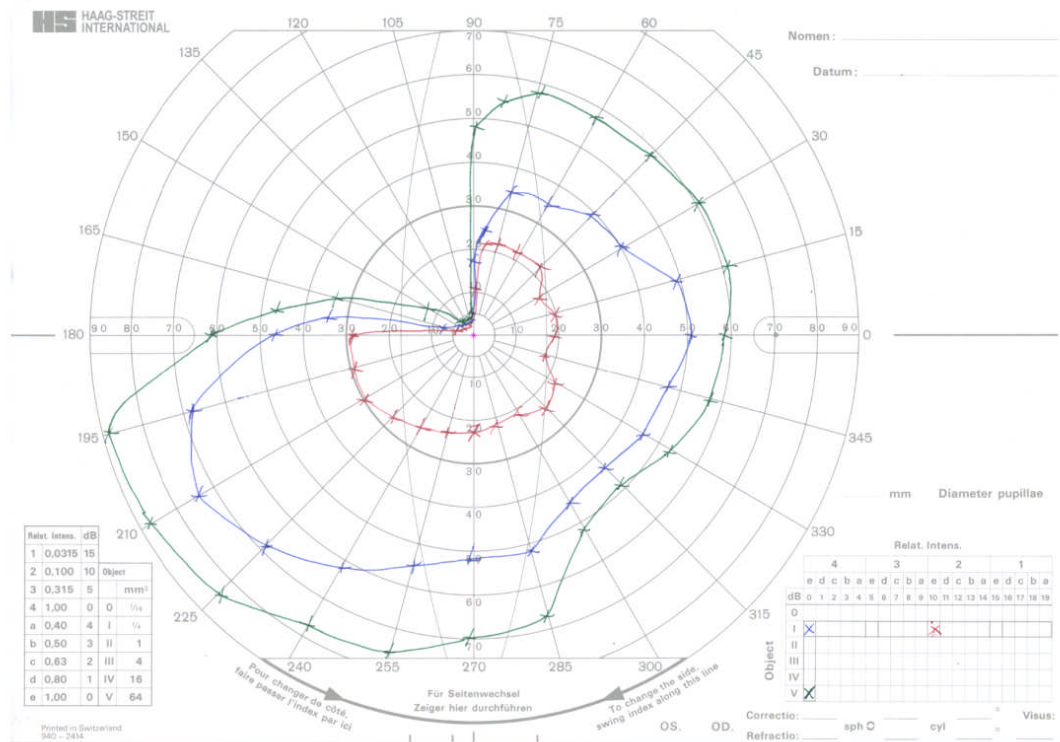


Figure 6.2 - Quantification of visual field loss with Goldmann perimetry

The top panel shows example Goldmann perimetry of the left eye with a postoperative left superior quadrantanopia (V4e = green, I4e = blue, I2e = red) and the detected centre (small pink cross). The bottom panel shows the segmented visual field (V4e isopters) split into the four quadrants.

6.5.5.3 Determination of Driving Eligibility

The eligibility of patients to drive was determined in accordance with UK Driver and Vehicle Licensing Agency regulations (Driver and Vehicle Licensing Agency 2013) (Section 4.4.8). For the first half of the study, those patients who had a VFD on Goldmann perimetry were referred to the Neuro-Ophthalmology Clinic at NHNN for binocular Esterman perimetry. When this equipment became available in the Epilepsy Society MRI Unit, all patients underwent assessment following the Goldmann kinetic perimetry at a single postoperative timepoint. Any assessment in which a false positive score of more than 20% was recorded was repeated in accordance with the guidelines.

Eligibility was assessed according to the stated criteria (Figure 6.3), although consideration on an individual basis or application of some leniency may occur with a non-progressive deficit. Thus scattered single points or a single cluster of up to 3 adjoining points were considered acceptable, whilst a cluster of 4 or more adjoining points wholly or partly within the central 20 degrees; loss of a single cluster of 3 adjoining missing points up to and including 20 degrees from fixation and any additional separate missed point(s) within the central 20 degree area; any central loss that is an extension of a hemianopia or quadrantanopia of size greater than 3 missed points were all considered unacceptable (Driver and Vehicle Licensing Agency 2013).

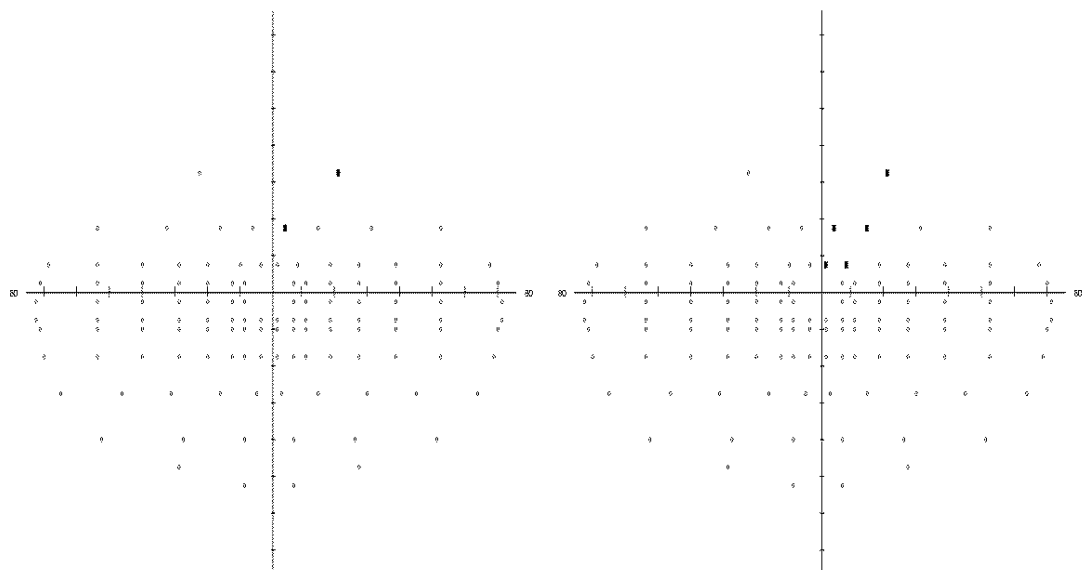


Figure 6.3 - Assessing driving eligibility with Esterman binocular perimetry

Example of an acceptable visual field loss (left) and an unacceptable visual field loss (right) following left ATLR.

6.6 Software for Image Registration

6.6.1 Introduction

The software to perform non-rigid image registration was developed by Pankaj Daga at the UCL Centre for Medical Image Computing for his PhD thesis and builds on earlier work by Marc Modat (Modat 2012). It is available as an open source package, NiftyReg (<http://sourceforge.net/projects/niftyreg>).

Additional software tools to perform gradient non-linearity correction and susceptibility correction using field maps were written by Pankaj Daga. This section summarises these tools and the work leading to the choice of method. Their combination into a complete intraoperative pipeline is described in Chapter 10.

6.6.2 Basics of Image Registration

Image registration aims to find the optimum transformation between two (or more) images in order to maximise their similarity. There are three basic transformation models:

1. **Rigid** - the image is moved by translation or rotation without any change in shape (6 degrees of freedom comprising 3 rotations and 3 translations)
2. **Affine** (global) - this consists of translation and rotation (as rigid) but also scaling and shearing (12 degrees of freedom)
3. **Non-rigid** (local) - localised changes (deformations) are applied to the image (many degrees of freedom)

Currently available neuronavigation software packages perform only rigid registration due to time constraints but this fails to account for the complex brain shift (deformation) that occurs during neurosurgery. Non-rigid registration was therefore used in this thesis.

6.6.3 NiftyReg Software

6.6.3.1 Global registration

An affine registration between floating (source) and reference (target) images is estimated. Most affine registration algorithms assume a global relationship between image intensities. However with intra- or postoperative images, this assumption is violated due to presence of tissue resection or additional features such as swabs. Therefore a global registration technique driven by *local* similarity measures was used.

Block-matching is used to establish correspondence between image blocks in the reference image and the corresponding region in the floating image (Ourselin et al. 2002). This is applied in an iterative manner starting from a low resolution down-sampled image working towards a higher resolution image. Each multiresolution level is initialised with the transformation estimated at the previous level. The transformation parameters that best fit the established correspondences are estimated using a least trimmed square optimisation, which is robust to outliers that might otherwise result in a suboptimal transformation. This optimisation technique is also computationally efficient.

6.6.3.2 Local registration

The non-rigid registration is based on Free-Form Deformation which is parameterised using cubic B-splines (Rueckert et al. 1999). A three-dimensional mesh of control points is generated at a specified spacing and the new co-ordinates of these control points are determined by the optimisation.

The image similarity metric is normalised mutual information (NMI), a voxel-intensity based similarity measure that employs the concept of entropy:

$$NMI(R, F(\mathbf{T})) = \frac{H(R) + H(F(\mathbf{T}))}{H(R, F(\mathbf{T}))}$$

where R is the reference image, $F(\mathbf{T})$ is the floating image F under transformation \mathbf{T} , $H(R)$, $H(F(\mathbf{T}))$ and $H(R, F(\mathbf{T}))$ are the two marginal entropies and the joint entropy respectively.

The objective function comprises the similarity metric (NMI) and two penalty terms. The penalty terms enforce smoothness and penalise large deformations (bending energy, BE) and aim to prevent folding (log of the Jacobian determinant, JAC):

$$\Omega(R_1, R_2, F_1(\mathbf{T}), F_2(\mathbf{T})) = \alpha \times NMI - \beta \times BE - \gamma \times JAC$$

where the weights $\alpha + \beta + \gamma = 1$.

The affine transformation from the global registration is used as a starting point for the optimisation which is implemented via a conjugate gradient ascent scheme. As this is computationally expensive, it was parallelised for use on multi-core graphical processing units (GPU) using the NVIDIA CUDA architecture to significantly reduce computational time (Modat et al. 2010).

6.6.3.3 Extensions for Present Work

The original algorithm considers a single reference image R and a single floating image F . This fails to capture the complementary information provided by structural and diffusion MRI when aligning preoperative and intraoperative images. Structural images provide information on the interfaces between different brain tissues whilst diffusion images provide information about the microstructural organisation of white matter bundles. The registration algorithm was extended to perform registration between a pair of reference images $\{R_1, R_2\}$ and a pair of floating images $\{F_1, F_2\}$. Each pair of images is rigidly aligned and the standard NMI measure is replaced by a multichannel NMI similarity measure (Daga et al. 2011a):

$$NMI(R_1, R_2, F_1(\mathbf{T}), F_2(\mathbf{T})) = \frac{H(R_1, R_2) + H(F_1(\mathbf{T}), F_2(\mathbf{T}))}{H(R_1, R_2, F_1(\mathbf{T}), F_2(\mathbf{T}))}$$

where $H(R_1, R_2)$ and $H(F_1(\mathbf{T}), F_2(\mathbf{T}))$ represent the joint entropy between the two reference images and the two deformed floating images respectively and $H(R_1, R_2, F_1(\mathbf{T}), F_2(\mathbf{T}))$ is the joint entropy between the four input images.

For the registration of preoperative to intra- or postoperative images, the T1-weighted volumetric acquisition and the FA map derived from the diffusion imaging were used. The accuracy of registration with the multichannel MNI measure was shown to be superior than using either structural or diffusion scans alone both for a numerical phantom and when using pre- and postoperative imaging to predict the post-operative VFD in patients undergoing ATLR (Daga et al. 2011a, Daga et al. 2012). The results of a cohort of 20 patients using the multichannel registration are reported in more detail in Chapter 9.

The original processing time of the multichannel registration of over 20 minutes was reduced to 3 minutes when implemented on a GPU and applied to intraoperative datasets (Daga et al. 2011b, Daga et al. 2012). This formulation was used for the work described in Chapter 10.

6.6.4 Gradient Non-Linearity Correction

The spherical harmonic coefficients describing the gradient non-linearity were obtained from the scanner manufacturers for both the GE Signa HDx scanner (pre- and postoperative imaging) and the Siemens Espree scanner (intraoperative imaging) (Janke et al. 2004). Custom-written software was used to calculate the necessary deformation field necessary to correct for gradient non-linearity artefacts.

For data acquired on the GE scanner, two-dimensional in-plane correction was performed on the scanner so only the deformation in the third dimension was computed (for the coronally acquired T1-weighted acquisition, this was anterior-posterior; for the axially acquired diffusion data, this was superior-inferior). Data from the Siemens scanner was available both without any correction and with on-scanner three-dimensional correction (DIS3D). Anatomical data already been corrected on the scanner were used, but the diffusion data were corrected offline so that the correction could be combined with the susceptibility artefact correction.

6.6.5 Magnetic Susceptibility Artefact Correction

By acquiring two images at different echo times, the phase difference can be determined and used to estimate the field map (Jezzard & Balaban 1995). Since the phase images are only uniquely defined in the range $(-\pi, \pi]$, they must be unwrapped in each voxel to determine the true phase by the addition of an unknown integer multiple of 2π :

$$\phi_t(i) = \phi_w(i) + 2\pi n_i$$

where $\phi_t(i)$ is the true phase at voxel i , $\phi_w(i)$ is the wrapped phase and n_i is the multiple to be estimated.

Using custom-written software, the n_i were estimated for the phase difference map to give an unwrapped phase difference map. The phase was modelled as a Markov Random Field and the most likely phase wraps were determined using a discrete optimisation algorithm based on graph cuts (Daga et al. 2013). The subsequent image registration step described in this paper was not used. The unwrapped phase difference map was then scaled by the echo time difference to generate a voxel displacement map that was converted to a deformation field:

$$Displacement = \frac{Phase\ difference \times Read - out\ time}{2\pi \times Echo\ time\ difference}$$

When correcting diffusion data, the deformations for the gradient non-linearity correction and the susceptibility correction were composed and applied in a single step to ensure that the images were not over-smoothed.

6.7 Conclusions

A large cohort of patients with medically refractory TLE was studied longitudinally with imaging (structural MRI, functional MRI, DTI), neuropsychology and visual fields before, 3-4 months and 12 months after surgery. A group of healthy controls were studied at similar timepoints. The following chapters describe the studies performed with this data.

7 DIFFUSION TENSOR IMAGING TRACTOGRAPHY TO VISUALISE THE RELATIONSHIP OF THE OPTIC RADIATION TO EPILEPTOGENIC LESIONS PRIOR TO NEUROSURGERY

7.1 Introduction

Around 30% of patients with focal epilepsies fail to respond to drug therapy and should be considered for surgical treatment. The majority of these patients have seizures arising from the anteromedial temporal lobe, for which ATLR is a well established and effective treatment (Wiebe et al. 2001). The remainder with neocortical epilepsy are most commonly treated by cortical resection (Roper, 2009), particularly if a focal lesion is demonstrated on neuroimaging and confirmed to be the epileptogenic focus.

The anatomy of the optic radiation has been reviewed in Section 4.3, and Meyer's loop is particularly susceptible to damage during ATLR. However the optic radiation has a long course passing from the lateral geniculate nucleus (LGN) through both the temporal and parietal lobes to the primary visual cortex in the occipital cortex. The optic radiation is therefore vulnerable at other points on its course when a neocortical resection is considered.

This chapter assesses the utility of preoperative tractography in patients with lesions lying near the presumed course of the optic radiation. Particular reference is made to optimising the technique, consideration of the risk of surgery, visualisation aiding surgical planning and the validation of results. The next chapter looks further at the role of different tractography methods in surgical planning and visualisation for surgery is developed further in Chapter 9 and 10.

7.2 Methods

7.2.1 Subjects

Ten patients (mean age 27.3 years, range 17-40 years, 3 males) with medically refractory epilepsy undergoing presurgical evaluation were assessed. All patients had structural MRI scans performed at 3T demonstrating lesions lying near the presumed course of the optic radiation. None of the patients had previously used vigabatrin. The most common diagnosis was dysembryoplastic neuroepithelial tumour (DNET, n=3). One patient apiece had focal cortical dysplasia (FCD), an epidermoid tumour, damage to an infantile head injury, an infarct, a cavernoma, tuberous sclerosis and a previous otogenic temporal lobe abscess. Seven of the patients subsequently underwent resective surgery. Patient demographics, clinical and imaging diagnoses and management plans are listed in Table 7.1. Outcomes are given according to the ILAE classification (Wieser et al. 2001).

No	Age/ Gender	Age of Onset	Imaging diagnosis	Location of optic radiation	Visual fields	Management plan (ILAE outcome) ICR = intracranial recordings
1	25/F	11y	Left parietal FCD	Just inferomedial to lesion	Normal (pre-/post-op)	ICR then resection – FCD IIb (class 1)
2	26/F	11y	Right inferior parietal DNET	Inferomedial to lesion, in close proximity	Normal (pre-/post-op)	Resection – DNET (class 1)
3	26/F	9y	Tuberous sclerosis, right parietal tuber	Well inferomedial to presumptive epileptogenic tuber	L hemianopia (post-op)	ICR, chose an extensive resection (class 1)
4	30/F	15y	Left otogenic temporal abscess	Meyer's loop confluent with abnormality	L sup quadrantanopia (post-op)	ICR then resection – HS (class 1)
5	17/F	11y	Right fusiform gyrus DNET	Superior to and separate to lesion	R sup quadrantanopia (post-op)	ATLR – DNET (class 1)
6	26/F	12y	Left parieto-occipital damage	Just inferior to and involving area of damage	Normal (pre-op)	Declined surgery (low chance of success and risk to vision)
7	39/M	5y	Right occipito-temporal damage	Passes directly through area of damage	Normal (pre-op)	Surgery not advised (extensive lesion, risk to vision)
8	40/M	7y	Left inferior occipital DNET	Most inferior part leads directly to lesion	Paracentral scotoma (pre-op)	Declined surgery (risk of VFD, has scotoma)
9	18/F	17y	Left frontotemporal epidermoid	Meyer's loop closely approaches posterior of lesion	Normal (pre-op), minor R sup quadrantanopia (post-op)	Advised further medication trials (risk to vision); eventually had surgery - epidermoid (class 1)
10	26/M	22y	Left temporal cavernoma	Displaced over superomedial aspect of cavernoma	Normal (pre-op), resolving R sup quadrantanopia (post-op)	Advised further medication trials (risk to vision); eventually had surgery - cavernoma (class 3)

Table 7.1 - Clinical and demographic characteristics of patients, management and visual outcomes

7.2.2 Tractography

Structural and DTI images were obtained and preprocessed as described in Chapter 6. As the previously described tractography method (Section 6.5.3.2.3) uses a single seed in Meyer's loop, this only depicts the inferior part of the optic radiation (conveying the upper visual quadrant) and gives a better depiction of the more anterior part of the optic radiation (see Chapter 8 for a comparison of tractography methods). For lesions located more posteriorly in the parietal lobe, it is important to also include the more superior part of the optic radiation (conveying the inferior visual quadrant) that runs directly posteriorly from the LGN.

Two adaptations were therefore made to the standard method. Firstly, two seeds were defined with the first seed in Meyer's loop as previously described (Figure 7.1a-c) and a second seed point in the LGN on two axial slices (Figure 7.1d) with a standardised volume of 18 voxels (152 mm^3 , $3 \times 3 \times 2$ voxels). Data from these two seed regions were amalgamated to visualise the entire optic radiation.

Secondly, two way points were defined. The first was in the lateral wall of the occipital horn of the lateral ventricle at the posterior extent of the corpus callosum as previously described (Figure 7.1e) and the second was in the primary visual cortex in a sagittal plane 8 voxels lateral to the midline (Figure 7.1f). This ensured that the more posterior portions of the tracts passing into the occipital cortex were delineated.

Connectivity maps were generated separately for the two seed regions in each hemisphere as described in Chapter 6 and combined into a single connectivity map by taking the maximum from the two connectivity maps on a voxelwise basis.

7.2.3 Coregistration and Display of Tractography Data

For each patient, a 12 degrees of freedom affine transform from diffusion space to anatomical space (either T1 or FLAIR) was calculated using FLIRT, the linear image registration tool in FSL. The first $b=0$ image to which all other diffusion volumes were registered was used as the source image with a normalised mutual information cost function to account for the differing image contrasts. These transformations were applied to the connectivity maps generated from the tractography and the result was overlaid on the anatomical images using the image viewing tool in FSL.

In order to display preoperative tractography data on postoperative data, an initial affine registration between the pre and post-operative anatomical images using FLIRT was followed by a non-linear Fast Free-Form Deformation using the NiftyReg toolkit (<http://sourceforge.net/projects/niftyreg/>) (Modat et al. 2010). This accounts for the brain shift and deformation occurring as a consequence of surgery and is the software tool that was further developed and evaluated for use with intraoperative MRI (Chapter 10).

7.2.4 Visual Fields

Pre- and post-operative visual fields were assessed by Goldmann perimetry as described in Chapter 6.

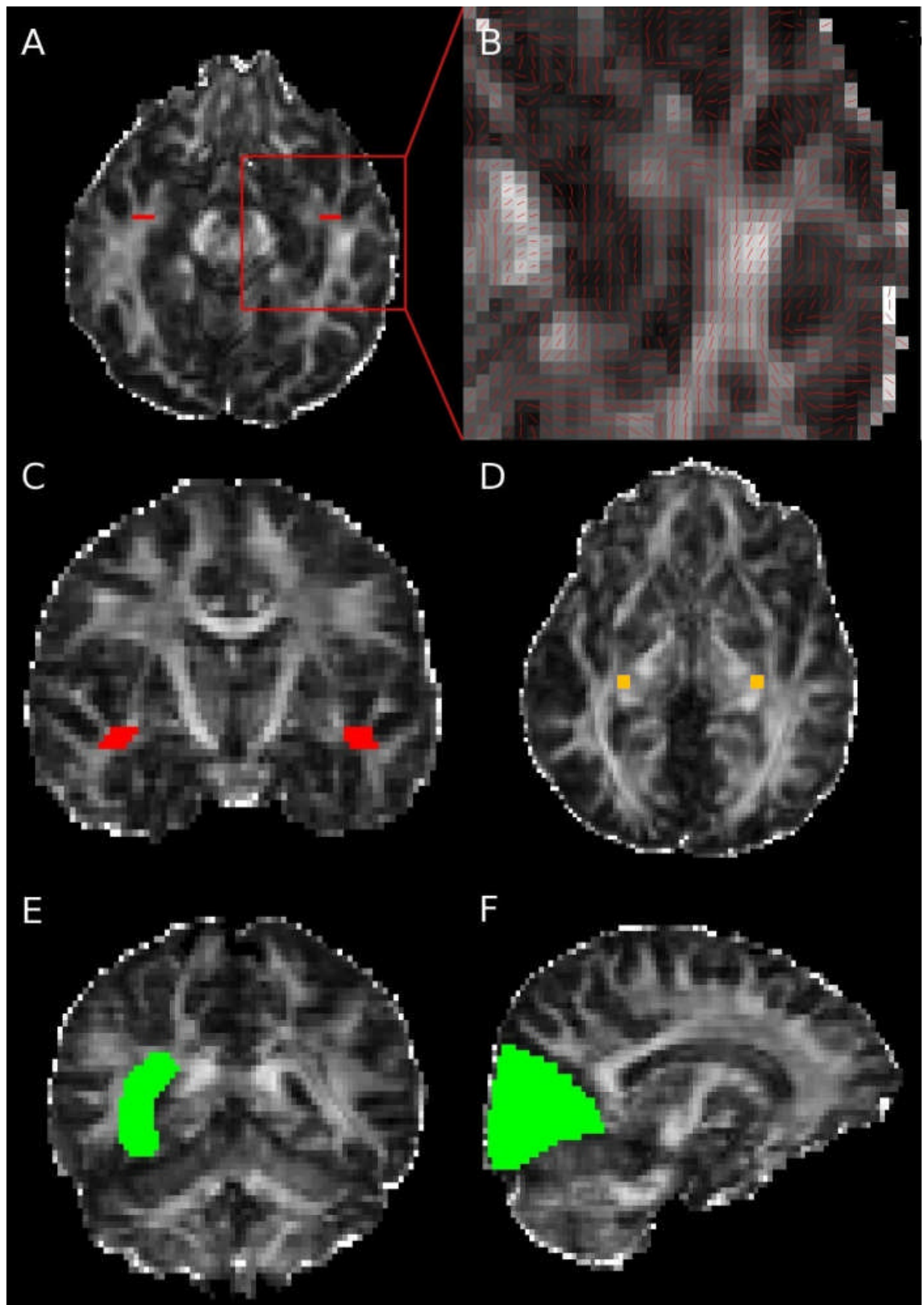


Figure 7.1 - Seed and way points for optic radiation tractography

Seed points were defined across Meyer's loop, red (A – axial slice, B – close up of axial slice with principle diffusion directions showing the high curvature of the loop, C – coronal slice) and in the LGN, orange (D). Way points, green, were defined in the stratum sagittale (lateral wall of the lateral ventricle) (E) and the primary visual cortex (F). Shown on the FA map.

7.3 Results

For each patient, the optic radiations were successfully delineated and the relationship to lesions demonstrated (Table 7.1).

7.3.1 Validation of tractography with post-operative outcome

Tractography may assist surgical planning by suggesting the optimum approach to a lesion and indicating the proximity of the lesion to the optic radiation. In patient 1, preoperative tractography identified the optic radiation passing just inferomedial to the left parietal FCD (Figure 7.2A-C). This was resected approaching from the superior aspect via an awake craniotomy to preserve language function. Only a single provoked seizure occurred in the 2 years following surgery and no visual field deficit (VFD) resulted. The area of resection approached but did not involve the optic radiation (Figure 7.2D).

In patient 2, tractography suggested that the right inferior parietal DNET should be approached superolaterally as the most superior portion of the optic radiation lay just deep to it (Figure 7.3A-C). Such an approach rendered the patient seizure free and without a VFD, consistent with postoperative imaging (Figure 7.3A-D).

Tractography can also assist in advising the patient about the risks to vision from surgery. In patient 3, a presumptive epileptogenic tuber well separate to the optic radiation was identified in the right parietal lobe on MRI, magnetoencephalography (MEG) and EEG (Figure 7.4A). Intracranial recordings however demonstrated rapid spread more posteriorly. The choice between a more conservative resection (low risk to vision) versus an extensive resection (certain hemianopia, but greater chance of seizure freedom) was discussed and the patient opted for the latter. She became seizure free but with a complete hemianopia (Figure 7.4B-D).

Patient 4 developed epilepsy at the age of 15 secondary to an otogenic left temporal lobe abscess. MRI revealed left hippocampal sclerosis (HS) and an extensive area of abnormality in the left temporal lobe, extending anteriorly to the level of the amygdala, and with the posterior extent well behind the fourth ventricle. Tractography demonstrated Meyer's loop abutting the area of abnormality (Figure 7.5), so the patient was advised about the high risk of a visual deficit. Intracranial EEG recordings confirmed seizure onset in the hippocampus, and the patient underwent a left anterior temporal lobe resection including the hippocampus and the majority of the area of damage. She is seizure free at 8 months, and has a right superior quadrantanopia.

Patient 5 had a right fusiform gyrus DNET distinct from the optic radiation (Figure 7.6A) but elected for a standard anterior temporal lobe resection to give the greatest chance of seizure freedom. This was achieved but caused a left superior quadrantanopia. Post-operative imaging shows that the resection included a small part of Meyer's loop (Figure 7.6B).

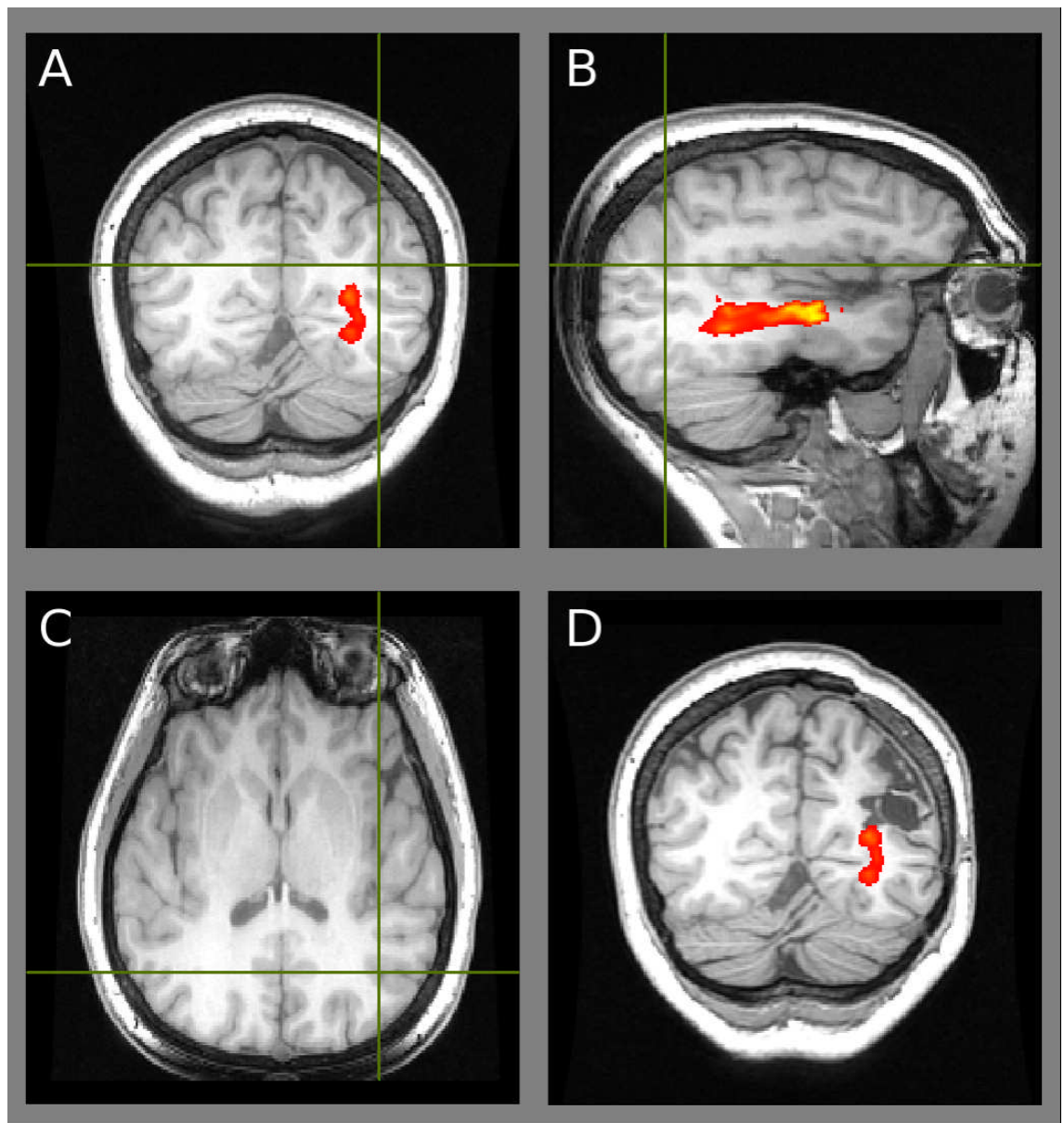


Figure 7.2 - Patient 1 with left parietal FCD

Preoperative tractography (A-C) showing the optic radiation passing inferomedial to FCD (crosshair) on a T1-weighted image. Postoperative T1-weighted image with overlaid preoperative tractography (D) showing no damage. Visual fields were normal.

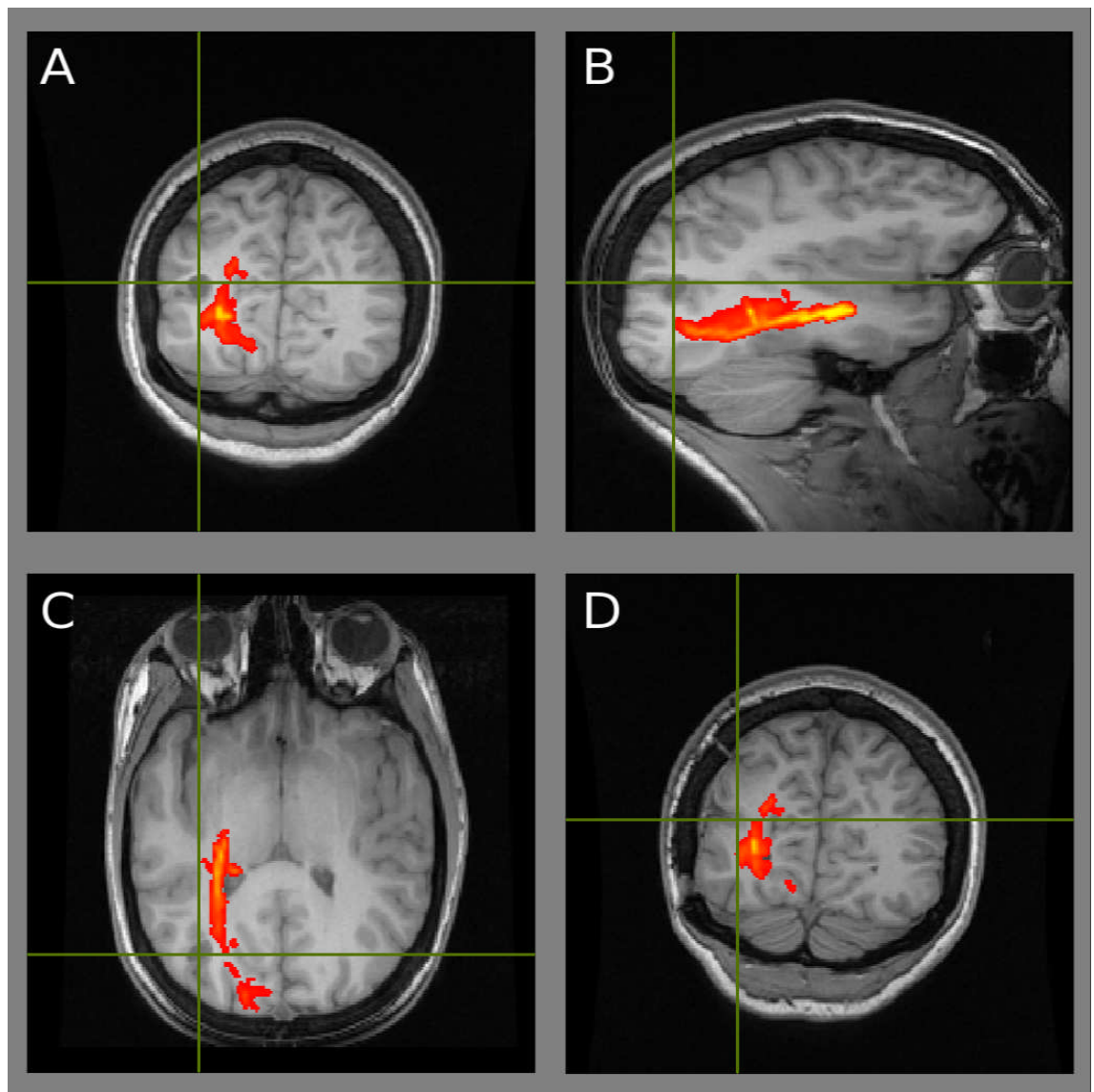


Figure 7.3 - Patient 2 with right inferior parietal DNET

Preoperative tractography (A-C) showing the optic radiation just inferomedial to the DNET (crosshair) on a T1-weighted volumetric image. Postoperative T1-weighted image with overlaid preoperative tractography (D) showing no damage. Visual fields were normal.

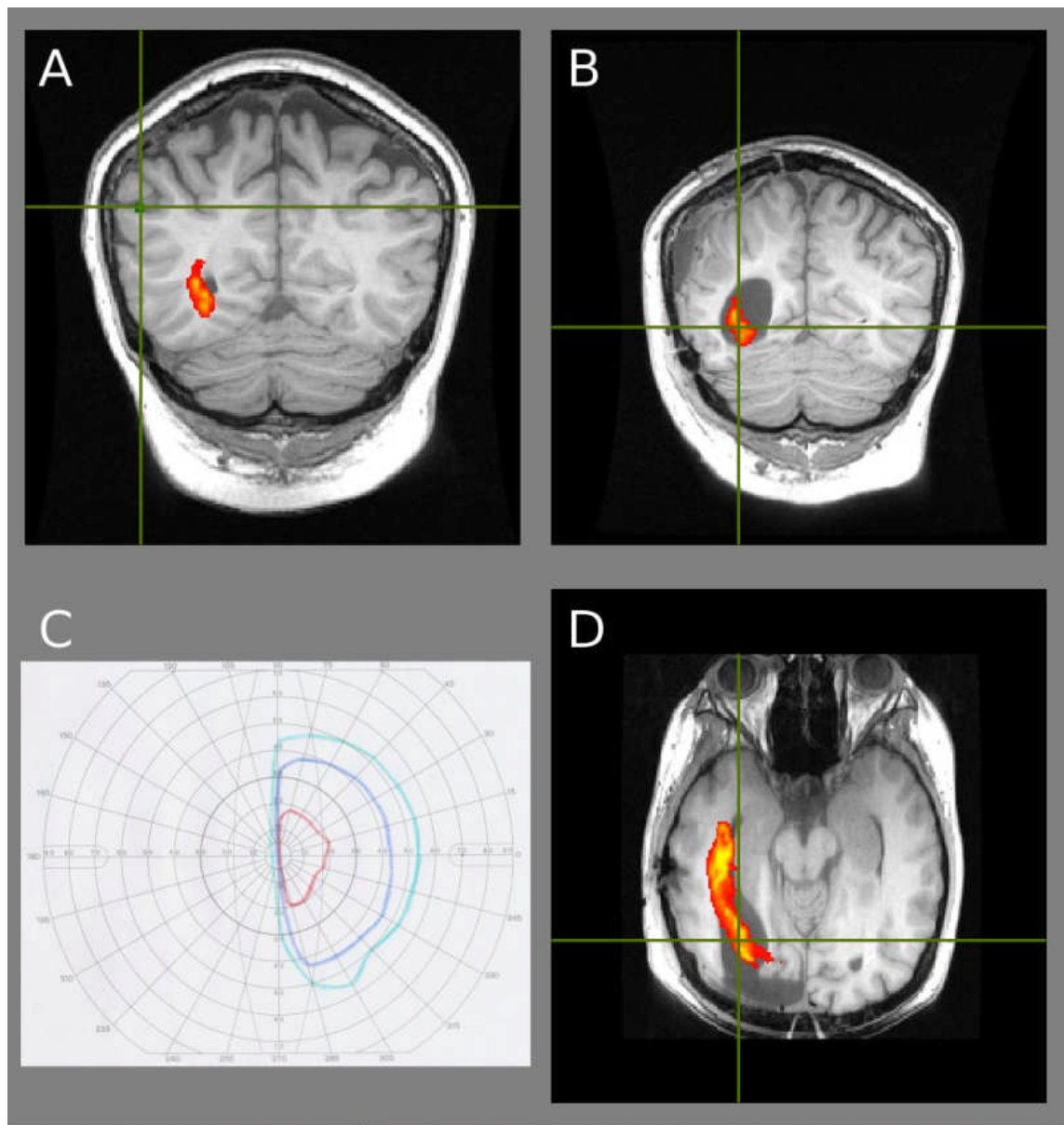


Figure 7.4 - Patient 3 with tuberous sclerosis

Preoperative tractography (A) showing the optic radiation well separate from the presumptive epileptogenic tuber identified on MEG (crosshair/green). Postoperative imaging of the extensive resection to achieve seizure freedom (B, D) confirms the damage to the optic radiation resulting in a left hemianopia (C, left eye shown).

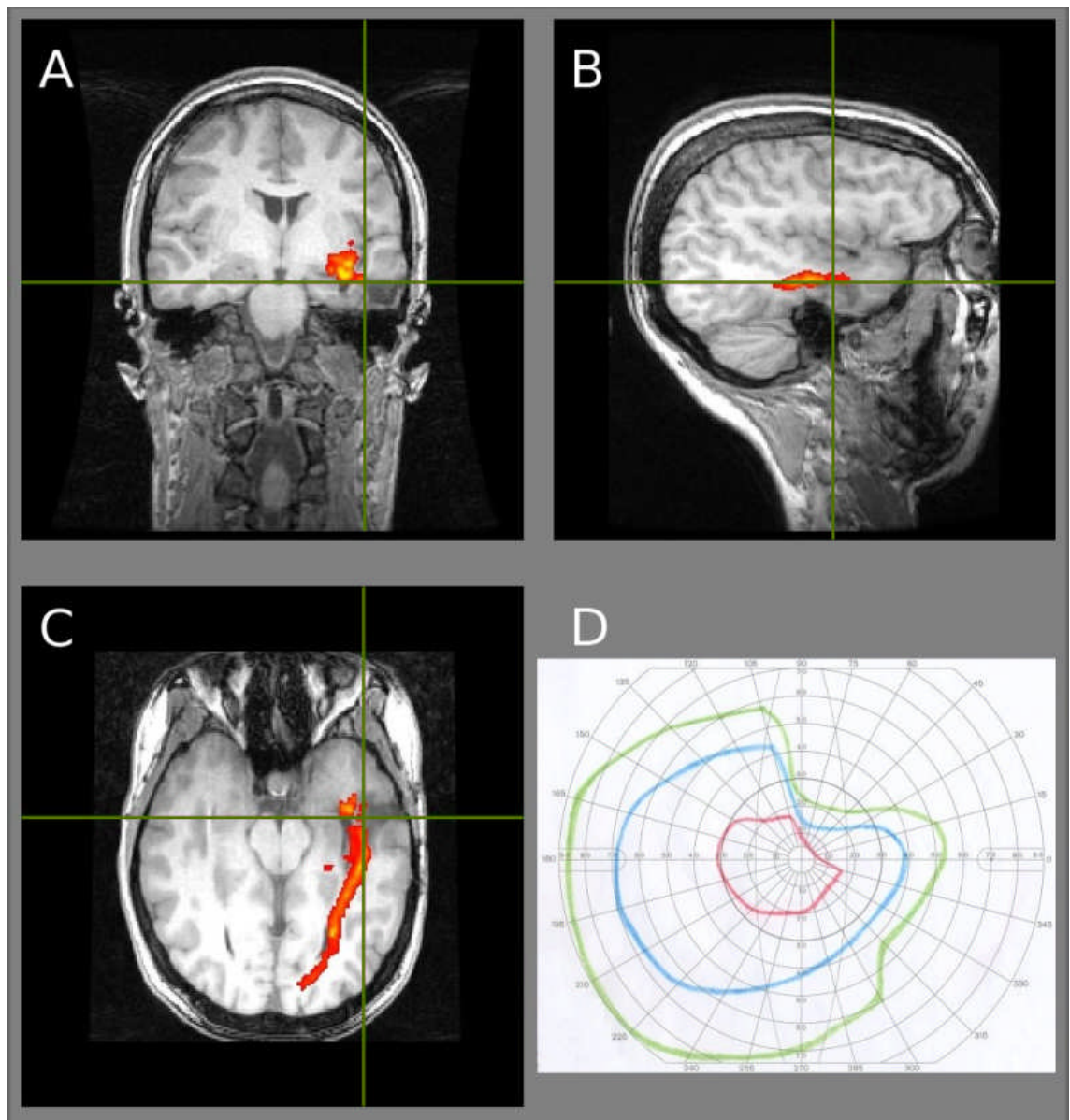


Figure 7.5 - Patient 4 with otogenic left temporal lobe abscess

Preoperative imaging showed the optic radiation was involved by the abscess (A-C), so surgery resulted in a partial right superior quadrantanopia (D).

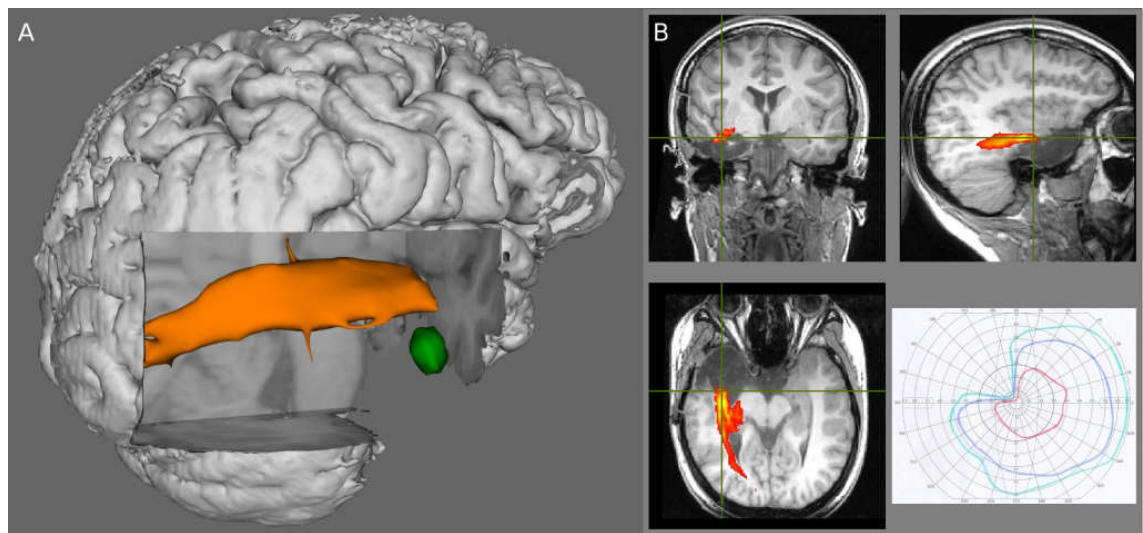


Figure 7.6 - Patient 5 with left fusiform gyrus DNET

3D rendering of preoperative tractography (A) showing DNET (green) separate from the optic radiation (orange). The patient elected for a standard ATLR resulting in a left superior quadrantanopia (B). The postoperative T1-weighted image with the overlaid preoperative tractography confirmed involvement of the optic radiation (B).

7.3.2 Tractography assists the decision not to proceed to surgery

In patient 6, imaging revealed extensive left parieto-occipital damage from an infantile head injury and visual fields were normal. As anatomical imaging suggested that the optic radiation may be at risk, tractography was performed confirming that the optic radiation was confluent with the area of damage, so surgical resection would cause a visual deficit (Figure 7.7A). The patient declined to pursue surgery due to the low odds of seizure freedom coupled with a postoperative VFD.

In patient 7, the optic radiation was shown to pass directly through the area of right occipito-temporal damage from an infarction (Figure 7.7B). Surgery was not pursued as the lesion was so extensive that the required surgery would cause too great a neurological deficit. Similarly, patient 8 with a left inferior occipital DNET had a pre-existing paracentral scotoma and tractography confirmed that the optic radiation passed directly towards the lesion. He declined further surgery as this would extend the visual deficit.

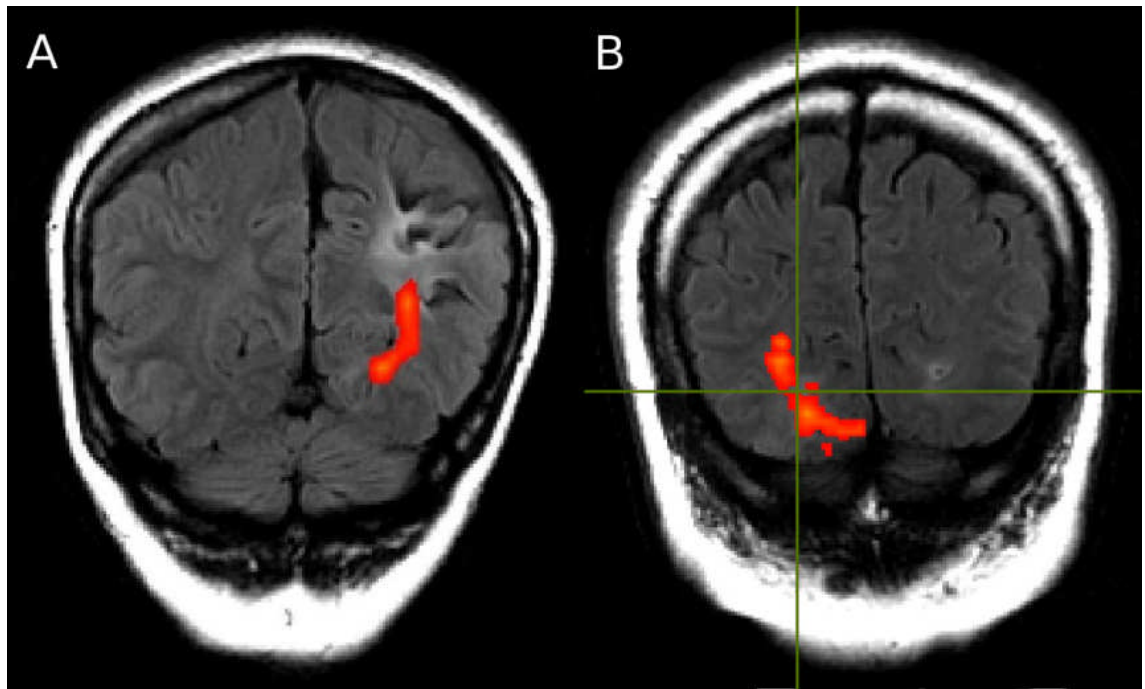


Figure 7.7 - Patients 6 and 7 with focal damage

T2 FLAIR image showing involvement of the optic radiation by the area of damage in patient 6 (A). Surgery was declined. T2 FLAIR image showing optic radiation passing directly through the area of damage from an infarct (crosshair) in patient 7 (B). Surgery was not pursued.

7.3.3 Tractography leads to a decision to defer surgery for now

Tractography can help inform the decision whether to pursue further medication trials or surgery depending upon the risk to vision. Patient 9, in whom MRI imaging demonstrated a large frontotemporal epidermoid tumour was advised that Meyer's loop would be at risk during a resection since this has been shown to be very close to the tumour (Figure 7.8). Although presumably an extrinsic tumour, surgical access would involve passing through or damage to neocortex. As she had only tried lamotrigine and levetiracetam, serial imaging and further medications trials were planned prior to considering surgery. However with further follow-up, eventually she became defined as refractory so underwent surgery rendering her seizure free but with a minor visual field deficit.

Patient 10 had a 4-year history of complex partial seizures which were previously controlled, but recurred with a bleed from a left temporal cavernoma. The optic radiation has been displaced superiorly over the cavernoma. The visual fields are normal and they would be at high risk in any operation (Figure 7.9). The patient was keen to pursue surgery, but in view of the imaging findings has been advised to consider further medication trials first. With further follow-up, he did undergo surgery at his insistence and in view of the risk of further bleeds but developed a partial superior quadrantanopia which resolved gradually in the months following surgery to a minor permanent deficit.

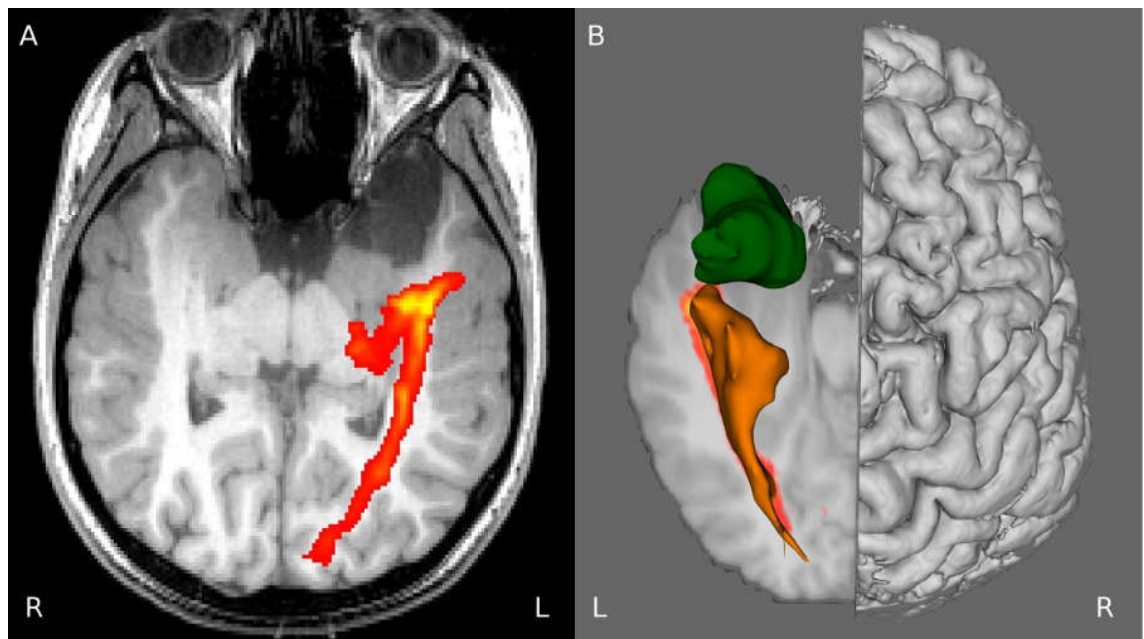


Figure 7.8 - Patient 9 with epidermoid tumour

Axial T1-weighted image showing the close approach of Meyer's loop to the epidermoid tumour (A). This is better appreciated in a 3D rendering (B).

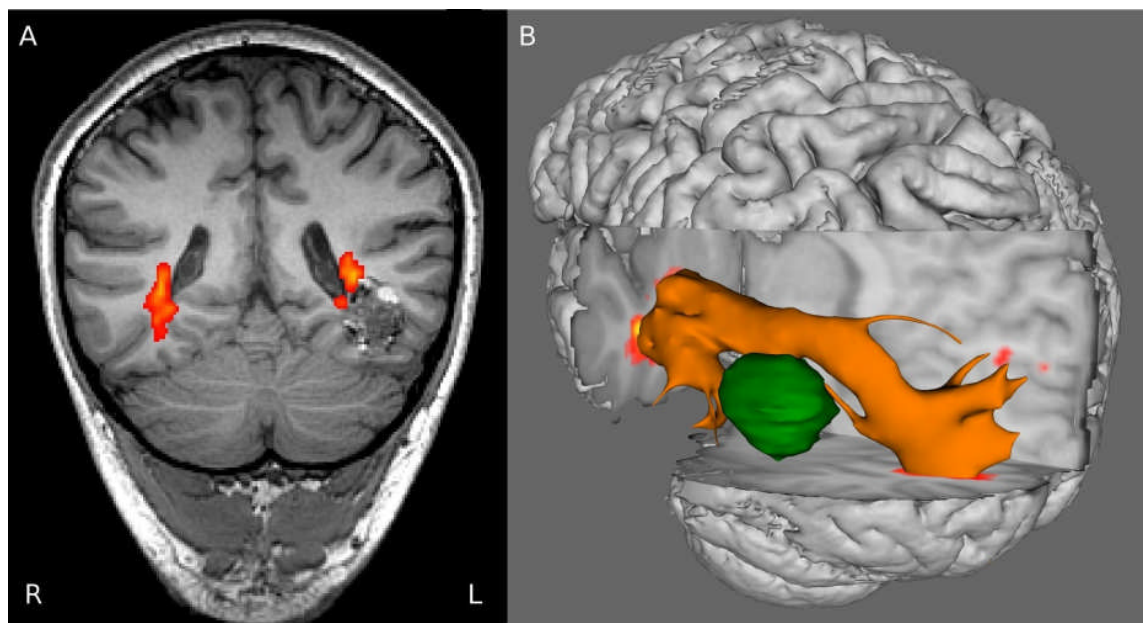


Figure 7.9 - Patient 10 with left temporal lobe cavernoma

Coronal FLAIR image showing optic radiation passing superomedial over cavernoma (A). 3D rendering viewed from the left clearly shows the displacement of the tract by the cavernoma (B).

7.4 Discussion

In this chapter, I have validated tractography of the optic radiation by comparison of data with post-operative visual fields and demonstrated how the results of this method may inform surgical decisions. Epilepsy surgery is potentially curative but damage to white matter tracts can cause serious morbidity. Imaging serves a central role in the workup for epilepsy surgery, both in the identification of the seizure onset zone (structural MRI, PET, ictal SPECT) and of eloquent areas (functional MRI, DTI tractography) (Duncan 2010).

Delineation of the optic radiation is important for several reasons. Firstly, there is great anatomical variability in the location of the optic radiation even in healthy subjects, and it may be displaced by pathology. In a post-mortem dissection study involving 25 subjects, the distance from the temporal pole to Meyer's loop varied from 22-37mm, whilst the breadth of the optic radiation at the posterior limit of the posterior horn of the lateral ventricles varied from 18-32mm (Ebeling & Reulen 1988). Further studies have been summarised in Section 4.5.

Secondly, the most common concern identified by patients with moderately severe epilepsy is driving (Gilliam et al. 1997). A severe VFD can be very disabling, but even a mild VFD may preclude a seizure-free patient from holding a driving licence. The assessment of and visual requirements for driving have been stated in Section 4.4.8.

Thirdly, the optic radiation often lies close to the epileptogenic zone. The most common surgical procedure for epilepsy, ATLR, risks damaging Meyer's loop of the optic radiation and work thus far has concentrated on this population. The size of resection and the distance from the tip of Meyer's loop to the temporal pole as shown on DTI is predictive of the postoperative VFD (Yogarajah et al. 2009). Surgery for patients with more posterior lesions is performed less frequently, presurgical evaluation may be more complex and surgery may result in a VFD involving the inferior field, which is more disabling than deficits involving the superior field.

Numerous methods have been published for the identification of the optic radiation. The majority rely on deterministic tractography algorithms which are prone to errors in regions of crossing fibres and noise. Probabilistic tractography algorithms, which model the noise inherent in diffusion data and voxels with crossing fibres are more resistant to such problems and can better delineate complex structures such as the tightly curving fibres of Meyer's loop (Nilsson et al., 2010, Section 4.6.1). The technique described herein is based on a previously published method designed to reliably identify Meyer's loop in patients undergoing ATLR (Yogarajah et al. 2009). However as Meyer's loop only represents the superior part of the visual fields, it is important also to delineate fibres running directly posteriorly from the LGN. The inclusion of a second seed located in the LGN and the combination of the tractography data from the two seed regions by taking the maximum observed connection probability on a voxelwise basis allows a robust delineation of the entire optic radiation. The importance of the choice of seed regions and waypoints is addressed further in Chapter 8.

The visualisation of the optic radiation on anatomical images and in 3D renderings with which the surgeon can interact allows a much better appreciation of the data and the relationship between structures. This can assist all stages of the surgical decision-making process. Patients may be better informed about the risk of a VFD than when relying on anatomical imaging alone. This can help the decision whether to pursue surgery and guide the procedure in those patients choosing to have an operation. A study of the utility of preoperative tractography in brain tumour resection showed that by providing information on the location of the corticospinal tract, optic radiation and arcuate fasciculus, the surgical approach and/or resection margins were altered in 18 out of 28 patients (Romano et al. 2009). In the present series, this was particularly true of patients 1 and 2.

As tractography is a relatively recent technique, further validation is necessary. The type of patient described in this series is uncommon and although this is the largest such series reported to date, only limited post-operative data were available. The probabilistic tractography technique used is less likely to underestimate the size of the tract in comparison to the more common deterministic tractography, and it may still be necessary to add a further safety zone to allow for the limitations of tractography and a surgical margin of error. Such an allowance would also allow for the distortions introduced by the EPI sequence used for diffusion data, although this is less of an issue for lesions that are not at the temporal pole. In Chapter 9, I further address the accuracy of probabilistic tractography by looking at how the data can explain the variance in the postoperative VFD in patients undergoing ATLR.

It would also be beneficial to allow preoperatively acquired tractography data to be available to the surgeon in real-time during surgery. In Chapter 10, I describe the use of an intraoperative MRI suite and how modelling of the complex brain shift resulting from the craniotomy and surgical resection allows the location of the optic radiation to be superimposed on the intraoperative anatomical imaging and incorporated into the neuronavigation suite. The aim of this is to use tractography data prospectively to further reduce or avoid post-operative visual field deficits.

8 DIFFUSION TENSOR IMAGING TRACTOGRAPHY OF THE OPTIC RADIATION FOR EPILEPSY SURGICAL PLANNING: A COMPARISON OF TWO METHODS

8.1 Introduction

Whilst tractography algorithms can be applied to diffusion imaging to non-invasively map out white matter pathways (Mori & van Zijl 2002), it is a complex and time-consuming process with results that depend upon the method employed. For example, the standard approach that concentrates on Meyer's loop was adapted to encompass the entire optic radiation with a better delineation of the more posterior portions in Chapter 0. It is difficult to directly compare published methods as there are many differences in the patient population, scan acquisition (e.g. scanner manufacturer, field strength, voxel size, number of gradient directions, b-value) and analysis parameters (e.g. software product, type of tractography algorithm, seed region and waypoint location, stopping criteria). For example, the variability in seed regions and waypoint locations is illustrated in Table 4.4.

In this chapter, I assess two methods for delineating the optic radiation using the same datasets and controlling as many parameters as possible. The aim is to compare different tractography analysis methods to determine the level of agreement between them and to identify the method that more reliably identifies different components of the optic radiation for use in different types of epilepsy surgery.

The first method described in Chapter 6 was designed for planning ATLR and pays special attention to accurate identification of Meyer's loop. The results obtained correlate with effect of ATLR on visual fields and the method is reproducible. However, it is time consuming for the operator and since it concentrates on Meyer's loop, subjective experience suggests that it performs less well with more posterior parts of the optic radiation. It was necessary to adapt this method for the preceding chapter on neurosurgical planning.

The second method was designed to semi-automatically identify the location of the lateral geniculate nucleus (LGN) thus reducing operator time and to use this region to delineate the whole of the optic radiation. This method was developed by Jonathan Ashmore and Laura Mancini in the Academic Neuroradiology Unit of the UCL Institute of Neurology and the analyses in this chapter were performed in conjunction with them.

8.2 Methods

8.2.1 Subjects

6 healthy controls (age 25-53 years, 4 males) and 4 patients with medically refractory epilepsy (age 18-42 years, 2 males) undergoing presurgical evaluation at the National Hospital for Neurology and Neurosurgery, London, UK were studied. These patients were randomly selected from the longitudinal cohort. Patient demographics and imaging diagnoses are listed in Table 8.1.

Number	Age	Gender	Imaging diagnosis
1	28	F	Right inferior parietal DNET
2	27	M	Left temporal cavernoma
3	42	M	Left occipital DNET
4	18	F	Right fusiform gyrus DNET

Table 8.1 - Demographics and imaging diagnoses of patients

8.2.2 Tractography

Structural and DTI images were obtained and preprocessed as described in Chapter 6. For method 1, the tractography parameters, seed region, waypoint and exclusion masks specified in Chapter 6 were used (Figure 6.1).

For method 2, the same tractography parameters were used but with a different seed region, waypoint, endpoint and exclusion mask. An automated method was used to identify the location of the LGN. This method consisted of first initiating tracts (with 5000 iterations) separately from two seed regions. For the first seed region, the optic tract between the chiasm and the LGN was identified on an axial slice. A coronal slice intersecting the optic tract was chosen on which 8 voxels were selected in the region of the optic tract (Figure 8.1a, b). For the second seed region, the calcarine fissure was identified on a sagittal slice close to the midline. The most lateral slice on which the calcarine fissure was still visible was chosen on which a large area was identified including voxels above and below the calcarine fissure (Figure 8.1a, c). No endpoints were defined on the tractography initiated separately from these two seed regions.

The two tracts obtained from these two seed regions were then thresholded so that only connection probabilities higher than 0.2% were selected in order to eliminate some artefactual tracts whilst retaining fascicles reaching the LGN area posterolateral to the cerebral peduncle. The product of these two connectivity distributions gives a probability distribution for the location of the LGN with the maximum

voxel of the distribution representing the closest region to the LGN where both optic tract and optic radiation overlap.

A second step of the analysis involved selecting a rectangular seed region comprising 12 voxels on each of two consecutive coronal slices including the area close to the LGN location identified with the automated method described and extending inferiorly from this location, in regions of high fractional anisotropy (Figure 8.1d-f). The optic radiation was identified by seeding from this region using the same endpoint located above and below the calcarine fissure described above (Figure 8.1c). Exclusion masks were also applied to each hemisphere positioned at the posterior region of the trigone, in the midline encompassing both the thalamus and corpus callosum and on a coronal slice in the medial thalamus, to eliminate erroneous tracts (Figure 8.1g-j).

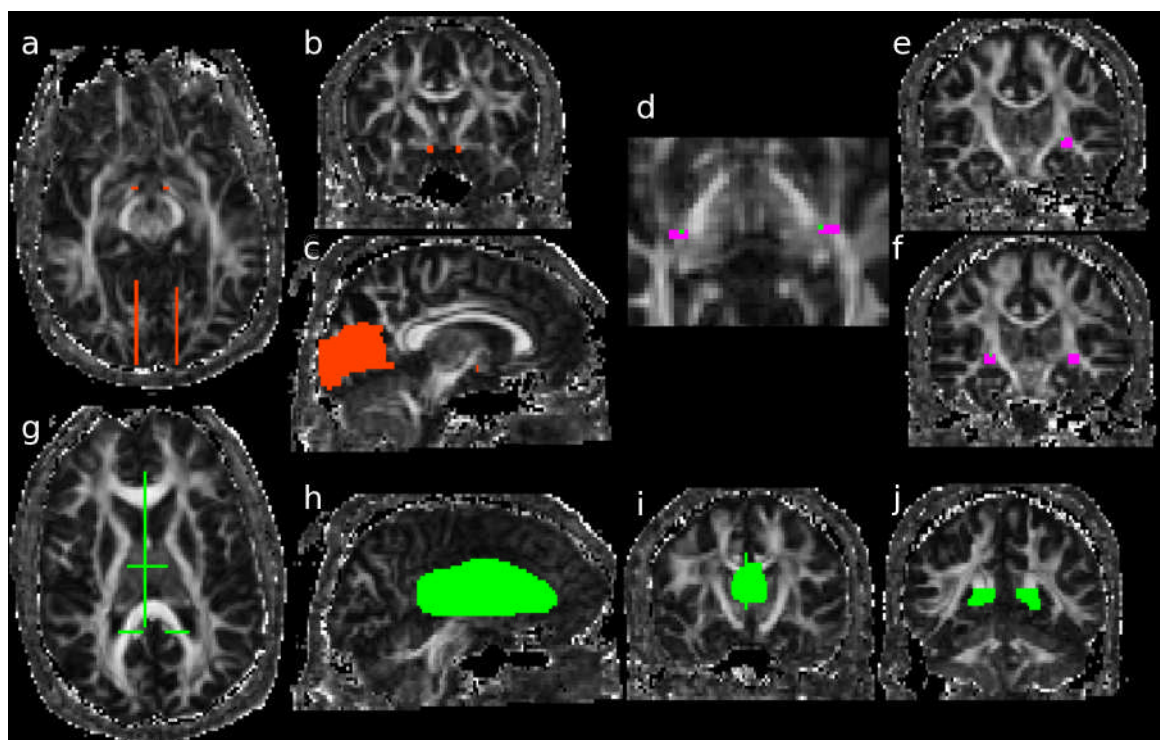


Figure 8.1 - Optic radiation tractography (method 2)

Seed regions in the optic tract (red) in the axial (a) and coronal planes (b). Large regions of interest (ROIs) including voxels above and below the calcarine fissure (red) lateral to the midline in the axial (a) and sagittal planes (c), used both as seed region for the identification of the LGN region and as an endpoint for the final identification of the optic radiation. Seed regions in the LGN region (pink) in axial (d) and coronal planes (e, f), with the voxel (green) closest to the LGN where the optic tract and optic radiation overlap. Exclusion masks (green) in the midline encompassing both the thalamus and corpus callosum (h), in the thalamus in a coronal plane (i), at the level of the trigone (j) and all three shown in the axial plane (g).

8.2.3 Volume of Optic Radiation and Degree of Overlap

For each of the 20 hemispheres, the number of voxels in the tract (thresholded at 0.05) was calculated for the two methods individually, along with the number of voxels common to both methods. The Dice Similarity Score quantified the degree of overlap giving a figure between 0 (no overlap) to 1 (complete overlap):

$$\text{Dice similarity score} = \frac{2 \times [\text{number of voxels common to both methods}]}{[\text{number of voxels (method 1)} + \text{number of voxels (method 2)}]}$$

8.2.4 Measurements of Meyer's Loop

The location of the temporal pole was identified in each hemisphere using the fractional anisotropy image (FA). The anterior extent of Meyer's loop from the tractography was then located to calculate the antero-posterior distance between the temporal pole and Meyer's loop (TP-ML distance) in voxels. These measurements were performed for each of the two methods. As the reproducibility of method 2 for identification of the TP-ML distance has not been previously assessed, the test-retest and inter-rater reliability of this distance was assessed using the intraclass correlation coefficient in SPSS Statistics 17.0 (SPSS Inc, Chicago, USA). The two raters were myself and Laura Mancini.

8.3 Results

8.3.1 Visual Comparison

Visual comparison of the results showed that the core of the delineated tract was common between the two methods both in healthy controls (Figure 8.2) and patients with epilepsy (Figure 8.3 and Figure 8.4). Method 1, which was designed to depict Meyer's loop, gave a much clearer visualisation of this structure and it was easier to perform measurements using this method. The frontal exclusion mask ensured fewer false tracts in the temporal pole and towards the anterior commissure (Figure 8.2), which were commonly seen using method 2, but it could not always eliminate the spurious tracts present in the insula (Figure 8.4).

Method 2 however gave a better depiction of the optic radiation as it reached the visual cortex, with the paths from method 1 tending to thin out more posteriorly. In addition, method 2 tended to delineate the optic radiation more superiorly than method 1 which is important when considering the relationship between the optic radiation and lesions such as the inferior parietal DNET in Patient 1 (Figure 8.3). It was for this reason that Method 1 was adapted in Chapter 7. Finally, method 2 failed to correctly delineate the portion of the optic radiation anterior to the large cavernoma in patient 2 (Figure 8.4).

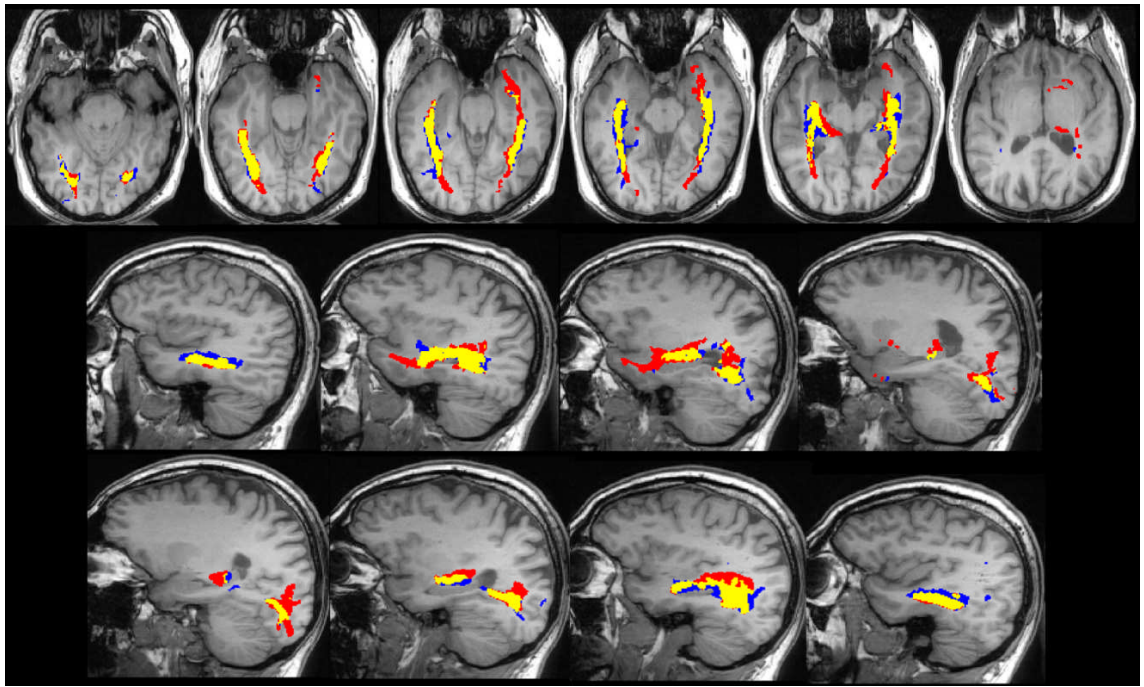


Figure 8.2 - Comparison of methods in a control subject

Optic radiation identified by method 1 only (blue), method 2 only (red) and both methods (yellow) overlaid on the T1-weighted image. The images are shown in radiological convention with axial slices from inferior to superior and sagittal slices from left to right.

8.3.2 Volume of Optic Radiation and Degree of Overlap

In controls, the average volume of the optic radiation was the same using both methods (Table 8.2). However, in patients there was a trend to lower tract volumes using method 2 (two-tailed paired t-test $p=0.07$) particularly in patient 2 ipsilateral to the lesion where the tractography failed.

The Dice Similarity Score revealed overlap varied between 0.160 and 0.612 (mean 0.400, standard deviation 0.132). Overlap was lower in the patients with epilepsy than in healthy controls (0.318 vs. 0.456, two-tailed t-test $p=0.018$). There was no significant change when the false tracts obtained in method 2 were masked out using the same frontal exclusion mask as in method 1.

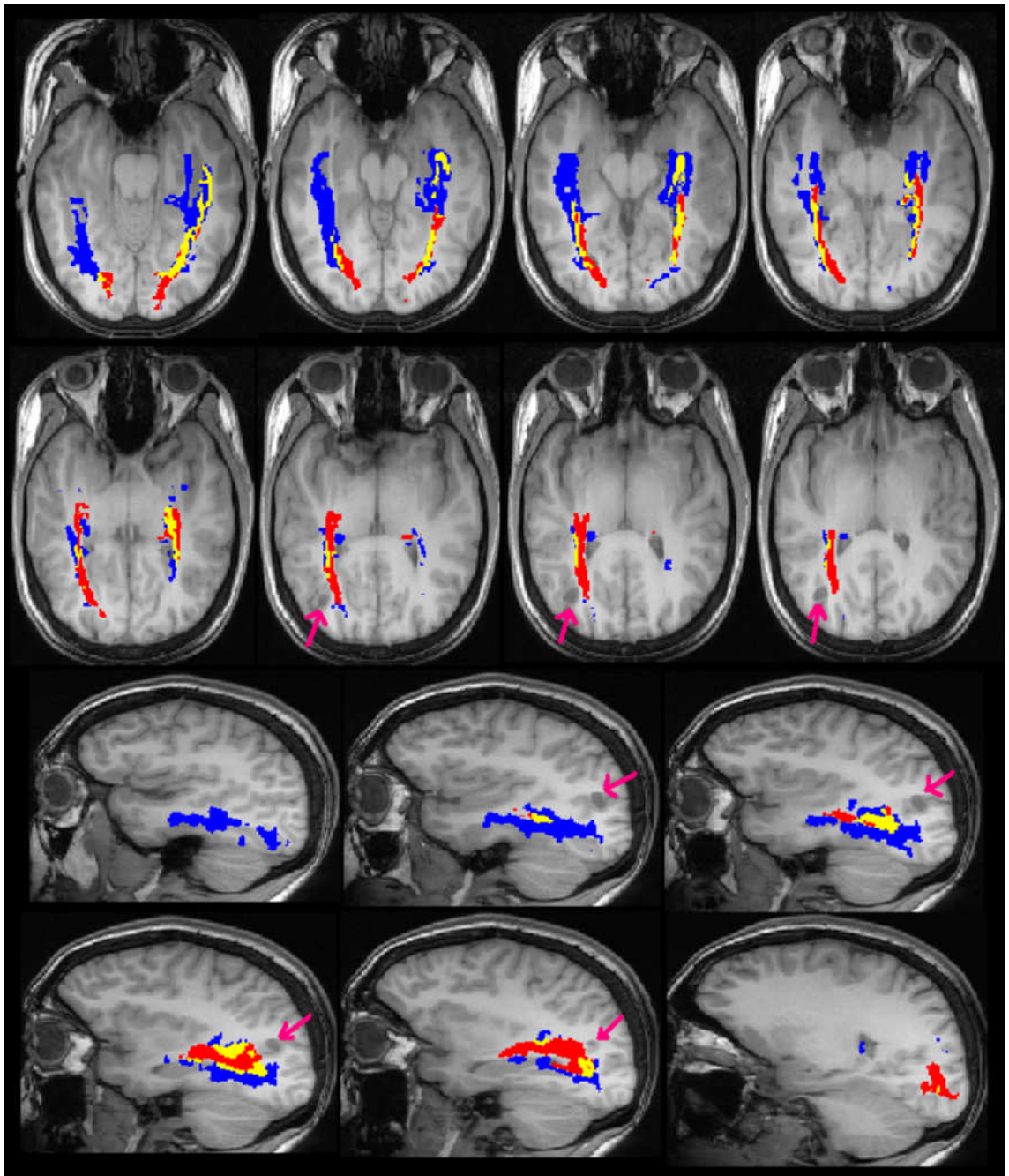


Figure 8.3 - Comparison of methods in patient 1 (right inferior parietal DNET)

Optic radiation identified in patient 1 by method 1 only (blue), method 2 only (red) and both methods (yellow) overlaid on the T1-weighted image. The arrows indicate the DNET. Image conventions as Figure 8.2.

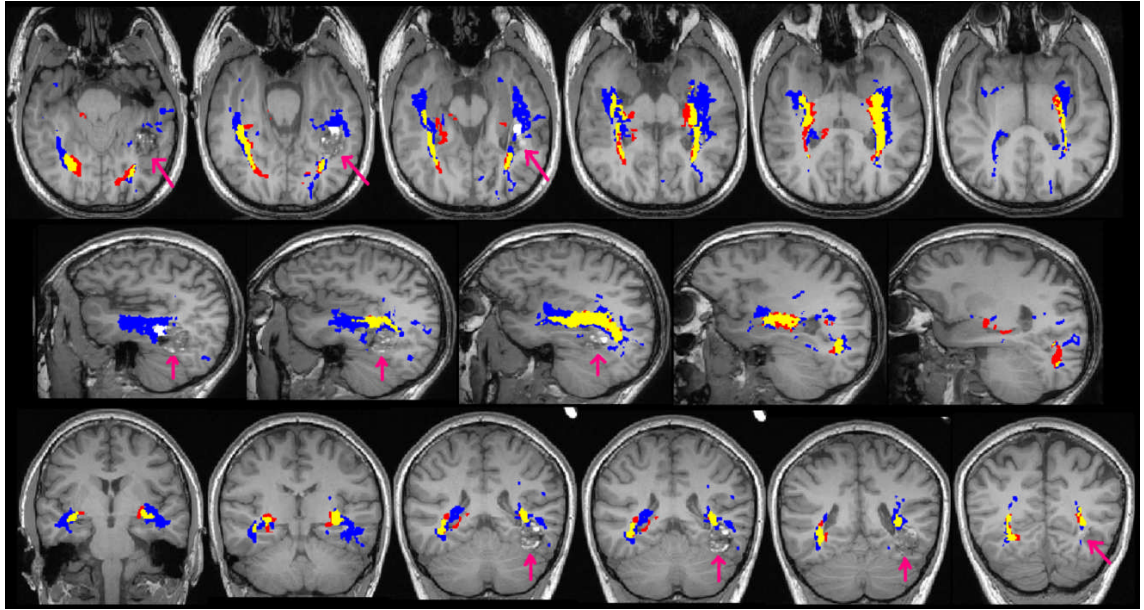


Figure 8.4 - Comparison of methods in patient 2 (left temporal cavernoma)

Optic radiation identified in patient 2 by method 1 only (blue), method 2 only (red) and both methods (yellow) overlaid on the T1-weighted image. The arrows indicate the cavernoma. Image conventions as Figure 8.2, with the coronal images being from anterior to posterior.

	Controls		Patients	
	Method 1	Method 2	Method 1	Method 2
Mean tract volume (voxels)	1455 (220)	1429 (415)	1423 (340)	1003 (263)
ML-TP distance in voxels (mean)	15-18 (16.6)	11-19 (16.9)	14-19 (16.3)	17-26 (18.5)
ML-TP distance in mm (mean)	28-34 (31)	21-36 (32)	26-36 (31)	32-49 (35)
Mean Dice Similarity Score (sd)	0.456 (0.114)		0.318 (0.118)	

Table 8.2 - Comparison of measurements from the two tractography methods

Mean tract volume and ML-TP distance in the different groups (controls, patients) using the two methods. The Dice Similarity Scores for controls and patients are also shown.

8.3.3 Measurements of Meyer's Loop

Method 1 was successful in all subjects whilst method 2 failed to identify Meyer's loop on the side of pathology in patient 2. There was no significant difference between the mean ML-TP distance in either controls or patients (Table 8.2), although there was a trend towards a greater distance in patients (paired t-test, $p=0.148$). For method 2, the intra-rater intraclass correlation coefficient was 0.826 with better agreement in controls than patients (0.898 versus 0.451). The measurements were identical in 13 hemispheres whilst in the other 6 hemispheres, there was up to 3 voxels difference in the TP-ML distance. With the second observer, method 2 did not produce an anatomically plausible tract in a single control hemisphere. Excluding this outlier, the inter-rater intraclass correlation coefficient was 0.560 (0.729 in controls and 0.319 in patients). There was agreement in 10 hemispheres and in the majority of the remainder the difference was 1 or 2 voxels. However there was a difference of 6 voxels in a single hemisphere of a patient.

8.4 Discussion

Tractography is a powerful technique enabling non-invasive *in vivo* delineation of white matter tracts. A key assumption is that the results are a faithful representation of the underlying axonal microstructure and thus the white matter tracts themselves. It is not usually possible to compare the results to the gold standard of post mortem dissection. As tractography results are of great utility in planning neurosurgical procedures where the optic radiation lies near the lesion (Romano et al. 2009), it is important to have confidence in the results.

Tractography is subject to a number of limitations and potential errors. Data acquisition using echo-planar imaging may be subject to errors through motion, eddy currents, susceptibility artefacts and noise. The voxel size is several orders of magnitude greater than the underlying axonal structure, so voxels may contain multiple fibres or be subject to partial volume effects. Particular problems include kissing or crossing fibres and areas of high curvature, such as Meyer's loop. The model chosen to represent the underlying axonal structure and the tractography algorithm both make assumptions, such as the presence of a single fibre population in each voxel, which may not be valid.

The degree to which these potential sources of error affect the results depends on many variables chosen during the process making it difficult to compare the different methods of published studies. By controlling as many variables as possible, including scanner type, acquisition parameters, preprocessing and diffusion model, a more direct comparison between two tractography methods was possible.

Deterministic methods are often favoured as they provide visually attractive results, with only limited processing required. Tractography between the LGN and the occipital cortex has been used to depict the optic radiation (Catani et al. 2003), including the different layers (Yamamoto et al. 2005). Critically however these algorithms underestimate the anterior extent of Meyer's loop and this is not improved by increasing the number of gradient directions (Yamamoto et al. 2007). In 18 subjects, the TP-ML distance

using a deterministic technique was 32-51mm (mean 41mm) compared to 17-42mm (mean 30mm) using a probabilistic technique (Nilsson et al. 2010). The latter is more concordant with dissectional data showing a TP-ML distance of 22-37mm (mean 27mm) (Ebeling & Reulen 1988). A more recent study suggesting reconstruction of the entire human visual pathway conceded that Meyer's loop was only fully reconstructed in half of the healthy controls (Hofer et al. 2010). Despite these limitations, such algorithms have been applied during neurosurgery (Chen et al. 2009).

Probabilistic tractography is more time consuming both computationally and for the operator but better delineates Meyer's loop (Nilsson et al. 2010). Seed regions either lateral to the LGN to avoid the brachium of the superior colliculus (Behrens et al. 2003a) or within the apex of Meyer's loop (Powell et al. 2005, Yogarajah et al. 2009) have been used. Both deterministic and probabilistic tractography results are sensitive to the location of the seed region. Even a single voxel displacement of seed region leads to a coefficient of variation of 2.5% in the mean FA of the optic radiation (Ciccarelli et al. 2003a). Such variability is confirmed by the relatively low Dice Similarity Scores in this study, in particular in the hemispheres with lesions.

Consideration has therefore been given to improving probabilistic tractography. A technique combining probabilistic tractography with prior anatomical knowledge gave anatomically plausible locations for Meyer's loop, but still required manual region of interest definition (Sherbondy et al. 2008). Complete automation of probabilistic tractography of the optic radiation has been proposed but no measurements of the location of Meyer's loop to confirm its validity were given (Clatworthy et al. 2010) and both these studies only assessed healthy controls.

The aim of this chapter was therefore to assess a novel method with different aims in comparison to an established method to determine their relative benefits. Visually whilst the core of the tracts was the same, method 1 better delineated the inferior portion of the optic radiation, presumably as the seed region was located within Meyer's loop, which conveys fibres to the inferior optic radiation, whilst method 2 used the LGN as a seed region. Tractography from this region would be expected to better delineate fibres passing directly posteriorly and thus in the more superior part of the optic radiation than those subject to the high curvature of Meyer's loop which was depicted with less consistency and reliability. When planning neurosurgical treatment for epilepsy with a resection in the vicinity of the optic radiation, it is important for a neurosurgeon to be aware of the limitations of the method used when assessing the surgical approach and the risk of causing a visual field deficit. The possibility of either underestimating or overestimating the extent of the tract must always be considered.

The other strengths and weaknesses of the methods fit with the aims of the techniques developed. Method 1 gave reliable visualisation of Meyer's loop with measurements compatible with dissectional data (Ebeling & Reulen 1988). Using this method, the ML-TP distance has previously been shown to correlate with postoperative visual field outcome and have high reproducibility (correlation coefficient 0.9, average difference 2mm, maximum 4mm) (Yogarajah et al. 2009). Method 2 was less consistent in the identification of the Meyer's loop with lower reproducibility of the ML-TP distance particularly in the patient subgroup. In one patient it failed to delineate the anterior part of the optic radiation adjacent to the

lesion, as it relied on a seed region and endpoint located either side of a haemosiderin-laden cavernoma causing signal dropout adjacent to the optic radiation. This effect may explain the trend towards ML-TP distance being greater within the patient subgroup using method 2 than method 1 and highlights the importance of assessing tractography techniques both in healthy controls and in the presence of pathology as most studies published to date only include healthy controls. It should however be noted that this reproducibility measure is of a single clinically important measure that method 1 was specifically designed to address. Overall the more posterior part of the tract was far better delineated with method 2 as an endpoint was specified in this area.

Method 2 also required significantly less operator time. The preprocessing of the DTI data common to both methods took 20 minutes. To process both hemispheres, method 1 required approximately 20-25 minutes of manual intervention and 60 minutes of processing time using a single core of a Sun Ultra 27 workstation with a 3.2GHz Intel Xeon processor. Method 2 required approximately 7 minutes of manual intervention and 150 minutes of processing time.

8.5 Conclusion

The tractography technique thus needs to be chosen according to the question being addressed and the anatomical area of interest. Method 1 would be favoured for ATLR (patients 2 and 4), whilst method 2 would be favoured for more posteriorly located lesions (patients 1 and 3). Method 1 will therefore be used in Chapters 9 and 10 which specifically address the role of tractography in ATLR. A combination of the both methods involving seeding from both the LGN and Meyer's loop was used in Chapter 7 in order to visualise the complete optic radiation with lesions lying near this structure, although there was no automation of the identification of the LGN.

9 OPTIC RADIATION TRACTOGRAPHY AND VISION IN ANTERIOR TEMPORAL LOBE RESECTION

9.1 Introduction

Meyer's loop is vulnerable to damage during ATLR with between 48% (Nilsson et al. 2004) and 100% (Barton et al. 2005) of patients experiencing a postoperative contralateral superior quadrantanopia (Section 4.4) that precludes driving in 4-50% of patients even if seizure free (Manji & Plant 2000, Pathak-Ray et al. 2002, Jeelani et al. 2010). Preservation of vision is key as driving is one of the most important goals for patients undergoing epilepsy surgery (Gilliam et al. 1997).

Tractography of the optic radiation can be used preoperatively to determine the distance between the temporal pole and Meyer's loop (Nilsson et al. 2007). This distance and the degree of resection are predictive of the extent of postoperative VFD (Yogarajah et al. 2009). As the optic radiation cannot be identified visually during surgery, the use of tractography data during image-guided surgery should reduce the risk of a VFD. However preoperative tractography is inaccurate as brain shifts of up to 11mm occur following craniotomy (Chen et al. 2009).

This chapter demonstrates the feasibility of a rapid novel image processing technique to propagate preoperative tractography data on to postoperative structural images by showing that the extent of damage to Meyer's loop as assessed by this technique is more highly predictive of visual field outcome following surgery than assessment using the combination of the degree of resection and location of Meyer's loop.

This method is extended to register preoperative tractography results to intraoperative MRI scans taken after craniotomy in Chapter 10. This makes these data available in real-time during image-guided surgery thus reducing the risk of optic radiation damage.

9.2 Methods

9.2.1 Subjects

Twenty patients (age range 17-56 years, median 38 years, 11 male) with medically refractory TLE undergoing ATLR at NHNN were assessed. All patients had structural MRI scans performed at 3T, video EEG telemetry, neuropsychology, neuropsychiatry and if necessary intracranial EEG recordings prior to surgery. Structural MRI scans, DTI and visual fields were acquired before surgery and at a median of 4 months (range 3-12 months) following surgery. Patients with pre-existing VFD were excluded. Patient demographics and clinical data are listed in Table 9.1.

No	Age/ Gender	Age of Onset	Imaging diagnosis	Histology	ILAE Outcome	VFD (% of UQ)
1	43/M	17y	L HS	HS	1	74%
2	45/M	35y	L HS	HS	1	No VFD
3	42/F	6y	R HS	HS	1	63%
4	45/F	3y	L HS	HS	1	39%
5	18/M	2y	L HS + PHG DNET	HS + DNET	3	28%
6	38/M	23y	L anterior temporal tumour	Ependymoma	1	No VFD
7	17/F	11y	R fusiform gyrus DNET	DNET	1	92%
8	23/M	18y	Non-lesional (RTLE)	MCD type II	5	51%
9	32/M	17y	L HS	HS	1	38%
10	40/F	30y	L amygdala, hippocampus, insula diffuse change	Temporal, amygdala gliosis	2	No VFD
11	38/M	9y	R HS	HS	5	No VFD
12	48/F	3y	L HS	HS	1	No VFD
13	26/M	7y	L HS	HS	1	21%
14	26/F	24y	L anterior temporal cavernoma	Cavernoma	2	No VFD
15	28/M	10y	Non-lesional (LTLE)	EFS	4	No VFD
16	41/M	1y	R HS	HS	1	No VFD
17	44/M	30y	L HS	HS	1	27%
18	31/F	3y	R HS	HS	3	32%
19	56/F	11y	R HS	HS	1	67%
20	41/F	9y	R HS + posterior temporoparietal FCD	HS	1	10%

Table 9.1 - Clinical and demographic characteristics of patients, seizure and visual outcomes

DNET = dysembryoplastic neuroepithelial tumour, EFS = end folium sclerosis, FCD = focal cortical dysplasia, HS = hippocampal sclerosis, PHG = parahippocampal gyrus, UQ = upper quadrant, VFD = visual field deficit

9.2.2 Tractography

Structural and DTI images were obtained and preprocessed as described in Chapter 6. Tractography of the optic radiation was performed by the standard method described there.

9.2.3 Resection Size Estimates and Meyer's Loop Location

All resections were carried out by a single surgeon with a modified Spencer approach, localising the lateral ventricles by proceeding from the middle cranial fossa floor up the collateral sulcus. Tractography data were not available during surgery. The next chapter describes patients in whom tractography data were displayed. The antero-posterior distance from the temporal pole to the anterior margin of Meyer's loop (TP-ML distance) was determined using the preoperative non-diffusion weighted image and the tractography results. The antero-posterior extent of resection was estimated by measuring the distance from the anterior tip of the middle cranial fossa to the posterior margin of resection on a postoperative sagittal image running through the lateral wall of temporal horn (Barton et al. 2005). These two measurements were expressed as a fraction of the antero-posterior distance from the temporal pole to the occipital pole to account for differences in head size (Yogarajah et al. 2009).

9.2.4 Propagation of Tractography and Measuring Damage

A novel two-step image registration technique to perform accurate registration of preoperative to postoperative images was utilised (Daga et al. 2011a). Automatic skull-stripping was performed on the postoperative images using Brain Extraction Tool in FSL (Smith 2002) to ensure that the registration was driven only by brain tissue.

A global image registration step using a multi-scale block-matching algorithm was followed by a local registration step was used to estimate the local, non-linear geometric transformations. A multichannel NMI similarity metric combining the structural MRI and fractional anisotropy (FA) images (Daga et al. 2011a) as described in section 6.6.3.3 was used.

The estimated transformation parameters were used to propagate the preoperative tractography representation of the optic radiation on the postoperative T1-weighted images (Figure 9.1). The amount by which Meyer's loop had been resected according to this registration was determined by measuring the antero-posterior distance between the most anterior portion of Meyer's loop and the resection margin on an axial slice (Figure 9.2).

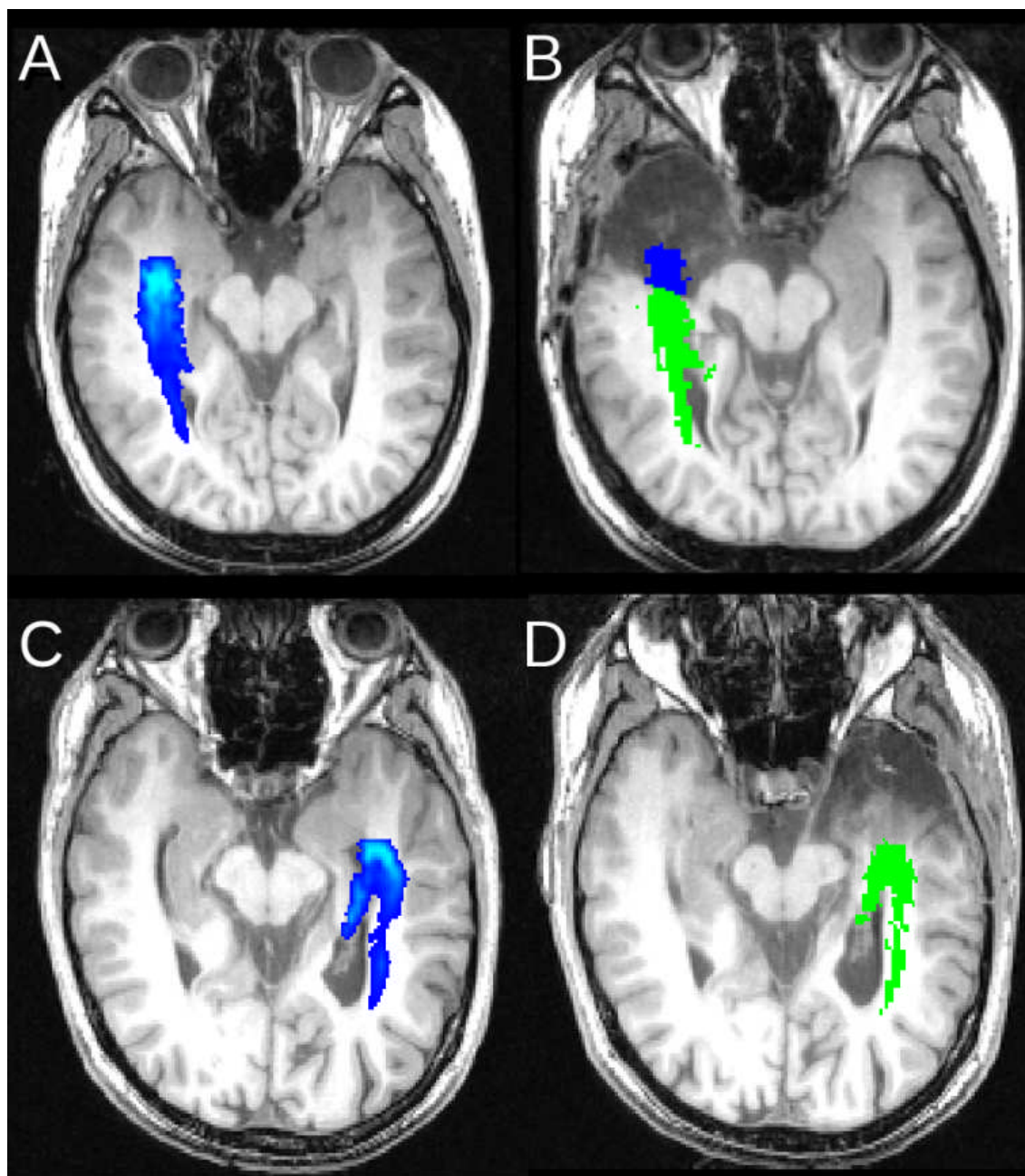


Figure 9.1 - Propagation of preoperative tractography on to postoperative imaging

Preoperative structural T1-weighted image and optic radiation (A) and postoperative structural T1-weighted image with propagated preoperative tractography (B) showing part of the optic radiation was resected (blue) in patient 7 who developed a severe VFD. Corresponding preoperative (C) and postoperative images (D) in patient 12 who did not develop a VFD.

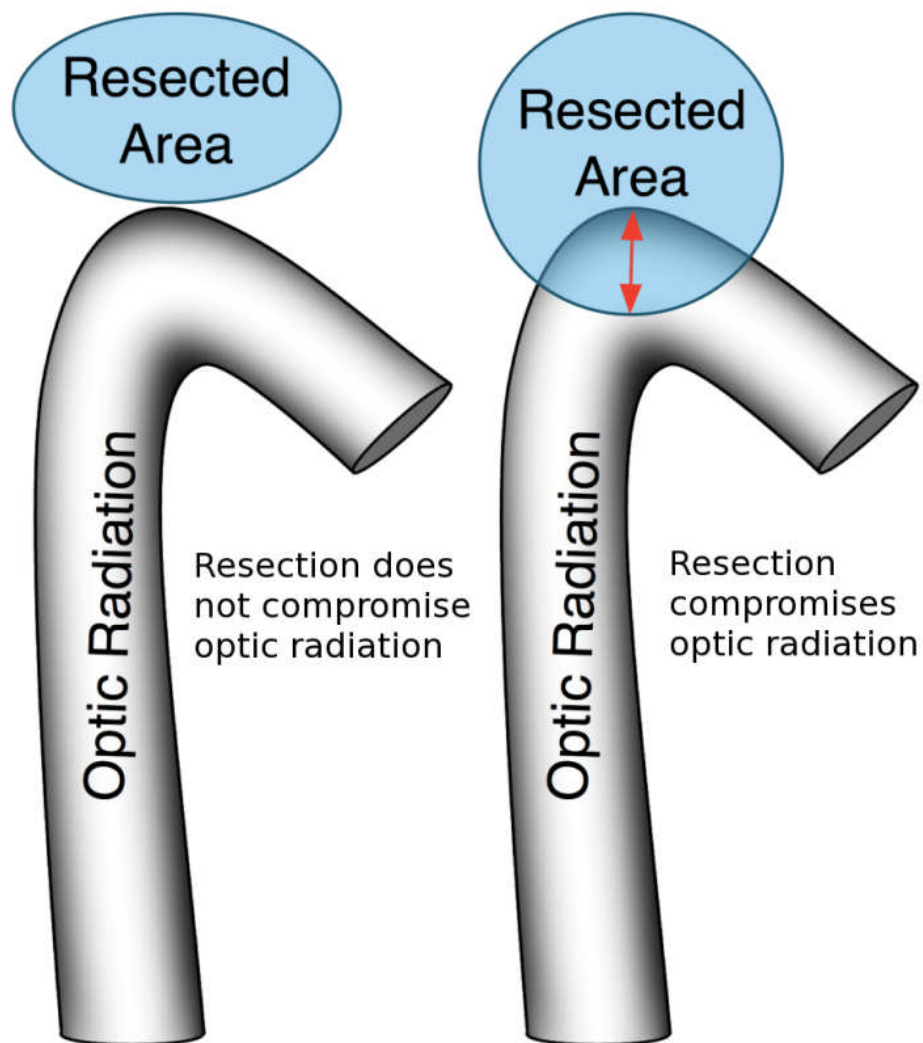


Figure 9.2 - Measurement of the antero-posterior extent of resection of Meyer's loop

Image courtesy of Pankaj Daga.

9.2.5 Visual Field Assessment

Post-operative visual fields were assessed in all patients using Goldmann perimetry as described in Chapter 6. The first ten patients had visual fields assessed by confrontation prior to surgery (as the perimeter was not yet available), and the remainder had preoperative Goldmann perimetry. The post-operative visual deficit was quantified with the V4e isopter using the formula given in Chapter 6.

The number of patients that would not be permitted to drive due to the VFD was determined in accordance with UK Driver and Vehicle Licensing Agency regulations (Driver and Vehicle Licensing Agency 2013) with additional binocular Esterman perimetry if necessary. Further details are given in Chapter 6.

9.2.6 Statistical Analysis

Statistical analyses were performed using SPSS Statistics 17.0 (SPSS Inc, Chicago, USA). Two-sample t-tests were used to compare the degree of resection and the ML-TP distances between patients not suffering a VFD and those with a postoperative VFD.

Two models were then used to model the relationship between the VFD and explanatory variables. The first model was a multiple regression analysis with VFD as the dependent variable and the ML-TP distance and resection size as the independent variables, both expressed as a fraction of the TP-OP distance. This model has previously been shown to be effective (Yogarajah et al. 2009). Partial regression plots were inspected for outliers and heteroskedasticity and only patients with a VFD were included as the degree of VFD cannot fall below zero for smaller resections.

The second model was a regression analysis with predicted damage to Meyer's loop as the single independent variable as this encompassed both the variability in the resection size and the location of Meyer's loop. If the image registration process is effective this should explain an equal or greater amount of the variance in the observed VFD.

9.3 Results

Twelve patients (60%) developed a postoperative VFD (10-92% of the upper quadrant, median 39%). In these patients, visual criteria for driving were satisfied in 5 patients but were not met in 6 patients. The final patient declined Esterman perimetry as they did not wish to drive, but on the basis of the Goldmann perimetry would be very likely to meet criteria. The resection size was 9.8-55.9% of the TP-OP distance (mean 31.2%). The largest resection (patient 8) was an outlier, with the next largest resection being 39.6%. Patient 8 had a non-lesional MRI with right posterior temporal discharges on intracranial EEG and thus underwent temporal lobe resection extending significantly posteriorly. The mean TP-ML distance was 32.1mm (range 26.3-37.5mm). The size of resection was significantly greater in those developing a VFD than those without a VFD (36.1% vs. 23.7%, two sample t-test $p=0.002$). However, the location of Meyer's loop did not differ between those who did and did not develop VFD (mean TP-ML distance 26.2% vs. 25.7%, 32.6mm vs. 31.7mm). These findings were not altered by exclusion of the outlier.

Propagation of preoperative tractography onto the postoperative images using the novel image registration technique showed that Meyer's loop lay 0.0mm to 17.6mm (mean 4.0mm) behind the resection margin in the 8 patients without a postoperative VFD. In the 12 patients developing a VFD, the resection extended to between 4.4mm and 18.7mm (mean 8.8mm) posterior to the anterior limit of Meyer's loop. There was a significant correlation between this A-P distance and the degree of visual loss (Spearman correlation coefficient 0.79, one-tailed $p=0.001$, Figure 9.3).

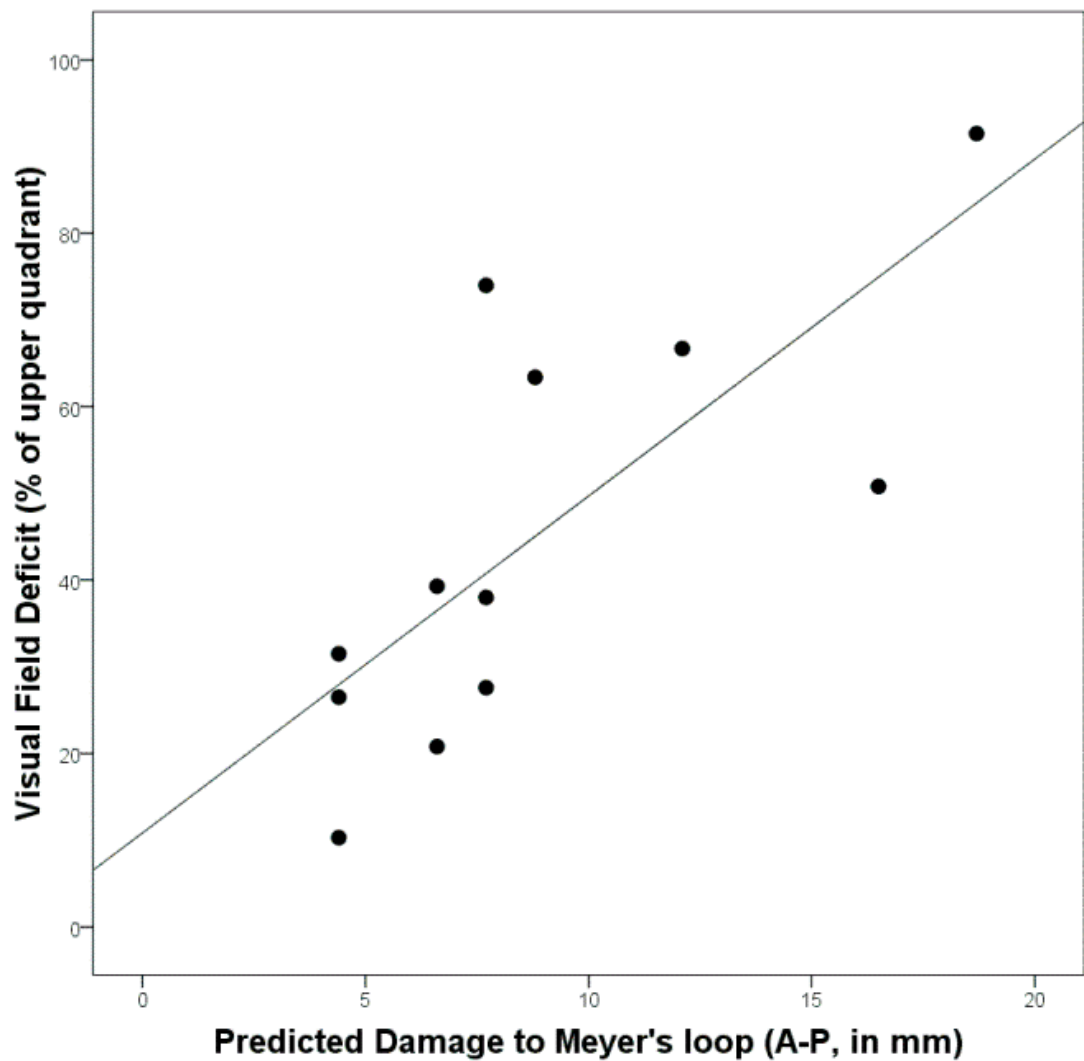


Figure 9.3 - Correlation between VFD and predicted damaged to Meyer's loop by image registration

A multiple regression model with preoperative ML-TP distance and resection size (corrected for head size) as the explanatory variables for the VFD was strongly influenced by an outlier identified on partial regression plots (patient 8). Further review revealed that the resection margin was gradually sloping inferiorly towards the more posterior extent of the resection with the optic radiation running in the roof. Therefore the estimate of the antero-posterior extent of resection greatly overestimated the potential damage to Meyer's loop.

With this patient excluded, the model explained only a small part of the variance of the VFD (adjusted R-squared 0.28, regression $p=0.11$). In contrast the simple regression model involving just the predicted damage to Meyer's loop via image registration explained much more of the variance in the VFD (adjusted R-squared 0.65, regression $p=0.002$). For each additional 1mm of damage to Meyer's loop, a further 5.0% of vision in the upper quadrant was lost. Further, this model remained highly significant when the outlier

was included since the measurement of predicted postoperative damage to Meyer's loop looks only at the axial plane in which Meyer's loop lies and is not subject to the same error.

By implementation of the algorithm on graphical processing units (Daga et al. 2011b), the mean registration time between pre- and postoperative images was 2 minutes 55 seconds. This makes the technique suitable for use in a neurosurgical setting which is assessed in the following chapter.

9.4 Discussion

9.4.1 Key Findings

The rationale of this study was to prove the possibility of registering preoperative tractographic representations of the optic radiation to postoperative scans in individual patients and to validate this technique by comparison with the VFD caused by surgery. Accurate registration explaining the majority of the variance in the measured postoperative VFD could be achieved within 3 minutes. This technique is suitable to apply intraoperatively using intraoperative MRI, so that the preoperative representation of the optic radiation is correctly displayed to the operating surgeon, taking account of the brain shift that occurs during surgery and facilitating the modification of the surgical approach to avoid damaging this critical pathway. This is assessed in Chapter 10.

9.4.2 Comparison with Previous Work

In a group of 21 patients undergoing ATLR, multiple linear regression analysis demonstrated that the preoperative TP-ML distance as assessed by probabilistic tractography and postoperative resection size were both predictive of postoperative VFD on Goldmann perimetry (Yogarajah et al. 2009). This model was therefore used as a comparator for the present study and the new image registration technique performed superiorly to this.

This previous study also suggested a greater risk of VFD with a lower TP-ML distance. In contrast, the present study shows no difference in the TP-ML distance between patients developing a VFD and those that do not. The size of resection was however significantly greater in patients with a postoperative VFD. This discrepancy may result from a more heterogeneous patient group including a lower proportion of pure hippocampal sclerosis and the resulting increased variability in resection size (10-56%). There was little overlap in the antero-posterior extent of the resection between those not developing a VFD (13.2-38.5mm) and those developing a VFD (33.0-78.1mm).

In 48 patients undergoing ATLR, pre- and intraoperative imaging including both structural and diffusion scans showed that the postoperative VFD significantly correlated with damage to Meyer's loop as assessed by intraoperative tractography (Chen et al. 2009). However, there were significant limitations in this study. First the tractography algorithm was a deterministic algorithm, and such algorithms underestimate Meyer's loop and are subject to error in regions of noise and crossing fibres. A direct comparison of deterministic and probabilistic algorithms in 18 subjects showed a TP-ML distance of 32-

51mm (mean 41mm) using a deterministic algorithm and 17-42mm (mean 30mm) with a probabilistic algorithm (Nilsson et al. 2010). Anatomical dissection suggests a range of 22-37mm (mean 27mm) (Ebeling & Reulen 1988). Second the visual outcome and damage to Meyer's loop were categorical and not true quantitative data. Finally the intraoperative data were not available in real-time to alter the surgical technique. Although preoperative tractography could be rigidly registered to the intraoperative images, this did not account for brain shift.

Preoperative deterministic tractography superimposed on the head-on surgical display has been used to guide entry into the temporal horn for selective amygdalo-hippocampectomy (Thudium et al. 2010), but following this entry brain shift from CSF leakage precludes further image guidance. This with gravity, cerebral oedema and the surgical procedure itself lead to an overall shift in the optic radiation of up to 11.1mm horizontally and 7.8mm vertically in either direction (Chen et al. 2009). Shift can only be accounted for using the suggested approach of acquiring and processing the tractography data prior to surgery and then using a comparison of pre- and intraoperative images to update the tractography results to align this with the intraoperative anatomy.

9.4.3 Implications for Driving

Driving is the key activity that a VFD may preclude. In 24 patients undergoing ATLR (20 hippocampal sclerosis) from 1986-1995, 25% failed UK driving criteria (Manji & Plant 2000) but in a subsequent larger study of 105 patients (91 hippocampal sclerosis) at the same centre covering 1998-2004, only 4% failed the same criteria (Jeelani et al. 2010). Another study found 50% of 14 patients failed to meet driving criteria following ATLR for hippocampal sclerosis, although in 2 patients this was due to prior vigabatrin usage (Pathak-Ray et al. 2002).

Assessment for driving in the UK typically uses automated binocular Esterman perimetry, which has been shown to be less sensitive for VFD and more lenient than the monocular Goldmann perimetry employed in the present study (Manji & Plant 2000) and the European Union Eyesight Working Group has recommended against its use within Europe (Eyesight Working Group 2005). Further all these studies concentrate on historical series in patients with predominantly hippocampal sclerosis. Improved imaging techniques and changes in surgical practice have enabled surgery in patients where it was not previously possible, including neocortical or non-lesional epilepsy (Duncan 2010). In the present series, only 12 patients had pure hippocampal sclerosis, with the remainder being dual pathology (2), other pathology (4) or non-lesional (2). In such patients, more extensive resections may be proposed with a corresponding greater risk of VFD which needs to be assessed. In the patients studied, a total of 6 patients (30%) failed to meet UK criteria for driving.

9.4.4 Strengths and Weaknesses

This study uses probabilistic tractography and a previously proven algorithm to ensure an accurate depiction of Meyer's loop of the optic radiation. Since neither rigid nor affine registrations account for the complex deformations seen during neurosurgery, a non-linear registration technique is used. Such a technique must be both accurate and computationally rapid. High accuracy is achieved by combining the complementary information from anatomical and diffusion scans in the registration process. The average transfer time of a patient between scanner and operating table in the intraoperative MRI suite at NHNN is 7-10 minutes. Implementation of the technique on graphical processing units (GPU) reduced computation time to under 3 minutes, well within the required timescale, whilst retaining an accurate result.

This study has limitations. The degree of damage to Meyer's loop cannot be measured directly as a gold standard and has been inferred from preoperative imaging and a registration algorithm to postoperative images. It is not possible to perform tractography on all postoperative diffusion images as a comparator as the tractography technique relies on a seed region across the base of Meyer's loop, a region that may have been resected during the surgery leading to a VFD. Comparisons of preoperative and postoperative tractography are also limited by variability within tractography resulting from minor changes in the seed location (Ciccarelli et al. 2003a). The nature of the relationship between the damage to Meyer's loop and the degree of VFD is unknown and the statistical analysis within this paper has assumed linearity as an approximation on the basis of the results obtained and previous studies. Measurement of a single antero-posterior distance is a relatively crude measure of damage to a complex structure such as the optic radiation; however, this is the quantity of most importance clinically for visual outcome.

The pre- and post-operative data were both of high quality and obtained on the same scanner. Intraoperative data will be acquired on a different scanner which through limitations imposed both by design and the time constraints of neurosurgery will yield images with lower spatial resolution and signal-to-noise ratio. In the next chapter, I use a high-field (1.5T) closed-bore Siemens Espree scanner which provides superior image quality to conventional low-field "double-donut" design interventional MR scanners. The signal-to-noise ratio is sufficient to facilitate the use of the proposed intensity based image registration algorithm. Image registration is performed using an iterative coarse-to-fine approach in which the coarser levels can recover the larger deformations and ensure the registration algorithm is more robust to noise by smoothing input images. The bivariate normalised mutual information similarity measure utilises complementary and shared information generated by structural and diffusion MRI and so provides additional spatial constraints in the registration process. I with colleagues have previously shown that this leads to better overall alignment (Daga et al. 2011a, Daga et al. 2011b).

As DTI data are acquired using an echo-planar imaging sequence, magnetic field inhomogeneities may cause geometric distortion at air-tissue interfaces such as the temporal pole so introducing additional inaccuracies into image registration. In the next chapter, software is utilised to perform distortion correction and algorithm is applied to intraoperative data.

9.4.5 Implications of Results

Despite advances in surgical technique, VFD remain common following temporal lobe epilepsy surgery. This study confirms the biological variability in the location of Meyer's loop and that increasing degrees of damage to this structure lead to a greater VFD. Rather than just using preoperative tractography data to try and predict the risk of damage to vision, making these data available during surgery using accurate image registration will be a significant advance. I suggest that real-time display in a neuronavigation suite of the location of the optic radiation will be highly beneficial in avoiding surgical damage and test this claim in Chapter 10. A key question is whether the provision of this additional information during surgery reduces the incidence or severity of VFD.

9.5 Conclusion

Image registration of preoperative optic radiation tractography to postoperative scans can be achieved rapidly and accurately. The predicted degree of damage to Meyer's loop explains much of the variation in the observed visual field deficit and significantly more than other measurements. It can be performed quickly enough for use during in a neurosurgical procedure. This is now assessed in Chapter 10.

10 INTRAOPERATIVE VISUALISATION OF THE OPTIC RADIATION REDUCES VISUAL FIELD DEFICITS

10.1 Introduction

Optic radiation tractography is useful for planning temporal lobe epilepsy surgery (Chapter 7) and non-linear registration of preoperative tractography onto postoperative imaging and measuring the degree of damage of Meyer's loop can accurately explain the postoperative VFD observed (Chapter 9). In this chapter, the techniques developed in this thesis are applied for the first time in real-time during image-guided surgery in an iMRI suite in a cohort of patients undergoing ATLR.

The aim is to evaluate the claim in the previous chapter that "real-time display in a neuronavigation suite of the location of the optic radiation will be highly beneficial in avoiding surgical damage". First, I assess whether display of tractography during ATLR can reduce the severity of VFD and increase the proportion of patients that can drive without affecting seizure outcome. Second, I assess whether correction for brain shift during surgery using iMRI confers additional benefit.

10.2 Methods

10.2.1 Subjects

I studied 21 patients (age range, 23-63 years; median, 36 years; 8 male) with medically refractory TLE undergoing ATLR. Patients underwent the standard assessment described in Chapter 6 before and 3 months following surgery (range 70-145 days). Intraoperative guidance of epilepsy surgery using imaging was approved by the National Hospital for Neurology and Neurosurgery and the Institute of Neurology Joint Research Ethics Committee and additional informed written consent was obtained for participants (Appendices G and H). Patient demographics and clinical data are listed in Table 10.1.

10.2.2 Comparison Cohort

For comparison to previous clinical practice, a cohort of patients was selected who underwent the same assessment and ATLR by the same neurosurgeon in a conventional operating theatre without tractography-based image guidance comprising 44 patients from the longitudinal cohort described in Chapter 6 (age range, 17-68 years; median, 39 years; 17 male; 21 left, 23 right ATLR). No patient had a preoperative VFD.

Age/ Gender	Age of Onset	Imaging diagnosis	Histology	ILAE Outcome	VFD (% of upper quadrant)
Cohort 1 (9 patients): without brain shift correction					
34/M	26y	Left PHG DNET	DNET	1/1	17.9%
30/F	29y	Left temporal cavernoma	Cavernoma	1/1	22.8%
31/F	18y	Right HS	HS	1/1	41.0%
44/F	19y	Right temporal extra-axial mass	Epidermoid	1/3	11.0%
36/F	23y	Right amygdala lesion	Gliosis	2/2	No VFD
32/F	25y	Right temporal cavernoma	Cavernoma	1/1	2.4%
40/M	8y	Left HS	HS	1/1	19.1%
44/F	30y	MRI-negative (right)	EFS	1/2	41.7%
46/F	18y	MRI-negative (right)	Negative	4/4	5.5%
Cohort 2 (12 patients): with brain shift correction					
27/F	22y	MRI-negative (right)	Gliosis	1/1	No VFD
30/M	28y	Right temporal cavernoma	Cavernoma	1/1	3.0%
52/M	16y	Left HS	HS	1/1	49.2%
29/F	3m	Left HS	HS	1/1	No VFD
63/M	17y	Left ITG dysplasia	Hamartoma	4/4	47.3%
48/F	12y	Right HS	HS	1/1	No VFD
23/M	15y	MRI-negative (right)	Gliosis	1/1	No VFD
30/F	7y	Previous right SAH for DNET	HS	1/2	14.5%
47/M	12y	MRI-negative (right)	EFS	1/3	23.6%
42/F	21y	Left HS	EFS	1/3	32.3%
43/F	38y	Left PHG cavernoma	Cavernoma	1/1	3.8%
35/M	2y	Previous right ATLR, residual HS	HS	1/1	25.0%

Table 10.1 - Clinical and demographic characteristics of patients, seizure and visual outcomes

EFS = end-folium sclerosis, HS = hippocampal sclerosis, ITG = inferior temporal gyrus, PHG = parahippocampal gyrus, VFD = visual field deficit. The ILAE outcomes are given at 3 months and 12 months following surgery.

10.2.3 Preoperative Imaging

10.2.3.1 Optic Radiation Tractography

Preoperative and postoperative MRI studies were performed on a 3T GE Signa HDx scanner as described in Chapter 6. The T1-weighted volumetric scan underwent full 3D correction for gradient non-linearity using manufacturer-supplied software on the scanner. Tractography was performed on the preoperative scans as described in Chapter 6.

10.2.3.2 Preparing Preoperative Data

10.2.3.2.1 Cohort 1

For cohort 1, the average of the non-diffusion weighted images from the DTI sequence was registered to the corrected T1-weighted scan using an affine transformation in FSL and this transformation was applied to the optic radiation tractography (Part 1 of Figure 10.1). The registered tractography data were thresholded at 0.05 and fused with the T1-weighted scan by mapping the intensities of the T1-weighted image into the range 0-2047 and the superimposed optic radiation tractography into the range 3072-4095. The resulting data were evaluated using the checklist in Appendix I.

The corrected T1-weighted scan, the average non-diffusion weighted image registered to the T1-weighted scan, the optic radiation tractography registered to the T1-weighted scan, the fused T1-weighted/optic radiation tractography image and the checklist were compressed and encrypted and transferred over a secure link to NHNN. All received data were subject to the additional quality control checks documented in Appendix I.

10.2.3.2.2 Cohort 2

In cohort 2, additional processing was performed to apply corrections to the diffusion data for through-plane gradient non-linearity and susceptibility artefacts (Part 2 of Figure 10.1). As the acquisition on the scanner only performs in-plane gradient non-linearity correction, custom-written software (Section 6.6.4) was used to calculate the deformation necessary to correct gradient non-linearities in the third dimension. Likewise, custom-written software (Section 6.6.5) was used to determine the deformation necessary to correct for magnetic susceptibility artefacts based on the field map (Daga et al. 2013). The two deformations were composed and applied to the non-diffusion weighted image from the DTI sequence, the FA image and the optic radiation tractography results. In patients who had preoperative imaging prior to the implementation of the field maps, only the correction for gradient non-linearity was applied as field maps were unavailable.

In this cohort in addition to the files listed above, the uncorrected DTI scan, the corrected and uncorrected versions of the non-diffusion weighted image, the FA image and the optic radiation tractography and the composed deformation field were transferred to NHNN and subject to the quality checks detailed in Appendix I.

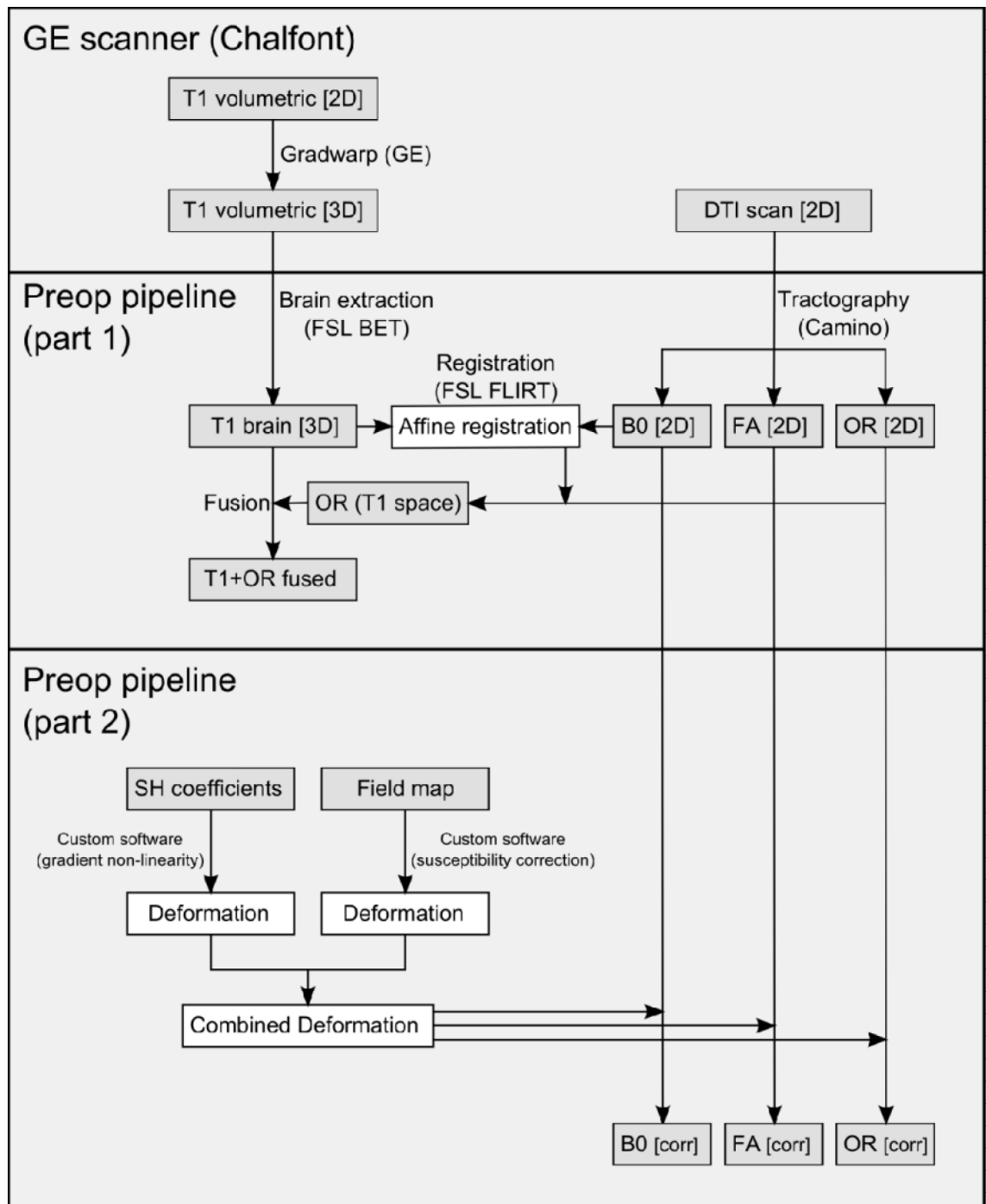


Figure 10.1 - Pipeline for processing of preoperative data

Part 1 was used for cohort 1 and parts 1 and 2 were used for cohort 2. Grey boxes refer to images, white boxes refer to transformations/deformations.

10.2.4 Intraoperative Imaging and Surgery

10.2.4.1 Overview

Patients underwent surgery in the iMRI suite at NHNN (Figure 10.2). The operating table is outside the 5 gauss line during surgery allowing standard surgical instruments to be used. For intraoperative imaging, the patient was transferred to a 1.5T Siemens Espree scanner (Siemens Healthcare, Erlangen, Germany) with a dedicated operating room 8-channel MR head coil (Noras, Hochberg, Germany) that incorporates a surgical headrest.

10.2.4.2 Imaging Protocol

Before surgery, anatomical scans were performed for use with the neuronavigation system. At the two intraoperative timepoints described below, both anatomical and diffusion scans were acquired (Figure 10.3).

The T1-weighted acquisition was a 3D FLASH sequence, TE 2.5ms, TR 5.25ms, field-of-view 28x28x22cm with 176 slices, matrix 256x256 (zero-filled to 512x512) giving a resolution of 0.546875x0.546875x1.25mm.

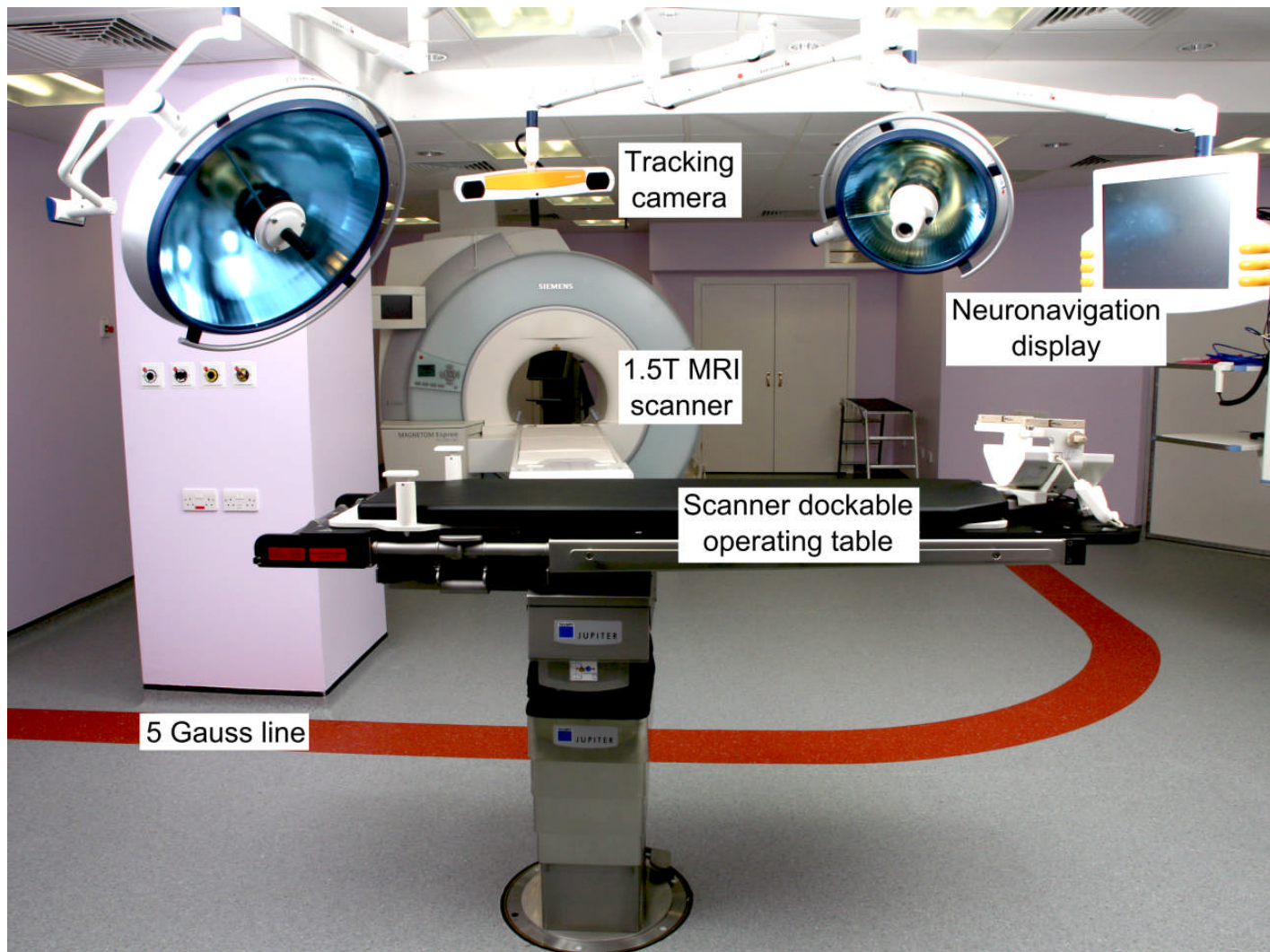
The diffusion-weighted acquisition was a single shot EPI, TE 94ms, TR 7400ms, field-of-view 21x21cm, matrix 84x84 with 49 slices giving a resolution of 2.5mm isotropic. There was a single non-diffusion weighted scan and 64 directions with a b-value of 1000 s/mm². The accompanying fieldmap was acquired with a gradient echo acquisition with TE 4.92 or 9.68ms, TR 631ms, field-of-view 21x21cm, matrix 72x72 giving a resolution of approximately 2.9mm isotropic.

10.2.4.3 Display of Imaging

During surgery, the BrainLab VectorVision sky navigation platform (BrainLab, Feldkirchen, Germany) provides real-time tracking of surgical markers and tools and visualisation. An OPMI Pentero confocal surgical microscope (Carl Zeiss Meditec, Jena, Germany) allows injection of colour overlays from the neuronavigation system. The location of the microscope's focal point is tracked using the navigation system and an array of four infra-red reflectors mounted on the microscope's optical head. Outlines were projected onto the navigation and operating microscope displays with solid lines used to depict the shape of the object in the focal plane and dashed lines to show the maximum extent below it thus allowing depth perception.

Figure 10.2 - Intraoperative MRI suite at NHNN (on next page)

Surgery takes place outside the 5-gauss line and the patient can be transferred to and from a 1.5T MRI scanner during surgery. Image copyright 2013 UCL ION/UCLH NHNN/Medical Illustration.



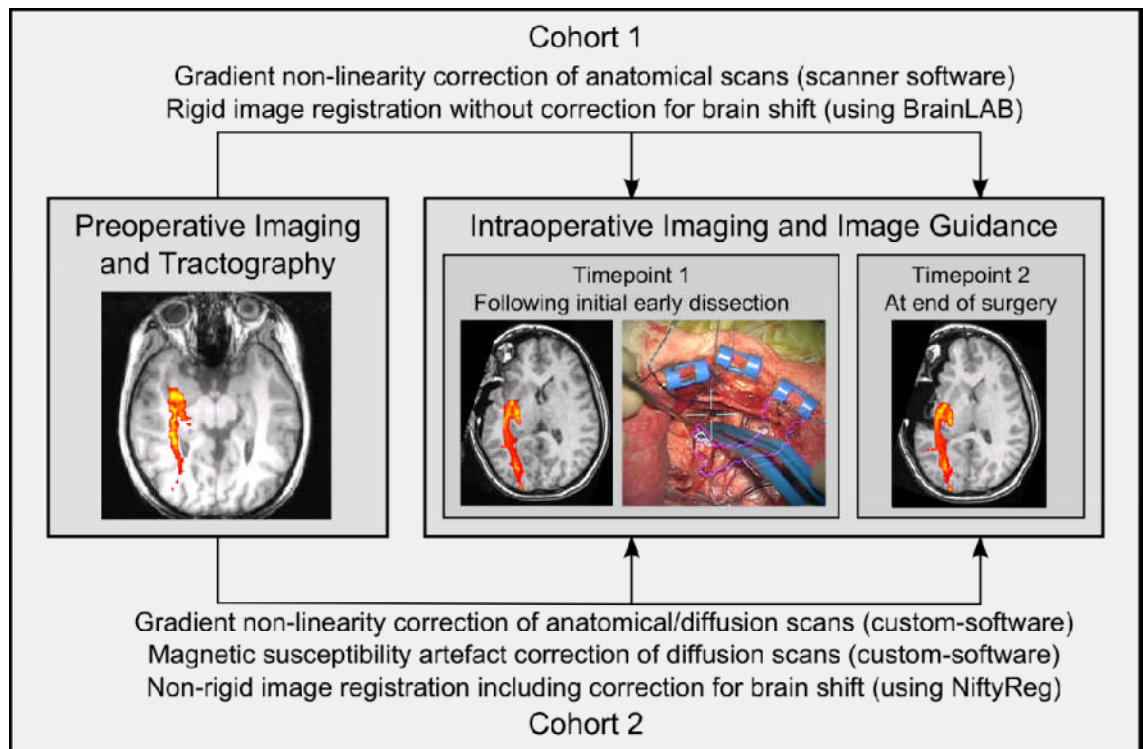


Figure 10.3 - Pipeline for registration of pre- and intraoperative images for display during surgery

Intraoperative images were acquired following the initial dissection and at the end of surgery.

10.2.4.4 Surgical and Imaging Approach

A variety of surgical approaches to the ventricle are possible with some accepting a VFD (Section 4.4.9). At my centre, the surgeon performs a modified Spencer ATLR (Spencer et al. 1984) approaching the ventricle from the floor of the middle cranial fossa via the collateral sulcus aiming to pass underneath the optic radiation. The first intraoperative scans (timepoint 1) were acquired after initial dissection. The outlines of the optic radiation and ventricle (manually delineated by a radiologist) were displayed to guide entry into the ventricle below the optic radiation (Figure 10.4 and Figure 10.5). The optic radiation was later displayed to allow the surgeon to disconnect the temporal stem by making a cut through the temporal stem to the amygdala whilst remaining anterior to the optic radiation. A second intraoperative scan (timepoint 2) was acquired at the end of surgery to confirm adequate resection and exclude immediate complications such as haemorrhage.

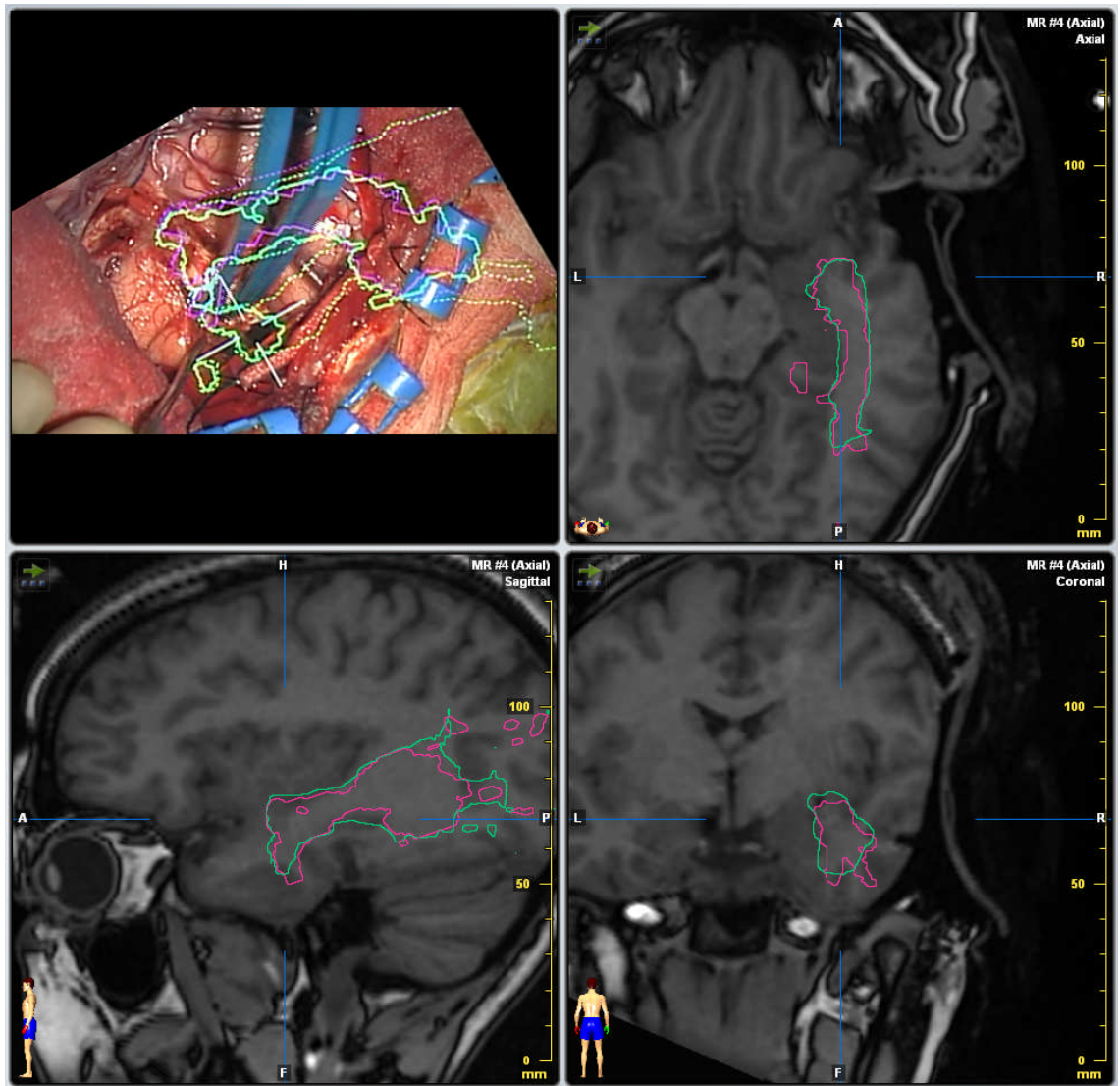


Figure 10.4 - BrainLab display of the first intraoperative image following initial dissection

The patient is undergoing right ATLR with the optic radiation before (pink) and after (green) correction for brain shift superimposed. The solid outlines refer to the structure in the focal plane and the dashed outlines refer to the maximum extent below this. Note that BrainLab shows right on the right (opposite to radiological convention). In the top left panel, the operating microscope view with these outlines and the ventricle (blue) is shown flipped and rotated to correspond with the sagittal view (original microscope images are shown in Figure 10.5).

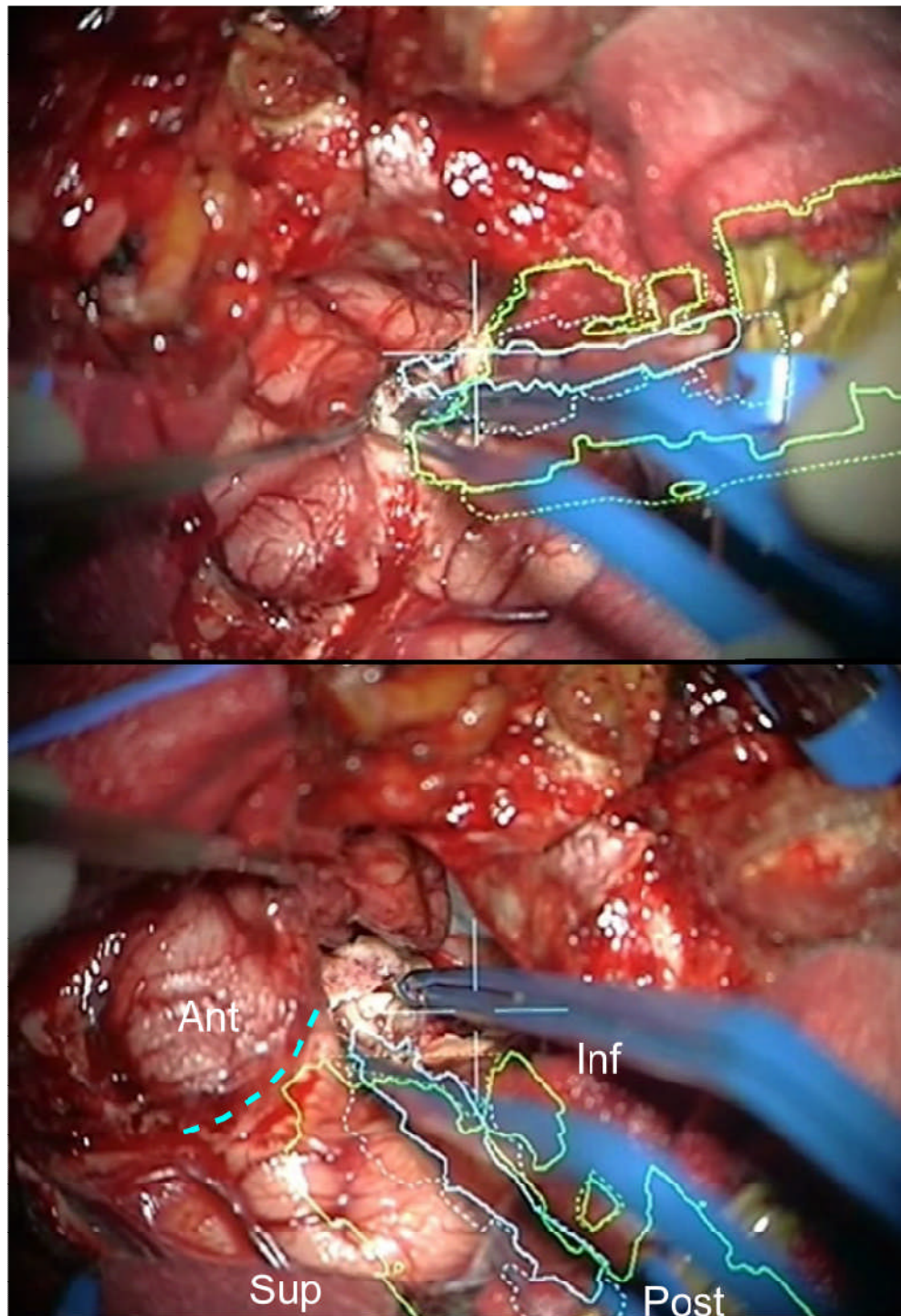


Figure 10.5 - Operating microscope display of a patient undergoing right ATL

The head is rotated in the operating position as indicated in the lower panel. The superimposed outlines are the optic radiation (yellow-green) and the ventricle (blue). Solid outlines refer to the structure in the focal plane and dashed outlines refer to the maximum extent below this. The top panel shows the surgeon approaching the tip of the temporal horn of the lateral ventricle from the middle cranial fossa whilst remaining inferior to the optic radiation. The bottom panel shows the point of entry into the lateral ventricle exposing the hippocampus. The next step of the operation is to transect the temporal stem along the dotted blue line remaining anterior to the maximal projection of the optic radiation.

10.2.4.5 Cohort 1

In the first cohort of patients (9 subjects), preoperative imaging was transferred to the neuronavigation system. The preoperative T1-weighted image was registered to the intraoperative T1-weighted image using a rigid transformation in BrainLab that does not correct for brain shift. The same transformation was applied to the fused preoperative T1-weighted image/optic radiation image and the optic radiation was segmented out by thresholding and converted to a three-dimensional object for display. Additional error margins of 1.5mm in the anatomical antero-posterior direction and a 1.5mm isotropic margin were added to account for the lack of compensation for susceptibility artefacts and potential brain shift respectively.

10.2.4.6 Cohort 2

In the second cohort of patients (12 subjects), preoperative and intraoperative images were transferred to a separate workstation for processing according to the pipeline shown in Figure 10.6. The T1-volumetric scan underwent gradient non-linearity correction on the scanner whilst the FA image derived from the diffusion data and the fieldmap were not corrected on the scanner.

The field map acquisition was first corrected for gradient non-linearity and then used to calculate the deformation field to correct for magnetic susceptibility artefacts (Daga et al. 2013). The deformation field to correct the gradient non-linearity of the FA image was also computed. These two deformations were combined and used to resample the FA image in the same of the intraoperative T1-weighted scan. The intraoperative T1-weighted and resampled FA image were reoriented to roughly anatomical orientation (to ensure the affine registration would be successful) and cropped (to ensure fast non-rigid registration and reduce memory requirements).

The preoperative T1-weighted image was also cropped and the preoperative non-diffusion weighted image was registered to this using an affine transformation. The same transformation was applied to the preoperative FA image to bring this into the space of the cropped preoperative T1 image.

The two pairs of images (preoperative/intraoperative T1-weighted/FA) were merged. An affine transformation between the cropped preoperative T1-weighted image and the reorientated and cropped intraoperative T1-weighted image was used to initialise a non-linear registration between these pairs of images which was performed as described in Section 6.6 (Daga et al. 2012).

The combination of the affine transformation from preoperative diffusion space to the cropped preoperative T1-weighted space and the non-rigid registration calculated above was used to map the preoperative optic radiation on to the cropped and reorientated intraoperative T1-weighted space. The cropping and reorientation steps were reversed to give the preoperative optic radiation tractography in the space of the full intraoperative T1-weighted image with non-linear registration accounting for brain shift. The corrected image was transferred to BrainLab for display. If no preoperative field map was available, an error margin of 1.5mm in the anatomical antero-posterior direction was added.

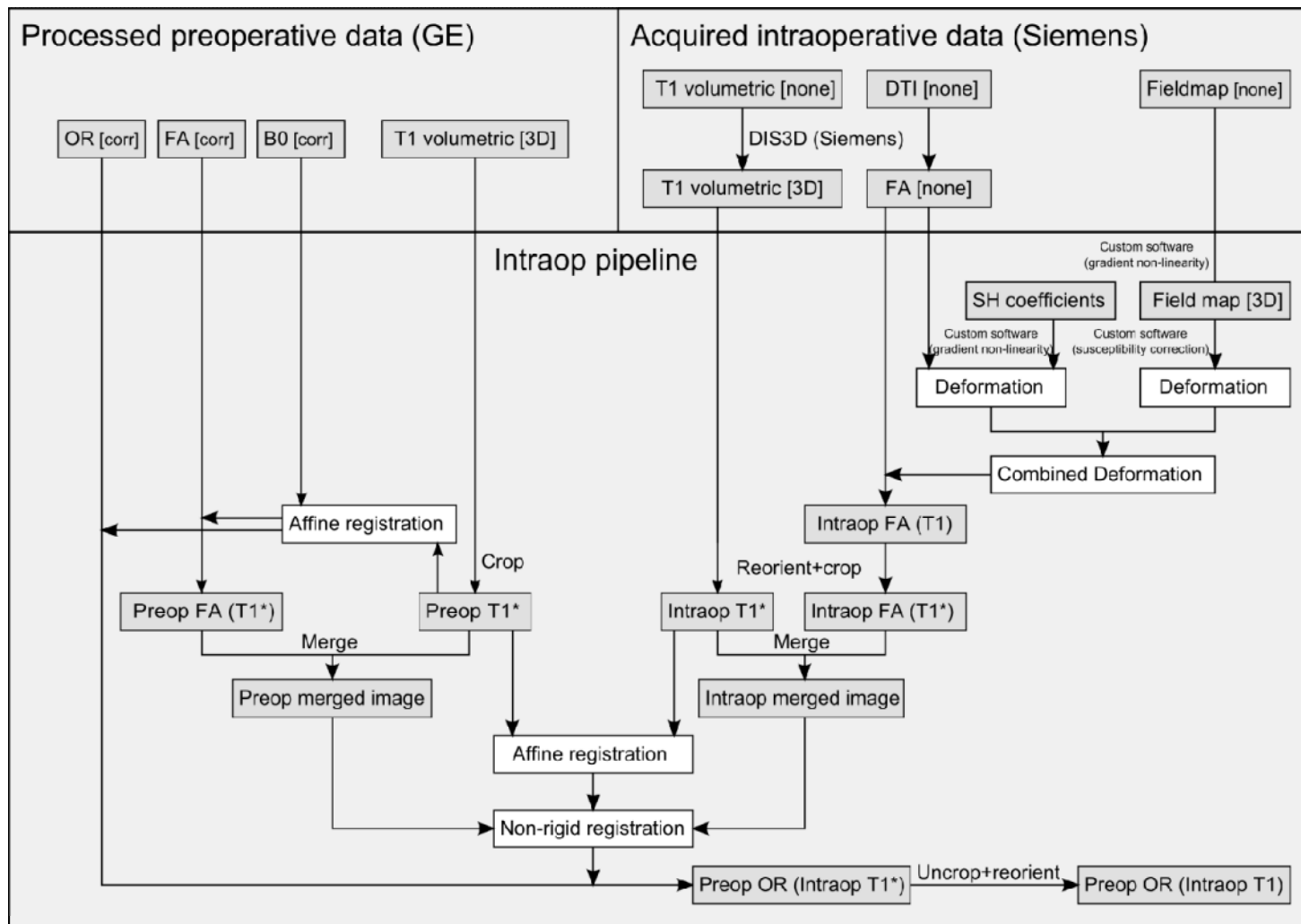


Figure 10.6 - Pipeline for intraoperative processing and display of images in cohort 2 (on prior page)

Grey boxes refer to images or other data, white boxes refer to transformations/deformations. The images in () refer to one image being in the space of another, with * denoted a cropped/reoriented version of the original image. The suffixes in [] refer to the corrections applied to the images (none = no gradient non-linearity correction, 3D = full gradient non-linearity correction, corr = gradient non-linearity and susceptibility correction). T1 = T1-weighted volumetric image, DTI = diffusion tensor image, FA = fractional anisotropy image, OR = optic radiation tractography, B0 = non-diffusion weighted image from DTI.

The pipeline was implemented as a Python script with the necessary images identified in a JSON (JavaScript Object Notation) file that was automatically generated and integrated with the hospital PACS system. Checkpoints were inserted requiring the user to manually confirm the integrity or plausibility of intermediate processing steps. Processing was performed using graphical processing units to ensure the entire procedure could be performed quickly enough not to delay surgery (Daga et al. 2011b).

10.2.5 Outcome Data

10.2.5.1 Primary Outcome: Visual fields

Visual loss was calculated on postoperative Goldmann perimetry using the V4e and I4e isopters as described in Section 6.5.5.2 and the number of patients not permitted to drive due to the VFD was determined in accordance with UK Driver and Vehicle Licensing Agency regulations (Driver and Vehicle Licensing Agency 2013) with additional binocular Esterman perimetry if necessary (Section 6.5.5.3).

10.2.5.2 Secondary Outcomes

To ascertain whether image guidance to avoid the optic radiation affected seizure freedom and the extent of hippocampal resection, seizure outcome at 3 months and 12 months was assessed using the ILAE classification (Wieser et al. 2001) and the extent of resection was determined by measuring the antero-posterior extent of the residual hippocampus on post-operative imaging starting from the coronal slice in which the greatest length of fornix was visible and moving anteriorly until no hippocampus remained (Cook et al. 1992).

After each operation the surgeon completed a questionnaire concerning how the data affected the surgical plan, whether it was useful to improve the safety of surgery and how it affected the duration of surgery. In view of the additional imaging time, the duration of scanning was recorded in 10 patients from cohort 2.

The degree of brain shift at the two intraoperative timepoints was assessed in cohort 2 using displacement fields generated from the non-linear registration. The displacement in comparison to rigid registration was determined in the brain as a whole, in the optic radiation and at the anterior tip of the temporal horn, a surgical landmark. Further, the amount of shift in each of the three orthogonal planes at the anterior tip of the temporal horn was determined.

10.2.6 Statistical Analysis

Statistical analyses were performed using PASW Statistics 18.0 (IBM, Armonk, USA). As VFD and degree of hippocampal resection were not normally distributed (Shapiro-Wilks test), the non-parametric independent-samples Mann-Whitney U or independent-samples Kruskal-Wallis tests were used to detect any difference in the distribution between groups. In contrast, the observed brain shifts were normally distributed (Shapiro-Wilks test).

10.3 Results

10.3.1 Visual Field Deficits

None of the 21 patients undergoing surgery with iMRI guidance developed a VFD that precluded driving. The VFD were 0-41.7% of the contralateral superior quadrant (median 17.9%, IQR 28.0%) in cohort 1, 0-49.2% (median 9.2%, IQR 30.5%) in cohort 2 and 0-49.2% (median 14.5%, IQR 27.5%) overall.

Four patients in the historical cohort had equivocal Goldmann perimetry but declined Esterman as they did not wish to drive. Of the remaining patients, 5/40 (12.5%) failed to meet driving criteria as a result of surgery. The VFD were 0-90.9% of the contralateral superior quadrant (median 24.0%, IQR 32.6%).

The distribution of VFD from those with iMRI guidance (cohorts 1 and 2 combined) was significantly different from those without iMRI guidance (Figure 10.7) (independent-samples Mann-Whitney U test $p=0.043$). The difference was not significant between the historical controls and each iMRI guided cohort individually.

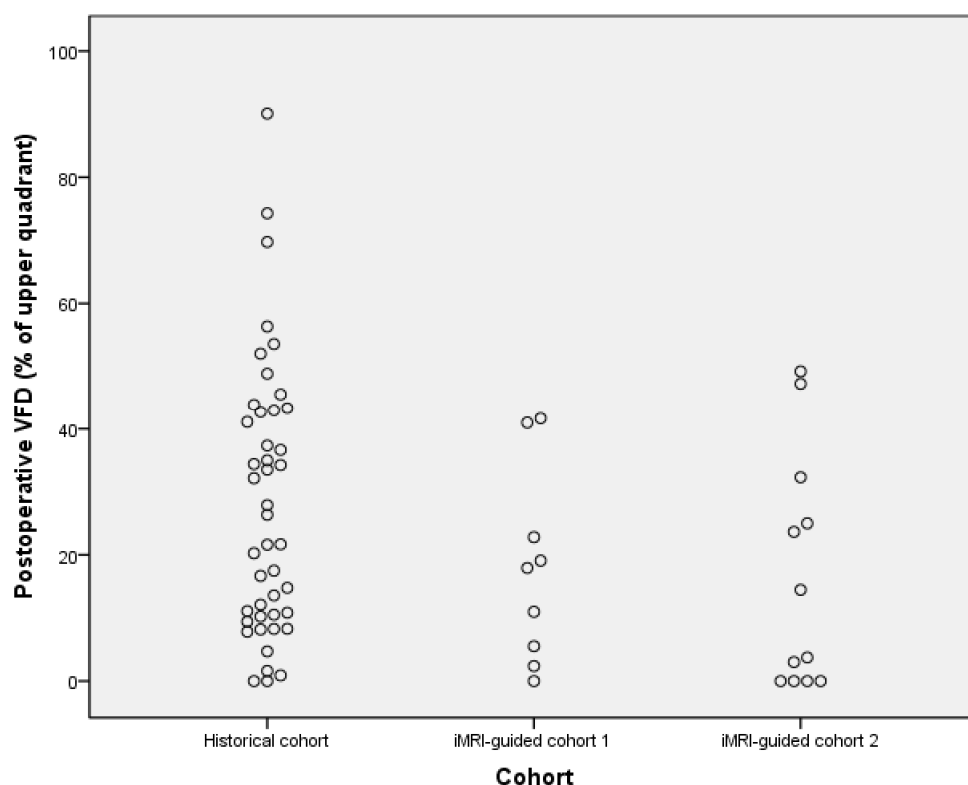
In cohort 2, two patients had previous surgery with one having a pre-existing minor VFD that did not preclude driving. Exclusion of these patients did not affect the significant difference but the median VFD fell to 3.4% (IQR 36.0%) in cohort 2 and to 11.0% (IQR 32.3%) in the iMRI-guided cohort overall.

10.3.2 Seizure Outcome

At 3 months, 89% of patients in cohort 1, 92% in cohort 2 and 91% in the historical cohort had a good outcome (ILAE groups 1 or 2) (Table 10.1). At 12 months, 78% in cohort 1, 75% in cohort 2 and 84% in the historical cohort had a good outcome.

10.3.3 Hippocampal Resection

The median antero-posterior extent of remaining hippocampus was 15.4mm (cohort 1), 16.0mm (cohort 2) and 13.2mm (historical cohort). There was no significant difference in the distribution between the groups (independent-samples Kruskal-Wallis test $p=0.43$).



10.3.4 Surgeon's Feedback

The duration of surgery was considered prolonged mainly by the scanning time. In a single case the surgery itself was lengthened to avoid the optic radiation. It was commonly reported that resection was shortened by the ease in entering the ventricle.

The initial scan for neuronavigation took on average 31 minutes measured from placing the MR coil over the patient to removal of the coil (including transfer to/from the scanner and the actual imaging time). The subsequent two scans which also include diffusion imaging took on average 54 minutes and 47 minutes respectively. In one patient, the second scan was not performed due to time constraints. A single patient developed a self-resolving brachial plexopathy following surgery.

10.3.6 Degree of Brain Shift

In the brain, the maximum displacements observed were 4.7-8.1mm (mean 6.5mm) at timepoint 1 and 8.7-13.8mm (mean 10.9mm) at timepoint 2. At the first timepoint, this was typically in the anterolateral temporal lobe or the frontal lobe and thus some distance from the optic radiation. In the operating position, these regions are the most superior so subject to the greatest effects of gravity. At the second timepoint, the maximum displacements were seen superior or posterior to the posterior margin of the resection where the brain sags into the void created.

Within the optic radiation, the maximum displacements were 2.8-6.8mm (mean 4.3mm) at timepoint 1 and 6.7-12.8mm (mean 9.3mm) at timepoint 2. These occurred in the anterolateral portion of Meyer's loop or the part of the optic radiation just posterior to this. The displacement of the anterior tip of the lateral ventricle was only 0.9-3.2mm (mean 1.9mm) at timepoint 1, but this landmark was not visible at the second timepoint. In all cases the landmark moved medially up to 2.8mm (mean 1.3mm) whilst the displacement in the other orthogonal axes occurred in either direction. In particular, the antero-posterior displacement was negligible (1.3mm anterior to 1.3mm posterior, mean magnitude of displacement 0.5mm).

10.4 Discussion

10.4.1 Key Findings

I have shown that display of the optic radiation with image guidance during ATLR reduces the severity of VFD and that no patient failed to meet visual criteria for driving as a result of surgery in comparison to 13% of recent historical controls. This was achieved with comparable seizure outcomes and hippocampal resection. Whilst it is technically possible to correct for intraoperative brain shift within neurosurgical time constraints, this did not further improve the outcome. The technique could be readily incorporated into surgery and the surgeon found it useful in all cases.

10.4.2 Vision and Driving

The inability to drive is one of the most important concerns of patients with epilepsy (Gilliam et al. 1997) and gaining a driving licence is a key aim of patients undergoing surgery (Taylor et al. 2001). Previous studies have shown that between 4% and 50% of patients fail to meet visual criteria for driving after ATLR (Manji & Plant 2000, Pathak-Ray et al. 2002, Jeelani et al. 2010). With improved imaging techniques and changes in surgical practice, surgery can now be undertaken in previously ineligible patients, including neocortical or nonlesional epilepsy, where the risk to vision may be greater. Six patients (27%) in our image-guided cohort were nonlesional.

10.4.3 Importance of Brain Shift

Serial imaging demonstrates progressive brain shift during tumour surgery (Nabavi et al. 2001). Brain shift during ATLR has also been assessed by one group (Chen et al. 2009) by performing deterministic

tractography on a preoperative and single intraoperative image taken at the end of surgery. Around the resection area, shifts of up to 11.1mm horizontally (mean 3.75mm) and up to 7.8mm vertically (mean 2.46mm) were found, but were not used to guide surgery. In the present study, I demonstrated the maximum brain shift in the optic radiation was up to 6.8mm (mean 4.3mm) and up to 12.8mm (mean 9.3mm) at the two timepoints, confirming that brain shift develops during surgery.

In this previous chapter, I demonstrated that each additional 1mm of damage to Meyer's loop causes an additional loss of 5% of the upper quadrant. Meyer's loop is closely related to the anterior tip of the lateral ventricle and is most at risk during the early part of surgery. However the displacement of this landmark was minimal (maximum 3.2mm, mean 1.9mm) with negligible movement in the antero-posterior direction which is the most critical direction when attempting dissection anterior to the optic radiation. This small extent of brain shift explains the lack of additional benefit from correcting for intraoperative brain shift in ATLR over and above the addition of an error margin.

10.4.4 Strengths and Limitations

I employed probabilistic tractography and a robust algorithm to delineate Meyer's loop of the optic radiation. Visual and other outcomes were systematically assessed in all patients in both the iMRI-guided cohort and the historical cohort. Whilst visual criteria for driving may differ between countries, guidelines in the UK and other European countries follow a European Union directive.

The intraoperative correction of all sources of image distortion, such as gradient non-linearity, susceptibility artefacts and brain shift took 8-9 minutes, the same time taken to transfer a patient from the scanner back to the operating table.

Intraoperative MRI enables the assessment of completeness of resection and immediate surgical complications but the key limitations are the cost and imaging time prolonging surgery, with the potential consequences of that.

10.5 Conclusion

This study implies that display of optic radiation tractography in the head up display of the operating microscope led to a change in surgical approach to avoid the optic radiation and mitigate the risk of causing a VFD.

As interventional MRI is expensive, prolongs surgery and is not widely available, the next step is to assess the benefit of incorporation of probabilistic tractography of the optic radiation into the operating microscope display of a commonly used neuronavigation system such as StealthStation (Medtronic, Minneapolis, USA), which would make this advance widely applicable. In addition, it would be possible to explore more economical ways of correcting for brain shift, such as intraoperative ultrasound.

11 STRUCTURAL CORRELATES OF IMPAIRED WORKING MEMORY IN HIPPOCAMPAL SCLEROSIS

11.1 Introduction

Recent data suggest that working memory is compromised in TLE (see Section 3.4) (Stretton & Thompson 2012). In patients with hippocampal sclerosis (HS) from the longitudinal cohort, reduced activation of the right superior parietal lobe and impaired deactivation of the ipsilateral hippocampus in a cohort of patient has been shown with functional MRI (Stretton et al. 2012) but the structural correlates remain unexplored in this population. A reasonable hypothesis is that the frontoparietal pathways affected in other conditions (Section 3.4) are involved in the working memory impairment observed in HS. A meta-analysis of DTI studies identified widespread bilateral changes within white matter pathways in TLE including the cingulum (Otte et al. 2012) although changes in the SLF were less consistent. The structural integrity of the temporal lobe itself in working memory has not been considered.

In this chapter, I investigate structural changes within the working memory network in a large cohort of patients with HS to address the following hypotheses:

1. Structural changes exist in the grey matter of the bilateral frontoparietal working memory network identified by fMRI and in white matter tracts connecting these regions
2. Working memory performance correlates with the structural changes in the frontoparietal network
3. Working memory involves and is affected by the structural integrity of the temporal lobes

The fMRI findings in this cohort are also described to enable comparison between the regions identified with functional and structural changes. The majority of the analysis of the fMRI data was undertaken by Jason Stretton.

11.2 Methods

11.2.1 Subjects

54 individuals with medically refractory TLE and unilateral HS (29 left; age range 18-56 years, median 42 years, 21 male) and 28 healthy age-matched controls (age range 19-64 years, median 37 years, 11 male) without any history of neurological or psychiatric disease were studied (Table 11.1). Clinical assessment and the definition of HS were as described in Chapter 6.

	Left HS (n=29)	Right HS (n=25)	Healthy controls (n=28)
Gender (male/female)	15/14	6/19	11/17
Handedness (left/right)	5/24	4/21	3/25
	Median (IQR)	Median (IQR)	Median (IQR)
Age (years)	40 (16)	42 (14)	37 (22)
Age at seizure onset (years)	13 (14)	9 (15)	n/a
Duration of epilepsy (years)	26 (22)	29 (23)	n/a
Seizures frequency (per month)	6 (12)	5 (10)	n/a

Table 11.1 - Clinical and demographic characteristics of patients and healthy controls

IQR = interquartile range.

11.2.2 Magnetic Resonance Imaging

Structural scans, including the T1-weighted volumetric image used for the voxel-based morphometry (VBM) analysis, diffusion tensor imaging and working memory fMRI were obtained as described in Chapter 6.

11.2.2.1 Working Memory fMRI

The paradigm described in Chapter 6 was used. Individual subject images for the ‘2-back’ minus ‘0-back’ contrast were compared in an analysis of variance (ANOVA) with group (control, left HS, right HS) as a factor to examine the main effects and to highlight regions demonstrating more or less activation in one group compared to another.

11.2.2.2 Voxel-Based Morphometry

T1-weighted images were segmented into grey matter, white matter and cerebrospinal fluid using New Segment in SPM8. The Diffeomorphic Anatomical Registration using Exponentiated Lie algebra (DARTEL) framework was used to produce a group template to which all subjects were registered (Ashburner 2007). Grey matter segmentations were normalised to MNI space applying modulation and smoothing with a Gaussian kernel of 8mm full-width at half-maximum (FWHM) to produce maps of grey matter volume (GMV). Total intracranial volumes were determined using a locally written script and included in all analyses to correct for the effects of brain size. A mask produced by thresholding the group grey matter template at 0.2 was used to confine analyses to grey matter.

ANOVA was performed to determine group differences in GMV. Further analysis was performed in the left and right HS patient subgroups to determine the relationship of GMV to a global measure of working memory (see below, threshold of $p=0.001$ uncorrected, minimum cluster size of 10).

11.2.2.3 DTI Processing and Analysis

Eddy current correction of the data was performed using `eddy_correct` in FSL (<http://www.fmrib.ox.ac.uk/fsl/>) and maps of FA and MD were generated for each patient using the FMRIB Diffusion Toolbox. The FA maps were aligned to the FMRIB58 template using non-linear registration within the TBSS framework and the same transformation was applied to the MD maps.

The resulting images were smoothed using an 8mm FWHM Gaussian kernel. A mask produced by thresholding the FMRIB58 template with an FA value of 0.2 was used to confine analyses to white matter. Group comparisons of left or right HS groups versus controls were performed using SPM8 (threshold of FWE $p < 0.05$) and regression analyses were performed in each subgroup to determine where diffusion measures correlated with a global measure of working memory (below, threshold of 0.001 uncorrected, minimum cluster size of 10). In view of the previously strong correlations observed between diffusion measures and age (Charlton et al. 2010), age was included as a covariate in all analyses.

Finally, the mean FA of the entire white matter skeleton produced by the TBSS framework was determined for each subject. The same measures were derived for the two key white matter tracts connecting the frontal and parietal lobes previously implicated in working memory (superior longitudinal fasciculus, SLF; cingulum) and one control tract (corticospinal tract, CST) using a mask derived from the Johns Hopkins University white matter tractography atlas. The correlation between these diffusion measures and working memory performance was determined using a one-tailed t-test with the hypothesis that reduced FA would correlate with impaired performance.

11.2.3 Neuropsychological Measures of Working Memory

Three working memory span tasks were administered to assess working memory capacity (see Section 6.5.4). The Digit Span Backwards task from the WAIS-III was used to measure verbal working memory whilst the Gesture Span task and the Motor Sequences task were used as measures of spatial span.

In order to explore the relationship between GMV, white matter integrity and working memory performance, and to avoid multiple comparisons, a single measure of working memory was derived using a principal component analysis (PCA) in PASW v18 (SPSS; Chicago, IL, USA). The scores from the three out-of-scanner span tasks were combined with the in-scanner performance (percentage correct) on the most demanding task, the 2-back condition.

A single component with eigenvalue greater than 1 was found which explained 65% of the variance. Seven subjects (4 left HS, 3 right HS) were excluded from the PCA and subsequent correlation analyses due to incomplete data through an inability to understand the instructions necessary to perform the fMRI paradigm. This component representing an overall measure of global working memory capacity was used for the correlation analyses.

11.3 Results

11.3.1 Working Memory Performance

Individuals with left or right HS both performed significantly less well than healthy controls on measures of working memory (Table 11.2, one-way ANOVA for each measure, $p < 0.005$). The working memory PCA score significantly differed between the patient groups and controls ($F(2,72) = 14.9$, $p < 0.001$).

Measure	Controls	Left HS	Right HS
Digit span backwards	4.61 (1.17)	3.41 (1.12)	3.21 (0.93)
Gesture span	3.14 (0.62)	2.42 (0.69)	2.71 (1.00)
Motor sequencing	6.07 (2.24)	4.12 (2.03)	3.87 (2.21)
2-back % correct	71.6% (20.5%)	48.4% (20.4%)	54.2% (23.4%)
Working memory PCA	0.70 (0.92)	-0.41 (0.72)	-0.42 (0.90)

Table 11.2 - Working memory scores in each group - mean (sd)

11.3.2 Working Memory fMRI

The multiple-item working memory network comprising the bilateral middle frontal gyrus (MFG) and superior parietal lobe (SPL) was identified using the 2-back minus 0-back contrast (Figure 11.1A). Both left and right HS groups showed significantly less activation in the right SPL compared to controls (Figure 11.1B, conjunction analysis, $z = 3.32$, uncorrected $p < 0.001$). No significant differences were identified in the frontoparietal network activation between left and right HS.

11.3.3 Voxel-Based Morphometry

Group comparisons between healthy controls and patients with left or right HS identified GMV loss confined to the left and right hippocampus respectively (FWE $p = 0.05$). At a lower threshold (uncorrected $p = 0.001$, minimum cluster size 10), GMV loss was also seen in the ipsilateral parietal lobe in both patient groups (Figure 11.2A, B). In the RHS subgroup, additional areas of GMV loss were observed throughout the right hemisphere (superior frontal, superior and middle temporal gyri, occipital region) and in the caudate nucleus bilaterally (Table 11.3 at end of chapter). A comparison of the atrophy between left and right HS groups revealed the respective hippocampi and additionally in right HS there were areas of atrophy within the right hemisphere, including the MFG and parietal lobe compared to left HS (uncorrected $p = 0.001$, minimum cluster size 10).

In left HS, working memory performance correlated with GMV in the right SPL (Figure 11.2C, uncorrected $p = 0.001$, minimum cluster size 10). In RHS, working memory performance correlated with GMV in the left and right frontal lobe, left posterior temporal lobe, precuneus and cerebellum (Table 11.4 at end of chapter).

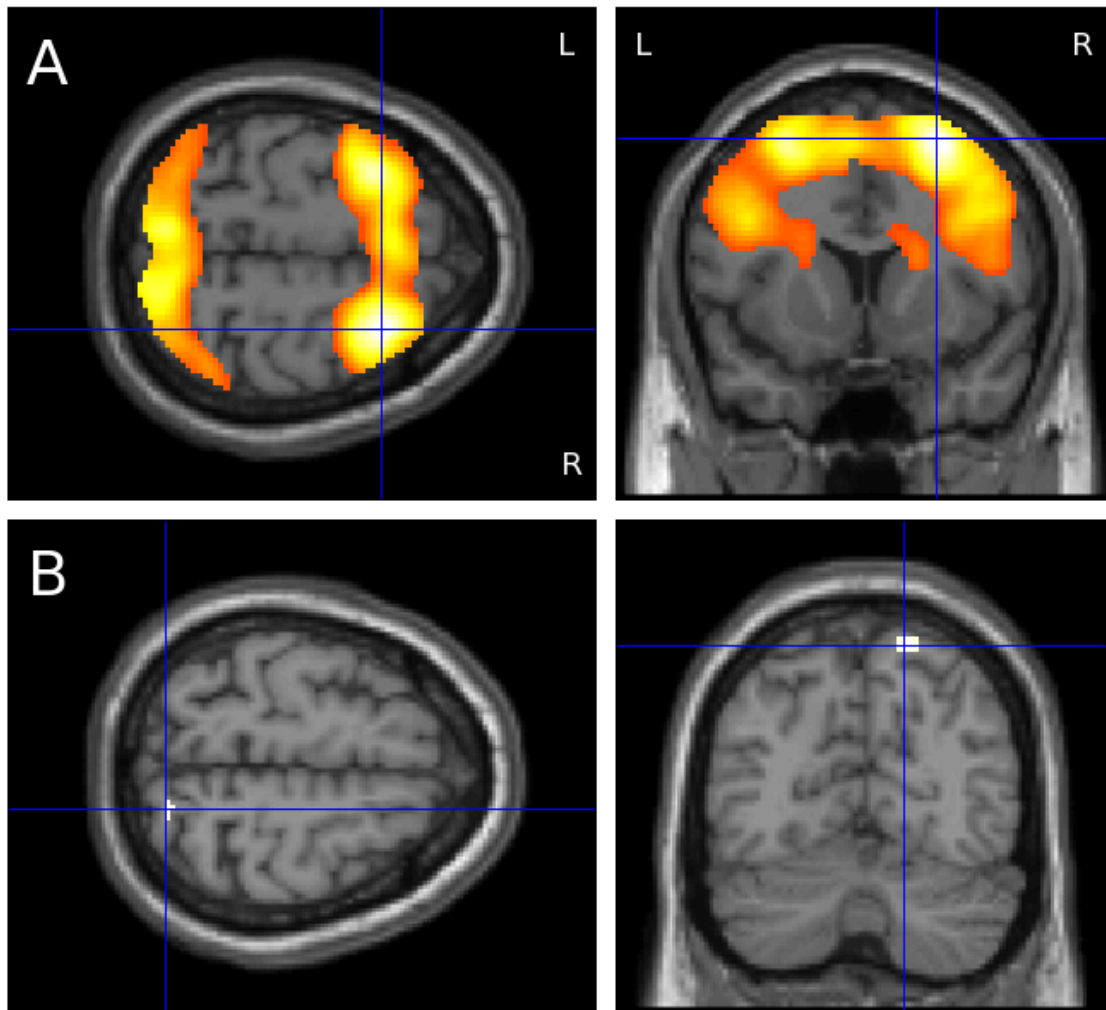


Figure 11.1 - Functional MRI findings with working memory task

(A) A bilateral frontoparietal working memory network was identified using the 2-back minus 0-back contrast in all subjects. (B) In both left and right HS groups there was significantly less activation in the right SPL compared to controls (uncorrected $p=0.001$, conjunction).

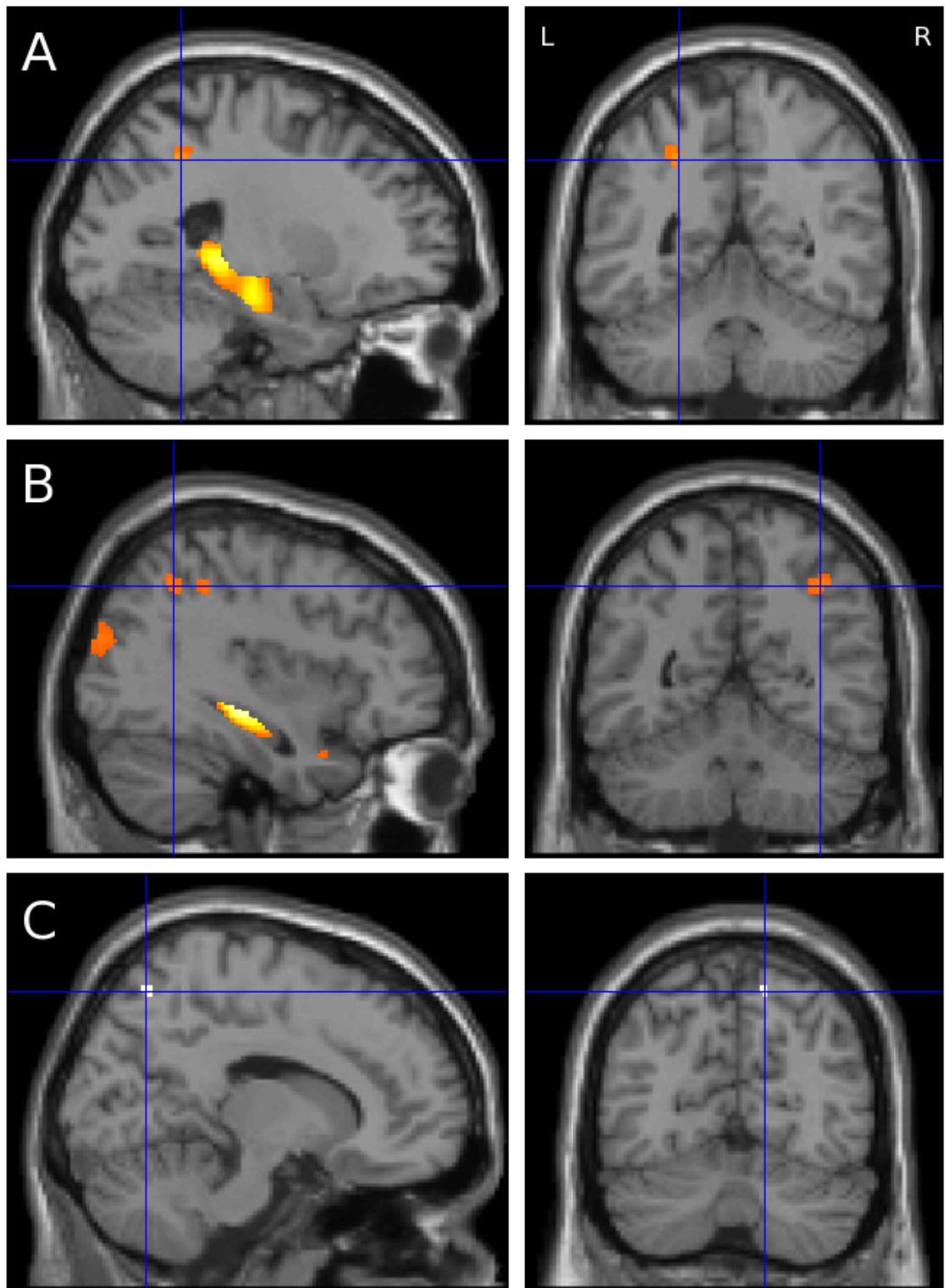


Figure 11.2 - Voxel-based morphometry findings and working memory

(A) In left HS, GMV loss was observed in the left hippocampus and left parietal lobe (uncorrected $p=0.001$). (B) In right HS, GMV loss occurred in the right hippocampus, right parietal lobe and other parts of the right hemisphere (uncorrected $p=0.001$). (C) Working memory performance correlated with GMV of the right SPL in left HS (uncorrected $p=0.001$).

11.3.4 Voxel-Based Analysis of DTI

The group comparison revealed reduced FA predominantly within the left temporal lobe and limbic system but also within the left inferior frontal, cuneus and cerebellum in left HS compared to controls. FA was reduced in the right temporal/limbic region, right middle frontal, precuneus and cerebellum in right HS compared to controls. These findings are comparable to previous reports (Focke et al. 2008). The baseline and longitudinal voxel-based DTI findings are described in more detail in Chapter 12.

In healthy controls, working memory correlated with higher FA in three small clusters within the left superior frontal gyrus (SFG) and right inferior temporal gyrus (Table 11.5 at end of chapter). In the left HS subgroup, correlations were observed in the frontoparietal working memory network - the right MFG and bilaterally in the parietal lobe at the extremities of the SLF - and also in the right cingulum and right inferior temporal lobe (Figure 11.3). In right HS, working memory correlated with higher FA in the left parietal lobe, right cingulum and several areas within the left temporal lobe - superior, middle and parahippocampal gyri - and cerebellum (Figure 11.4).

In left HS, lower MD within the frontoparietal working memory network - left SFG and bilateral SPL at either end of the SLF - and the right cingulum and orbitofrontal cortex correlated with better working memory performance (Figure 11.5 and Table 11.6 at end of chapter). No significant negative correlations were observed in healthy controls or right HS.

11.3.5 Tract-Based Analysis of DTI

Mean FA of the TBSS skeleton was significantly reduced in both left (0.421, $p=0.001$) and right HS (0.421, $p<0.001$) compared to healthy controls (0.441). In the left HS subgroup, a single outlier with mean FA three standard deviations below the group mean was excluded from subsequent analyses.

In left HS, working memory performance correlated with mean FA of the left SLF (one tailed $p=0.013$), right SLF ($p=0.021$), left cingulum ($p=0.019$) and right cingulum ($p=0.025$). No correlations were observed with the mean FA of either corticospinal tract, or in the control or right HS subgroups. None of these correlations remained significant following a Bonferroni correction for multiple comparisons. Working memory performance correlated with the mean FA of the entire TBSS skeleton ($p=0.021$) in left HS, but not in healthy controls or right HS.

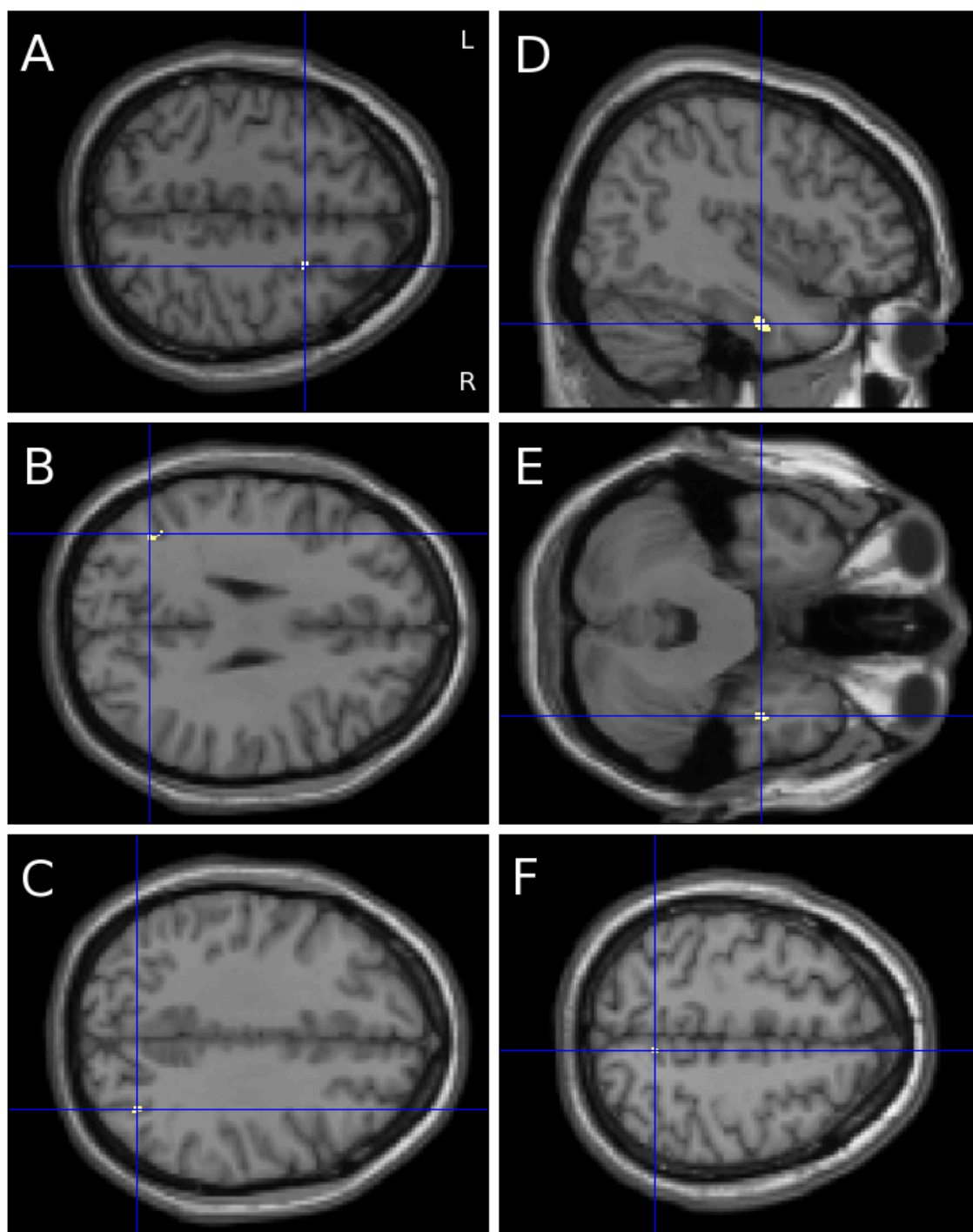


Figure 11.3 - DTI findings (FA) in left HS and working memory

Better working memory performance correlated with higher FA in the frontoparietal working memory network (right MFG, A; bilateral parietal lobe, B and C), the right inferior temporal lobe (D and E) and the right cingulum (F).

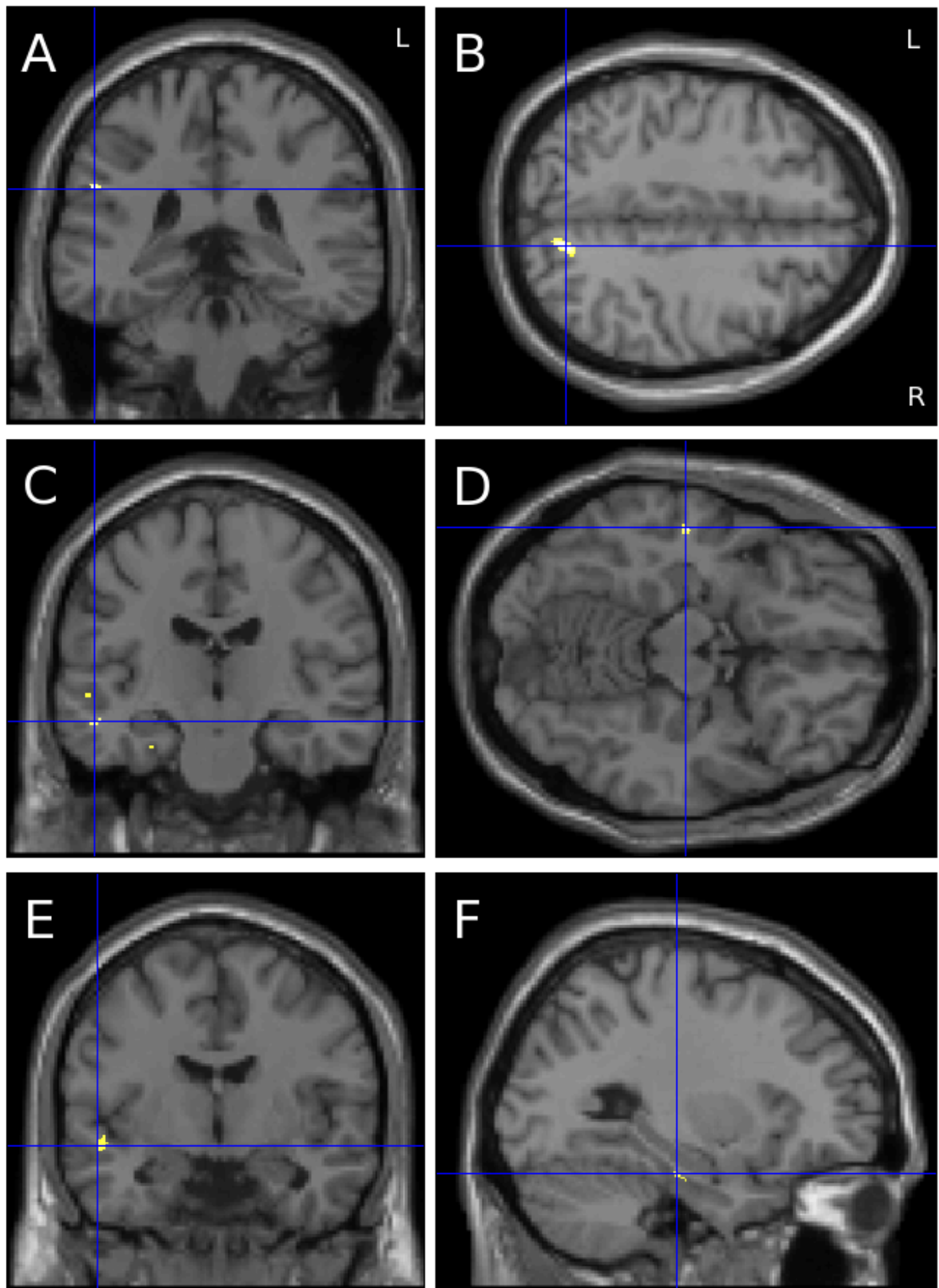


Figure 11.4 - DTI findings (FA) in right HS and working memory

Better working memory performance correlated with higher FA in the left parietal lobe (A), right cingulum (B), several regions of the left temporal lobe (C-F) and the cerebellum (not shown).

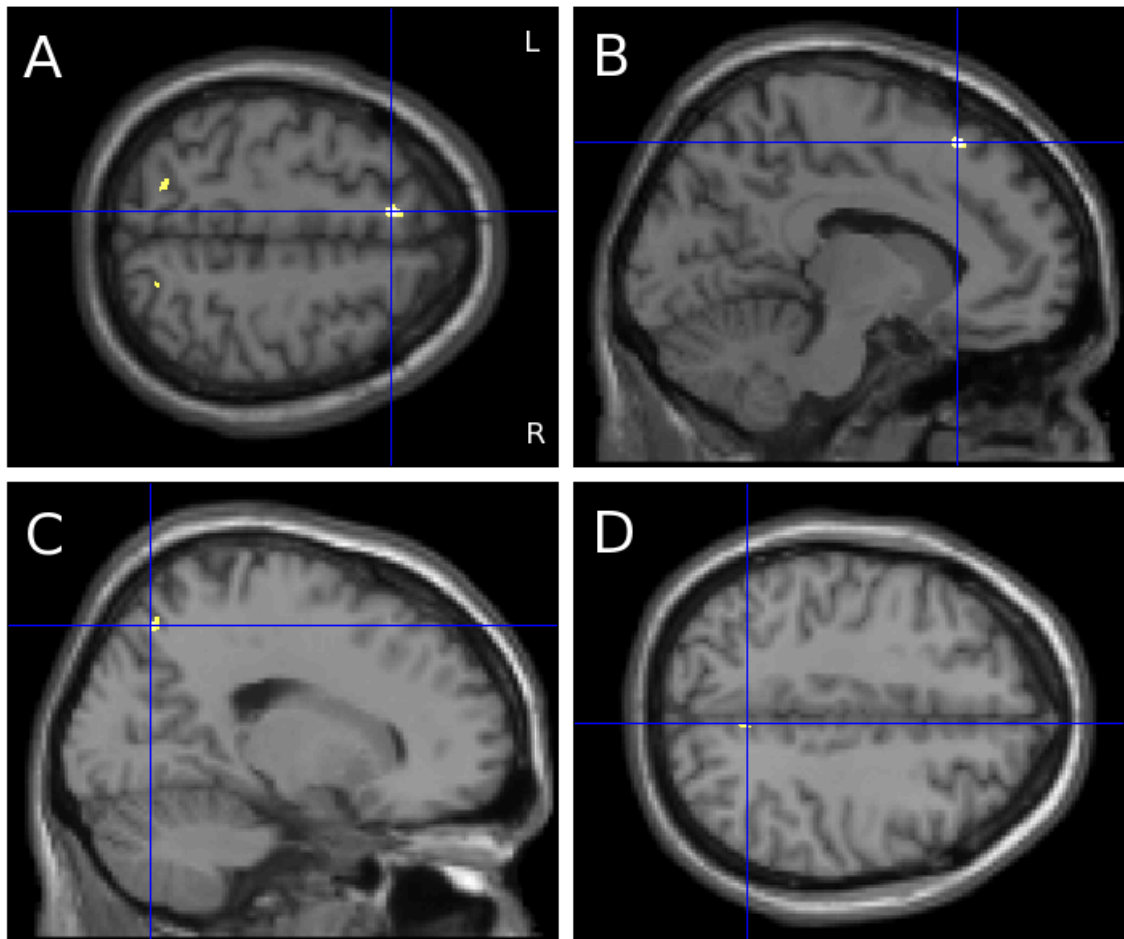


Figure 11.5 - DTI findings (MD) in left HS and working memory

Better working memory performance correlated with lower MD in the frontoparietal working memory network (left SFG, A and B; bilateral SPL, A and C), the right cingulum (D) and the right orbitofrontal cortex (not shown).

11.4 Discussion

11.4.1 Summary of Results

A bilateral frontoparietal working memory network was delineated in controls and patients with HS using fMRI with reduced activation of the right parietal lobe seen in left and right HS. Both VBM and DTI indicated the effect of TLE on this frontoparietal network, especially the parietal lobe, and suggested a role of the temporal lobe contralateral to the seizure focus in the maintenance of working memory performance (Figure 11.6).

In left HS, grey matter loss was seen within the ipsilateral hippocampus and parietal lobe, with the maintenance of the GMV of the contralateral parietal lobe associated with better performance. DTI demonstrated that white matter connections within the frontoparietal network - the extremities of the SLF bilaterally and the right cingulum - and the integrity of the contralateral temporal lobe were important for working memory performance.

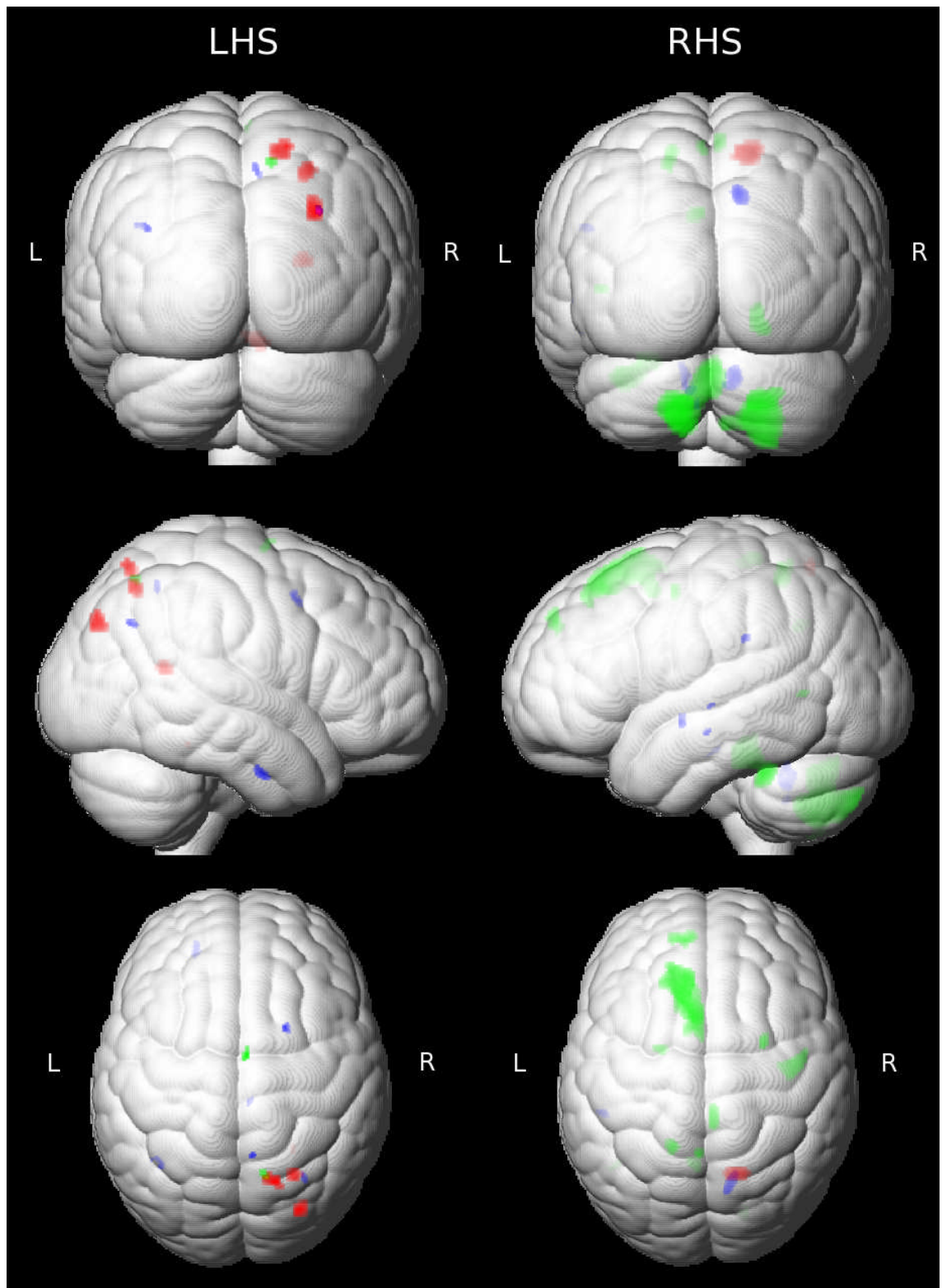


Figure 11.6 - Summary of changes observed in the working memory network in left and right HS.

Areas of reduced activation in the 2-back minus 0-back contrast for the working memory fMRI task (red); areas where the degree of grey matter atrophy correlated with working memory performance (green); and areas where working memory performance correlated with FA (blue).

In right HS, grey matter loss was also seen in the ipsilateral hippocampus, parietal lobe and other parts of this hemisphere. The structural integrity of the frontoparietal network was related to performance as working memory correlated with GMV in both frontal lobes and the precuneus and FA of the left parietal lobe and right cingulum. Both GMV and FA of the contralateral temporal lobe were related to performance.

11.4.2 Impaired Working Memory in TLE

Working memory is crucial for daily life and is dependent upon distributed neural networks including bilateral frontoparietal brain regions. These data provide further evidence that working memory is disrupted in TLE (reviewed in Stretton & Thompson 2012).

11.4.3 Frontoparietal Working Memory Network

The frontoparietal working memory network comprises strongly interconnected anterior (dorsolateral and ventrolateral prefrontal) and posterior (parietal cortex) regions (D'Esposito 2008) that undergo combined functional and structural maturation (Klingberg et al. 2002). Areas adjoining the superior frontal sulcus are consistently activated during both visuospatial and non-spatial working memory tasks (reviewed in Klingberg 2006) and are required for the voluntary control of attention, whilst the superior parietal lobe is involved in continuous updating of information (Owen et al. 2005) and manipulation of information within working memory (Koenigs et al. 2009).

Cortical thickness in these regions is related to verbal working memory performance following traumatic brain injury (Wilde et al. 2011) and frontal and parietal lesion burden correlates with attention and verbal working memory in multiple sclerosis (Sperling et al. 2001). Reduced functional (Liao et al. 2011) and structural (Riley et al. 2010) frontoparietal connectivity has been demonstrated in TLE. My data demonstrate reduced fMRI activation of the parietal lobe in both left and right HS. This was in the right hemisphere for both patient groups, in keeping with the right parietal dominance of the spatial working memory task employed (Smith & Jonides 1998, Owen et al. 2005).

11.4.4 Changes in Frontoparietal Grey Matter

VBM demonstrated GMV loss within the ipsilateral parietal lobe in both patient groups, and in left HS the integrity of grey matter in the contralateral parietal lobe was associated with better working memory, implying an important role for this part of the brain. The more widespread correlations observed in RHS may reflect the increased sensitivity of the working memory performance measure to seizures arising from the right hemisphere in view of the right dominance of the spatial working memory task.

Cortical thinning has been reported in patients with TLE, both HS and non-lesional, in areas that include the parietal lobe bilaterally (Labate et al. 2011). Further a meta-analysis of VBM studies in TLE showed that bilateral parietal atrophy was commonly observed (Keller & Roberts 2008).

All the studies in this meta-analysis used SPM2 or earlier, a 1.5T or 2T scanner and some involved heterogeneous populations whilst the present study includes a homogeneous population of patients with HS, data acquired on a 3T scanner and employs the DARTEL registration framework (Ashburner 2007)

included within the latest version of SPM. This registration framework was developed to improve intersubject registration and iteratively generates a group-specific template from the subjects. The templates generated however do not include the thalamus. The present study detected fewer regions of altered GMV than the meta-analysis, particularly in left HS. This may reflect increased sensitivity from the meta-analysis pooling several studies some of which include a greater number of participants, particularly controls, than the present study.

11.4.5 Voxel-Based Changes in Frontoparietal White Matter

The frontal and parietal cortices are connected by two major white matter pathways. The SLF is the primary direct pathway connecting the frontal and parietal cortices and runs between the MFG/dorsolateral prefrontal cortex and the supramarginal gyrus in the inferior parietal lobe. The cingulum forms part of the limbic system, runs within the cingulate gyrus around the corpus callosum and connects the prefrontal cortex and parietal lobes thus playing a role in working memory (Kondo et al. 2004), and continues inferiorly to terminate in the anteromedial temporal lobe. The anterior cingulate is thought to be required for executive control of attention and performance monitoring (Barch et al. 1997, Carter et al. 1998) whilst the posterior cingulate mediates spatial attention and orientation (Hirono et al. 1998, Small et al. 2003).

In children, development of verbal working memory correlates with FA of the left SLF and cingulum (Ostby et al. 2011) and development of spatial working memory correlates with FA at the extreme of the SLF adjacent to the left superior frontal sulcus (Nagy et al. 2004). Diffusion characteristics of the SLF predict spatial working memory performance in children (Vestergaard et al. 2011) and verbal working memory in adults (Burzynska et al. 2011). Working memory training promotes plasticity with changes observed around the inferior parietal sulcus, body of the corpus callosum and in the frontoparietal region (Takeuchi et al. 2010).

Frontoparietal white matter changes have also been observed in disease. Following traumatic brain injury, working memory performance correlates with FA in the left frontal region and cingulum (Wilde et al. 2011) and loss of integrity of the left SLF in recent onset schizophrenia is associated with impaired verbal working memory (Karlsgodt et al. 2008). In multiple sclerosis, working memory performance correlates with integrity of SLF, cingulum, forceps major and body and splenium of the corpus callosum (Dineen et al. 2009).

In left HS, I found that working memory performance correlated with diffusion characteristics of the frontal and parietal white matter bilaterally. The regions identified lie adjacent to the grey matter of the working memory network at the extremes of the SLF bilaterally and also within the right cingulum. In RHS, fewer areas were observed including the left parietal lobe and right cingulum. This supports the involvement of these two tracts in patients with TLE and the interpretation that impaired frontoparietal connectivity impacts on working memory performance. The differences between the groups are compatible with previous data showing more extensive and bilateral white matter changes in left HS than right HS (Ahmadi et al. 2009) with the left hemisphere postulated to be more vulnerable to early insults as it matures more slowly than the right hemisphere (Kemmons et al. 2011).

11.4.6 Tract-Based Changes in Frontoparietal White Matter

In view of the importance of the SLF and cingulum, I explored the correlation between their integrity and working memory performance. Whilst working memory performance correlated with the FA of the SLF and cingulum bilaterally in left HS, interpretation must be cautious as working memory performance also correlated with the mean FA of the entire white matter skeleton and these correlations do not remain significant after correction for multiple comparisons. In normal aging, an age-related fall in whole brain FA and rise in MD correlated with declining working memory (Charlton et al. 2006). Similarly, impaired working memory following traumatic brain injury correlated with global mean FA making any tract-specific correlations less specific (Palacios et al. 2011).

Changes along white matter tracts do not occur uniformly. Maps of diffusion parameters along the length of the uncinate, arcuate and inferior longitudinal fasciculi in patients with drug-resistant TLE demonstrate that these parameters may only be changed in part of the tracts with an emphasis on the extremities (Bernasconi et al. 2011). It is noteworthy that the changes observed, particularly within the left HS population, occur at either end of the SLF and so any whole tract based measures may fail to observe the full extent of these more local effects.

11.4.7 The Role of the Temporal Lobe

Two main hypotheses have been postulated for the disruption of working memory in TLE. Firstly, propagation of epileptic activity from the epileptogenic zone to eloquent cortex responsible for working memory (Hermann et al. 1988, Vlooswijk et al. 2011). Secondly, involvement of temporal structures, particularly the hippocampus, in the working memory network (Corcoran & Upton 1993).

The evidence for hippocampal involvement is conflicting. Initial reports suggest working memory is hippocampal-dependent with activation during different working memory functions, including encoding (Karlsgodt et al. 2005, Mainy et al. 2007), maintenance (Axmacher et al. 2007) and retrieval (Schon et al. 2009). Recently, however, there has been increasing recognition of the role of hippocampal deactivation. In healthy volunteers, bilateral hippocampal deactivation occurs (Astur & Constable 2004, Astur et al. 2005) and progressive deactivation with increasing working memory load (Cousijn et al. 2012) is relevant to task performance (Hampson et al. 2006). In TLE, deactivation of the ipsilateral hippocampus is disrupted and related to working memory performance (Stretton et al. 2012).

In my study, GMV of the left posterior temporal region correlated with working memory performance in RHS. FA of the right inferior temporal lobe was related to performance in both healthy controls and left HS, whilst in RHS the correlations were observed in the left temporal lobe. Contralateral hippocampal deactivation was preserved in both left and right HS (Stretton & Thompson 2012) and the structural integrity of the contralateral temporal lobe appears important in working memory performance. Together, these suggest that the temporal lobe plays a key role in the working memory network.

11.4.8 Strengths and Limitations

This study included a large homogeneous population of patients with TLE and HS who had both functional and structural imaging. Three modalities were employed to provide complementary information on both the grey matter (fMRI, VBM) and white matter (DTI) changes underlying impaired working memory in TLE. A single measure of working memory was derived to avoid the problems of multiple comparisons inherent in many studies. It does however combine both verbal and non-verbal measures of working memory and there is some evidence for material-specific lateralisation (Smith & Jonides 1998).

For VBM, the latest and most accurate form of intersubject image coregistration, DARTEL, was used to maximise accuracy, which in combination with a smaller group size and 3T acquisition may explain some of the differences observed in comparison to previous literature. For DTI, although the TBSS framework was used to coregister images, a voxel-based approach was subsequently employed to provide whole brain coverage. This technique was chosen to ensure the detection of changes not just confined to the white matter skeleton. This is important in light of recent data suggesting that tracts are not uniformly affected in TLE and many of the changes detected lie at the extremities of the white matter tracts in close proximity to the grey matter regions subserving working memory functions. All voxel-based analyses are however subject to limitations of the accuracy of image coregistration and results can vary with the choice of smoothing kernel size (Jones et al. 2005, Smith et al. 2006).

Changes in diffusion parameters are non-specific and could reflect a variety of underlying neuropathological changes, including the geometry and organization of axons, degree of myelination and axonal diameter, density and spacing (Basser & Pierpaoli 1996, Beaulieu 2002). Although DTI data have previously been combined with magnetic resonance spectroscopy to demonstrate axonal loss (Charlton et al. 2006) the spatial resolution is very poor. Current developments in DTI could disentangle the contribution by different factors to alterations in FA (Chapter 13).

11.5 Conclusion

This chapter provides evidence that working memory is affected in TLE and that there is impaired integrity of both grey and white matter in functionally relevant areas. I suggest that this forms the structural basis of the impairment of working memory in TLE, indicating widespread and functionally significant structural changes in patients with apparently isolated HS.

A cross-sectional study cannot determine whether these changes arose at the time of or before the onset of epilepsy or are a result of ongoing seizure activity. Longitudinal studies of medically and surgically treated patients to address this crucial point are required. In addition, combining functional and structural connectivity analyses of the temporal lobe could further explore the role of the temporal lobe in working memory.

Region	Cluster size (mm ³)	Z score	MNI coordinates
GMV: Left HS < Controls			
Left hippocampus	6770	6.98	-30,-30,-5
Left inferior parietal lobe	496	3.97	-24,-51,42
Left occipital lobe (calcarine)	199	3.48	-18,-103,-6
GMV: Left HS > Controls			
Right anterior cingulate	64	3.32	10,20,27
Right parietal lobe (postcentral)	44	3.25	12,-37,78
GMV: Right HS < Controls			
Right hippocampus	6318	7.21	33,-25,-6
Right occipital lobe (calcarine)	1823	4.49	15,-97,3
Right middle temporal gyrus (posterior)	2157	4.44	52,-64,7
Right middle frontal gyrus	1286	4.09	24,-12,52
Right superior temporal gyrus (anterior)	577	4.09	33,9,-30
Right caudate	520	3.75	15,6,21
Right occipital lobe (superior)	1944	3.73	24,-93,27
Right superior temporal gyrus (posterior)	263	3.72	56,-34,19
Right inferior parietal lobe	1073	3.67	42,-46,49
Right middle temporal gyrus	830	3.59	60,-37,1
Right occipital lobe (inferior occipital gyrus)	543	3.56	33,-82,-11
Right occipital lobe (calcarine)	250	3.52	-9,-73,10
Right middle temporal gyrus (posterior)	429	3.38	52,-72,25
Right posterior cerebellum	290	3.38	8,-67,-35
Left caudate	203	3.37	-15,6,19
Left occipital lobe (Brodmann area 18)	57	3.21	-20,-103,-5
Right precentral gyrus	41	3.19	51,-12,45
Left occipital lobe (calcarine)	34	3.18	-6,-96,4
GMV: Right HS > Controls			
None			

Table 11.3 - Regions of GMV loss in patients compared to controls

Uncorrected $p=0.001$, 10 voxel clusters = 33.75mm³.

Region	Cluster size (mm ³)	Z score	MNI coordinates
Left HS			
Right SFG (SMA)	49	3.33	3,-6,72
Right superior parietal lobe	51	3.25	14,-66,57
Left SFG (inferior)	47	3.24	-24,51,-20
Right HS			
Left frontal (medial SFG)	4384	4.05	-9,30,52
Posterior cerebellum	6649	3.88	0,-75,-32
Left cerebellum (fusiform)	2376	3.74	-22,-34,-23
Right frontal (MFG)	98	3.61	30,2,66
Right frontal (precentral)	1121	3.60	47,-9,42
Right cerebellum (inferior)	4590	3.59	24,-73,-51
Right frontal (paracentral lobule)	257	3.55	4,-36,66
Left precuneus	64	3.48	-2,-55,63
Left precuneus	182	3.48	-9,-60,34
Left precuneus	263	3.46	-18,-51,55
Left frontal (SFG)	408	3.44	-16,54,37
Right occipital (lingual gyrus)	405	3.38	20,-85,-8
Left frontal (SFG)	132	3.34	-21,-3,51
Left temporal (posterior MTG)	44	3.28	-45,-61,4

Table 11.4 - Regions where GMV correlated with working memory performance

Uncorrected $p=0.001$, 10 voxel clusters = 33.75 mm³.

MFG = middle frontal gyrus, MTG = middle temporal gyrus, SFG = superior frontal gyrus, SMA = supplementary motor area

Region	Cluster size (mm ³)	Z score	MNI coordinates
Healthy controls (positive correlation)			
Right ITG	33	3.54	49,-7,-35
Left SFG	14	3.48	-17,35,45
Left SFG	15	3.42	-22,-8,62
Healthy controls (negative correlation)			
Left superior parietal lobe / SLF	28	3.53	-34,-51,55
Left HS (positive correlation)			
Right MFG	59	3.79	25,8,50
Right ITG / fusiform gyrus	89	3.46	42,-8,-33
Left MFG	96	3.41	-21,47,-6
Left inferior parietal lobe (angular gyrus / SLF)	43	3.40	-40,-62,29
Right posterior cingulum	11	3.35	5,-29,43
Right posterior cingulum	37	3.34	7,-56,54
Right inferior parietal lobe	31	3.27	34,-68,37
Left HS (negative correlation)			
Left frontal (paracentral lobule)	22	3.55	-10,-30,71
Left parietal (postcentral)	31	3.32	-45,-24,58
Right HS (positive correlation)			
Right precuneus / cingulum	300	4.06	13,-70,43
Left inferior parietal lobe (supramarginal / SLF)	47	4.01	-52,-36,29
Left posterior MTG / R ILF	30	3.88	-52,-18,-14
Right anterior cerebellum	423	3.79	10,-56,-35
Left anterior cerebellum	219	3.71	-9,-55,-37
Left posterior STG / R ILF	29	3.41	-56,-20,-2
Left anterior PHG / cingulum	19	3.32	-28,-22,-22
Left anterior STG / R ILF	49	3.24	-51,-6,-10
Left posterior cerebellum	20	3.24	-5,-55,-46
Right HS (negative correlation)			
Right posterior cerebellum	15	3.20	28,-58,-53

Table 11.5 - Regions where FA correlated with working memory performance

Uncorrected p=0.001, age as covariate, 10 voxel clusters = 10 mm³.

ILF = inferior longitudinal fasciculus, ITG = inferior temporal gyrus, MFG = middle frontal gyrus, SFG = superior frontal gyrus, SLF = superior longitudinal fasciculus, STG = superior temporal gyrus

Region	Cluster size (mm ³)	Z score	MNI coordinates
Healthy controls (positive correlation)			
Right precuneus / occipital	50	3.43	17,-77,44
Healthy controls (negative correlation)			
None			
Left HS (positive correlation)			
None			
Left HS (negative correlation)			
Left SFG (medial) / cingulum	90	3.94	-10,25,55
Right superior parietal lobe / R IFOF	57	3.57	19,-70,52
Left superior parietal lobe / L SLF	25	3.38	-21,-63,56
Right frontal (orbitofrontal)	15	3.38	29,28,-20
Right cingulum	34	3.31	5,-58,43
Left parietal (postcentral)	17	3.31	-60,-12,22
Right frontal (orbitofrontal)	16	3.24	30,54,-8
Right HS (positive correlation)			
None			
Right HS (negative correlation)			
None			

Table 11.6 - Regions where MD correlated with working memory performance

Uncorrected $p=0.001$, age as covariate, 10 voxel clusters = 10 mm³.

IFOF = inferior fronto-occipital fasciculus, SFG = superior frontal gyrus, SLF = superior longitudinal fasciculus

12 LONGITUDINAL CHANGES IN DIFFUSION PARAMETERS FOLLOWING ANTERIOR TEMPORAL LOBE RESECTION

12.1 Introduction

Diffusion tensor imaging (DTI) enables the non-invasive assessment of white matter structure (Basser 1995) and is ideally suited for both cross-sectional and longitudinal studies. Cross-sectional white matter changes in TLE have been extensively studied and reveal abnormalities in diffusion parameters involving the ipsilateral temporal lobe white matter but also extending into structures such as the fornix, cingulum, external capsule and corpus callosum (see Section 3.2.2). However longitudinal changes following surgery have been less well addressed (see Section 3.2.3).

Several indices of tissue microstructure can be derived from DTI (see Section 2.4.2). Following surgical axonal transection, Wallerian degeneration of downstream white matter tracts leads to a reduction in fractional anisotropy (FA), a measure of the degree of directionality of water diffusion and by inference tissue integrity, and an increase in mean diffusivity (MD), a measure of the magnitude of diffusion (Wieshmann et al. 1999, Werring et al. 2000). Wallerian degeneration comprises two phases with an acute phase of fragmentation and dying-back of axons (lasting days to weeks) followed by a chronic phase of degradation and phagocytosis of myelin sheaths (lasting weeks to months). These can be distinguished by considering two components of mean diffusivity, axial diffusivity (AD) along the length of the axon and radial diffusivity (RD) perpendicular to this. An initial decrease in AD representing axonal degeneration is followed by a later increase in RD representing the myelin loss in both animal models (Song et al. 2003) and in patients with epilepsy undergoing corpus callosotomy (Concha et al. 2006).

Diffusion parameters may also be altered by seizures themselves and a localised reduction in MD without alteration in FA may be observed immediately after a seizure (Diehl et al. 2005). Baseline alterations in diffusion parameters could either represent acute functional changes through fluid shifts induced by seizures or chronic structural changes (Concha et al. 2006). Following surgery, Wallerian degeneration would be expected to occur only in tracts transected during surgery. Therefore changes elsewhere, including contralateral cortex, could result from a reversal of the acute effects of seizures or structural plasticity, whereby chronic structural changes are reversed.

Although several studies have investigated changes in white matter structure following temporal lobe surgery (Concha et al. 2007, Schoene-Bake et al. 2009, McDonald et al. 2010, Yogarajah et al. 2010, Nguyen et al. 2011, Faber et al. 2013, Liu et al. 2013), key limitations include small group sizes, a lack of healthy controls or preoperative data for comparison, heterogeneity in the surgical approaches or the timing of the postoperative imaging and only studying a single postoperative timepoint, predefined regions of interest or a single diffusion parameter (see Table 3.2).

In this chapter, I systematically assess the longitudinal changes in white matter following surgery avoiding these limitations. I investigate the baseline white matter changes in a large cohort of patients with TLE in comparison to healthy controls and then determine the longitudinal changes following a single surgical operation (ATLR) at two predefined postoperative timepoints using a whole brain approach. I employ tract-based spatial statistics (TBSS), a voxel-based technique optimised for diffusion data (Smith et al. 2006) that has high sensitivity to white matter changes in TLE (Focke et al. 2008) and avoids the problems of spatial smoothing (Jones et al. 2005) inherent in other techniques (see Section 2.6). This study design enables separation of the effects of the underlying disease from post-surgical changes, and a better understanding of the reversibility or otherwise of the baseline changes.

12.2 Methods

12.2.1 Subjects

I studied 20 patients with medically refractory left TLE (age range, 18–52 years; median, 35 years; 10 male) and 19 patients with right TLE (age range, 17–66 years; median, 41 years; 4 male) who underwent clinical assessment as detailed in Chapter 6 including DTI scans before surgery and at 3–4 months and 12 months following surgery.

All patients underwent ATLR by a single surgeon who employed a modified Spencer approach. Access to the temporal horn of the lateral ventricle was from the floor of the middle cranial fossa via the collateral sulcus. An anterolateral resection was followed by en bloc resection of the mesial structures. In addition, 14 healthy age-matched controls without any history of neurological or psychiatric disease were studied with DTI scans at three similar timepoints.

Clinical and demographic information are listed in Table 12.1. There was no significant difference in the distribution of age, age of onset or duration of epilepsy between the groups (independent samples Kruskal-Wallis test). Postoperative seizure outcome was determined at 12 months using the ILAE classification (Wieser et al. 2001) (Section 1.3.6.6.1).

12.2.2 DTI Processing

DTI scans were acquired as described in Chapter 6 (Section 6.5.3.2). Processing was undertaken with the FMRIB Diffusion Toolbox in FSL version 4.1.7 (Smith et al. 2004). Eddy current correction was performed using `eddy_correct`, brain extraction was performed with BET (Smith 2002) and diffusion tensors were fitted using `dtifit` to give FA, MD, AD and RD images. Voxelwise statistical analysis of these images was carried out using TBSS (Smith et al. 2006).

For the standard TBSS protocol, all subjects' FA data was aligned to a common space using nonlinear registration (FNIRT) and the mean FA image was thinned to create a skeleton representing the centres of all tracts common to the group. Each subject's aligned FA data was projected onto this skeleton and the

resulting data fed into voxelwise cross-subject statistics. The same transformations were used for the MD, RD and AD data.

Statistical inference was performed using a permutation based non-parametric method with 10000 permutations (Nichols & Holmes 2002) and threshold-free cluster enhancement (TFCE) was used to correct for multiple comparisons with a corrected p-value of <0.05 considered significant. TFCE is more sensitive than traditional cluster-based methods and avoids the need to set an arbitrary threshold or to smooth data (Smith & Nichols 2009). For the baseline comparisons, unpaired t-tests were used to determine the significant differences in diffusion parameters between either the left or right TLE group and healthy controls.

Significant clusters were displayed on the mean FA image from the group and identified with reference to the atlas tools supplied with FSL (ICBM-DTI-81 white-matter labels atlas and JHU white-matter tractography atlas). For both the cross sectional and longitudinal analyses, changes in FA and MD were the primary outcome with AD and RD measures used to clarify the nature of changes in significant regions.

Group	Controls (n=14)	LTLE (n=20)	RTLE (n=19)
Gender (M/F)	8/6	10/10	4/15
Handedness (R/L)	10/4	17/3	17/3
Age at scan	22-53 (39.5)	18-52 (35)	17-66 (41)
Age at onset	N/A	0.3-35 (12)	1-44 (11)
Duration of epilepsy	N/A	2-51 (16)	3-52 (22)
Days to first postoperative scan	75-361 (168)	81-183 (105.5)	75-243 (103)
Days to second postoperative scan	217-944 (456)	284-473 (377.5)	337-445 (384)
ILAE outcome at 12 months	N/A	Group 1: 15 Group 2: 3 Group 3: 1 Group 4: 1	Group 1: 14 Group 2: 1 Group 3: 2 Group 4: 1 Group 5: 1
Histological diagnosis	N/A	HS (n=13) HS + DNET (n=2) EFS (n=1) Gliosis (n=1) Cavernoma (n=2) Ependymoma (n=1)	HS (n=11) HS + FCD (n=1) EFS (n=4) DNET (n=3)

Table 12.1 - Clinical and demographic characteristics of patients

Data are given as range (median). HS = hippocampal sclerosis, DNET = dysembryoplastic neuroepithelial tumour, EFS = end folium sclerosis, FCD = focal cortical dysplasia.

12.2.3 Longitudinal Data

For the longitudinal analysis, the standard TBSS protocol was adapted to account for the surgical resection and the non-independence of data. Preoperative images were registered to the FMRIB58_FA standard space template using the standard approach. I delineated the surgical resection on the postoperative non-diffusion weighted image, dilated it and used it to create a brain mask excluding the resection. Each postoperative image was registered to the corresponding preoperative image using affine registration with FLIRT then non-linear registration with FNIRT with this mask used to weight the registration to avoid considering the area of resection. This warp and the warp from the preoperative image to the template were combined to directly register the postoperative image to the template with a single resampling and without considering the information from the resected area. This approach has been previously used by my group (Yogarajah et al. 2010).

For the statistical analysis, exchangeability blocks were defined each including the three datasets from each subject to account for the repeated measures and to ensure that the statistical test was of changes within subject. Comparisons were performed between the baseline scans and each set of postoperative scans considering each group (controls, left and right TLE) separately.

For each patient group (left or right TLE), a group resection mask was generated by registering the individual manually delineated resections to the template using the combined warp calculated as above, averaging these and then thresholding at 10%. The group resection masks were used to remove areas of significant change detected by TBSS due solely to an absence of that region following surgery.

After application of the group resection mask, clusters of significantly altered FA were deprojected and reverse normalized into the space of the native pre- and postoperative diffusion images. Mean FA, MD, AD and RD were calculated separately for clusters of decreased and increased FA at each timepoint to determine the magnitude of changes at the individual level. Baseline values and those at 12 months following surgery were compared using paired t-tests.

12.3 Results

12.3.1 Baseline Changes

12.3.1.1 Left TLE

In patients with left TLE, there were widespread reductions in FA compared to controls. Affected areas included the ipsilateral fornix, internal and external capsules, uncinate fasciculus (UF), superior longitudinal fasciculus (SLF), inferior longitudinal fasciculus (ILF), inferior fronto-occipital fasciculus (IFOF) and the posterior thalamic radiation/optic radiation (PTR/OR) (Figure 12.1 and Table 12.3 at end of chapter). There were also bilateral reductions in FA within the corpus callosum, cerebral peduncles and corona radiata. More limited increases in MD were observed in the left hemisphere including the fornix,

internal and external capsules, UF, ILF, IFOF and corpus callosum (Figure 12.2 and Table 12.3 at end of chapter).

12.3.1.2 Right TLE

In patients with right TLE, there were also widespread reductions in FA compared in controls. These were predominantly bilateral involving the fornix (both crura and column/body), internal and external capsules, UF, ILF, IFOF, PTR/OR, cingulate gyrus, corpus callosum, cerebral peduncles and corona radiata. In addition, there were reductions in the right parahippocampal cingulum (PHC) and SLF (Figure 12.3 and Table 12.4 at end of chapter). Bilateral increases in MD were observed in the internal and external capsules, UF, IFOF, corpus callosum and cerebral peduncles whilst increases confined to the right hemisphere were seen in the fornix, PHC, SLF, ILF and PTR/OR (Figure 12.4 and Table 12.4 at end of chapter).

12.3.1.3 Underlying Changes

In both groups, an increase in RD without a change in AD was found to underlie the observed changes in FA and MD. There were no significant changes in AD and no increases in FA or reductions in MD in either group.

12.3.2 Longitudinal Changes

12.3.2.1 Left TLE

Following left ATLR, a reduction in FA was seen in efferent tracts from the temporal lobe including the fornix, UF, PHC and PTR/OR (Figure 12.5 and Table 12.5 at end of chapter). Decreases in FA were observed in the more inferior parts of other tracts, including the internal and external capsules, corona radiata, SLF, ILF, IFOF, whilst a large contiguous area of increased FA was seen in the more superior parts of these tracts. Changes were present by 3-4 months with only a small further increase in extent of both decreased and increased FA by 12 months (Figure 12.5). A more limited region of increased MD was seen at 3-4 months including the fornix, UF, internal and external capsules, corona radiata, PTR/OR, SLF, ILF and IFOF that became less extensive by 12 months (Figure 12.6).

12.3.2.2 Right TLE

Following right ATLR, a reduction in FA was seen in the corpus callosum and efferent tracts from the temporal lobe including the fornix, UF and PHC/cingulum (Figure 12.7 and Table 12.6 at end of chapter). Decreases in FA were also observed in the more inferior parts of the internal and external capsules, corona radiata, PTR/OR, SLF, ILF and IFOF whilst there were increases in a contiguous region including the more superior parts of these structures. In contrast to left TLE, whilst the majority of changes were present by 3-4 months, these changes became more widespread by 12 months and only reached significance at the later timepoint in regions such as the right external capsule (Figure 12.7). Less widespread increases in MD were observed including the fornix, corpus callosum, internal and external capsules, corona radiata, SLF, ILF, IFOF and UF. Many of these changes were only significant at 3-4 months having resolved by 12 months (Figure 12.8).

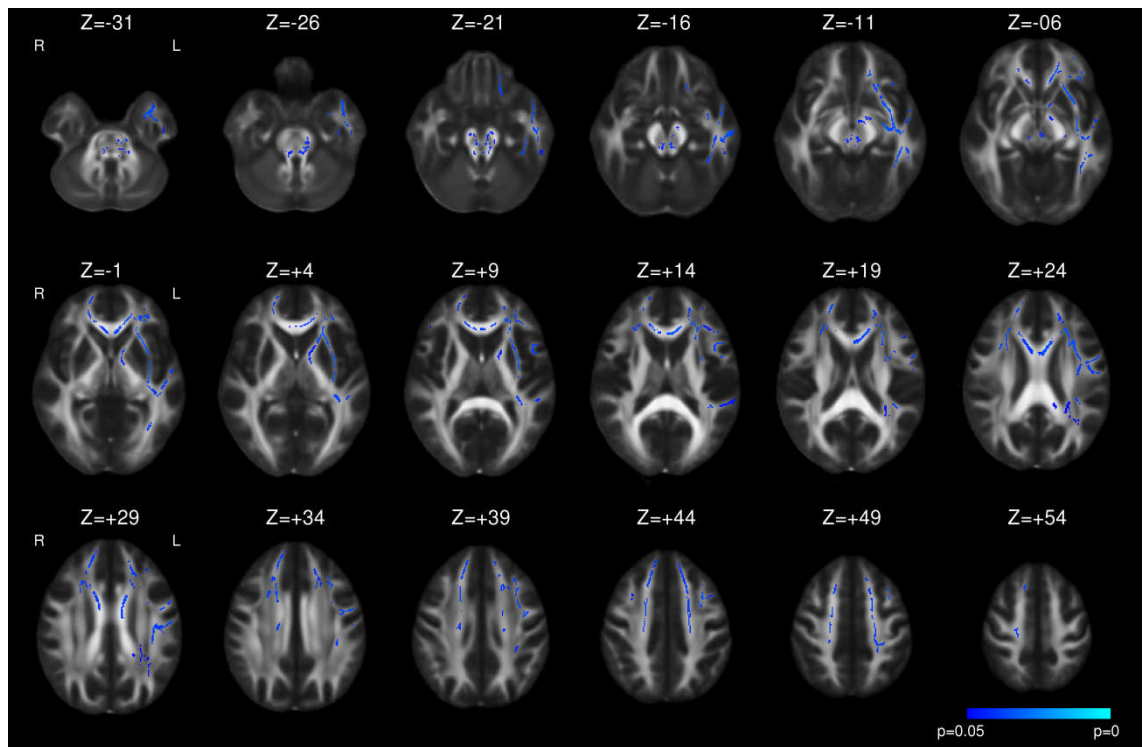


Figure 12.1 - Whole brain TBSS analysis of changes in FA in left TLE compared to controls

Decreases (blue to light blue) are shown with threshold-free cluster-enhanced correction ($p < 0.05$).

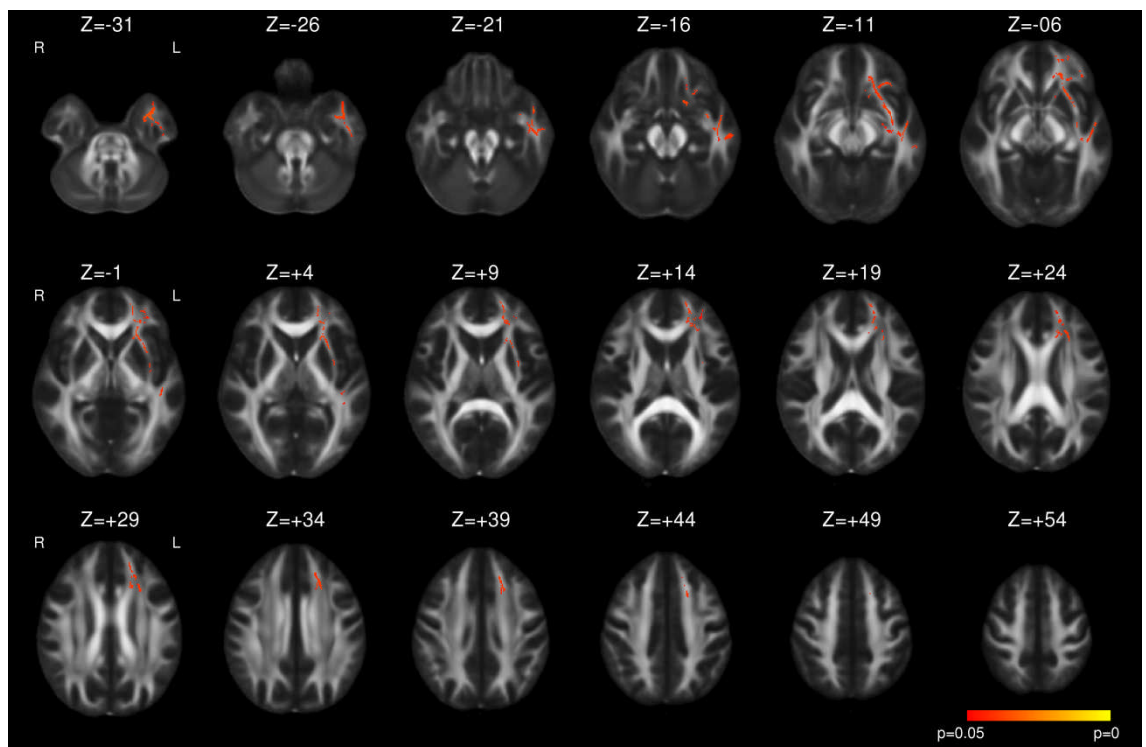


Figure 12.2 - Whole brain TBSS analysis of changes in MD in left TLE compared to controls

Increases (red to yellow) are shown with threshold-free cluster-enhanced correction ($p < 0.05$).

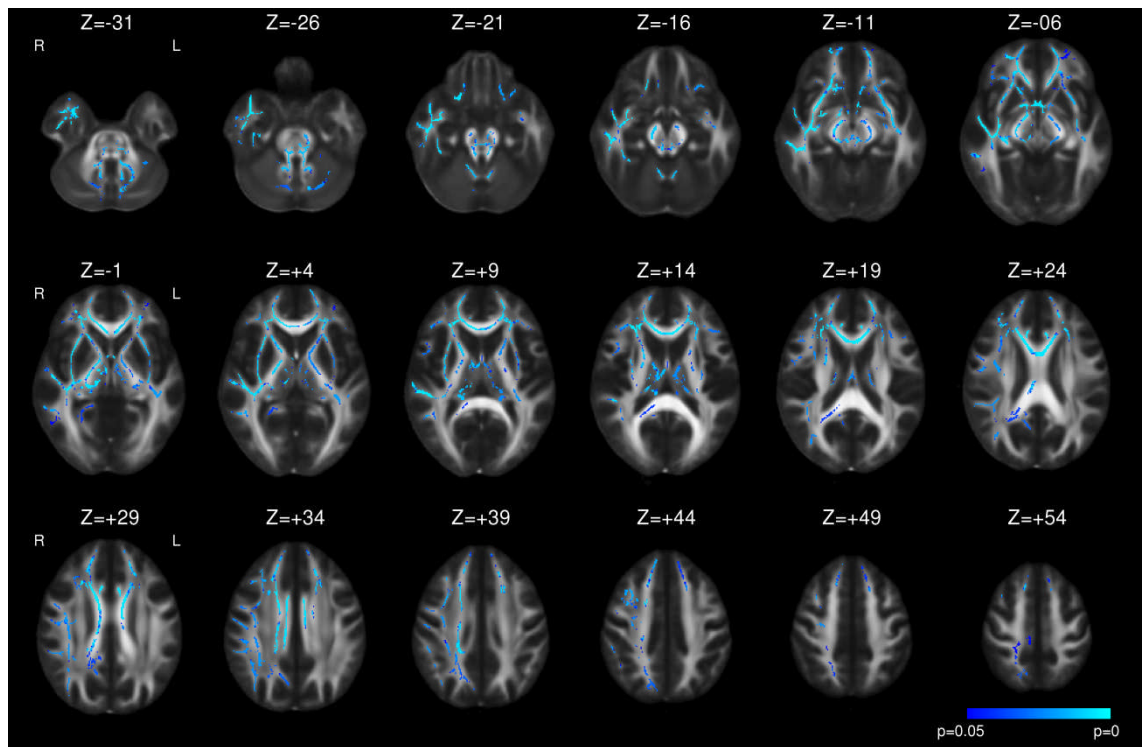


Figure 12.3 - Whole brain TBSS analysis of changes in FA in right TLE compared to controls

Decreases (blue to light blue) are shown with threshold-free cluster-enhanced correction ($p < 0.05$).

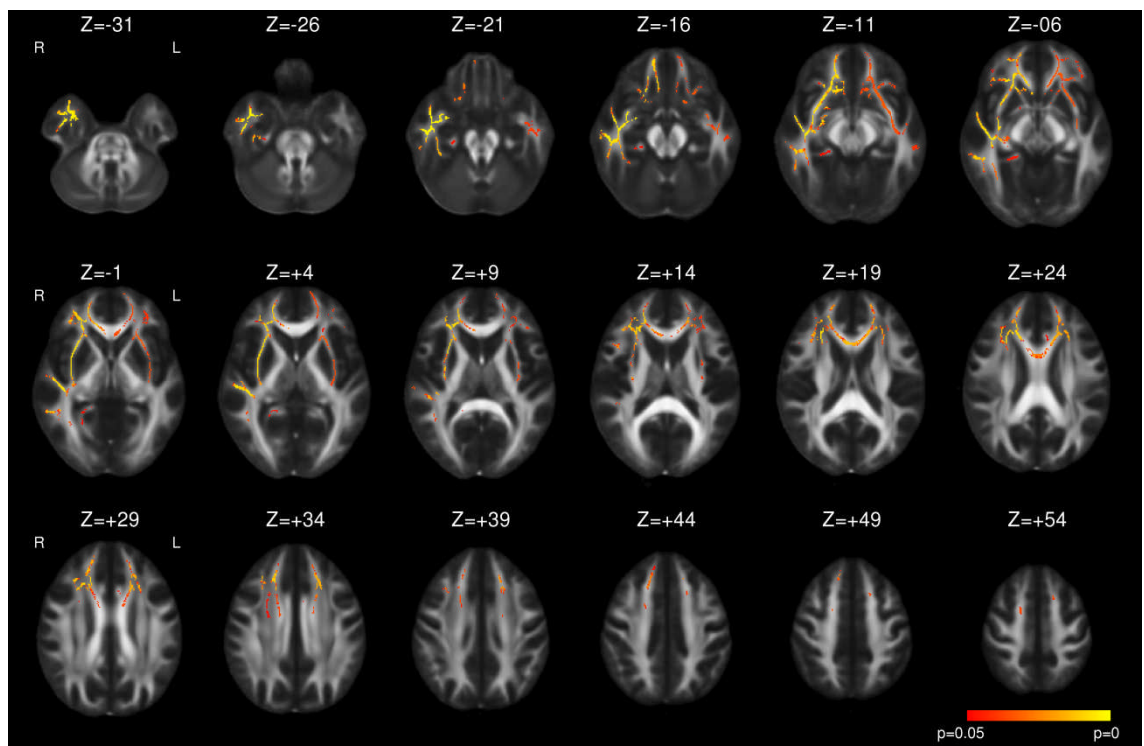


Figure 12.4 - Whole brain TBSS analysis of changes in MD in right TLE compared to controls

Increases (red to yellow) are shown with threshold-free cluster-enhanced correction ($p < 0.05$).

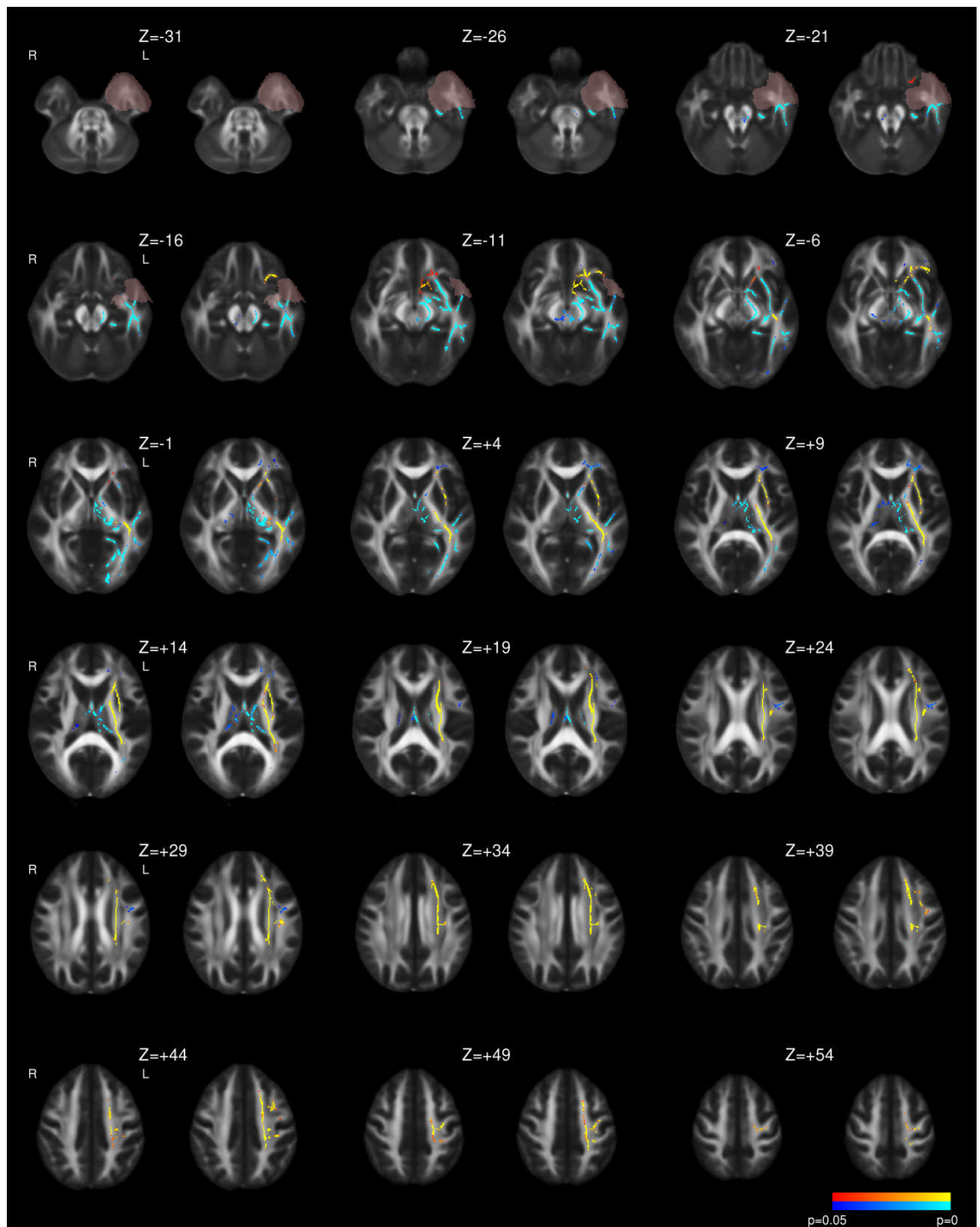


Figure 12.5 - Whole brain TBSS analysis of changes in FA following left ATL

Decreases (blue to light blue) and increases (red to yellow) are shown with threshold-free cluster-enhanced correction ($p < 0.05$). For each pair of images, the comparison of 3-4 months following surgery to preoperative imaging is on the left and the comparison of 12 months following surgery to preoperative imaging is on the right. The mask for the resected area is shown in pink.

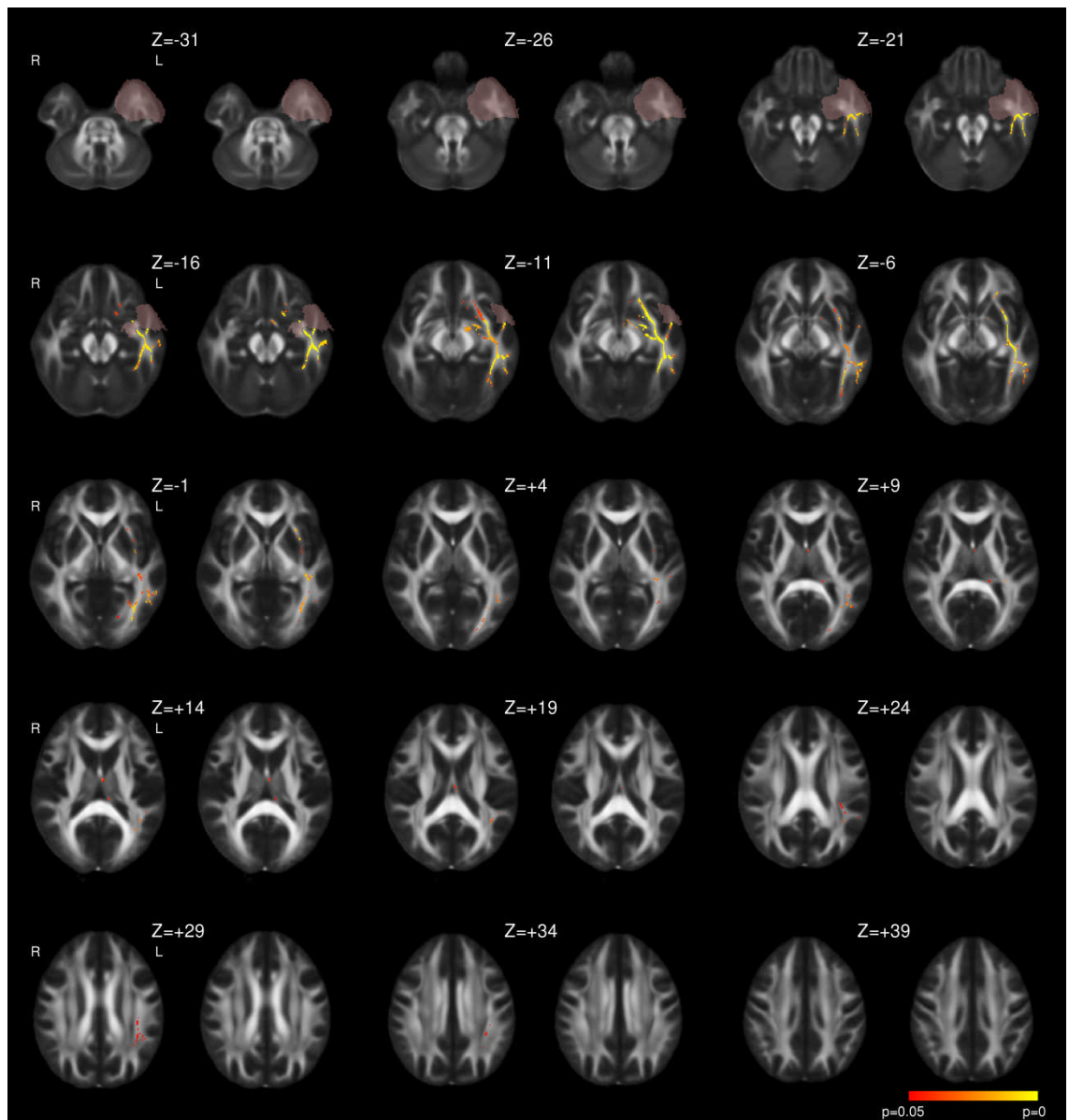


Figure 12.6 - Whole brain TBSS analysis of changes in MD following left ATL resection

Decreases (blue to light blue) and increases (red to yellow) are shown with threshold-free cluster-enhanced correction ($p < 0.05$). For each pair of images, the comparison of 3-4 months following surgery to preoperative imaging is on the left and the comparison of 12 months following surgery to preoperative imaging is on the right. The mask for the resected area is shown in pink.

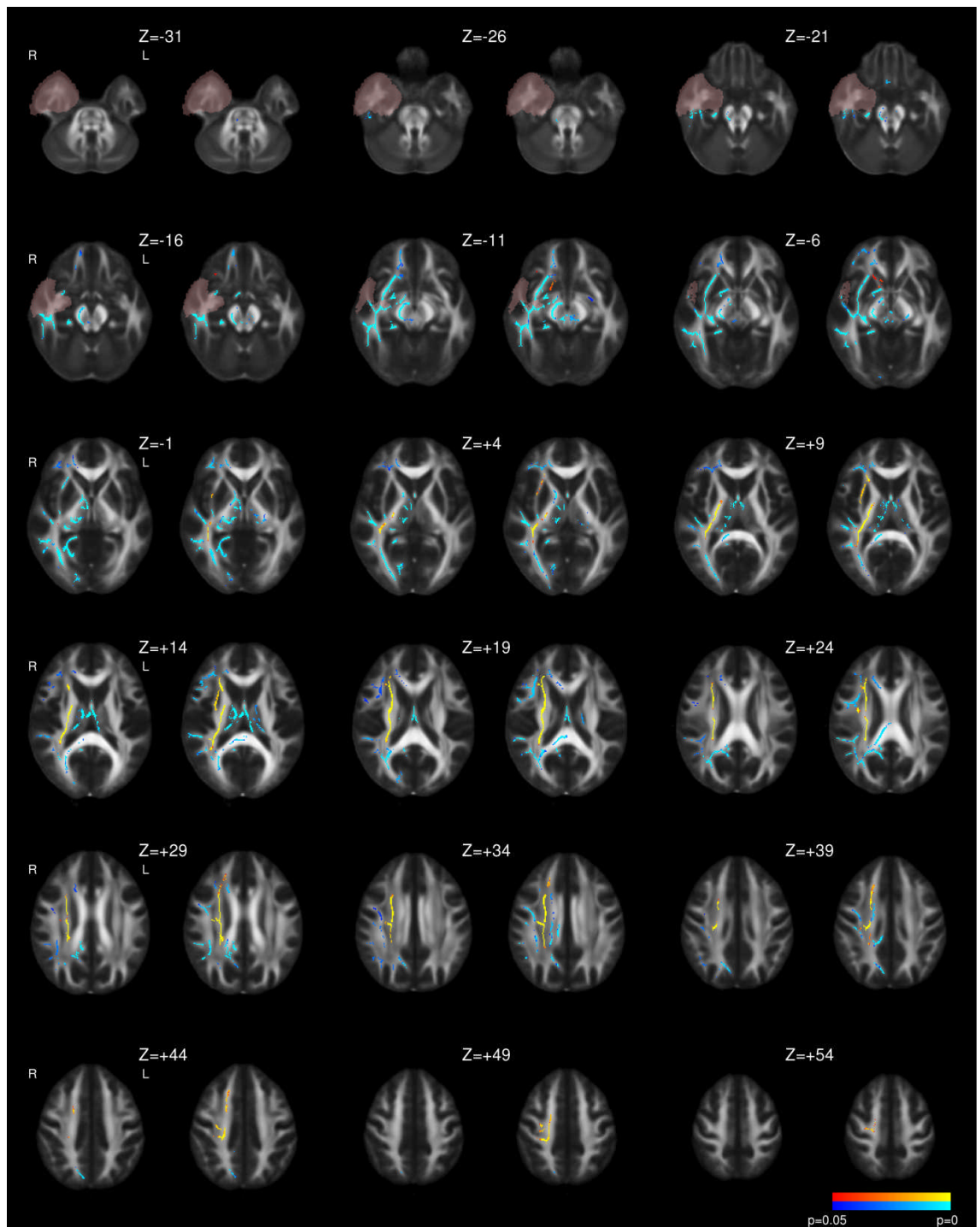


Figure 12.7 - Whole brain TBSS analysis of changes in FA following right ATL R

Decreases (blue to light blue) and increases (red to yellow) are shown with threshold-free cluster-enhanced correction ($p < 0.05$). For each pair of images, the comparison of 3-4 months following surgery to preoperative imaging is on the left and the comparison of 12 months following surgery to preoperative imaging is on the right. The mask for the resected area is shown in pink.

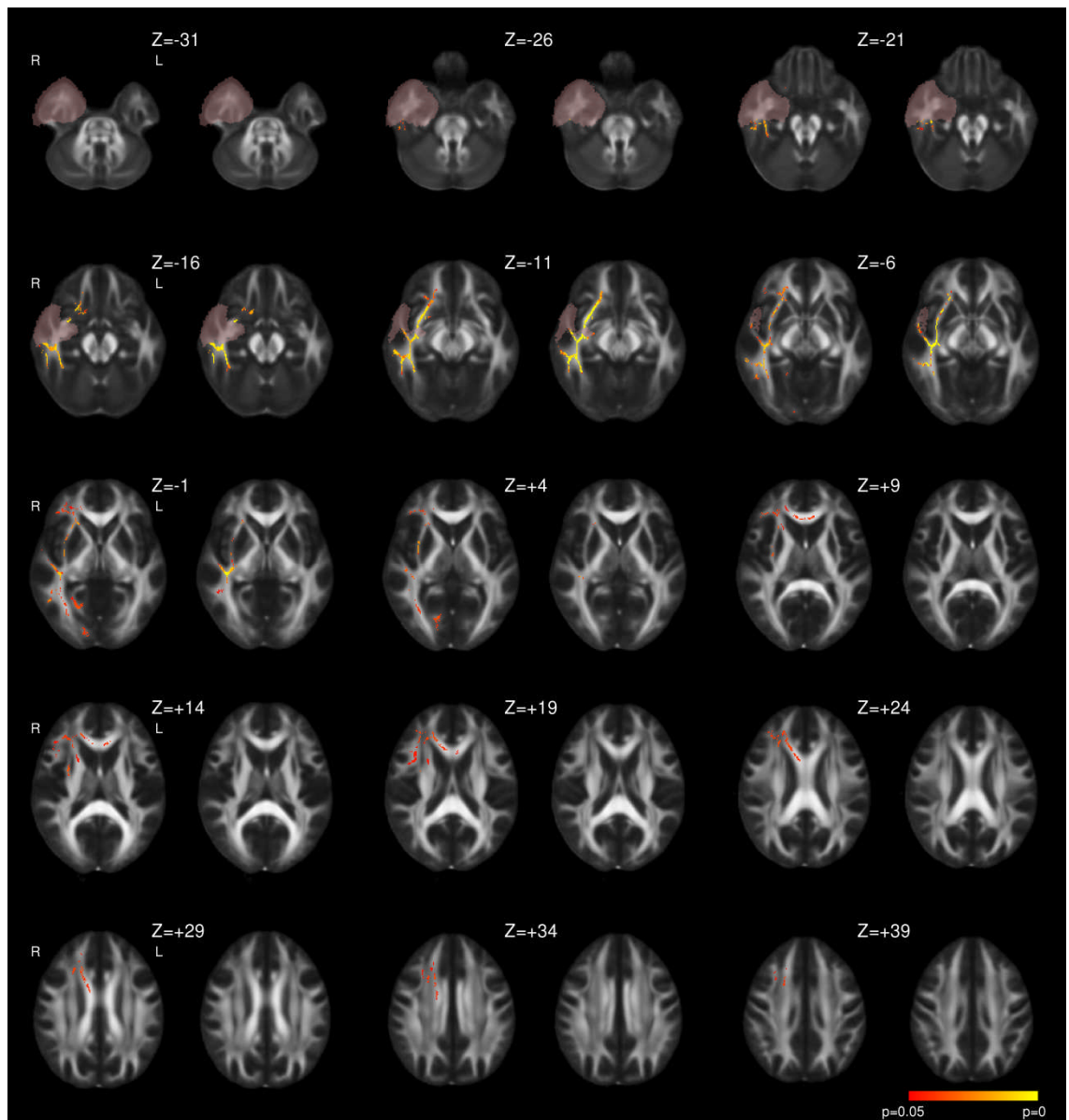


Figure 12.8 - Whole brain TBSS analysis of changes in MD following right ATL

Decreases (blue to light blue) and increases (red to yellow) are shown with threshold-free cluster-enhanced correction ($p < 0.05$). For each pair of images, the comparison of 3-4 months following surgery to preoperative imaging is on the left and the comparison of 12 months following surgery to preoperative imaging is on the right. The mask for the resected area is shown in pink.

12.3.2.3 Underlying Changes

In both groups of patients, the areas of increased MD were mostly a subset of those with decreased FA and the changes in these regions were predominantly driven by an increase in RD. There were some changes in AD, with reductions in the cerebral peduncles, ipsilateral fornix and part of the internal capsule and some increases in regions of increased MD.

In the deprojected reverse normalized cluster of decreased FA, the decrease in FA of 10.1% (left TLE, $p < 0.001$) or 7.5% (right TLE, $p < 0.001$) was associated with an increase in MD by 5.8% (left, $p < 0.001$) or 3.3% (right, $p < 0.001$) and RD by 10.9% (left, $p < 0.001$) or 7.3% (right, $p < 0.001$) but no significant change in AD (Table 12.2).

In contrast, in the contiguous area of increased FA and stable MD, the predominant change was an increase in AD with smaller areas of reduced RD in the ipsilateral internal capsule, corona radiata and posterior thalamic radiation. The increase in FA was 8.5% (left, $p < 0.001$) or 10.3% (right, $p < 0.001$), the increase in AD was 4.3% (left, $p < 0.001$) or 5.8% (right, $p < 0.001$) and the decrease in RD was 3.8% (left, $p < 0.001$) or 5.3% (right, $p < 0.001$) with no significant change in MD (Table 12.2).

No changes in any diffusion parameter were observed in healthy controls at either timepoint.

12.4 Discussion

12.4.1 Summary of Findings

At baseline, widespread reductions in FA encompassing both temporal and extratemporal structures were seen with more limited areas of increased MD. The changes were predominantly unilateral in left TLE but more bilateral in right TLE. Increased RD was found to underlie the change.

Following surgery, decreases in FA were seen in ipsilateral efferent tracts from the temporal lobe including the fornix, UF and cingulum. Elsewhere in the internal and external capsules, corona radiata, SLF, ILF and IFOF, ipsilateral decreases in FA were seen in the more inferior portions whilst increases in FA were seen in the more superior portions. The areas of reduced FA that were partly accompanied by increased MD were associated mainly with an increase in RD whilst the areas of increased FA but stable MD were associated with an increase in AD and to a lesser extent a reduction in RD.

In left TLE, little progression in FA changes was observed between 3-4 months and 12 months following surgery whilst in right TLE, the changes became more marked over this period. Changes in MD were less extensive by 12 months, particularly in right TLE. In both groups, postoperative changes were predominantly ipsilateral with only minimal contralateral changes.

Parameter	Baseline	3-4 months	12 months	% change (p-value)
<i>Left TLE: cluster of decreased FA</i>				
FA	0.424 (0.030)	0.384 (0.032)	0.381 (0.031)	-10.1% (p<0.001)
MD	0.840 (0.049)	0.882 (0.057)	0.889 (0.054)	+5.8% (p<0.001)
AD	1.254 (0.045)	1.258 (0.045)	1.263 (0.043)	+0.7% (p=0.204)
RD	0.632 (0.054)	0.695 (0.066)	0.701 (0.062)	+10.9% (p<0.001)
<i>Left TLE: cluster of increased FA</i>				
FA	0.438 (0.024)	0.467 (0.022)	0.476 (0.021)	+8.5% (p<0.001)
MD	0.755 (0.032)	0.759 (0.033)	0.757 (0.031)	+0.3% (p=0.474)
AD	1.143 (0.035)	1.184 (0.043)	1.193 (0.039)	+4.3% (p<0.001)
RD	0.561 (0.034)	0.547 (0.033)	0.540 (0.032)	-3.8% (<0.001)
<i>Right TLE: cluster of decreased FA</i>				
FA	0.441 (0.023)	0.411 (0.024)	0.408 (0.024)	-7.5% (p<0.001)
MD	0.795 (0.028)	0.822 (0.034)	0.821 (0.037)	+3.3% (p<0.001)
AD	1.207 (0.026)	1.206 (0.029)	1.200 (0.029)	-0.6% (p=0.168)
RD	0.589 (0.035)	0.631 (0.041)	0.632 (0.043)	+7.3% (p<0.001)
<i>Right TLE: cluster of increase FA</i>				
FA	0.469 (0.028)	0.505 (0.028)	0.517 (0.021)	+10.3% (p<0.001)
MD	0.725 (0.019)	0.729 (0.020)	0.728 (0.019)	+0.5% (p=0.407)
AD	1.136 (0.049)	1.187 (0.043)	1.201 (0.046)	+5.8% (p<0.001)
RD	0.519 (0.021)	0.500 (0.024)	0.492 (0.016)	-5.3% (p<0.001)

Table 12.2 - Summary of magnitude of longitudinal changes in diffusion parameters in the clusters of significantly altered FA in patients with TLE

Values are quoted as mean (standard deviation). MD, AD, RD and given in units of $\text{mm}^2 \text{s}^{-1} \times 10^{-3}$. The % change is the change from baseline to 12 months post surgery.

12.4.2 Biological Basis of Baseline Changes

The baseline changes of reduced FA, increased MD and RD are in keeping with previous reports (Arfanakis et al. 2002, Concha et al. 2005, Gross et al. 2006, Focke et al. 2008) and are likely to be a consequence of damaged or deficient myelination (Song et al. 2003). Other possibilities include altered membrane permeability or altered neuronal packing density (Arfanakis et al. 2002). I found more bilateral changes in right TLE than left TLE, the converse of previous studies (Ahmadi et al. 2009, Kemmotsu et al. 2011). However as diffusion changes in right TLE were found to be more widespread and bilateral in females than males (Oguz et al. 2013), the gender imbalance in the right TLE group, which was 79% female, could explain this difference. The presence of baseline changes highlights the importance of including controls and preoperative imaging, as a previous study comparing postoperative imaging in patients to healthy controls and demonstrating widespread reductions in FA within ipsilateral tracts was unable to conclude whether these changes were pre-existing as a result of the disease or developed following surgery (Schoene-Bake et al. 2009).

12.4.3 Dichotomy of Longitudinal Changes

Following surgery, the observed changes can be split into two contrasting regions. In tracts involved in or nearby the resection, the observed changes (reduced FA, increased MD and RD) are in keeping with the chronic phase of Wallerian degeneration following axonal transaction and comparable to previously reported progressive changes following surgery within the ipsilateral fornix and cingulum (Concha et al. 2007) and other tracts (McDonald et al. 2010, Yogarajah et al. 2010).

There is a second distinct more superiorly located region including the corona radiata, internal and external capsules and nearby tracts in which an increase in FA without altered MD is driven mainly by a rise in AD but also a fall in RD. My group has previously reported similar longitudinal changes in a different cohort (Yogarajah et al. 2010) which was the first study to conclusively report an increase in FA following surgery. Including a control group in the present study allows a comparison of these changes to baseline abnormalities and by studying two postoperative timepoints I demonstrated that in right TLE, additional changes develop by 12 months, particularly an increase in FA in the external capsule.

12.4.4 Biological Implications and Causes of Increased Postoperative FA

Postoperative changes could represent reversal of a functional, metabolic, disruption (Concha et al. 2005, Yogarajah et al. 2010) and support for this view comes from other imaging modalities. FDG-PET shows a normalization of glucose metabolism in the remaining ipsilateral temporal cortex (Gogoleva et al. 1997) and extratemporal regions including the inferior frontal lobe, thalamus and parietal lobe (Spanaki et al. 2000, Takaya et al. 2009) following surgery. Moreover, magnetic resonance spectroscopy shows that N-acetylaspartate (NAA)/creatine (Cr) ratios normalise in the ipsilateral (Cendes et al. 1997, Serles et al. 2001) and contralateral (Hugg et al. 1996, Lantz et al. 2006) temporal cortex in patients rendered seizure free by surgery.

Following a seizure, an acute reduction in MD without a change in FA is observed (Diehl et al. 2005). This differs from the baseline changes (reduced FA, increased MD), is not the converse of the recovery following surgery (increased FA, unchanged MD) and the acute effects of seizures are unlikely to have a significant contribution in my study as all but three patients had been seizure free for the 24 hours prior to baseline imaging.

An alternative explanation is underlying structural changes that may partially reverse. Previous data suggest that the bilateral baseline diffusion changes within the fornix, cingulum and external capsule fail to normalise in the contralateral hemisphere following surgery that resulted in seizure freedom (Concha et al. 2007) and the authors used these data to argue for an underlying preoperative structural, rather than functional change. In the present study, I show that some of the preoperative diffusion changes do reverse in more distant ipsilateral cortex, although similarly I did not see any resolution of contralateral changes. Changes could be driven by the resolution of structural changes or the effects of plasticity and neuronal remodelling. For example, the increase in AD could represent axonal regeneration whilst the reduction in RD could represent improvement in myelination.

Caution must however be attached to the interpretation of the observed postoperative increases in FA as selective degeneration of a single fibre population from two crossing fibre populations in the corona radiata has previously been shown to lead to a paradoxical rise in FA in patients with Alzheimer's disease (Douaud et al. 2011). Whilst this may be contributory in the corona radiata and adjacent tracts, it seems less likely in the internal and external capsules where fibres are expected to be more coherent.

12.4.5 Time Course of Postoperative Change

The time course of postoperative changes can only be assessed by longitudinal studies involving more than one postoperative timepoint. McDonald and colleagues looked at changes in FA using a region-of-interest based approach in a 7 patients at 2 months and 12 months following ATLR (McDonald et al. 2010). A reduction of FA in ipsilateral tracts including the UF, PHC, ILF, IFOF, corpus callosum and bilateral fornix was seen by 2 months with no further change by 12 months. These changes were confirmed in the present study, but by using a larger sample and whole brain analysis I was also able to detect increases in FA and show some limited progression between 3-4 months and 12 months. I also investigated other diffusion indices to clarify the nature of these changes.

Another study looked at patients with left TLE only undergoing SAH (Faber et al. 2013). Follow up was at 3-6 months and 12 months, although the intervals were wide with the late group (11-23 months). The reported changes were reduced FA in the fornix and PHC at 3-6 months and later in the UF. Supplementary data suggest reductions in FA were more widespread predominantly ipsilaterally along with some increases in the ipsilateral SLF and ILF, which is in keeping with the present findings. However a serious limitation of this study is that the groups at 3-6 months and 12 months were not the same thus precluding any true inference on longitudinal changes.

The time course I observed suggests that the majority of postoperative change occurs within the first few months following surgery, although changes in right TLE appeared to occur slightly later and continue beyond this point. No previous studies exist to compare the time course between left and right TLE. The majority of the patients were right handed and structural plasticity may occur more readily in the dominant hemisphere. Alternatively, the more bilateral baseline changes in the right TLE group may contribute to the slower time course of plasticity. Since the groups were matched on demographic and clinical variables aside from gender, this finding needs replication to ensure that gender is not a contributor.

12.4.6 Strengths and Limitations

This is the first study of patients undergoing temporal lobe epilepsy surgery with diffusion imaging both before and at two postoperative timepoints that also includes a control group with imaging at the same timepoints. This enables a baseline comparison and a detailed study of longitudinal changes. The large cohort allowed separate analysis of left and right TLE. All patients underwent the same surgery (ATLR) by the same surgeon, as other operations may yield different consequences.

Rather than limiting the analysis to certain tracts of interest, a whole brain analysis was performed using TBSS to give the highest sensitivity and reliability and hand drawn resection masks were employed to optimise image registration and exclude the resected regions from the detected changes. Whilst some prior studies investigated only changes in FA, I considered multiple diffusion parameters to provide a clearer explanation for the changes.

As the majority of changes were present at the first postoperative scan, further information may come from earlier timepoints. Without these, the early stages of Wallerian degeneration cannot be detected. A recent paper looking at diffusion changes in the first week following surgery found findings inconsistent with axonal injury models but that could instead have resulted from axonal swelling (Liu et al. 2013). There are also practical difficulties in early scans. Future work should look at changes at earlier timepoints such as 2, 4 and 8 weeks.

I included all patients, both seizure free and otherwise, in the analysis whilst others have only studied seizure free patients (Concha et al. 2007, McDonald et al. 2010, Nguyen et al. 2011). Although the majority of patients were seizure free, in patients with ongoing seizures this could induce diffusion changes that confound any changes from plasticity and reduce the sensitivity of the analysis.

12.5 Conclusion

I demonstrated widespread baseline changes in diffusion parameters in patients with TLE in the temporal lobe and extratemporal structures. Following surgery, changes consistent with Wallerian degeneration occurred in the ipsilateral temporal lobe and adjacent tracts whilst there are changes compatible with structural plasticity more superiorly in the ipsilateral hemisphere. The majority of changes were present within 3-4 months after surgery, but further progression occurred up to 12 months particularly in right TLE. Only minimal change occurred in the contralateral cortex following surgery. This study provides a description of the postoperative changes and future work will look at how these changes relate to changes in clinical outcomes, such as language or memory function on neuropsychological assessment.

Baseline decreases in FA	Corpus callosum, genu (p=0.034)
	Corpus callosum, body (p=0.035)
	Corpus callosum, splenium (p=0.049)
	Left fornix (cres) (p=0.035)
	Left anterior limb of internal capsule (p=0.033)
	Left posterior limb of internal capsule (p=0.043)
	Left retrolenticular part of internal capsule (p=0.035)
	Left anterior corona radiata (p=0.033)
	Right anterior corona radiata (p=0.036)
	Left superior corona radiata (p=0.034)
	Right superior corona radiata (p=0.036)
	Left posterior corona radiata (p=0.048)
	Left posterior thalamic radiation (p=0.037)
	Left inferior fronto-occipital fasciculus (p=0.033)
	Left inferior longitudinal fasciculus (p=0.034)
	Left external capsule (p=0.033)
	Left superior longitudinal fasciculus (p=0.034)
	Left uncinate fasciculus (p=0.034)
	Left corticospinal tract (p=0.041)
	Left cerebral peduncle (p=0.042)
	Right cerebral peduncle (p=0.045)
	Left superior cerebellar peduncle (p=0.042)
	Right superior cerebellar peduncle (p=0.042)
	Middle cerebellar peduncle (p=0.041)
	Left inferior cerebellar peduncle (p=0.045)
	Left medial lemniscus (p=0.041)
	Right medial lemniscus (p=0.045)
Baseline increases in MD	Corpus callosum, genu (p=0.040)
	Left fornix (cres) (p=0.043)
	Left anterior limb of internal capsule (p=0.038)
	Left anterior corona radiata (p=0.038)
	Left inferior fronto-occipital fasciculus (p=0.038)
	Left inferior longitudinal fasciculus (p=0.033)
	Left external capsule (p=0.038)
	Left uncinate fasciculus (p=0.038)

Table 12.3 - Baseline changes in diffusion parameters in left TLE

The p-values for the maximum changes are given.

Baseline decreases in FA	Corpus callosum, genu (p=0.003)
	Corpus callosum, body (p=0.003)
	Corpus callosum, splenium (p=0.006)
	Column/body of fornix (p=0.012)
	Left fornix (cres) (p=0.001)
	Right fornix (cres) (p=0.003)
	Left anterior limb of internal capsule (p=0.022)
	Right anterior limb of internal capsule (p=0.005)
	Left posterior limb of internal capsule (p=0.022)
	Right posterior limb of internal capsule (p=0.005)
	Left retrolenticular portion of internal capsule (p=0.019)
	Right retrolenticular portion of internal capsule (p=0.004)
	Left anterior corona radiata (p=0.007)
	Right anterior corona radiata (p=0.003)
	Left superior corona radiata (p=0.009)
	Right superior corona radiata (p=0.004)
	Right posterior corona radiata (p=0.006)
	Right posterior thalamic radiation/optic radiation (p=0.023)
	Left inferior fronto-occipital fasciculus (p=0.007)
	Right inferior fronto-occipital fasciculus (p=0.003)
	Left inferior longitudinal fasciculus (p=0.013)
	Right inferior longitudinal fasciculus (p=0.003)
	Left external capsule (p=0.010)
	Right external capsule (p=0.003)
	Left cingulate gyrus (p=0.005)
	Right cingulate gyrus (p=0.005)
	Right parahippocampal cingulum (p=0.040)
	Right superior longitudinal fasciculus (p=0.017)
	Right superior fronto-occipital fasciculus (p=0.012)
	Left uncinate fasciculus (p=0.010)
	Right uncinate fasciculus (p=0.003)
	Left corticospinal tract (p=0.012)
	Right corticospinal tract (p=0.032)
	Left cerebral peduncle (p=0.014)
	Right cerebral peduncle (p=0.005)
	Left superior cerebellar peduncle (p=0.012)
	Right superior cerebellar peduncle (p=0.011)
	Middle cerebellar peduncle (p=0.012)
	Left inferior cerebellar peduncle (p=0.012)
	Right inferior cerebellar peduncle (p=0.012)
	Left medial lemniscus (p=0.012)
	Right medial lemniscus (p=0.012)

Baseline increases in MD	Corpus callosum, genu (p=0.008)
	Corpus callosum, body (p=0.012)
	Right fornix (cres) (p=0.005)
	Left anterior limb of internal capsule (p=0.033)
	Right anterior limb of internal capsule (p=0.023)
	Right retrolenticular portion of internal capsule (p=0.006)
	Left anterior corona radiata (p=0.016)
	Right anterior corona radiata (p=0.007)
	Left superior corona radiata (p=0.026)
	Right superior corona radiata (p=0.029)
	Right posterior thalamic radiation/optic radiation (p=0.029)
	Left inferior fronto-occipital fasciculus (p=0.016)
	Right inferior fronto-occipital fasciculus (p=0.002)
	Left inferior longitudinal fasciculus (p=0.033)
	Right inferior longitudinal fasciculus (p=0.002)
	Left external capsule (p=0.032)
	Right external capsule (p=0.002)
	Left cingulate gyrus (p=0.048)
	Right parahippocampal cingulum (p=0.046)
	Right superior longitudinal fasciculus (p=0.033)
	Left uncinate fasciculus (p=0.033)
	Right uncinate fasciculus (p=0.002)

Table 12.4 - Baseline changes in diffusion parameters in right TLE

The p-values for the maximum changes are given.

Postoperative reduction in FA following left ATLR	Left fornix (cres) (p<0.001)
	Column/body of fornix (p<0.001)
	Left uncinate fasciculus (p<0.001)
	Left parahippocampal cingulum (p<0.001)
	Left cerebral peduncle (p<0.001) (containing corticopontine, corticospinal, corticobulbar fibres)
	Left posterior thalamic radiation/optic radiation (p<0.001, p=0.009)
	Left corticospinal tract (p<0.001, p=0.009)
	Left superior cerebellar peduncle (p=0.034 at 3-4 months only)
Postoperative reduction in FA following left ATLR only in part of tract (increases elsewhere)	Right cerebral peduncle (p=0.034 at 12 months only)
	Left anterior limb of internal capsule (p<0.001, p=0.002)
	Left posterior limb of internal capsule (p<0.001)
	Left retrolenticular portion of internal capsule (p=0.005 at 12 months only)
	Left anterior corona radiata (p=0.034, p=0.017)
	Left inferior fronto-occipital fasciculus (p<0.001)
	Left inferior longitudinal fasciculus (p<0.001)
	Left external capsule (p<0.001)
Postoperative increases in FA following left ATLR	Left superior longitudinal fasciculus (p<0.001) (temporal portion)
	Left anterior limb of internal capsule (p<0.001)
	Left posterior limb of internal capsule (p<0.001)
	Left retrolenticular portion of internal capsule (p<0.001)
	Left anterior corona radiata (p<0.001)
	Left superior corona radiata (p<0.001)
	Left posterior corona radiata (p<0.001)
	Left posterior thalamic radiation/optic radiation (p<0.001)
Postoperative increases in MD following left ATLR	Left inferior longitudinal fasciculus (p<0.001)
	Left inferior fronto-occipital fasciculus (p<0.001)
	Left external capsule (p<0.001)
	Left superior longitudinal fasciculus (p<0.001) (frontoparietal portion)
	Left retrolenticular portion of internal capsule (p=0.024, p=0.002)
	Left anterior corona radiata (p=0.004 at 12 months only)
	Left posterior thalamic radiation/optic radiation (p=0.008, p=0.019)
	Left inferior fronto-occipital fasciculus (p=0.003, p<0.001)
	Left inferior longitudinal fasciculus (p=0.003, p<0.001)
	Left external capsule (p=0.002, p<0.001)
	Left fornix (p=0.003, p<0.001)
	Left superior longitudinal fasciculus (p=0.025 at 3-4 months only)
	Left uncinate fasciculus (p=0.002, p<0.001)

Table 12.5 - Summary of longitudinal diffusion changes following left ATLR

The p-values for the maximum change at 3-4 months and 12 months within each region are given. A single p-value is quoted if they are the same.

Postoperative reduction in FA following right ATLR	Corpus callosum, genu (p=0.035, p=0.014)
	Corpus callosum, body (p=0.035, p=0.004)
	Corpus callosum, splenium (p=0.001, p=0.003)
	Right fornix (cres) (p<0.001)
	Column/body of fornix (p<0.001)
	Right cingulate gyrus (p=0.003)
	Right parahippocampal cingulum (p<0.001)
	Right uncinate fasciculus (p<0.001)
	Right cerebral peduncle (p<0.001)
	Left cerebral peduncle (p=0.011, 12 months only)
	Left anterior limb of internal capsule (p=0.012, 12 months only)
	Right corticospinal tract (p=0.002, 12 months only)
	Right superior cerebellar peduncle (p=0.039, 12 months only)
	Middle cerebellar peduncle (p=0.004, 12 months only)
Postoperative reduction in FA following right ATLR only in part of tract (increases elsewhere)	Right anterior limb of internal capsule (p<0.001, p=0.003)
	Right posterior limb of internal capsule (p<0.001)
	Right retrolenticular portion of internal capsule (p=0.001, 12 months only)
	Right anterior corona radiata (p<0.001)
	Right superior corona radiata (p=0.011, 12 months only)
	Right posterior corona radiata (p=0.003, p=0.004)
	Right posterior thalamic radiation/optic radiation (p<0.001, p=0.003)
	Right inferior fronto-occipital fasciculus (p<0.001)
	Right inferior longitudinal fasciculus (p<0.001)
	Right external capsule (p<0.001)
Postoperative increases in FA following right ATLR	Right superior longitudinal fasciculus (p<0.001)
	Right anterior limb of internal capsule (p<0.001)
	Right posterior limb of internal capsule (p<0.001)
	Right retrolenticular portion of internal capsule (p<0.001)
	Right anterior corona radiata (p<0.001)
	Right superior corona radiata (p<0.001)
	Right posterior corona radiata (p<0.001)
	Right posterior thalamic radiation/optic radiation (p<0.001)
	Right inferior fronto-occipital fasciculus (p<0.001)
	Right inferior longitudinal fasciculus (p=0.001, p<0.001)
Postoperative increases in MD following right ATLR	Right external capsule (p=0.005, 12 months only)
	Right superior longitudinal fasciculus (p=0.003, p<0.001)
	Corpus callosum, genu (p=0.036, 3-4 months only)
	Corpus callosum, body (p=0.036, 3-4 months only)
	Right fornix (cres) (p=0.002, 12 months only)
	Right anterior limb of internal capsule (p=0.021, 3-4 months only)
	Right retrolenticular portion of internal capsule (p=0.009, p<0.001)
	Right anterior corona radiata (p=0.016, p=0.001)
	Right superior corona radiata (p=0.034, 3-4 months only)
	Right posterior thalamic radiation/optic radiation (p=0.016)
	Right inferior fronto-occipital fasciculus (p=0.005, p<0.001)

Right inferior longitudinal fasciculus (p=0.006, p<0.001)
Right external capsule (p=0.005, p<0.001)
Right superior longitudinal fasciculus (p=0.034, 3-4 months only)
Right uncinate fasciculus (p=0.005, p<0.001)

Table 12.6 - Summary of longitudinal diffusion changes following right ATL

The p-values for the maximum change at 3-4 months and 12 months within each region are given. A single p-value is quoted if they are the same.

13 ADVANCED DIFFUSION MODELS COULD AID ASSESSING PATIENTS WITH FOCAL CORTICAL DYSPLASIA

13.1 Introduction

Identification of the epileptogenic zone is critical in planning surgical treatment but up to 20-30% of patients have normal structural MRI scans (Duncan 2010). Drug-resistant epilepsy is associated with malformations of cortical development (MCD) in 15-20% of adult patients and over 50% of paediatric patients.

The most common type, focal cortical dysplasia (FCD), is frequently not detected on structural MRI and up to 42% of MRI-negative patients undergoing surgery have FCD (Chapman et al. 2005). FCD is characterised by disrupted laminar architecture and columnar organisation and abnormal cells, including dysmorphic neurons and balloon cells (Blumcke et al. 2011). Studies on neocortical tissue from surgically-resected temporal lobe specimens with FCD demonstrate altered diffusion parameters in the extracellular space and, in type II, a reduced intracellular volume fraction (ICVF) (Vargova et al. 2011).

Typical neuroimaging features of FCD including cortical thickening and blurring of the grey-white matter boundary on T1-weighted images and cortical and subcortical signal hyperintensities on T2-weighted images are not always present (Barkovich & Kuzniecky 1996). Diffusion tensor imaging (DTI) demonstrates abnormal diffusion indices in underlying white matter, including reduced fractional anisotropy (FA) and increased mean diffusivity (MD) (Section 3.2.4). However these are non-specific, extend beyond the area of abnormality (Eriksson et al. 2001) and cannot evaluate dysplastic grey matter due to the low FA and signal contamination by cerebrospinal fluid (CSF).

The assumption inherent in DTI that each voxel contains a single tissue compartment with Gaussian diffusion is increasingly recognised as inadequate (Section 2.8). Multi-compartment models more accurately reflect the diffusion MR signal by modelling several tissue compartments and distinguishing restricted non-Gaussian diffusion (intracellular) from hindered Gaussian diffusion (extracellular space) but the lengthy scans required are often clinically unfeasible (Panagiotaki et al. 2012).

The NODDI (neurite orientation dispersion and density imaging) model includes three compartments for each voxel - intracellular, extracellular and CSF - and provides additional estimates of tissue microstructure in both grey and white matter. It distinguishes two key variables contributing to changes in FA - neurite density (ICVF) and fibre orientation dispersion - with a clinically feasible scan protocol of 20 minutes (Zhang et al. 2012) so could potentially assist the identification and understanding of FCD.

This chapter describes a preliminary study in which the NODDI model is applied for the first time in a clinical population of patients with epilepsy and suspected dysplasia on conventional imaging. The aims are to determine firstly whether the parameters estimates are compatible with the underlying disrupted tissue microstructure and secondly whether they potentially provide useful additional clinical information for localising the abnormality.

13.2 Methods

13.2.1 Subjects

Five patients (four with structural imaging compatible with FCD, one with tuberous sclerosis, TS) were scanned on a 3T GE Signa HDx scanner with a full clinical protocol and a NODDI protocol optimised for the scanner (Alexander 2008). Patient demographics and clinical data are listed in Table 13.1.

Patient	Age/ Gender	Seizure onset (yr)	Structural MRI report	Video EEG localisation
1	21/M	2	Right MFG resection with residual FCD	Right frontocentral
2	27/M	8	Left ITG FCD	Left anterior temporal
3	62/M	17	Left ITG FCD/dysplasia	Left anterior temporal
4	31/F	6	Cortical tubers, largest in right ITG	Right anterior temporal
5	28/M	10	Normal, then L MFG MCD (FCD or polymicrogyria)	Left frontocentral

Table 13.1 - Clinical and demographic characteristics of patients

FCD = focal cortical dysplasia, ITG = inferior temporal gyrus, MFG = middle frontal gyrus.

13.2.2 Magnetic Resonance Imaging

The NODDI protocol consisted of two high angular resolution diffusion imaging shells (single-shot EPI, 50x2.5mm axial slices, 96x96 matrix zero-filled to 128x128, field-of-view 24x24cm, TE 85ms, TR 13s, 9 non-diffusion weighted acquisitions, 24 directions with b-value 700s/mm², 48 directions with b-value 2000s/mm², maximum gradient strength 40mT/m, slew rate 150T/m/s, total scan time 20 minutes). Optimised gradient directions from the Camino software package generated using electrostatic energy minimization were used (Cook et al. 2007). The scan duration was less than that of the standard DTI sequence employed for the rest of this thesis which was achieved by omitting cardiac gating.

13.2.3 NODDI Tissue Model

Previous work has described hindered Gaussian diffusion in the extracellular space defined by the cell membranes of cell bodies and glia and restricted non-Gaussian diffusion in the intracellular space bounded by axonal and dendritic membranes (collectively termed neurites) (Assaf & Cohen 2000).

The NODDI issue model distinguishes three types of microstructural environment - intracellular, extracellular and cerebrospinal fluid (isotropic) - with the normalised MR signal A given by:

$$A = (1 - v_{iso})(v_{ic}A_{ic} + (1 - v_{ic})A_{ec}) + v_{iso}A_{iso}$$

where A_{ic} , A_{ec} , A_{iso} are the normalised signal of the respective compartments and v_{ic} and v_{iso} are the intracellular and cerebrospinal fluid volume fractions. Note that the intracellular volume fraction is expressed as fraction of the non-CSF compartment, so that by definition intracellular and extracellular volume fractions sum to 1.

The intracellular compartment bounded by neurite membranes shows restricted diffusion. It is modelled as a set of sticks (cylinders of zero radius) with an orientation distribution that can range from highly parallel to highly dispersed. The orientation distribution function is modelled with a Watson distribution with mean orientation μ and a concentration parameter κ that reflects the orientation dispersion around μ .

The extracellular compartment around the neurites is occupied by glia and also cell bodies in gray matter and shows hindered diffusion. It is modelled by Gaussian anisotropic diffusion. The parallel and perpendicular diffusivities are not free parameters but are related to the intrinsic free diffusivity by equations involving the neurite density and orientation dispersion.

The cerebrospinal fluid compartment is modelled as isotropic Gaussian diffusion.

13.2.4 Model Fitting

There are six parameters for the model:

v_{ic} : intra-cellular volume fraction

κ : concentration parameter of Watson distribution

μ : mean orientation of Watson distribution

d_{\parallel} : intrinsic free diffusivity

v_{iso} : isotropic (CSF) volume fraction

d_{iso} : isotropic (CSF) diffusivity

Two parameters were fixed to typical *in vivo* values ($d_{\parallel}=1.7\times10^{-3}\text{mm}^2\text{s}^{-1}$, $d_{iso}=3.0\times10^{-3}\text{mm}^2\text{s}^{-1}$) whilst fitting of the remaining parameters was performed with the NODDI MatLAB Toolbox (<http://cmic.cs.ucl.ac.uk/mig>).

The parameter v_{ic} was used as a measure of intracellular volume fraction (ICVF) as a fraction of the non-CSF compartment and was considered to a marker of neurite density. The concentration parameter of the Watson distribution κ was transformed to give the orientation dispersion index (ODI), an index of the degree of dispersion of the fibre orientations ranging from 0 (no dispersion) to 1 (fully dispersed) using the following formula:

$$ODI = \frac{2}{\pi} \arctan \left(\frac{1}{\kappa} \right)$$

A mask comprising all brain voxels with a CSF fraction (v_{iso}) below 90% was applied to the maps as fitting of ICVF and ODI may be inaccurate in voxels that are predominantly CSF.

13.2.5 Statistical Analysis

In view of the small sample size, the parametric maps were first qualitatively compared to abnormalities in the structural images and maps of standard DTI measures (FA and MD). In addition, the contrast-to-noise ratio was determined for the diffusion scans using the following formula (Song et al. 2004):

$$CNR = \frac{|S_{lesion} - S_{contralateral}|}{\sqrt{[(SD_{lesion})^2 + (SD_{contralateral})^2]/2}}$$

where S_{lesion} and $S_{contralateral}$ represent the mean values in the lesion and homologous contralateral cortex and SD_{lesion} and $SD_{contralateral}$ are the standard deviations in these regions of interest.

13.3 Results

13.3.1 Qualitative Results

In three patients with suspected FCD (patients 1, 2 and 3) and the patient with TS (patient 4), areas of reduced ICVF were clearly identified that co-localised with the abnormality (Figure 13.1 and Figure 13.2). No change was apparent in the ODI. Of particular note, the change in ICVF was more conspicuous than on conventional structural or diffusion images (Figure 13.2).

In the fifth patient, the structural imaging was initially felt to be normal but on review a malformation of cortical development, most likely FCD or possibly polymicrogyria, was detected. The abnormal area was clearly evident on NODDI imaging, with reduced ICVF and increased ODI (Figure 13.3).

The structural and diffusion images for all subjects are shown in Figure 13.4 for an easy side-by-side comparison.

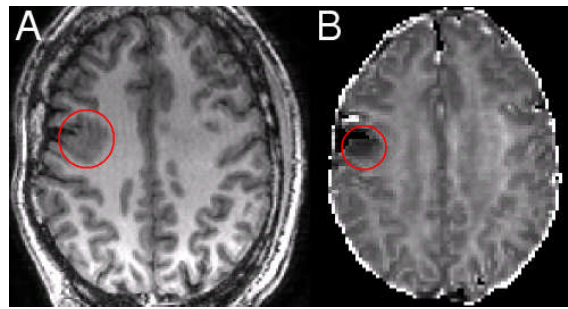


Figure 13.1 - Residual FCD following a right middle frontal gyrus resection (patient 1)

The residual FCD on the T1-weighted image (A) corresponds with an area of reduced ICVF (B).

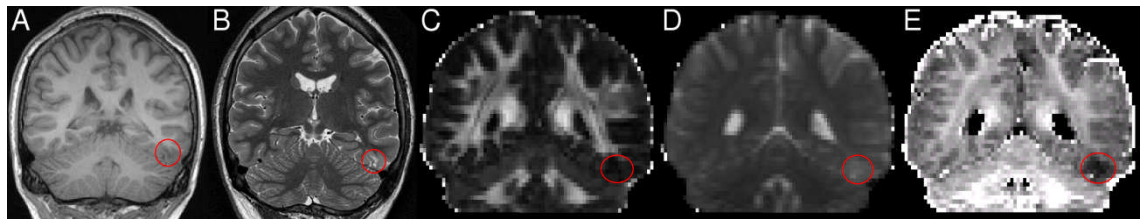


Figure 13.2 - Left inferior temporal gyrus FCD (patient 2)

The FCD is poorly defined on structural images including volumetric T1-weighted (A) and T2-weighted PROPELLER (B) and standard DTI images including FA (C) and MD (D) but easily visible as reduced ICVF (E).

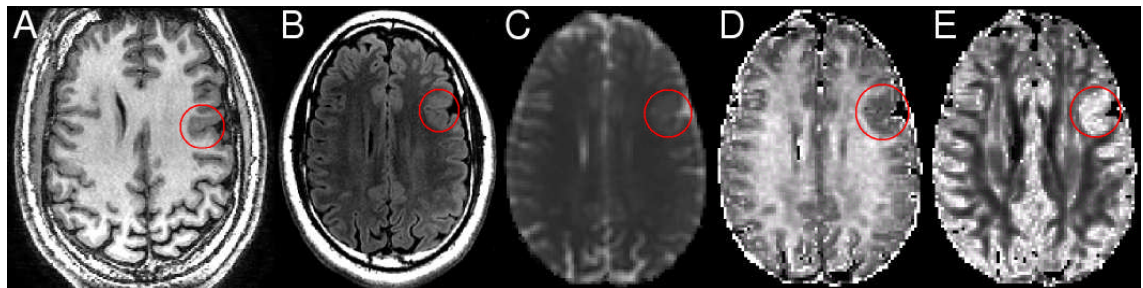

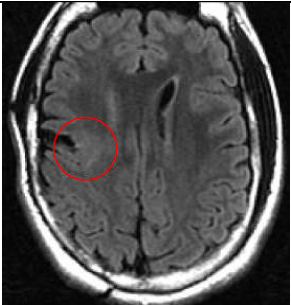
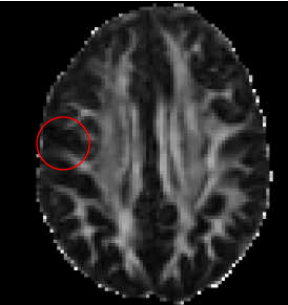
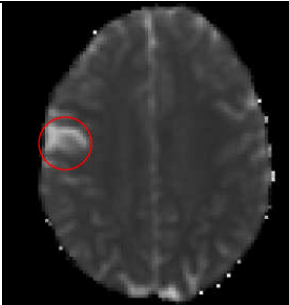

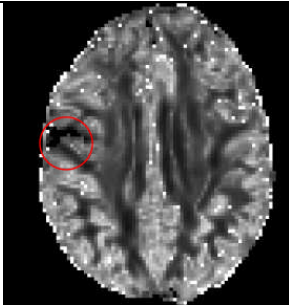

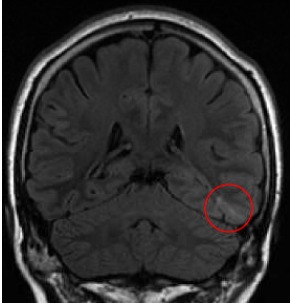
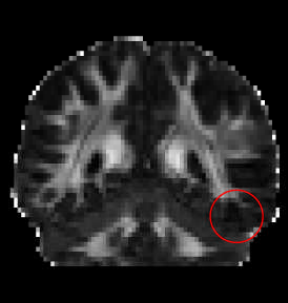
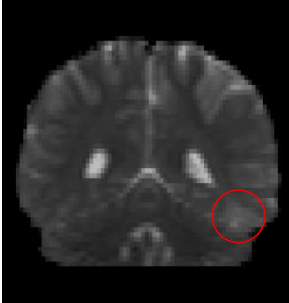
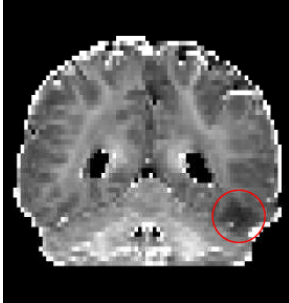

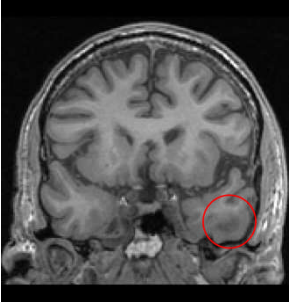
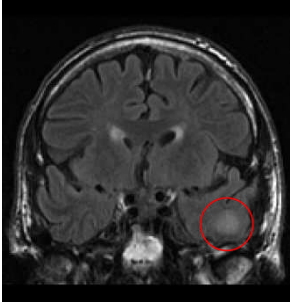

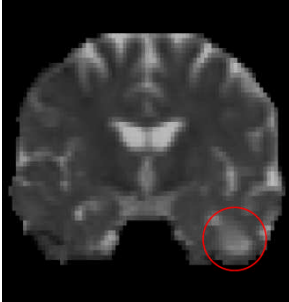
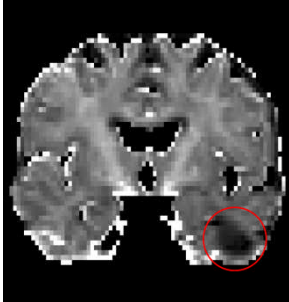
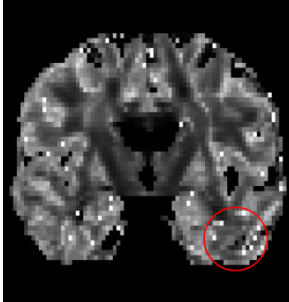


Figure 13.3 - Left middle frontal gyrus MCD (patient 5)

The MCD is seen on structural images including T1-weighted (A) and T2-weighted FLAIR (B) and DTI images such as MD (C) but more clearly seen as reduced intracellular volume fraction (D) and increased fibre dispersion (E).

Pt	T1 volumetric	T2 FLAIR	DTI - FA	DTI - MD	NODDI - ICVF	NODDI - ODI
1						
2						
3						

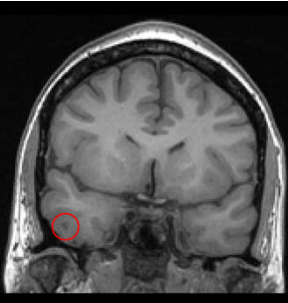
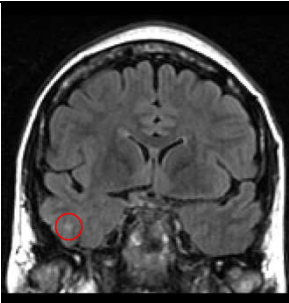


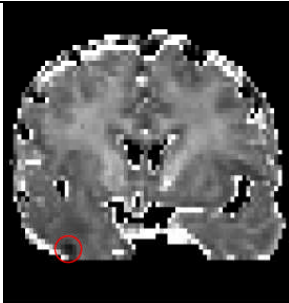
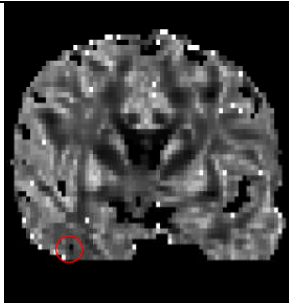

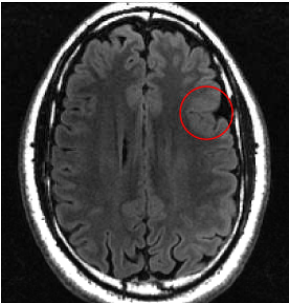
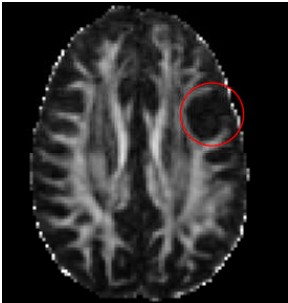
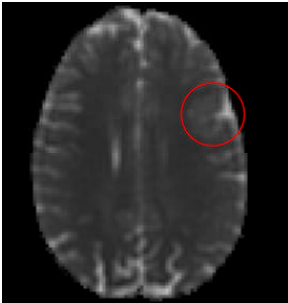
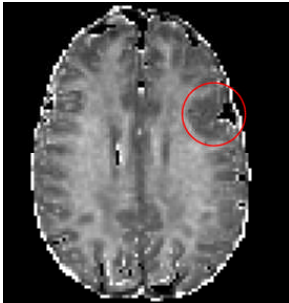

	T1 volumetric	T2 FLAIR	DTI - FA	DTI - MD	NODDI - ICVF	NODDI - ODI
4						
5						

Figure 13.4 - Summary of clinical, DTI and NODDI scans on subjects

The structural scans are shown on the left (T1-weighted volumetric and T2-weighted FLAIR), the standard diffusion contrasts are shown in the middle (FA and MD) and the novel measures derived from NODDI are shown on the right (ICVF and ODI).

13.3.2 Quantitative Results

The mean contrast-to-noise ratio (CNR) for the ICVF across all subjects was 3.60 (standard deviation 1.73). This was significantly greater than the CNR for FA (mean 1.21, standard deviation 0.45; two-tailed paired t-test $p=0.041$) and showed a trend to being greater than the CNR for MD (mean 2.80, standard deviation 1.34; two-tailed paired t-test $p=0.080$). The results are summarised in Table 13.2.

Patient	CNR (FA)	CNR (MD)	CNR (ICVF)
1	0.56	2.97	4.75
2	1.50	3.30	2.57
3	1.16	3.60	4.57
4	1.74	3.12	5.06
5	1.09	0.46	1.05
Mean (SD)	1.21 (0.45)	2.80 (1.34)	3.60 (1.73)

Table 13.2 - Comparison of contrast-to-noise ratios for different diffusion contrasts

13.4 Discussion

13.4.1 Key Findings

The additional microstructural information readily identified the area of abnormality in all patients. The consistent change was a localised fall in the ICVF that is compatible with previous iontophoretic data (Vargova et al. 2011), more readily identifiable than on other clinical or diffusion images with a higher CNR than FA or MD images and more localised than previous diffusion studies employing FA and MD. The tubers in tuberous sclerosis are histologically comparable to FCD type IIb and the differential diagnosis of polymicrogyria (in patient 5) is also associated with a reduced neuronal density (Judkins et al. 2011) that manifests as reduced ICVF.

13.4.2 Interpretation

DTI indices such as FA reflect many underlying parameters including neuronal density, fibre orientation dispersion, axonal diameter and degree of myelination and are thus non-specific. The NODDI model disentangles some of the different factors contributing to the change in FA. In particular, it separates the influence of neurite density and orientation dispersion into distinct indices. The technique is suitable for both grey and white matter. Moreover, by modelling CSF as a separate compartment, it avoids CSF contamination, a further confound on traditional indices such as FA.

Previous studies have suggested that in FCD the reduced FA may result from increased or abnormally located grey matter or pathological white matter with abnormal myelination or ectopic neurones, whilst the increase in MD may result from defective neurogenesis or cell loss resulting in increased extracellular

space (Eriksson et al. 2001). In this small series the results support the interpretation that diffusion changes are in part due to an increase in extracellular space.

13.4.3 Limitations and Future Work

This study presents preliminary data that needs confirmation in a larger cohort and comparison with post-surgical histology. In particular, I included predominantly patients with abnormalities detected on conventional imaging to establish the validity of the technique. This may now be usefully extended to larger number of patients with malformations and acquired cerebral lesions to characterise the range of findings and then to those individuals with no discernible abnormality on conventional brain imaging. As the data are inherently quantitative, a larger cohort would enable voxel-based quantitative comparisons with a group of healthy controls as has previously been performed on FLAIR images in MRI-negative patients (Focke et al. 2009).

The main limitation is the relatively large voxel size of diffusion imaging (here 1.875x1.875x2.5mm) in comparison to what can be obtained with structural imaging (typically 1mm isotropic) although grey and white matter can still be resolved. Reducing voxel size whilst maintaining a clinically feasible scan duration is possible only with the stronger imaging gradients available on modern scanners (50-60mT/m).

13.5 Conclusion

In conclusion, I have shown that NODDI is viable to apply to a clinical population and the findings of reduced ICVF are compatible with the known pathology of FCD. NODDI may assist the clinical identification of FCD in patients with epilepsy that is not easily seen on other imaging sequences and requires further study. The sequence can be readily implemented on MRI scanners from all manufacturers.

14 OVERALL CONCLUSION

14.1 Main Findings and Contribution

The main findings and contributions from each study are:

Chapter 7: Diffusion Tensor Imaging Tractography to Visualise the Relationship of the Optic Radiation to Epileptogenic Lesions Prior to Neurosurgery

- The optic radiation can be successfully delineated by tractography in patients with lesions near to the optic radiation
- The entire optic radiation can be identified by seeding from both Meyer's loop and the lateral geniculate nucleus
- The results can be shown on anatomical images and in 3D renderings and have been validated with post-operative visual outcomes
- Tractography of the optic radiation can assist neurosurgical planning by suggesting the optimum approach to a lesion or by indicating the proximity of a lesion to the optic radiation
- Tractography can assist advising patients on the risks to vision inherent in surgery, and the decision not to proceed to surgery or to defer surgery in favour of further medication trials

Chapter 8: Diffusion Tensor Imaging Tractography of the Optic Radiation for Epilepsy Surgical Planning: a Comparison of Two Methods

- The choice of seed region and waypoints can have a significant effect on tractography results, so an appropriate technique for the surgical target needs to be chosen
- The core of the tract is common between different methods, but there is substantial variation in other parts of the tracts
- Tractography based on seeding from Meyer's loop delineates the more inferior portion of the optic radiation and yields reliable measurements of the distance from the temporal pole to Meyer's loop
- Tractography based on seeding from the LGN and including an endpoint in the occipital cortex delineates the more superior portion of the optic radiation and gives a better depiction of the posterior parts of the tract

Chapter 9: Optic Radiation Tractography and Vision in Anterior Temporal Lobe Resection

- Variability in the location of Meyer's loop can be shown by diffusion imaging and increasing degrees of damage lead to a greater visual field deficit
- It is feasible to propagate preoperative tractography onto postoperative images using both the anatomical and diffusion images for registration within the time constraints of a neurosurgical procedure
- Validity is confirmed by showing that the predicted extent of damage to Meyer's loop is more highly predictive of the visual field deficit than the combination of degree of resection and Meyer's loop to temporal pole distance
- Each additional millimetre of damage to Meyer's loop (in the antero-posterior direction) leads to an additional 5% loss of visual field in the upper quadrant

Chapter 10: Intraoperative Visualisation of the Optic Radiation Reduces Visual Field Deficits

- It is feasible to propagate preoperative tractography onto intraoperative images and additionally correct for the key sources of distortion within 8-9 minutes
- The data can be readily displayed on the operating microscope display and the surgeon reported that it was helpful in all cases
- The additional image guidance enables the neurosurgeon to reduce the severity of visual field deficits and prevents any significant deficits that preclude driving
- It is technically possible to correct for brain shift during neurosurgery, but this does not further improve the visual outcome
- The altered surgical approach does not lead to any adverse change in the seizure outcome or the degree of hippocampal resection
- The displacement of the temporal horn of the lateral ventricle during the early part of ATLR is minimal, around 2mm, and is negligible in the antero-posterior direction

Chapter 11: Structural Correlates of Impaired Working Memory in Hippocampal Sclerosis

- Working memory is impaired in hippocampal sclerosis and associated with reduced activation of the right superior parietal lobe during a working memory task
- In patients with hippocampal sclerosis, there is grey matter atrophy of the ipsilateral hippocampus and parietal lobe, regions that are important for working memory
- Working memory performance correlates with the structural integrity of frontoparietal white matter connections and the contralateral temporal lobe

Chapter 12: Longitudinal Changes in Diffusion Parameters Following Anterior Temporal Lobe Resection

- There are widespread baseline changes in diffusion parameter in patients with temporal lobe epilepsy that are compatible with altered myelination
- Changes compatible with Wallerian degeneration occur in efferent tracts and nearby regions following temporal lobe surgery
- Changes compatible with structural plasticity occur in the corona radiata, internal and external capsule and nearby tracts following surgery
- The majority of changes are present by 3 months, but the time course of change is slower in patients with right temporal lobe epilepsy than left

Chapter 13: Advanced Diffusion Models Could Aid Assessing Patients with Focal Cortical Dysplasia

- Regions of focal cortical dysplasia can be readily identified using an advanced diffusion model (NODDI) by the consistent finding of a localised fall in intracellular volume, which is compatible with iontophoretic studies
- The area of abnormality is more readily identified with NODDI than with conventional clinical or diffusion images and has a higher contrast-to-noise ratio
- NODDI is viable to apply to a clinical population and may assist in the clinical identification of focal cortical dysplasia in patients with epilepsy

14.2 Limitations and Future Studies

14.2.1 Tractography

Many of my results rely on tractography of the optic radiation. Tractography is an inexact technique with numerous limitations that deserve further discussion.

A fundamental assumption of the diffusion tensor model employed in this thesis is that the predominant diffusion direction within each voxel is representative of the bulk direction of fibres within that voxel (Section 2.7.1). Although this technique can be extended to model two fibre populations that cross at an angle of perhaps 60 degrees or greater (Section 6.5.3.2), this is still a very limited description of the underlying anatomy. In particular, tractography may fail in fibres crossing at lesser angles or in regions of more complex fibre structure, such as fanning or kissing fibres. This is particularly relevant in the optic radiation where the tightly curving fibres of Meyer's loop are located adjacent to the fibres of the uncinate fasciculus.

The dimensions of each voxel are several orders of magnitude greater than the size of the underlying axons that are being modelled. A single voxel may thus contain multiple fibre populations of differing orientation and structure. It is unlikely that a significant reduction in voxel size will be possible (Section 2.7.5), but one technique that could be assessed in the future is ZOOM DTI, whereby higher resolution voxels of a small field-of-view can be obtained (Salmenpera et al. 2006). Since the optic radiation runs mostly in an antero-posterior plane, it would be possible to perform imaging of only a small subset of axial slices to cover this structure.

The advantages of probabilistic tractography algorithms over deterministic algorithms have already been discussed (Section 4.6.1). Nevertheless the probabilistic tractography algorithm used in this thesis, multi-tensor PICO, still relies on a diffusion tensor model with its associated limitations (Section 2.8.1). There are now better models available that avoid some of these limitations, in particular constrained spherical deconvolution (Tournier et al. 2007). This permits a direct estimation of the fibre orientation distribution (FOD) for each voxel that can account for multiple fibre populations including those crossing at lesser angles. The diffusion data acquired for this project have 52 diffusion-weighted directions so are suitable for this technique. Future work will look at tractography of the optic radiation using the software package MRtrix (www.brain.org.au/software/mrtrix). It would be important to show that equivalent or superior results are obtained. Constrained spherical deconvolution would also be particularly beneficial for looking at tracts such as the superior longitudinal fasciculus (Chapter 11) since there is a region where there are several adjacent fibre populations running in different directions (corpus callosum left-right, superior longitudinal fasciculus anterior-posterior, corona radiata superior-inferior) (Tournier et al. 2007).

An assumption inherent in tractography is that the results obtained are a faithful representation of the underlying anatomy. For the reasons already stated, and others, the tracts may differ from reality. It is possible that false tracts are obtained or the technique may fail entirely. In this thesis, if poor quality results were obtained there were usually improved by minor changes in this seed region. However it unfortunately is not possible to use the gold standard of post mortem histology and in studies such as Chapter 7, only limited postoperative visual outcome data were available for validation of the tractography results.

Tractography can be time consuming for two main reasons. Firstly, the selection of seed regions requires manual intervention and as noted these regions may need to be altered. The second method in Chapter 8 provides a small degree of automation for the identification of the LGN seed region whilst a much more fully automated technique has been described in the literature (Clatworthy et al. 2010). I am exploring whether the selection of seed regions and waypoints can be performed by an algorithm that compares any given new scan to a database of previous scans and seed regions to generate corresponding regions for the new scan (Cardoso et al. 2012).

The second reason contributing to lengthy processing is the actual computational processing time of probabilistic tractography. It is typically run with a Monte-Carlo simulation in which multiple iterations must be evaluated and in this thesis 50000 iterations from each seed voxel were used. Such processing is eminently suitable for parallelisation and hence could be implemented on graphical processing units in

the same way as the non-rigid registration algorithm (Section 6.6.3). This would allow much faster processing, and perhaps even interactive selection of the seed region with the resulting tracts shown in real-time.

Tractography should not be considered in isolation as there are numerous other data of importance during surgical treatment including functionally eloquent cortex (fMRI), metabolically underactive regions (PET), regions of ictal hyperperfusion (SPECT) and vessels (magnetic resonance angiography). Visualisation could be further extended to include these other data in multi-modality imaging.

14.2.2 Sources of Image Distortion

Aside from errors inherent in tractography, there are other sources of error from diffusion imaging. As the scan acquisition is around 20 minutes, there is a higher risk of subject motion during the scan and images can be distorted by eddy currents. The `eddy_correct` routine in FSL was used to correct for both of these sources of error in this thesis. This performs an affine registration of each diffusion (or non-diffusion) weighted image to the first non-diffusion weighted image. There are now however superior tools to correct for eddy current induced distortions that model the effect of eddy currents on the image. One such tool is now available in the latest version of FSL.

Gradient non-linearity and magnetic susceptibility artefacts were corrected using custom software (Section 6.6). The correction of magnetic susceptibility artefacts was based on the acquisition of field maps, but such correction is inaccurate in regions of high field inhomogeneity. This includes the brain/air interface, or resection margin in intraoperative imaging. An alternative approach is to use non-linear image registration. It may be possible to combine field map and image registration based techniques by assigning a confidence level to each part of the fieldmap and using this to adaptively guide a subsequent image registration step with greater weight being placed on image registration in areas with low confidence in the fieldmap (Daga et al. 2013). Whilst this shows promise, it has not been evaluated in a clinical setting but could be evaluated for use with intraoperative MRI.

The corrections for gradient non-linearity and magnetic susceptibility artefacts were applied separately from the motion correction and eddy current induced distortion correction. Theoretically it would be better to develop software that could apply all corrections in a single step to ensure that there is only a single resampling of the acquired data. However, this may make little difference in practice.

Even if all sources of distortion are corrected, an unanswered question is whether to add a safety margin to the final results and if so to what extent. When tractography data were used for intraoperative guidance, error margins were added only to account for the estimated errors resulting from corrections that were not applied. This included brain shift and magnetic susceptibility artefacts (Section 10.2.4). This gave excellent results so it may not be necessary to add such a safety margin. It is still important however to make sure that the neurosurgeon is aware of the limitations of the technique and the possibility of tractography to under- or overestimate the extent of tracts.

14.2.3 Visual Outcomes

The quantification of visual field deficits was performed by Goldmann perimetry. This is known to be affected by both subject and observer variability (Parrish et al. 1984). There were only two observers for the visual fields, myself and Jason Stretton, and the same observer was used for both pre- and post-operative assessments aside from exceptional circumstances where this was not possible. I therefore chose to eliminate the intersession variability by measuring the visual field deficit by comparison of the ipsilateral and contralateral upper quadrants at a single postoperative timepoint. If a patient had a stronger eye, or an uncorrected refractive error, any size discrepancy between the visual fields in each eye could slightly bias the results. Nevertheless, this assessment was much more detailed than other previous methods for quantification of the deficit (Barton et al. 2005).

The visual assessment for driving was performed using the DVLA mandated binocular Esterman perimetry. This can be particularly lenient and was not recommended by the Eyesight Working Group (Eyesight Working Group 2005). Although the minimum visual field requirement across Europe is set by a European Directive (2009/112/EC), other countries may employ more stringent requirements or assessment methods and therefore the risk of failing to meet driving criteria could be greater. In addition, outside Europe regulations vary widely so the results may not necessarily translate into clinical practice in all countries.

The measure of damage to Meyer's loop that was used for correlational analysis in Chapter 9 was the antero-posterior distance. A single distance is a crude measurement of the degree of damage to a complex structure such as the optic radiation and the correlational analysis was based on the assumption of a linear relationship between the antero-posterior damage and the measured visual deficit whereas the actual relationship could be more complex. The results obtained were consistent with this assumption which may reflect the fact that the antero-posterior distance is the most clinically relevant measurement. It may in the future be possible to perform a more detailed assessment of the degree of damage to Meyer's loop or even try to explain the shape of the deficit by the nature of damage to Meyer's loop (in this thesis, I only consider the size of deficit).

14.2.4 Intraoperative MRI

The benefits of intraoperative MRI shown in Chapter 10 were significant, but it necessitates significant initial capital investment and subsequent running costs in order to provide the necessary staffing to ensure safe application. The duration of surgery is prolonged by the additional imaging and there are potential adverse consequences of this. Although other series have shown no increase in the anaesthetic risk (Section 5.3.2), I observed a single case of self-resolving brachial plexopathy which was attributed to a prolonged period of immobility in a particular orientation during surgery.

The results obtained suggest that the display of the optic radiation tractography is more critical than the ability to correct for brain shift. Therefore future work will look at the display of optic radiation tractography within a conventional neurosurgical operating theatre using a neuronavigation system widely available both in the UK and abroad. It may be possible to use more economical techniques such as

intraoperative ultrasound to correct for brain shift, or even use the information obtained with the present series to better model the effects of temporal lobe epilepsy surgery on brain shift.

The technique also needs to be extended and assessed in relation to other tracts such as the corticospinal tract in frontal lobe epilepsy surgery.

14.2.5 Working Memory

The structural changes demonstrated that correlate with the decline in working memory (Chapter 11) are non-specific and could be caused by a variety of underlying structural changes (Section 2.6.2). Application of improved models of diffusion tissue, including NODDI (Chapter 13), could provide more detailed information on microstructural changes occurring in epilepsy.

The working memory study was solely cross-sectional highlighting the changes present in patients with temporal lobe epilepsy before surgery. Working memory does improve to some extent following surgery and future studies will look at how the longitudinal structural changes described in Chapter 12 are related to changes in neuropsychological variables, including measures of working memory. It would also be beneficial to combine functional and structural connectivity analyses to provide complementary information and to further explore the role of the temporal lobe in working memory.

14.2.6 Longitudinal Study

The longitudinal study demonstrated that the majority of changes have occurred by 3 months. Given the time commitment for repeated scanning, it is only feasible to include relatively few postoperative timepoints but future studies should look at earlier timepoints to help clarify the recent observations on diffusion changes within the first fortnight following surgery (Liu et al. 2013) and to show what happens in the next few months. By including only seizure free patients in the analysis, it may become more sensitive to plasticity and other changes without the confounding factor of changes induced by ongoing seizures but there were not sufficient numbers to do this. Future work could investigate whether observed changes correlate with postoperative neuropsychological outcome.

14.2.7 NODDI

The cohort for this pilot study was small and included only patients with pathology demonstrated on conventional MRI. The next step is to apply the same technique but in a population who are MRI negative to see if previously undetected pathology can be identified. It is possible to retrospectively fit a simplified version of the NODDI model (in which the CSF compartment is omitted) to previously acquired single shell diffusion data. This could be applied in previously MRI negative patients who have been assessed for surgery and had a focus identified by other techniques, such as intracranial EEG. It would also be possible to use the NODDI model to better understand the changes observed in working memory network (Chapter 12) or the baseline and longitudinal changes following surgery (Chapter 13). It may for example be possible to demonstrate changes in ICVF in a homogeneous population of patients with hippocampal sclerosis.

14.3 Possible Research Questions

Possible research questions from the previous discussion are now summarised:

- Can a better delineation of the optic radiation be achieved using a partial field-of-view and smaller voxel sizes with a technique such as ZOOM DTI?
- Does constrained spherical deconvolution give an equivalent or superior delineation of the optic radiation (and other tracts) to the multitensor model?
- Can the seed regions and waypoints for tractography be accurately automated using an atlas-based technique and a database of previous scans with corresponding regions of interest?
- Can probabilistic tractography be performed in (near) real time using graphical processing units to allow interactive seed region selection?
- How can tractography data be best combined with data from other modalities and visualised for surgical planning (multimodal imaging)?
- Can the image distortion in echo planar sequences for tractography be better corrected using newer tools for eddy current induced distortions in conjunction with an algorithm combining field map and image registration based techniques?
- Aside from explaining the severity of visual field deficits, is it possible to model the shape of a visual field deficit from the imaging findings?
- Can the beneficial visual outcomes with intraoperative MRI guidance be equally well achieved with visualisation in a conventional operating theatre without correction for brain shift?
- Can correction of brain shift be achieved more economically in such a setting using intraoperative ultrasound and is this beneficial?
- Is similar benefit achieved by display of the corticospinal tract in frontal lobe epilepsy surgery?
- In what way do structural changes identified in the working memory network alter following temporal lobe surgery and is this related to postoperative working memory performance?
- More generally, do changes in diffusion parameters following temporal lobe surgery explain other postoperative neuropsychological outcomes?
- What is the early time course of changes in diffusion parameters in the first few months following temporal lobe surgery?
- Can the nature of underlying longitudinal changes in tissue microstructure be further clarified with other diffusion models, such as NODDI?
- Can retrospective fitting of the NODDI model to previously acquired diffusion data in patients with focal cortical dysplasia identify the location of the abnormality?
- Can retrospective fitting of the NODDI model to previously acquired diffusion data in patients with hippocampal sclerosis demonstrate focal changes in the additional parameters?
- Does the NODDI tissue model provide useful additional data in patients with lesions other than focal cortical dysplasia and do the parameters correlate with the underlying histology?
- Can the NODDI tissue model identify focal cortical dysplasia, or other abnormalities, prospectively in patients who are otherwise MRI-negative being considered for surgery?

14.4 Clinical Relevance and Final Conclusion

I have shown that tractography of the optic radiation is clinically beneficial for planning epilepsy surgery and can be displayed during neurosurgery to reduce the chance of a visual field deficit. This was introduced into clinical practice and improved a highly relevant outcome for patients.

I showed that structural integrity of frontoparietal white matter connections and the contralateral temporal lobe is important in explaining the deficit in working memory in patients with hippocampal sclerosis. This provides further understanding of the aetiology of an important day-to-day deficit.

I demonstrated changes consistent with both Wallerian degeneration and structural plasticity in the white matter following anterior temporal lobe resection. Further work will reveal how these changes are related to cognitive outcomes from surgery and assist rehabilitation from surgery.

I evaluated a novel diffusion model, NODDI, and demonstrated that this has the potential to assist in the clinical identification of focal cortical dysplasia in patients where the abnormality is hard to detect on conventional clinical imaging and suggest that it may also be of benefit in patients who are MRI negative.

APPENDICES

The appendices include the various information sheets, consent forms and checklists/log sheets used during this thesis:

- Appendix A – Patient Information Sheet for the main study
- Appendix B – Control Information Sheet for the main study
- Appendix C – Consent form for the main study
- Appendix D – Log form for patients in main study
- Appendix E – Edinburgh handedness inventory for main study
- Appendix F – Checklist for healthy volunteers for main study
- Appendix G – Patient Information Sheet for intraoperative MRI study
- Appendix H – Consent form for intraoperative MRI study
- Appendix I – Checklist for processing of tractography data and transfer to intraoperative MRI
- Appendix J – Log sheet for images acquired and displayed during surgery in intraoperative MRI

Appendix A: Patient Information Sheet for the main study

Appendix B: Control Information Sheet for the main study

Appendix C: Consent form for the main study

Appendix D: Log form for patients in main study

Appendix E: Edinburgh handedness inventory for main study

Appendix F: Checklist for healthy volunteers for main study

Appendix G: Patient Information Sheet for intraoperative MRI study

Appendix H: Consent form for intraoperative MRI study

Appendix I: Checklist for processing of tractography data and transfer to intraoperative MRI

Appendix J: Log sheet for images acquired and displayed during surgery in intraoperative MRI

REFERENCES

- Afzali M, Soltanian-Zadeh H, Elisevich KV (2011) Tract based spatial statistical analysis and voxel based morphometry of diffusion indices in temporal lobe epilepsy. *Comput. Biol. Med.* 41:1082-1091.
- Ahmadi ME, Hagler DJ, Jr., McDonald CR, Tecoma ES, Iragui VJ, Dale AM, Halgren E (2009) Side matters: diffusion tensor imaging tractography in left and right temporal lobe epilepsy. *AJNR Am. J. Neuroradiol.* 30:1740-1747.
- Alexander DC (2008) A general framework for experiment design in diffusion MRI and its application in measuring direct tissue-microstructure features. *Magn Reson. Med.* 60:439-448.
- Alexander DC, Barker GJ, Arridge SR (2002) Detection and modeling of non-Gaussian apparent diffusion coefficient profiles in human brain data. *Magn Reson. Med.* 48:331-340.
- Archer DP, McTaggart Cowan RA, Falkenstein RJ, Sutherland GR (2002) Intraoperative mobile magnetic resonance imaging for craniotomy lengthens the procedure but does not increase morbidity. *Can. J. Anaesth.* 49:420-426.
- Archip N, Clatz O, Whalen S, Kacher D, Fedorov A, Kot A, Chrisochoides N, Jolesz F, Golby A, Black PM, Warfield SK (2007) Non-rigid alignment of pre-operative MRI, fMRI, and DT-MRI with intra-operative MRI for enhanced visualization and navigation in image-guided neurosurgery. *Neuroimage.* 35:609-624.
- Arfanakis K, Hermann BP, Rogers BP, Carew JD, Seidenberg M, Meyerand ME (2002) Diffusion tensor MRI in temporal lobe epilepsy. *Magn Reson. Imaging* 20:511-519.
- Arora J, Pugh K, Westerveld M, Spencer S, Spencer DD, Todd Constable R (2009) Language lateralization in epilepsy patients: fMRI validated with the Wada procedure. *Epilepsia* 50:2225-2241.
- Ashburner J (2007) A fast diffeomorphic image registration algorithm. *Neuroimage.* 38:95-113.
- Assaf BA, Mohamed FB, Abou-Khaled KJ, Williams JM, Yazeji MS, Haselgrove J, Faro SH (2003) Diffusion tensor imaging of the hippocampal formation in temporal lobe epilepsy. *AJNR Am. J. Neuroradiol.* 24:1857-1862.

Assaf Y, Basser PJ (2005) Composite hindered and restricted model of diffusion (CHARMED) MR imaging of the human brain. *Neuroimage*. 27:48-58.

Assaf Y, Blumenfeld-Katzir T, Yovel Y, Basser PJ (2008) AxCaliber: a method for measuring axon diameter distribution from diffusion MRI. *Magn Reson. Med*. 59:1347-1354.

Assaf Y, Cohen Y (1998) Non-mono-exponential attenuation of water and N-acetyl aspartate signals due to diffusion in brain tissue. *J. Magn Reson*. 131:69-85.

Assaf Y, Cohen Y (2000) Assignment of the water slow-diffusing component in the central nervous system using q-space diffusion MRS: implications for fiber tract imaging. *Magn Reson. Med*. 43:191-199.

Astur RS, Constable RT (2004) Hippocampal dampening during a relational memory task. *Behav. Neurosci*. 118:667-675.

Astur RS, St Germain SA, Baker EK, Calhoun V, Pearlson GD, Constable RT (2005) fMRI hippocampal activity during a virtual radial arm maze. *Appl. Psychophysiol. Biofeedback* 30:307-317.

Axmacher N, Haupt S, Cohen MX, Elger CE, Fell J (2009) Interference of working memory load with long-term memory formation. *Eur. J. Neurosci*. 29:1501-1513.

Axmacher N, Mormann F, Fernandez G, Cohen MX, Elger CE, Fell J (2007) Sustained neural activity patterns during working memory in the human medial temporal lobe. *J. Neurosci*. 27:7807-7816.

Babb TL, Wilson CL, Crandall PH (1982) Asymmetry and ventral course of the human geniculostriate pathway as determined by hippocampal visual evoked potentials and subsequent visual field defects after temporal lobectomy. *Exp. Brain Res*. 47:317-328.

Bailey P, Gibbs FA (1951) The surgical treatment of psychomotor epilepsy. *J. Am. Med. Assoc*. 145:365-370.

Barch DM, Braver TS, Nystrom LE, Forman SD, Noll DC, Cohen JD (1997) Dissociating working memory from task difficulty in human prefrontal cortex. *Neuropsychologia* 35:1373-1380.

Barkovich AJ, Kuzniecky RI (1996) Neuroimaging of focal malformations of cortical development. *J. Clin. Neurophysiol*. 13:481-494.

Barton JJ, Hefter R, Chang B, Schomer D, Drislane F (2005) The field defects of anterior temporal lobectomy: a quantitative reassessment of Meyer's loop. *Brain* 128:2123-2133.

Basser PJ (1995) Inferring microstructural features and the physiological state of tissues from diffusion-weighted images. *NMR Biomed.* 8:333-344.

Basser PJ, Mattiello J, LeBihan D (1994) Estimation of the effective self-diffusion tensor from the NMR spin echo. *J. Magn Reson. B* 103:247-254.

Basser PJ, Pierpaoli C (1996) Microstructural and physiological features of tissues elucidated by quantitative-diffusion-tensor MRI. *J. Magn Reson. B* 111:209-219.

Basser PJ, Pierpaoli C (1998) A simplified method to measure the diffusion tensor from seven MR images. *Magn Reson. Med.* 39:928-934.

Bassi L, Ricci D, Volzone A, Allsop JM, Srinivasan L, Pai A, Ribes C, Ramenghi LA, Mercuri E, Mosca F, Edwards AD, Cowan FM, Rutherford MA, Counsell SJ (2008) Probabilistic diffusion tractography of the optic radiations and visual function in preterm infants at term equivalent age. *Brain* 131:573-582.

Baxendale S, Thompson PJ, Duncan JS (2008) Improvements in memory function following anterior temporal lobe resection for epilepsy. *Neurology* 71:1319-1325.

Baxendale SA, Thompson PJ, Van PW (1998a) A test of spatial memory and its clinical utility in the pre-surgical investigation of temporal lobe epilepsy patients. *Neuropsychologia* 36:591-602.

Baxendale SA, Van PW, Thompson PJ, Connelly A, Duncan JS, Harkness WF, Shorvon SD (1998b) The relationship between quantitative MRI and neuropsychological functioning in temporal lobe epilepsy. *Epilepsia* 39:158-166.

Beaulieu C (2002) The basis of anisotropic water diffusion in the nervous system - a technical review. *NMR Biomed* 15:435-455.

Beaulieu C, Allen PS (1994a) Determinants of anisotropic water diffusion in nerves. *Magn Reson. Med.* 31:394-400.

Beaulieu C, Allen PS (1994b) Water diffusion in the giant axon of the squid: implications for diffusion-weighted MRI of the nervous system. *Magn Reson. Med.* 32:579-583.

Beck RW, Bergstrom TJ, Lichter PR (1985) A clinical comparison of visual field testing with a new automated perimeter, the Humphrey Field Analyzer, and the Goldmann perimeter. *Ophthalmology* 92:77-82.

Behrens TE, Berg HJ, Jbabdi S, Rushworth MF, Woolrich MW (2007) Probabilistic diffusion tractography with multiple fibre orientations: What can we gain? *Neuroimage*. 34:144-155.

Behrens TE, Johansen-Berg H, Woolrich MW, Smith SM, Wheeler-Kingshott CA, Boulby PA, Barker GJ, Sillery EL, Sheehan K, Ciccarelli O, Thompson AJ, Brady JM, Matthews PM (2003a) Non-invasive mapping of connections between human thalamus and cortex using diffusion imaging. *Nat. Neurosci.* 6:750-757.

Behrens TE, Woolrich MW, Jenkinson M, Johansen-Berg H, Nunes RG, Clare S, Matthews PM, Brady JM, Smith SM (2003b) Characterization and propagation of uncertainty in diffusion-weighted MR imaging. *Magn Reson. Med.* 50:1077-1088.

Benjamin CF, Singh JM, Prabhu SP, Warfield SK (2012) Optimization of tractography of the optic radiations. *Hum. Brain Mapp.* Published online: 08-Dec-2012; doi: 10.1002/hbm.22204.

Berg AT, Berkovic SF, Brodie MJ, Buchhalter J, Cross JH, van Emde BW, Engel J, French J, Glauser TA, Mathern GW, Moshe SL, Nordli D, Plouin P, Scheffer IE (2010) Revised terminology and concepts for organization of seizures and epilepsies: report of the ILAE Commission on Classification and Terminology, 2005-2009. *Epilepsia* 51:676-685.

Berg AT, Langfitt J, Shinnar S, Vickrey BG, Sperling MR, Walczak T, Bazil C, Pacia SV, Spencer SS (2003) How long does it take for partial epilepsy to become intractable? *Neurology* 60:186-190.

Bernasconi N, Concha L, Kim H, Bernhardt B (2011) Mapping diffusion abnormalities along white matter tracts in temporal lobe epilepsy. *65th Annual Meeting of American Epilepsy Society, Baltimore* 1:223.

Binder JR, Swanson SJ, Sabsevitz DS, Hammeke TA, Raghavan M, Mueller WM (2010) A comparison of two fMRI methods for predicting verbal memory decline after left temporal lobectomy: language lateralization versus hippocampal activation asymmetry. *Epilepsia* 51:618-626.

Bjork A, Kugelberg E (1957) Visual field defects after temporal lobectomy. *Acta Ophthalmol. (Copenh)* 35:210-216.

Black PM, Moriarty T, Alexander E, III, Stieg P, Woodard EJ, Gleason PL, Martin CH, Kikinis R, Schwartz RB, Jolesz FA (1997) Development and implementation of intraoperative magnetic resonance imaging and its neurosurgical applications. *Neurosurgery* 41:831-842.

Blumcke I, Thom M, Aronica E, Armstrong DD, Vinters HV, Palmini A, Jacques TS, Avanzini G, Barkovich AJ, Battaglia G, Becker A, Cepeda C, Cendes F, Colombo N, Crino P, Cross JH, Delalande O, Dubeau F, Duncan J, Guerrini R, Kahane P, Mathern G, Najm I, Ozkara C, Raybaud C, Represa A, Roper SN, Salamon N, Schulze-Bonhage A, Tassi L, Vezzani A, Spreafico R (2011) The clinicopathologic spectrum of focal cortical dysplasias: a consensus classification proposed by an ad hoc Task Force of the ILAE Diagnostic Methods Commission. *Epilepsia* 52:158-174.

Bonelli SB, Powell RH, Yogarajah M, Samson RS, Symms MR, Thompson PJ, Koepp MJ, Duncan JS (2010) Imaging memory in temporal lobe epilepsy: predicting the effects of temporal lobe resection. *Brain* 133:1186-1199.

Bonelli SB, Thompson PJ, Yogarajah M, Vollmar C, Powell RH, Symms MR, McEvoy AW, Micallef C, Koepp MJ, Duncan JS (2012) Imaging language networks before and after anterior temporal lobe resection: results of a longitudinal fMRI study. *Epilepsia* 53:639-650.

Bonilha L, Edwards JC, Kinsman SL, Morgan PS, Fridriksson J, Rorden C, Rumboldt Z, Roberts DR, Eckert MA, Halford JJ (2010) Extrahippocampal gray matter loss and hippocampal deafferentation in patients with temporal lobe epilepsy. *Epilepsia* 51:519-528.

Bozzao A, Romano A, Angelini A, D'Andrea G, Calabria LF, Coppola V, Mastronardi L, Fantozzi LM, Ferrante L (2010) Identification of the pyramidal tract by neuronavigation based on intraoperative magnetic resonance tractography: correlation with subcortical stimulation. *Eur. Radiol.* 20:2475-2481.

Braver TS, Cohen JD, Nystrom LE, Jonides J, Smith EE, Noll DC (1997) A parametric study of prefrontal cortex involvement in human working memory. *Neuroimage.* 5:49-62.

Buchfelder M, Fahlbusch R, Ganslandt O, Stefan H, Nimsky C (2002) Use of intraoperative magnetic resonance imaging in tailored temporal lobe surgeries for epilepsy. *Epilepsia* 43:864-873.

Buchfelder M, Ganslandt O, Fahlbusch R, Nimsky C (2000) Intraoperative magnetic resonance imaging in epilepsy surgery. *J. Magn Reson. Imaging* 12:547-555.

Burzynska AZ, Nagel IE, Preuschhof C, Li SC, Lindenberger U, Backman L, Heekeren HR (2011) Microstructure of frontoparietal connections predicts cortical responsivity and working memory performance. *Cereb. Cortex* 21:2261-2271.

Callicott JH, Mattay VS, Bertolino A, Finn K, Coppola R, Frank JA, Goldberg TE, Weinberger DR (1999) Physiological characteristics of capacity constraints in working memory as revealed by functional MRI. *Cereb. Cortex* 9:20-26.

Canavan AG, Passingham RE, Marsden CD, Quinn N, Wyke M, Polkey CE (1989) Sequence ability in parkinsonians, patients with frontal lobe lesions and patients who have undergone unilateral temporal lobectomies. *Neuropsychologia* 27:787-798.

Cardoso MJ, Winston G, Modat M, Keihaninejad S, Duncan J, Ourselin S (2012) Geodesic shape-based averaging. *Med. Image Comput. Comput. Assist. Interv.* 15:26-33.

Carter CS, Braver TS, Barch DM, Botvinick MM, Noll D, Cohen JD (1998) Anterior cingulate cortex, error detection, and the online monitoring of performance. *Science* 280:747-749.

Catani M, Howard RJ, Pajevic S, Jones DK (2002) Virtual in vivo interactive dissection of white matter fasciculi in the human brain. *Neuroimage*. 17:77-94.

Catani M, Jones DK, Donato R, Ffytche DH (2003) Occipito-temporal connections in the human brain. *Brain* 126:2093-2107.

Cave CB, Squire LR (1992) Intact verbal and nonverbal short-term memory following damage to the human hippocampus. *Hippocampus* 2:151-163.

Cendes F, Andermann F, Dubeau F, Matthews PM, Arnold DL (1997) Normalization of neuronal metabolic dysfunction after surgery for temporal lobe epilepsy. Evidence from proton MR spectroscopic imaging. *Neurology* 49:1525-1533.

Chanraud S, Zahr N, Sullivan EV, Pfefferbaum A (2010) MR diffusion tensor imaging: a window into white matter integrity of the working brain. *Neuropsychol. Rev.* 20:209-225.

Chapman K, Wyllie E, Najm I, Ruggieri P, Bingaman W, Luders J, Kotagal P, Lachhwani D, Dinner D, Luders HO (2005) Seizure outcome after epilepsy surgery in patients with normal preoperative MRI. *J. Neurol. Neurosurg. Psychiatry* 76:710-713.

Charlton RA, Barrick TR, Lawes IN, Markus HS, Morris RG (2010) White matter pathways associated with working memory in normal aging. *Cortex* 46:474-489.

Charlton RA, Barrick TR, McIntyre DJ, Shen Y, O'Sullivan M, Howe FA, Clark CA, Morris RG, Markus HS (2006) White matter damage on diffusion tensor imaging correlates with age-related cognitive decline. *Neurology* 66:217-222.

Chen X, Weigel D, Ganslandt O, Buchfelder M, Nimsky C (2009) Prediction of visual field deficits by diffusion tensor imaging in temporal lobe epilepsy surgery. *Neuroimage*. 45:286-297.

Choi C, Rubino PA, Fernandez-Miranda JC, Abe H, Rhoton AL, Jr. (2006) Meyer's loop and the optic radiations in the transsylvian approach to the mediobasal temporal lobe. *Neurosurgery* 59:ONS228-ONS235.

Ciccarelli O, Parker GJ, Toosy AT, Wheeler-Kingshott CA, Barker GJ, Boulby PA, Miller DH, Thompson AJ (2003a) From diffusion tractography to quantitative white matter tract measures: a reproducibility study. *Neuroimage*. 18:348-359.

Ciccarelli O, Toosy AT, Hickman SJ, Parker GJ, Wheeler-Kingshott CA, Miller DH, Thompson AJ (2005) Optic radiation changes after optic neuritis detected by tractography-based group mapping. *Hum. Brain Mapp*. 25:308-316.

Ciccarelli O, Toosy AT, Parker GJ, Wheeler-Kingshott CA, Barker GJ, Miller DH, Thompson AJ (2003b) Diffusion tractography based group mapping of major white-matter pathways in the human brain. *Neuroimage*. 19:1545-1555.

Clatworthy PL, Williams GB, Acosta-Cabronero J, Jones SP, Harding SG, Johansen-Berg H, Baron JC (2010) Probabilistic tractography of the optic radiations--an automated method and anatomical validation. *Neuroimage*. 49:2001-2012.

Clatz O, Delingette H, Talos IF, Golby AJ, Kikinis R, Jolesz FA, Ayache N, Warfield SK (2005) Robust nonrigid registration to capture brain shift from intraoperative MRI. *IEEE Trans. Med. Imaging* 24:1417-1427.

Concha L, Beaulieu C, Collins DL, Gross DW (2009) White-matter diffusion abnormalities in temporal-lobe epilepsy with and without mesial temporal sclerosis. *J. Neurol. Neurosurg. Psychiatry* 80:312-319.

Concha L, Beaulieu C, Gross DW (2005) Bilateral limbic diffusion abnormalities in unilateral temporal lobe epilepsy. *Ann. Neurol.* 57:188-196.

Concha L, Beaulieu C, Wheatley BM, Gross DW (2007) Bilateral white matter diffusion changes persist after epilepsy surgery. *Epilepsia* 48:931-940.

Concha L, Gross DW, Wheatley BM, Beaulieu C (2006) Diffusion tensor imaging of time-dependent axonal and myelin degradation after corpus callosotomy in epilepsy patients. *Neuroimage.* 32:1090-1099.

Concha L, Livy DJ, Beaulieu C, Wheatley BM, Gross DW (2010) In vivo diffusion tensor imaging and histopathology of the fimbria-fornix in temporal lobe epilepsy. *J. Neurosci.* 30:996-1002.

Cook MJ, Fish DR, Shorvon SD, Straughan K, Stevens JM (1992) Hippocampal volumetric and morphometric studies in frontal and temporal lobe epilepsy. *Brain* 115 (Pt 4):1001-1015.

Cook PA, Alexander DC, Parker GJ (2004) Modelling noise-induced fibre-orientation error in diffusion-tensor MRI. *IEEE Int Symp Biomed Imaging* 1:332-335.

Cook PA, Bai Y, Nedjati-Gilani S, Seunarine KK, Hall MG, Parker GJ, Alexander DC (2006) Camino: open-source diffusion-MRI reconstruction and processing. *14th Scientific Meeting of the International Society for Magnetic Resonance in Medicine, Seattle* 2759.

Cook PA, Symms M, Boulby PA, Alexander DC (2007) Optimal acquisition orders of diffusion-weighted MRI measurements. *J. Magn Reson. Imaging* 25:1051-1058.

Coppens JR, Mahaney KB, Abdulrauf SI (2005) An anteromedial approach to the temporal horn to avoid injury to the optic radiation fibers and uncinate fasciculus: anatomical and technical note. *Neurosurg. Focus.* 18:E3.

Corcoran R, Upton D (1993) A role for the hippocampus in card sorting? *Cortex* 29:293-304.

Cousijn H, Rijpkema M, Qin S, van Wingen GA, Fernandez G (2012) Phasic deactivation of the medial temporal lobe enables working memory processing under stress. *Neuroimage.* 59:1161-1167.

Cox RG, Levy R, Hamilton MG, Ewen A, Farran P, Neil SG (2011) Anesthesia can be safely provided for children in a high-field intraoperative magnetic resonance imaging environment. *Paediatr. Anaesth.* 21:454-458.

Cushing H (1921) Distortions of the visual fields in the case of brain tumours: the field defects produced by temporal lobe lesions. *Trans. Am. Neurol. Assoc.* 374-420.

D'Esposito M (2008) Working memory. *Handb. Clin. Neurol.* 88:237-247.

Daga P, Modat M, Winston G, White M, Mancini L, McEvoy AW, Thornton J, Yousry T, Duncan JS, Ourselin S (2013) Susceptibility artefact correction by combining B0 field maps and non-rigid registration using graph cuts. *Proc.SPIE* 8669:86690B.

Daga P, Winston G, Modat M, Cardoso MJ, Stretton J, Symms M, McEvoy AW, Hawkes D, Duncan J, Ourselin S (2011a) Integrating structural and diffusion MR information for optic radiation localisation in focal epilepsy patients. *IEEE Int Symp Biomed Imaging* 353-356.

Daga P, Winston G, Modat M, Cardoso MJ, White M, McEvoy AW, Thornton J, Hawkes D, Duncan J, Ourselin S (2011b) Improved neuronavigation through integration of intraoperative anatomical and diffusion images in an interventional MRI suite. *Lecture Notes in Computer Science* 6689:168-178.

Daga P, Winston G, Modat M, White M, Mancini L, Cardoso MJ, Symms M, Stretton J, McEvoy AW, Thornton J, Micallef C, Yousry T, Hawkes DJ, Duncan JS, Ourselin S (2012) Accurate localization of optic radiation during neurosurgery in an interventional MRI suite. *IEEE Trans. Med. Imaging* 31:882-891.

Davies KG, Bell BD, Bush AJ, Hermann BP, Dohan FC, Jr., Jaap AS (1998) Naming decline after left anterior temporal lobectomy correlates with pathological status of resected hippocampus. *Epilepsia* 39:407-419.

de Tisi J, Bell GS, Peacock JL, McEvoy AW, Harkness WF, Sander JW, Duncan JS (2011) The long-term outcome of adult epilepsy surgery, patterns of seizure remission, and relapse: a cohort study. *Lancet* 378:1388-1395.

Diehl B, Busch RM, Duncan JS, Piao Z, Tkach J, Luders HO (2008) Abnormalities in diffusion tensor imaging of the uncinate fasciculus relate to reduced memory in temporal lobe epilepsy. *Epilepsia* 49:1409-1418.

Diehl B, Piao Z, Tkach J, Busch RM, LaPresto E, Najm I, Bingaman B, Duncan J, Luders H (2010) Cortical stimulation for language mapping in focal epilepsy: correlations with tractography of the arcuate fasciculus. *Epilepsia* 51:639-646.

Diehl B, Symms MR, Boulby PA, Salmenpera T, Wheeler-Kingshott CA, Barker GJ, Duncan JS (2005) Postictal diffusion tensor imaging. *Epilepsy Res.* 65:137-146.

Dineen RA, Vilisaar J, Hlinka J, Bradshaw CM, Morgan PS, Constantinescu CS, Auer DP (2009) Disconnection as a mechanism for cognitive dysfunction in multiple sclerosis. *Brain* 132:239-249.

Douaud G, Jbabdi S, Behrens TE, Menke RA, Gass A, Monsch AU, Rao A, Whitcher B, Kindlmann G, Matthews PM, Smith S (2011) DTI measures in crossing-fibre areas: increased diffusion anisotropy reveals early white matter alteration in MCI and mild Alzheimer's disease. *Neuroimage.* 55:880-890.

Driver and Vehicle Licensing Agency (2013) *At a glance. Guide to the current Medical Standards of Fitness to Drive.* Drivers Medical Group, DVLA, Swansea.

Dumas de la Roque A, Oppenheim C, Chassoux F, Rodrigo S, Beuvon F, Daumas-Duport C, Devaux B, Meder JF (2005) Diffusion tensor imaging of partial intractable epilepsy. *Eur. Radiol.* 15:279-285.

Duncan JS (2010) Imaging in the surgical treatment of epilepsy. *Nat. Rev. Neurol.* 6:537-550.

Ebeling U, Reulen HJ (1988) Neurosurgical topography of the optic radiation in the temporal lobe. *Acta Neurochir. (Wien.)* 92:29-36.

Ebeling U, von Cramon D (1992) Topography of the uncinate fascicle and adjacent temporal fiber tracts. *Acta Neurochir. (Wien.)* 115:143-148.

Egan RA, Shults WT, So N, Burchiel K, Kellogg JX, Salinsky M (2000) Visual field deficits in conventional anterior temporal lobectomy versus amygdalohippocampectomy. *Neurology* 55:1818-1822.

Eichenbaum H (2000) A cortical-hippocampal system for declarative memory. *Nat. Rev. Neurosci.* 1:41-50.

Einstein A (1905) Über die von der molekularkinetischewn Theorie der wärme geforderte Bewegung von in ruhenden Flüssigkeiten suspendierten Teilchen. *Ann. Physik.* 4:549-560.

Ellmore TM, Beauchamp MS, Breier JJ, Slater JD, Kalamangalam GP, O'Neill TJ, Disano MA, Tandon N (2010) Temporal lobe white matter asymmetry and language laterality in epilepsy patients. *Neuroimage*. 49:2033-2044.

Ellmore TM, Beauchamp MS, O'Neill TJ, Dreyer S, Tandon N (2009) Relationships between essential cortical language sites and subcortical pathways. *J. Neurosurg*. 111:755-766.

Engel J, Cascino GD, Ness PCV, Rasmussen TB, Ojemann LM (1993) Outcome with respect to epileptic seizures. In Engel J (eds) *Surgical treatment of the epilepsies*, Raven Press, New York, pp. 609-621.

Engel J, Jr., Wiebe S, French J, Sperling M, Williamson P, Spencer D, Gumnit R, Zahn C, Westbrook E, Enos B (2003) Practice parameter: temporal lobe and localized neocortical resections for epilepsy: report of the Quality Standards Subcommittee of the American Academy of Neurology, in association with the American Epilepsy Society and the American Association of Neurological Surgeons. *Neurology* 60:538-547.

Eriksson SH, Rugg-Gunn FJ, Symms MR, Barker GJ, Duncan JS (2001) Diffusion tensor imaging in patients with epilepsy and malformations of cortical development. *Brain* 124:617-626.

Eyesight Working Group (2005) *New standards for the visual function of drivers*. European Driving Licence Committee, Brussels.

Faber J, Schoene-Bake JC, Trautner P, von LM, Elger CE, Weber B (2013) Progressive fiber tract affections after temporal lobe surgery. *Epilepsia* 54:e53-e57.

Falconer MA, Hill D, Mitchell W, Pond DA (1955) Treatment of temporal-lobe epilepsy by temporal lobectomy; a survey of findings and results. *Lancet* 268:827-835.

Falconer MA, Wilson JL (1958) Visual field changes following anterior temporal lobectomy: their significance in relation to Meyer's loop of the optic radiation. *Brain* 81:1-14.

Fisher RS, van Emde BW, Blume W, Elger C, Genton P, Lee P, Engel J, Jr. (2005) Epileptic seizures and epilepsy: definitions proposed by the International League Against Epilepsy (ILAE) and the International Bureau for Epilepsy (IBE). *Epilepsia* 46:470-472.

Flugel D, Cercignani M, Symms MR, O'Toole A, Thompson PJ, Koepp MJ, Foong J (2006) Diffusion tensor imaging findings and their correlation with neuropsychological deficits in patients with temporal lobe epilepsy and interictal psychosis. *Epilepsia* 47:941-944.

Focke NK, Bonelli SB, Yogarajah M, Scott C, Symms MR, Duncan JS (2009) Automated normalized FLAIR imaging in MRI-negative patients with refractory focal epilepsy. *Epilepsia* 50:1484-1490.

Focke NK, Yogarajah M, Bonelli SB, Bartlett PA, Symms MR, Duncan JS (2008) Voxel-based diffusion tensor imaging in patients with mesial temporal lobe epilepsy and hippocampal sclerosis. *Neuroimage*. 40:728-737.

Foldvary N, Lee N, Thwaites G, Mascha E, Hammel J, Kim H, Friedman AH, Radtke RA (1997) Clinical and electrographic manifestations of lesional neocortical temporal lobe epilepsy. *Neurology* 49:757-763.

Frank LR (2002) Characterization of anisotropy in high angular resolution diffusion-weighted MRI. *Magn Reson. Med*. 47:1083-1099.

French LA (1962) Studies on the optic radiations. The significance of small field defects in the region of the vertical meridian. *J. Neurosurg*. 19:522-528.

Gil-Nagel A, Risinger MW (1997) Ictal semiology in hippocampal versus extrahippocampal temporal lobe epilepsy. *Brain* 120 (Pt 1):183-192.

Gilliam F, Kuzniecky R, Faught E, Black L, Carpenter G, Schrodt R (1997) Patient-validated content of epilepsy-specific quality-of-life measurement. *Epilepsia* 38:233-236.

Gleissner U, Helmstaedter C, Elger CE (1998) Right hippocampal contribution to visual memory: a presurgical and postsurgical study in patients with temporal lobe epilepsy. *J. Neurol. Neurosurg. Psychiatry* 65:665-669.

Gogoleva SM, Ryvlin P, Sindou M, Fischer G, Jouviet A, Saint PG, Veyre L, Froment JC, Mauguiere F, Cinotti L (1997) Brain glucose metabolism with [18F]-fluorodeoxyglucose and positron emission tomography before and after surgical resection of epileptogenic cavernous angiomas. *Stereotact. Funct. Neurosurg*. 69:225-228.

Goncalves Pereira PM, Oliveira E, Rosado P (2006) Apparent diffusion coefficient mapping of the hippocampus and the amygdala in pharmaco-resistant temporal lobe epilepsy. *AJNR Am. J. Neuroradiol.* 27:671-683.

Gong G, Concha L, Beaulieu C, Gross DW (2008) Thalamic diffusion and volumetry in temporal lobe epilepsy with and without mesial temporal sclerosis. *Epilepsy Res.* 80:184-193.

Goradia D, Chugani HT, Govindan RM, Behen M, Juhasz C, Sood S (2011) Reorganization of the right arcuate fasciculus following left arcuate fasciculus resection in children with intractable epilepsy. *J. Child Neurol.* 26:1246-1251.

Govindan RM, Chugani HT, Makki MI, Behen ME, Dornbush J, Sood S (2008) Diffusion tensor imaging of brain plasticity after occipital lobectomy. *Pediatr. Neurol.* 38:27-33.

Gross DW, Bastos A, Beaulieu C (2005) Diffusion tensor imaging abnormalities in focal cortical dysplasia. *Can. J. Neurol. Sci.* 32:477-482.

Gross DW, Concha L, Beaulieu C (2006) Extratemporal white matter abnormalities in mesial temporal lobe epilepsy demonstrated with diffusion tensor imaging. *Epilepsia* 47:1360-1363.

Gu L, Li J, Feng DF, Cheng ET, Li DC, Yang XQ, Wang BC (2013) Detection of white matter lesions in the acute stage of diffuse axonal injury predicts long-term cognitive impairments: a clinical diffusion tensor imaging study. *J. Trauma Acute. Care Surg.* 74:242-247.

Gulani V, Webb AG, Duncan ID, Lauterbur PC (2001) Apparent diffusion tensor measurements in myelin-deficient rat spinal cords. *Magn Reson. Med.* 45:191-195.

Hahn EL (1950) Spin echoes. *Phys. Rev.* 80:580-594.

Hampson M, Driesen NR, Skudlarski P, Gore JC, Constable RT (2006) Brain connectivity related to working memory performance. *J. Neurosci.* 26:13338-13343.

Harrington DO (1961) Visual field character in temporal and occipital lobe lesions. Localizing values of congruity and incongruity in incomplete homonymous hemianopsia. *Arch. Ophthalmol.* 66:778-792.

Hauser WA, Annegers JF, Kurland LT (1993) Incidence of epilepsy and unprovoked seizures in Rochester, Minnesota: 1935-1984. *Epilepsia* 34:453-468.

Helmstaedter C, Grunwald T, Lehnertz K, Gleissner U, Elger CE (1997a) Differential involvement of left temporolateral and temporomesial structures in verbal declarative learning and memory: evidence from temporal lobe epilepsy. *Brain Cogn* 35:110-131.

Helmstaedter C, Kurthen M, Linke DB, Elger CE (1997b) Patterns of language dominance in focal left and right hemisphere epilepsies: relation to MRI findings, EEG, sex, and age at onset of epilepsy. *Brain Cogn* 33:135-150.

Helmstaedter C, Kurthen M, Lux S, Reuber M, Elger CE (2003) Chronic epilepsy and cognition: a longitudinal study in temporal lobe epilepsy. *Ann. Neurol.* 54:425-432.

Hendriks MP, Aldenkamp AP, van d, V, Alpherts WC, Vermeulen J (2002) Memory Complaints in Medically Refractory Epilepsy: Relationship to Epilepsy-Related Factors. *Epilepsy Behav.* 3:165-172.

Henry TR, Mazziotta JC, Engel J, Jr. (1993) Interictal metabolic anatomy of mesial temporal lobe epilepsy. *Arch. Neurol.* 50:582-589.

Henry TR, Sutherling WW, Engel J, Jr., Risinger MW, Levesque MF, Mazziotta JC, Phelps ME (1991) Interictal cerebral metabolism in partial epilepsies of neocortical origin. *Epilepsy Res.* 10:174-182.

Henze R, Brunner R, Thiemann U, Parzer P, Klein J, Resch F, Stieltjes B (2012) The Optic Radiation and the Cerebellar Peduncles in Adolescents with First-Admission Schizophrenia -A Diffusion Tensor Imaging Study. *J. Neuroimaging*. Published online: 23-Jan-2012; doi: 10.1111/j.1552-6569.2011.00668.x.

Hermann BP, Seidenberg M, Schoenfeld J, Davies K (1997) Neuropsychological characteristics of the syndrome of mesial temporal lobe epilepsy. *Arch. Neurol.* 54:369-376.

Hermann BP, Wyler AR, Richey ET (1988) Wisconsin Card Sorting Test performance in patients with complex partial seizures of temporal-lobe origin. *J. Clin. Exp. Neuropsychol.* 10:467-476.

Hermann BP, Wyler AR, Somes G, Clement L (1994) Dysnomia after left anterior temporal lobectomy without functional mapping: frequency and correlates. *Neurosurgery* 35:52-56.

Hervas-Navidad R, tuzarra-Corral A, Lucena-Martin JA, Castaneda-Guerrero M, Vela-Yebra R, Sanchez A (2002) [Defects in the visual field in resective surgery for temporal lobe epilepsy]. *Rev. Neurol.* 34:1025-1030.

Hirono N, Mori E, Ishii K, Ikejiri Y, Imamura T, Shimomura T, Hashimoto M, Yamashita H, Sasaki M (1998) Hypofunction in the posterior cingulate gyrus correlates with disorientation for time and place in Alzheimer's disease. *J. Neurol. Neurosurg. Psychiatry* 64:552-554.

Hofer S, Karaus A, Frahm J (2010) Reconstruction and dissection of the entire human visual pathway using diffusion tensor MRI. *Front Neuroanat.* 4:15.

Holmes G (1918) Disturbances of vision by cerebral lesions. *Br. J. Ophthalmol.* 2:353-384.

Hori T, Tabuchi S, Kurosaki M, Kondo S, Takenobu A, Watanabe T (1993) Subtemporal amygdalohippocampectomy for treating medically intractable temporal lobe epilepsy. *Neurosurgery* 33:50-56.

Hori T, Yamane F, Ochiai T, Kondo S, Shimizu S, Ishii K, Miyata H (2007) Selective subtemporal amygdalohippocampectomy for refractory temporal lobe epilepsy: operative and neuropsychological outcomes. *J. Neurosurg.* 106:134-141.

Hoult DI, Saunders JK, Sutherland GR, Sharp J, Gervin M, Kolansky HG, Kripiakevich DL, Procca A, Sebastian RA, Dombay A, Rayner DL, Roberts FA, Tomanek B (2001) The engineering of an interventional MRI with a movable 1.5 Tesla magnet. *J. Magn Reson. Imaging* 13:78-86.

Hugg JW, Butterworth EJ, Kuzniecky RI (1999) Diffusion mapping applied to mesial temporal lobe epilepsy: preliminary observations. *Neurology* 53:173-176.

Hugg JW, Kuzniecky RI, Gilliam FG, Morawetz RB, Fraught RE, Hetherington HP (1996) Normalization of contralateral metabolic function following temporal lobectomy demonstrated by 1H magnetic resonance spectroscopic imaging. *Ann. Neurol.* 40:236-239.

Hughes TS, bou-Khalil B, Lavin PJ, Fakhoury T, Blumenkopf B, Donahue SP (1999) Visual field defects after temporal lobe resection: a prospective quantitative analysis. *Neurology* 53:167-172.

International League Against Epilepsy (1981) Proposal for revised clinical and electroencephalographic classification of epileptic seizures. From the Commission on Classification and Terminology of the International League Against Epilepsy. *Epilepsia* 22:489-501.

International League Against Epilepsy (1989) Proposal for revised classification of epilepsies and epileptic syndromes. Commission on Classification and Terminology of the International League Against Epilepsy. *Epilepsia* 30:389-399.

Jackson GD, Berkovic SF, Duncan JS, Connelly A (1993) Optimizing the diagnosis of hippocampal sclerosis using MR imaging. *AJNR Am. J. Neuroradiol.* 14:753-762.

Janke A, Zhao H, Cowin GJ, Galloway GJ, Doddrell DM (2004) Use of spherical harmonic deconvolution methods to compensate for nonlinear gradient effects on MRI images. *Magn Reson. Med.* 52:115-122.

Jansen FE, Braun KP, van NO, Huiskamp G, Vincken KL, van Huffelen AC, van der Grond J (2003) Diffusion-weighted magnetic resonance imaging and identification of the epileptogenic tuber in patients with tuberous sclerosis. *Arch. Neurol.* 60:1580-1584.

Jeelani NU, Jindahra P, Tamber MS, Poon TL, Kabasele P, James-Galton M, Stevens J, Duncan J, McEvoy AW, Harkness W, Plant GT (2010) 'Hemispherical asymmetry in the Meyer's Loop': a prospective study of visual-field deficits in 105 cases undergoing anterior temporal lobe resection for epilepsy. *J. Neurol. Neurosurg. Psychiatry* 81:985-991.

Jensen I, Seedorff HH (1976) Temporal lobe epilepsy and neuro-ophthalmology. Ophthalmological findings in 74 temporal lobe resected patients. *Acta Ophthalmol. (Copenh)* 54:827-841.

Jezzard P, Balaban RS (1995) Correction for geometric distortion in echo planar images from B0 field variations. *Magn Reson. Med.* 34:65-73.

Joint Epilepsy Council of the UK and Ireland (2011) *Epilepsy prevalence, incidence and other statistics*. Joint Epilepsy Council, Leeds.

Jolesz FA (1995) Interventional magnetic resonance imaging, computed tomography, and ultrasound. *Acad. Radiol.* 2 Suppl 2:S124-S125.

Jones DK, Knosche TR, Turner R (2013) White matter integrity, fiber count, and other fallacies: The do's and don'ts of diffusion MRI. *Neuroimage*. 73:239-254.

Jones DK, Symms MR, Cercignani M, Howard RJ (2005) The effect of filter size on VBM analyses of DT-MRI data. *Neuroimage*. 26:546-554.

Judkins AR, Martinez D, Ferreira P, Dobyns WB, Golden JA (2011) Polymicrogyria includes fusion of the molecular layer and decreased neuronal populations but normal cortical laminar organization. *J. Neuropathol. Exp. Neurol.* 70:438-443.

Kaibara T, Myles ST, Lee MA, Sutherland GR (2002) Optimizing epilepsy surgery with intraoperative MR imaging. *Epilepsia* 43:425-429.

Kamada K, Todo T, Morita A, Masutani Y, Aoki S, Ino K, Kawai K, Kirino T (2005) Functional monitoring for visual pathway using real-time visual evoked potentials and optic-radiation tractography. *Neurosurgery* 57:121-127.

Karlsgodt KH, Shirinyan D, van Erp TG, Cohen MS, Cannon TD (2005) Hippocampal activations during encoding and retrieval in a verbal working memory paradigm. *Neuroimage*. 25:1224-1231.

Karlsgodt KH, van Erp TG, Poldrack RA, Bearden CE, Nuechterlein KH, Cannon TD (2008) Diffusion tensor imaging of the superior longitudinal fasciculus and working memory in recent-onset schizophrenia. *Biol. Psychiatry* 63:512-518.

Katz A, Awad IA, Kong AK, Chelune GJ, Naugle RI, Wyllie E, Beauchamp G, Luders H (1989) Extent of resection in temporal lobectomy for epilepsy. II. Memory changes and neurologic complications. *Epilepsia* 30:763-771.

Keller SS, Ahrens T, Mohammadi S, Gerdes JS, Moddel G, Kellinghaus C, Kugel H, Weber B, Ringelstein EB, Deppe M (2013) Voxel-based statistical analysis of fractional anisotropy and mean diffusivity in patients with unilateral temporal lobe epilepsy of unknown cause. *J. Neuroimaging* 23:352-359.

Keller SS, Roberts N (2008) Voxel-based morphometry of temporal lobe epilepsy: an introduction and review of the literature. *Epilepsia* 49:741-757.

Keller SS, Schoene-Bake JC, Gerdes JS, Weber B, Deppe M (2012) Concomitant fractional anisotropy and volumetric abnormalities in temporal lobe epilepsy: cross-sectional evidence for progressive neurologic injury. *PLoS. One.* 7:e46791.

Kemmotsu N, Girard HM, Bernhardt BC, Bonilha L, Lin JJ, Tecoma ES, Iragui VJ, Hagler DJ, Jr., Halgren E, McDonald CR (2011) MRI analysis in temporal lobe epilepsy: cortical thinning and white matter disruptions are related to side of seizure onset. *Epilepsia* 52:2257-2266.

Kennedy KM, Raz N (2009) Aging white matter and cognition: differential effects of regional variations in diffusion properties on memory, executive functions, and speed. *Neuropsychologia* 47:916-927.

Kettenbach J, Kacher DF, Kanan AR, Rostenberg B, Fairhurst J, Stadler A, Kienreich K, Jolesz FA (2006) Intraoperative and interventional MRI: recommendations for a safe environment. *Minim. Invasive. Ther. Allied Technol.* 15:53-64.

Kikuta K, Takagi Y, Nozaki K, Hanakawa T, Okada T, Miki Y, Fushimi Y, Fukuyama H, Hashimoto N (2006) Early experience with 3-T magnetic resonance tractography in the surgery of cerebral arteriovenous malformations in and around the visual pathway. *Neurosurgery* 58:331-337.

Kim CH, Koo BB, Chung CK, Lee JM, Kim JS, Lee SK (2010) Thalamic changes in temporal lobe epilepsy with and without hippocampal sclerosis: a diffusion tensor imaging study. *Epilepsy Res.* 90:21-27.

Kim H, Piao Z, Liu P, Bingaman W, Diehl B (2008) Secondary white matter degeneration of the corpus callosum in patients with intractable temporal lobe epilepsy: a diffusion tensor imaging study. *Epilepsy Res.* 81:136-142.

Kimiwada T, Juhasz C, Makki M, Muzik O, Chugani DC, Asano E, Chugani HT (2006) Hippocampal and thalamic diffusion abnormalities in children with temporal lobe epilepsy. *Epilepsia* 47:167-175.

Kinoshita Y, Ohnishi A, Kohshi K, Yokota A (1999) Apparent diffusion coefficient on rat brain and nerves intoxicated with methylmercury. *Environ. Res.* 80:348-354.

Klingberg T (2006) Development of a superior frontal-intraparietal network for visuo-spatial working memory. *Neuropsychologia* 44:2171-2177.

- Klingberg T, Forssberg H, Westerberg H (2002) Increased brain activity in frontal and parietal cortex underlies the development of visuospatial working memory capacity during childhood. *J. Cogn Neurosci.* 14:1-10.
- Knake S, Salat DH, Halgren E, Halko MA, Greve DN, Grant PE (2009) Changes in white matter microstructure in patients with TLE and hippocampal sclerosis. *Epileptic. Disord.* 11:244-250.
- Koenigs M, Barbey AK, Postle BR, Grafman J (2009) Superior parietal cortex is critical for the manipulation of information in working memory. *J. Neurosci.* 29:14980-14986.
- Kondo H, Morishita M, Osaka N, Osaka M, Fukuyama H, Shibasaki H (2004) Functional roles of the cingulo-frontal network in performance on working memory. *Neuroimage.* 21:2-14.
- Krolak-Salmon P, Guenot M, Tiliket C, Isnard J, Sindou M, Mauguire F, Vighetto A (2000) Anatomy of optic nerve radiations as assessed by static perimetry and MRI after tailored temporal lobectomy. *Br. J. Ophthalmol.* 84:884-889.
- Kubben PL, ter Meulen KJ, Schijns OE, ter Laak-Poort MP, van Overbeeke JJ, van SH (2011) Intraoperative MRI-guided resection of glioblastoma multiforme: a systematic review. *Lancet Oncol.* 12:1062-1070.
- Kumari V, Gray JA, Ffytche DH, Mitterschiffthaler MT, Das M, Zachariah E, Vythelingum GN, Williams SC, Simmons A, Sharma T (2003) Cognitive effects of nicotine in humans: an fMRI study. *Neuroimage.* 19:1002-1013.
- Kwan P, Arzimanoglou A, Berg AT, Brodie MJ, Allen Hauser W, Mathern G, Moshe SL, Perucca E, Wiebe S, French J (2010) Definition of drug resistant epilepsy: consensus proposal by the ad hoc Task Force of the ILAE Commission on Therapeutic Strategies. *Epilepsia* 51:1069-1077.
- Kwan P, Brodie MJ (2000) Early identification of refractory epilepsy. *N. Engl. J. Med.* 342:314-319.
- Labate A, Cerasa A, Aguglia U, Mumoli L, Quattrone A, Gambardella A (2011) Neocortical thinning in "benign" mesial temporal lobe epilepsy. *Epilepsia* 52:712-717.
- Langfitt JT, Rausch R (1996) Word-finding deficits persist after left anterotemporal lobectomy. *Arch. Neurol.* 53:72-76.

Lantz G, Seeck M, Lazeyras F (2006) Extent of preoperative abnormalities and focus lateralization predict postoperative normalization of contralateral ¹H-magnetic resonance spectroscopy metabolite levels in patients with temporal lobe epilepsy. *AJNR Am. J. Neuroradiol.* 27:1766-1769.

Law N, Bouffet E, Laughlin S, Laperriere N, Briere ME, Strother D, McConnell D, Hukin J, Fryer C, Rockel C, Dickson J, Mabbott D (2011) Cerebello-thalamo-cerebral connections in pediatric brain tumor patients: impact on working memory. *Neuroimage.* 56:2238-2248.

Lazar M, Weinstein DM, Tsuruda JS, Hasan KM, Arfanakis K, Meyerand ME, Badie B, Rowley HA, Haughton V, Field A, Alexander AL (2003) White matter tractography using diffusion tensor deflection. *Hum. Brain Mapp.* 18:306-321.

Le Bihan D, Breton E, Lallemand D, Grenier P, Cabanis E, Laval-Jeantet M (1986) MR imaging of intravoxel incoherent motions: application to diffusion and perfusion in neurologic disorders. *Radiology* 161:401-407.

Lee JH, Chung CK, Song IC, Chang KH, Kim HJ (2004a) Limited utility of interictal apparent diffusion coefficient in the evaluation of hippocampal sclerosis. *Acta Neurol. Scand.* 110:53-58.

Lee SK, Kim DI, Mori S, Kim J, Kim HD, Heo K, Lee BI (2004b) Diffusion tensor MRI visualizes decreased subcortical fiber connectivity in focal cortical dysplasia. *Neuroimage.* 22:1826-1829.

Lee TM, Yip JT, Jones-Gotman M (2002) Memory deficits after resection from left or right anterior temporal lobe in humans: a meta-analytic review. *Epilepsia* 43:283-291.

Lhatoo SD, Johnson AL, Goodridge DM, MacDonald BK, Sander JW, Shorvon SD (2001) Mortality in epilepsy in the first 11 to 14 years after diagnosis: multivariate analysis of a long-term, prospective, population-based cohort. *Ann. Neurol.* 49:336-344.

Liacu D, Idy-Peretti I, Ducreux D, Bouilleret V, de Marco G (2012) Diffusion tensor imaging tractography parameters of limbic system bundles in temporal lobe epilepsy patients. *J. Magn Reson. Imaging* 36:561-568.

Liang D, Schulder M (2012) The role of intraoperative magnetic resonance imaging in glioma surgery. *Surg. Neurol. Int* 3:S320-S327.

- Liao W, Zhang Z, Pan Z, Mantini D, Ding J, Duan X, Luo C, Wang Z, Tan Q, Lu G, Chen H (2011) Default mode network abnormalities in mesial temporal lobe epilepsy: a study combining fMRI and DTI. *Hum. Brain Mapp.* 32:883-895.
- Liegeois F, Connelly A, Cross JH, Boyd SG, Gadian DG, Vargha-Khadem F, Baldeweg T (2004) Language reorganization in children with early-onset lesions of the left hemisphere: an fMRI study. *Brain* 127:1229-1236.
- Lin JJ, Riley JD, Juranek J, Cramer SC (2008) Vulnerability of the frontal-temporal connections in temporal lobe epilepsy. *Epilepsy Res.* 82:162-170.
- Liu M, Gross DW, Wheatley BM, Concha L, Beaulieu C (2013) The acute phase of Wallerian degeneration: Longitudinal diffusion tensor imaging of the fornix following temporal lobe surgery. *Neuroimage.* 74:128-139.
- Londono A, Castillo M, Lee YZ, Smith JK (2003) Apparent diffusion coefficient measurements in the hippocampi in patients with temporal lobe seizures. *AJNR Am. J. Neuroradiol.* 24:1582-1586.
- Ludwig E and Klingler J (1956) *Atlas Cerebri Humani*. S. Karger, Basel.
- Lui YW, Nusbaum AO, Barr WB, Johnson G, Babb JS, Orbach D, Kim A, Laloties G, Devinsky O (2005) Correlation of apparent diffusion coefficient with neuropsychological testing in temporal lobe epilepsy. *AJNR Am. J. Neuroradiol.* 26:1832-1839.
- MacDonald BK, Cockerell OC, Sander JW, Shorvon SD (2000) The incidence and lifetime prevalence of neurological disorders in a prospective community-based study in the UK. *Brain* 123 (Pt 4):665-676.
- Maillard L, Vignal JP, Gavaret M, Guye M, Biraben A, McGonigal A, Chauvel P, Bartolomei F (2004) Semiologic and electrophysiologic correlations in temporal lobe seizure subtypes. *Epilepsia* 45:1590-1599.
- Mainy N, Kahane P, Minotti L, Hoffmann D, Bertrand O, Lachaux JP (2007) Neural correlates of consolidation in working memory. *Hum. Brain Mapp.* 28:183-193.
- Malmgren K, Thom M (2012) Hippocampal sclerosis--origins and imaging. *Epilepsia* 53 Suppl 4:19-33.

Manji H, Plant GT (2000) Epilepsy surgery, visual fields, and driving: a study of the visual field criteria for driving in patients after temporal lobe epilepsy surgery with a comparison of Goldmann and Esterman perimetry. *J. Neurol. Neurosurg. Psychiatry* 68:80-82.

Marino R, Jr., Rasmussen T (1968) Visual field changes after temporal lobectomy in man. *Neurology* 18:825-835.

Maruyama K, Kamada K, Shin M, Itoh D, Masutani Y, Ino K, Tago M, Saito N (2007) Optic radiation tractography integrated into simulated treatment planning for Gamma Knife surgery. *J. Neurosurg.* 107:721-726.

Matsumoto R, Okada T, Mikuni N, Mitsueda-Ono T, Taki J, Sawamoto N, Hanakawa T, Miki Y, Hashimoto N, Fukuyama H, Takahashi R, Ikeda A (2008) Hemispheric asymmetry of the arcuate fasciculus: a preliminary diffusion tensor tractography study in patients with unilateral language dominance defined by Wada test. *J. Neurol.* 255:1703-1711.

Mattson RH, Cramer JA, Collins JF (1996) Prognosis for total control of complex partial and secondarily generalized tonic clonic seizures. Department of Veterans Affairs Epilepsy Cooperative Studies No. 118 and No. 264 Group. *Neurology* 47:68-76.

McDonald CR, Ahmadi ME, Hagler DJ, Tecoma ES, Iragui VJ, Gharapetian L, Dale AM, Halgren E (2008) Diffusion tensor imaging correlates of memory and language impairments in temporal lobe epilepsy. *Neurology* 71:1869-1876.

McDonald CR, Hagler DJ, Jr., Girard HM, Pung C, Ahmadi ME, Holland D, Patel RH, Barba D, Tecoma ES, Iragui VJ, Halgren E, Dale AM (2010) Changes in fiber tract integrity and visual fields after anterior temporal lobectomy. *Neurology* 75:1631-1638.

McIntosh AM, Wilson SJ, Berkovic SF (2001) Seizure outcome after temporal lobectomy: current research practice and findings. *Epilepsia* 42:1288-1307.

Meng L, Xiang J, Kotecha R, Rose D, Zhao H, Zhao D, Yang J, Degrauw T (2010) White matter abnormalities in children and adolescents with temporal lobe epilepsy. *Magn Reson. Imaging* 28:1290-1298.

- Mengesha T, bu-Ata M, Haas KF, Lavin PJ, Sun DA, Konrad PE, Pearson M, Wang L, Song Y, bou-Khalil BW (2009) Visual field defects after selective amygdalohippocampectomy and standard temporal lobectomy. *J. Neuroophthalmol.* 29:208-213.
- Merhof D, Soza G, Stadlbauer A, Greiner G, Nimsky C (2007) Correction of susceptibility artifacts in diffusion tensor data using non-linear registration. *Med. Image Anal.* 11:588-603.
- Meyer A (1907) The connections of the occipital lobes and the present state of the cerebral visual affections. *Trans. Ass. Am. Phys.* 22:7-16.
- Miyagi Y, Shima F, Ishido K, Araki T, Taniwaki Y, Okamoto I, Kamikaseda K (2003) Inferior temporal sulcus approach for amygdalohippocampectomy guided by a laser beam of stereotactic navigator. *Neurosurgery* 52:1117-1123.
- Modat M (2012) *Efficient Dense Non-Rigid Registration using the Free-Form Deformation Framework*. PhD thesis, University College London.
- Modat M, Ridgway GR, Taylor ZA, Lehmann M, Barnes J, Hawkes DJ, Fox NC, Ourselin S (2010) Fast free-form deformation using graphics processing units. *Comput. Methods Programs Biomed.* 98:278-284.
- Mori N, Miki Y, Kasahara S, Maeda C, Kanagaki M, Urayama S, Sawamoto N, Fukuyama H, Togashi K (2009) Susceptibility-weighted imaging at 3 Tesla delineates the optic radiation. *Invest Radiol.* 44:140-145.
- Mori S, Crain BJ, Chacko VP, van Zijl PC (1999) Three-dimensional tracking of axonal projections in the brain by magnetic resonance imaging. *Ann. Neurol.* 45:265-269.
- Mori S, van Zijl PC (2002) Fiber tracking: principles and strategies - a technical review. *NMR Biomed.* 15:468-480.
- Morris AA (1956) Temporal lobectomy with removal of uncus, hippocampus, and amygdala; results for psychomotor epilepsy three to nine years after operation. *AMA. Arch. Neurol. Psychiatry* 76:479-496.
- Moseley ME, Cohen Y, Kucharczyk J, Mintorovitch J, Asgari HS, Wendland MF, Tsuruda J, Norman D (1990a) Diffusion-weighted MR imaging of anisotropic water diffusion in cat central nervous system. *Radiology* 176:439-445.

Moseley ME, Cohen Y, Mintorovitch J, Chileuitt L, Shimizu H, Kucharczyk J, Wendland MF, Weinstein PR (1990b) Early detection of regional cerebral ischemia in cats: comparison of diffusion- and T2-weighted MRI and spectroscopy. *Magn Reson. Med.* 14:330-346.

Moseley ME, Kucharczyk J, Asgari HS, Norman D (1991) Anisotropy in diffusion-weighted MRI. *Magn Reson. Med.* 19:321-326.

Nabavi A, Black PM, Gering DT, Westin CF, Mehta V, Pergolizzi RS, Jr., Ferrant M, Warfield SK, Hata N, Schwartz RB, Wells WM, III, Kikinis R, Jolesz FA (2001) Serial intraoperative magnetic resonance imaging of brain shift. *Neurosurgery* 48:787-797.

Nagy Z, Westerberg H, Klingberg T (2004) Maturation of white matter is associated with the development of cognitive functions during childhood. *J. Cogn Neurosci.* 16:1227-1233.

National Institute of Health and Clinical Excellence (2012) *The epilepsies: the diagnosis and management of the epilepsies in adults and children in primary and secondary care*. NICE, London.

Nguyen D, Vargas MI, Khaw N, Seeck M, Delavelle J, Lovblad KO, Haller S (2011) Diffusion tensor imaging analysis with tract-based spatial statistics of the white matter abnormalities after epilepsy surgery. *Epilepsy Res.* Published online: 03-Mar-2011; doi: 10.1016/j.eplepsyres.2011.02.001.

Nichols TE, Holmes AP (2002) Nonparametric permutation tests for functional neuroimaging: a primer with examples. *Hum. Brain Mapp.* 15:1-25.

Niemeyer P (1958) The transventricular amygdala-hippocampectomy in temporal lobe epilepsy. In Baldwin M and Bailey P (eds) *Temporal Lobe Epilepsy*, Charles C Thomas, Springfield, IL, pp. 461-482.

Niendorf T, Dijkhuizen RM, Norris DG, van Lookeren Campagne M, Nicolay K (1996) Biexponential diffusion attenuation in various states of brain tissue: implications for diffusion-weighted imaging. *Magn Reson. Med.* 36:847-857.

Nilsson D, Go C, Rutka JT, Rydenhag B, Mabbott DJ, Snead OC, III, Raybaud CR, Widjaja E (2008) Bilateral diffusion tensor abnormalities of temporal lobe and cingulate gyrus white matter in children with temporal lobe epilepsy. *Epilepsy Res.* 81:128-135.

Nilsson D, Malmgren K, Rydenhag B, Frisen L (2004) Visual field defects after temporal lobectomy -- comparing methods and analysing resection size. *Acta Neurol. Scand.* 110:301-307.

- Nilsson D, Starck G, Ljungberg M, Ribbelin S, Jonsson L, Malmgren K, Rydenhag B (2007) Intersubject variability in the anterior extent of the optic radiation assessed by tractography. *Epilepsy Res.* 77:11-16.
- Nilsson DT, Rydenhag B, Malmgren K, Starck G, Ljungberg M (2010) Anatomical accuracy and feasibility of probabilistic and deterministic tractography of the optic radiation. *Epilepsia* 51(Suppl. 4):91.
- Nimsky C, Ganslandt O, Buchfelder M, Fahlbusch R (2006a) Intraoperative visualization for resection of gliomas: the role of functional neuronavigation and intraoperative 1.5 T MRI. *Neurol. Res.* 28:482-487.
- Nimsky C, Ganslandt O, Cerny S, Hastreiter P, Greiner G, Fahlbusch R (2000) Quantification of, visualization of, and compensation for brain shift using intraoperative magnetic resonance imaging. *Neurosurgery* 47:1070-1079.
- Nimsky C, Ganslandt O, Fahlbusch R (2006b) Implementation of fiber tract navigation. *Neurosurgery* 58:ONS-303.
- O'Brien TJ, So EL, Mullan BP, Hauser MF, Brinkmann BH, Bohnen NI, Hanson D, Cascino GD, Jack CR, Jr., Sharbrough FW (1998) Subtraction ictal SPECT co-registered to MRI improves clinical usefulness of SPECT in localizing the surgical seizure focus. *Neurology* 50:445-454.
- Oguz KK, Tezer I, Sanverdi E, Has AC, Bilginer B, Dolgun A, Saygi S (2013) Effect of patient sex on white matter alterations in unilateral medial temporal lobe epilepsy with hippocampal sclerosis assessed by diffusion tensor imaging. *AJNR Am. J. Neuroradiol.* 34:1010-1015.
- Oh DS, Black PM (2005) A low-field intraoperative MRI system for glioma surgery: is it worthwhile? *Neurosurg. Clin. N. Am.* 16:135-141.
- Okada T, Miki Y, Kikuta K, Mikuni N, Urayama S, Fushimi Y, Yamamoto A, Mori N, Fukuyama H, Hashimoto N, Togashi K (2007) Diffusion tensor fiber tractography for arteriovenous malformations: quantitative analyses to evaluate the corticospinal tract and optic radiation. *AJNR Am. J. Neuroradiol.* 28:1107-1113.
- Oldfield RC (1971) The assessment and analysis of handedness: the Edinburgh inventory. *Neuropsychologia* 9:97-113.

- Olesen PJ, Nagy Z, Westerberg H, Klingberg T (2003) Combined analysis of DTI and fMRI data reveals a joint maturation of white and grey matter in a fronto-parietal network. *Brain Res. Cogn Brain Res.* 18:48-57.
- Ostby Y, Tamnes CK, Fjell AM, Walhovd KB (2011) Morphometry and connectivity of the fronto-parietal verbal working memory network in development. *Neuropsychologia* 49:3854-3862.
- Otte WM, van EP, Sander JW, Duncan JS, Dijkhuizen RM, Braun KP (2012) A meta-analysis of white matter changes in temporal lobe epilepsy as studied with diffusion tensor imaging. *Epilepsia* 53:659-667.
- Ourselin S, Stefanescu R, Pennec X (2002) Robust registration of multi-modal images: Towards real-time clinical applications. *Proceedings of the 5th International Conference on Medical Image Computing and Computer-Assisted Intervention-Part II* 2489:140-147.
- Owen AM, McMillan KM, Laird AR, Bullmore E (2005) N-back working memory paradigm: a meta-analysis of normative functional neuroimaging studies. *Hum. Brain Mapp.* 25:46-59.
- Pajevic S, Pierpaoli C (1999) Color schemes to represent the orientation of anisotropic tissues from diffusion tensor data: application to white matter fiber tract mapping in the human brain. *Magn Reson. Med.* 42:526-540.
- Palacios EM, Fernandez-Espejo D, Junque C, Sanchez-Carrion R, Roig T, Tormos JM, Bargallo N, Vendrell P (2011) Diffusion tensor imaging differences relate to memory deficits in diffuse traumatic brain injury. *BMC. Neurol.* 11:24.
- Palacios EM, Sala-Llonch R, Junque C, Roig T, Tormos JM, Bargallo N, Vendrell P (2012) White matter integrity related to functional working memory networks in traumatic brain injury. *Neurology* 78:852-860.
- Panagiotaki E, Schneider T, Siow B, Hall MG, Lythgoe MF, Alexander DC (2012) Compartment models of the diffusion MR signal in brain white matter: a taxonomy and comparison. *Neuroimage.* 59:2241-2254.
- Park TS, Bourgeois BF, Silbergeld DL, Dodson WE (1996) Subtemporal transparahippocampal amygdalohippocampectomy for surgical treatment of mesial temporal lobe epilepsy. Technical note. *J. Neurosurg.* 85:1172-1176.

Parker GJ, Alexander DC (2003) Probabilistic Monte Carlo based mapping of cerebral connections utilising whole-brain crossing fibre information. *Inf. Process Med. Imaging* 18:684-695.

Parker GJ, Haroon HA, Wheeler-Kingshott CA (2003) A framework for a streamline-based probabilistic index of connectivity (PICO) using a structural interpretation of MRI diffusion measurements. *J. Magn Reson. Imaging* 18:242-254.

Parker GJ, Stephan KE, Barker GJ, Rowe JB, MacManus DG, Wheeler-Kingshott CA, Ciccarelli O, Passingham RE, Spinks RL, Lemon RN, Turner R (2002) Initial demonstration of in vivo tracing of axonal projections in the macaque brain and comparison with the human brain using diffusion tensor imaging and fast marching tractography. *Neuroimage*. 15:797-809.

Parrish RK, Schiffman J, Anderson DR (1984) Static and kinetic visual field testing. Reproducibility in normal volunteers. *Arch. Ophthalmol.* 102:1497-1502.

Pathak-Ray V, Ray A, Walters R, Hatfield R (2002) Detection of visual field defects in patients after anterior temporal lobectomy for mesial temporal sclerosis-establishing eligibility to drive. *Eye (Lond)* 16:744-748.

Penfield W (1954) Temporal lobe epilepsy. *Br. J. Surg.* 41:337-343.

Penfield W, Baldwin M (1952) Temporal lobe seizures and the technic of subtotal temporal lobectomy. *Ann. Surg.* 136:625-634.

Peuskens D, van LJ, Van CF, van den Bergh R, Goffin J, Plets C (2004) Anatomy of the anterior temporal lobe and the frontotemporal region demonstrated by fiber dissection. *Neurosurgery* 55:1174-1184.

Pfeuty M, Thivard L, Dupont S, Adam C, Baulac M, Samson S (2011) Postoperative recovery of hippocampal contralateral diffusivity in medial temporal lobe epilepsy correlates with memory functions. *J. Neurol. Neurosurg. Psychiatry* 82:340-343.

Piras F, Caltagirone C, Spalletta G (2010) Working memory performance and thalamus microstructure in healthy subjects. *Neuroscience* 171:496-505.

Powell HW, Parker GJ, Alexander DC, Symms MR, Boulby PA, Barker GJ, Thompson PJ, Koepp MJ, Duncan JS (2008a) Imaging language pathways predicts postoperative naming deficits. *J. Neurol. Neurosurg. Psychiatry* 79:327-330.

Powell HW, Parker GJ, Alexander DC, Symms MR, Boulby PA, Wheeler-Kingshott CA, Barker GJ, Koepp MJ, Duncan JS (2005) MR tractography predicts visual field defects following temporal lobe resection. *Neurology* 65:596-599.

Powell HW, Parker GJ, Alexander DC, Symms MR, Boulby PA, Wheeler-Kingshott CA, Barker GJ, Koepp MJ, Duncan JS (2007) Abnormalities of language networks in temporal lobe epilepsy. *Neuroimage*. 36:209-221.

Powell HW, Parker GJ, Alexander DC, Symms MR, Boulby PA, Wheeler-Kingshott CA, Barker GJ, Noppeney U, Koepp MJ, Duncan JS (2006) Hemispheric asymmetries in language-related pathways: a combined functional MRI and tractography study. *Neuroimage*. 32:388-399.

Powell HW, Richardson MP, Symms MR, Boulby PA, Thompson PJ, Duncan JS, Koepp MJ (2008b) Preoperative fMRI predicts memory decline following anterior temporal lobe resection. *J. Neurol. Neurosurg. Psychiatry* 79:686-693.

Pujari VB, Jimbo H, Dange N, Shah A, Singh S, Goel A (2008) Fiber dissection of the visual pathways: analysis of the relationship of optic radiations to lateral ventricle: a cadaveric study. *Neurol. India* 56:133-137.

Rahmathulla G, Recinos PF, Traul DE, Avitsian R, Yunak M, Harper NT, Barnett GH, Recinos VR (2012) Surgical briefings, checklists, and the creation of an environment of safety in the neurosurgical intraoperative magnetic resonance imaging suite. *Neurosurg. Focus*. 33:E12-

Rasmussen AT (1943) The extent of recurrent geniculocalcarine fibers (loop or Archambault and Meyer) as demonstrated by gross brain dissection. *Anat. Rec*. 85:277-282.

Renowden SA, Matkovic Z, Adams CB, Carpenter K, Oxbury S, Molyneux AJ, Anslow P, Oxbury J (1995) Selective amygdalohippocampectomy for hippocampal sclerosis: postoperative MR appearance. *AJNR Am. J. Neuroradiol*. 16:1855-1861.

- Richardson MP, Strange BA, Duncan JS, Dolan RJ (2003) Preserved verbal memory function in left medial temporal pathology involves reorganisation of function to right medial temporal lobe. *Neuroimage*. 20 Suppl 1:S112-S119.
- Richardson MP, Strange BA, Thompson PJ, Baxendale SA, Duncan JS, Dolan RJ (2004) Pre-operative verbal memory fMRI predicts post-operative memory decline after left temporal lobe resection. *Brain* 127:2419-2426.
- Riley JD, Franklin DL, Choi V, Kim RC, Binder DK, Cramer SC, Lin JJ (2010) Altered white matter integrity in temporal lobe epilepsy: association with cognitive and clinical profiles. *Epilepsia* 51:536-545.
- Rodrigo S, Oppenheim C, Chassoux F, Golestani N, Cointepas Y, Poupon C, Semah F, Mangin JF, Le Bihan D, Meder JF (2007) Uncinate fasciculus fiber tracking in mesial temporal lobe epilepsy. Initial findings. *Eur. Radiol.* 17:1663-1668.
- Romano A, D'Andrea G, Minniti G, Mastronardi L, Ferrante L, Fantozzi LM, Bozzao A (2009) Pre-surgical planning and MR-tractography utility in brain tumour resection. *Eur. Radiol.* 19:2798-2808.
- Romano A, Ferrante M, Cipriani V, Fasoli F, Ferrante L, D'Andrea G, Fantozzi LM, Bozzao A (2007) Role of magnetic resonance tractography in the preoperative planning and intraoperative assessment of patients with intra-axial brain tumours. *Radiol. Med.* 112:906-920.
- Rubino GJ, Farahani K, McGill D, Van De Wiele B, Villablanca JP, Wang-Mathieson A (2000) Magnetic resonance imaging-guided neurosurgery in the magnetic fringe fields: the next step in neuronavigation. *Neurosurgery* 46:643-653.
- Rubino PA, Rhoton AL, Jr., Tong X, Oliveira E (2005) Three-dimensional relationships of the optic radiation. *Neurosurgery* 57:219-227.
- Rueckert D, Sonoda LI, Hayes C, Hill DL, Leach MO, Hawkes DJ (1999) Nonrigid registration using free-form deformations: application to breast MR images. *IEEE Trans. Med. Imaging* 18:712-721.
- Saling MM (2009) Verbal memory in mesial temporal lobe epilepsy: beyond material specificity. *Brain* 132:570-582.

Salmenpera TM, Simister RJ, Bartlett P, Symms MR, Boulby PA, Free SL, Barker GJ, Duncan JS (2006) High-resolution diffusion tensor imaging of the hippocampus in temporal lobe epilepsy. *Epilepsy Res.* 71:102-106.

Sander JW (1993) Some aspects of prognosis in the epilepsies: a review. *Epilepsia* 34:1007-1016.

Sander JW, Hart YM, Johnson AL, Shorvon SD (1990) National General Practice Study of Epilepsy: newly diagnosed epileptic seizures in a general population. *Lancet* 336:1267-1271.

Sander JW, Shorvon SD (1996) Epidemiology of the epilepsies. *J. Neurol. Neurosurg. Psychiatry* 61:433-443.

Saur D, Kreher BW, Schnell S, Kummerer D, Kellmeyer P, Vry MS, Umarova R, Musso M, Glauche V, Abel S, Huber W, Rijntjes M, Hennig J, Weiller C (2008) Ventral and dorsal pathways for language. *Proc. Natl. Acad. Sci. U. S. A* 105:18035-18040.

Saykin AJ, Stafiniak P, Robinson LJ, Flannery KA, Gur RC, O'Connor MJ, Sperling MR (1995) Language before and after temporal lobectomy: specificity of acute changes and relation to early risk factors. *Epilepsia* 36:1071-1077.

Schmierer K, Wheeler-Kingshott CA, Tozer DJ, Boulby PA, Parkes HG, Yousry TA, Scaravilli F, Barker GJ, Tofts PS, Miller DH (2008) Quantitative magnetic resonance of postmortem multiple sclerosis brain before and after fixation. *Magn Reson. Med.* 59:268-277.

Schmitz B, Nimsky C, Wendel G, Wienerl J, Ganslandt O, Jacobi K, Fahlbusch R, Schuttler J (2003) Anesthesia during high-field intraoperative magnetic resonance imaging experience with 80 consecutive cases. *J. Neurosurg. Anesthesiol.* 15:255-262.

Schoene-Bake JC, Faber J, Trautner P, Kaaden S, Tittgemeyer M, Elger CE, Weber B (2009) Widespread affections of large fiber tracts in postoperative temporal lobe epilepsy. *Neuroimage.* 46:569-576.

Schon K, Quiroz YT, Hasselmo ME, Stern CE (2009) Greater working memory load results in greater medial temporal activity at retrieval. *Cereb. Cortex* 19:2561-2571.

Schwartz TH, Marks D, Pak J, Hill J, Mandelbaum DE, Holodny AI, Schulder M (2002) Standardization of amygdalohippocampectomy with intraoperative magnetic resonance imaging: preliminary experience. *Epilepsia* 43:430-436.

- Seidenberg M, Hermann B, Wyler AR, Davies K, Dohan FC, Jr., Leveroni C (1998) Neuropsychological outcome following anterior temporal lobectomy in patients with and without the syndrome of mesial temporal lobe epilepsy. *Neuropsychology*. 12:303-316.
- Serles W, Li LM, Antel SB, Cendes F, Gotman J, Olivier A, Andermann F, Dubeau F, Arnold DL (2001) Time course of postoperative recovery of N-acetyl-aspartate in temporal lobe epilepsy. *Epilepsia* 42:190-197.
- Setsompop K, Kimmlingen R, Eberlein E, Witzel T, Cohen-Adad J, McNab JA, Keil B, Tisdall MD, Hoecht P, Dietz P, Cauley SF, Tountcheva V, Matschl V, Lenz VH, Heberlein K, Potthast A, Thein H, Van HJ, Toga A, Schmitt F, Lehne D, Rosen BR, Wedeen V, Wald LL (2013) Pushing the limits of in vivo diffusion MRI for the Human Connectome Project. *Neuroimage*. 80:220-233.
- Sherbondy AJ, Dougherty RF, Napel S, Wandell BA (2008) Identifying the human optic radiation using diffusion imaging and fiber tractography. *J. Vis.* 8:12-11.
- Shimizu H, Suzuki I, Ishijima B (1989) Zygomatic approach for resection of mesial temporal epileptic focus. *Neurosurgery* 25:798-801.
- Shon YM, Kim YI, Koo BB, Lee JM, Kim HJ, Kim WJ, Ahn KJ, Yang DW (2010) Group-specific regional white matter abnormality revealed in diffusion tensor imaging of medial temporal lobe epilepsy without hippocampal sclerosis. *Epilepsia* 51:529-535.
- Short SJ, Elison JT, Goldman BD, Styner M, Gu H, Connelly M, Maltbie E, Woolson S, Lin W, Gerig G, Reznick JS, Gilmore JH (2013) Associations between white matter microstructure and infants' working memory. *Neuroimage*. 64:156-166.
- Sincoff EH, Tan Y, Abdulrauf SI (2004) White matter fiber dissection of the optic radiations of the temporal lobe and implications for surgical approaches to the temporal horn. *J. Neurosurg.* 101:739-746.
- Small DM, Gitelman DR, Gregory MD, Nobre AC, Parrish TB, Mesulam MM (2003) The posterior cingulate and medial prefrontal cortex mediate the anticipatory allocation of spatial attention. *Neuroimage*. 18:633-641.
- Smith EE, Jonides J (1998) Neuroimaging analyses of human working memory. *Proc. Natl. Acad. Sci. U. S. A* 95:12061-12068.

Smith SM (2002) Fast robust automated brain extraction. *Hum. Brain Mapp.* 17:143-155.

Smith SM, Jenkinson M, Johansen-Berg H, Rueckert D, Nichols TE, Mackay CE, Watkins KE, Ciccarelli O, Cader MZ, Matthews PM, Behrens TE (2006) Tract-based spatial statistics: voxelwise analysis of multi-subject diffusion data. *Neuroimage.* 31:1487-1505.

Smith SM, Jenkinson M, Woolrich MW, Beckmann CF, Behrens TE, Johansen-Berg H, Bannister PR, De Luca M, Drobnjak I, Flitney DE, Niazy RK, Saunders J, Vickers J, Zhang Y, De Stefano N, Brady JM, Matthews PM (2004) Advances in functional and structural MR image analysis and implementation as FSL. *Neuroimage.* 23 Suppl 1:S208-S219.

Smith SM, Nichols TE (2009) Threshold-free cluster enhancement: addressing problems of smoothing, threshold dependence and localisation in cluster inference. *Neuroimage.* 44:83-98.

Snook L, Plewes C, Beaulieu C (2007) Voxel based versus region of interest analysis in diffusion tensor imaging of neurodevelopment. *Neuroimage.* 34:243-252.

Sommer B, Grummich P, Coras R, Kasper BS, Blumcke I, Hamer HM, Stefan H, Buchfelder M, Roessler K (2013) Integration of functional neuronavigation and intraoperative MRI in surgery for drug-resistant extratemporal epilepsy close to eloquent brain areas. *Neurosurg. Focus.* 34:E4.

Song SK, Sun SW, Ju WK, Lin SJ, Cross AH, Neufeld AH (2003) Diffusion tensor imaging detects and differentiates axon and myelin degeneration in mouse optic nerve after retinal ischemia. *Neuroimage.* 20:1714-1722.

Song SK, Sun SW, Ramsbottom MJ, Chang C, Russell J, Cross AH (2002) Dysmyelination revealed through MRI as increased radial (but unchanged axial) diffusion of water. *Neuroimage.* 17:1429-1436.

Song X, Pogue BW, Jiang S, Doyley MM, Dehghani H, Tosteson TD, Paulsen KD (2004) Automated region detection based on the contrast-to-noise ratio in near-infrared tomography. *Appl. Opt.* 43:1053-1062.

Spalding JM (1952) Wounds of the visual pathway. I. The visual radiation. *J. Neurol. Neurosurg. Psychiatry* 15:99-109.

Spanaki MV, Kopylev L, DeCarli C, Gaillard WD, Liow K, Fazilat S, Fazilat S, Reeves P, Sato S, Kufta C, Theodore WH (2000) Postoperative changes in cerebral metabolism in temporal lobe epilepsy. *Arch. Neurol.* 57:1447-1452.

Spencer DD, Spencer SS, Mattson RH, Williamson PD, Novelly RA (1984) Access to the posterior medial temporal lobe structures in the surgical treatment of temporal lobe epilepsy. *Neurosurgery* 15:667-671.

Spencer S, Huh L (2008) Outcomes of epilepsy surgery in adults and children. *Lancet Neurol.* 7:525-537.

Sperling RA, Guttmann CR, Hohol MJ, Warfield SK, Jakab M, Parente M, Diamond EL, Daffner KR, Olek MJ, Orav EJ, Kikinis R, Jolesz FA, Weiner HL (2001) Regional magnetic resonance imaging lesion burden and cognitive function in multiple sclerosis: a longitudinal study. *Arch. Neurol.* 58:115-121.

Squire LR (1992) Memory and the hippocampus: a synthesis from findings with rats, monkeys, and humans. *Psychol. Rev.* 99:195-231.

Staempfli P, Rienmueller A, Reischauer C, Valavanis A, Boesiger P, Kollias S (2007) Reconstruction of the human visual system based on DTI fiber tracking. *J. Magn Reson. Imaging* 26:886-893.

Steinmeier R, Fahlbusch R, Ganslandt O, Nimsky C, Buchfelder M, Kaus M, Heigl T, Lenz G, Kuth R, Huk W (1998) Intraoperative magnetic resonance imaging with the magnetom open scanner: concepts, neurosurgical indications, and procedures: a preliminary report. *Neurosurgery* 43:739-747.

Stejskal EO, Tanner JE (1965) Spin diffusion measurements: spin echoes in the presence of a time-dependent field gradient. *J. Chem. Phys.* 42:288-292.

Stretton J, Thompson PJ (2012) Frontal lobe function in temporal lobe epilepsy. *Epilepsy Res.* 98:1-13.

Stretton J, Winston G, Sidhu M, Centeno M, Vollmar C, Bonelli S, Symms M, Koepp M, Duncan JS, Thompson PJ (2012) Neural correlates of working memory in Temporal Lobe Epilepsy--an fMRI study. *Neuroimage.* 60:1696-1703.

Sugranyes G, Kyriakopoulos M, Dima D, O'Muircheartaigh J, Corrigall R, Pendelbury G, Hayes D, Calhoun VD, Frangou S (2012) Multimodal analyses identify linked functional and white matter abnormalities within the working memory network in schizophrenia. *Schizophr. Res.* 138:136-142.

- Sun GC, Chen XL, Zhao Y, Wang F, Hou BK, Wang YB, Song ZJ, Wang D, Xu BN (2011) Intraoperative high-field magnetic resonance imaging combined with fiber tract neuronavigation-guided resection of cerebral lesions involving optic radiation. *Neurosurgery* 69:1070-1084.
- Sun SW, Liang HF, Trinkaus K, Cross AH, Armstrong RC, Song SK (2006) Noninvasive detection of cuprizone induced axonal damage and demyelination in the mouse corpus callosum. *Magn Reson. Med.* 55:302-308.
- Takahashi M, Hackney DB, Zhang G, Wehrli SL, Wright AC, O'Brien WT, Uematsu H, Wehrli FW, Selzer ME (2002) Magnetic resonance microimaging of intraaxonal water diffusion in live excised lamprey spinal cord. *Proc. Natl. Acad. Sci. U. S. A* 99:16192-16196.
- Takahashi M, Iwamoto K, Fukatsu H, Naganawa S, Iidaka T, Ozaki N (2010) White matter microstructure of the cingulum and cerebellar peduncle is related to sustained attention and working memory: a diffusion tensor imaging study. *Neurosci. Lett.* 477:72-76.
- Takaya S, Mikuni N, Mitsueda T, Satow T, Taki J, Kinoshita M, Miyamoto S, Hashimoto N, Ikeda A, Fukuyama H (2009) Improved cerebral function in mesial temporal lobe epilepsy after subtemporal amygdalohippocampectomy. *Brain* 132:185-194.
- Takeuchi H, Sekiguchi A, Taki Y, Yokoyama S, Yomogida Y, Komuro N, Yamanouchi T, Suzuki S, Kawashima R (2010) Training of working memory impacts structural connectivity. *J. Neurosci.* 30:3297-3303.
- Taoka T, Sakamoto M, Iwasaki S, Nakagawa H, Fukusumi A, Hirohashi S, Taoka K, Kichikawa K, Hoshida T, Sakaki T (2005) Diffusion tensor imaging in cases with visual field defect after anterior temporal lobectomy. *AJNR Am. J. Neuroradiol.* 26:797-803.
- Taoka T, Sakamoto M, Nakagawa H, Nakase H, Iwasaki S, Takayama K, Taoka K, Hoshida T, Sakaki T, Kichikawa K (2008) Diffusion tensor tractography of the Meyer loop in cases of temporal lobe resection for temporal lobe epilepsy: correlation between postsurgical visual field defect and anterior limit of Meyer loop on tractography. *AJNR Am. J. Neuroradiol.* 29:1329-1334.
- Taylor DC, McMacKin D, Staunton H, Delanty N, Phillips J (2001) Patients' aims for epilepsy surgery: desires beyond seizure freedom. *Epilepsia* 42:629-633.

Tecoma ES, Laxer KD, Barbaro NM, Plant GT (1993) Frequency and characteristics of visual field deficits after surgery for mesial temporal sclerosis. *Neurology* 43:1235-1238.

Thivard L, Lehericy S, Krainik A, Adam C, Dormont D, Chiras J, Baulac M, Dupont S (2005) Diffusion tensor imaging in medial temporal lobe epilepsy with hippocampal sclerosis. *Neuroimage*. 28:682-690.

Thivard L, Tanguy ML, Adam C, Clemenceau S, Dezamis E, Lehericy S, Dormont D, Chiras J, Baulac M, Dupont S (2007) Postoperative recovery of hippocampal contralateral diffusivity in medial temporal lobe epilepsy. *Epilepsia* 48:599-604.

Thudium MO, Campos AR, Urbach H, Clusmann H (2010) The basal temporal approach for mesial temporal surgery: sparing the meyer loop with navigated diffusion tensor tractography. *Neurosurgery* 67:385-390.

Tiwari VN, Jeong JW, Asano E, Rothermel R, Juhasz C, Chugani HT (2011) A sensitive diffusion tensor imaging quantification method to detect language laterality in children: correlation with the Wada test. *J. Child Neurol.* 26:1516-1521.

Tournier JD, Calamante F, Connelly A (2007) Robust determination of the fibre orientation distribution in diffusion MRI: non-negativity constrained super-resolved spherical deconvolution. *Neuroimage*. 35:1459-1472.

Tournier JD, Calamante F, Gadian DG, Connelly A (2004) Direct estimation of the fiber orientation density function from diffusion-weighted MRI data using spherical deconvolution. *Neuroimage*. 23:1176-1185.

Tuch DS (2004) Q-ball imaging. *Magn Reson. Med.* 52:1358-1372.

Tuch DS, Reese TG, Wiegell MR, Makris N, Belliveau JW, Wedeen VJ (2002) High angular resolution diffusion imaging reveals intravoxel white matter fiber heterogeneity. *Magn Reson. Med.* 48:577-582.

Turner R, Le Bihan D, Chesnick AS (1991) Echo-planar imaging of diffusion and perfusion. *Magn Reson. Med.* 19:247-253.

Vajkoczy P, Krakow K, Stodieck S, Pohlmann-Eden B, Schmiedek P (1998) Modified approach for the selective treatment of temporal lobe epilepsy: transsylvian-transcisternal mesial en bloc resection. *J. Neurosurg.* 88:855-862.

- Van Buren JM, Baldwin M (1958) The architecture of the optic radiation in the temporal lobe of man. *Brain* 81:15-40.
- Vargova L, Homola A, Cicanic M, Kuncova K, Krsek P, Marusic P, Sykova E, Zamecnik J (2011) The diffusion parameters of the extracellular space are altered in focal cortical dysplasias. *Neurosci. Lett.* 499:19-23.
- Vaz SA (2004) Nonverbal memory functioning following right anterior temporal lobectomy: a meta-analytic review. *Seizure.* 13:446-452.
- Vestergaard M, Madsen KS, Baare WF, Skimminge A, Ejersbo LR, Ramsøy TZ, Gerlach C, Akesson P, Paulson OB, Jernigan TL (2011) White matter microstructure in superior longitudinal fasciculus associated with spatial working memory performance in children. *J. Cogn Neurosci.* 23:2135-2146.
- Vlooswijk MC, Jansen JF, Jeukens CR, Majoie HJ, Hofman PA, de Krom MC, Aldenkamp AP, Backes WH (2011) Memory processes and prefrontal network dysfunction in cryptogenic epilepsy. *Epilepsia* 52:1467-1475.
- Walker DG, Talos F, Bromfield EB, Black PM (2002) Intraoperative magnetic resonance for the surgical treatment of lesions producing seizures. *J. Clin. Neurosci.* 9:515-520.
- Wang A, Mirsattari SM, Parrent AG, Peters TM (2011) Fusion and visualization of intraoperative cortical images with preoperative models for epilepsy surgical planning and guidance. *Comput. Aided Surg.* 16:149-160.
- Wang F, Sun T, Li XG, Liu NJ (2008) Diffusion tensor tractography of the temporal stem on the inferior limiting sulcus. *J. Neurosurg.* 108:775-781.
- Wang XQ, Lang SY, Hong LU, Lin MA, Yan-Ling MA, Yang F (2010a) Changes in extratemporal integrity and cognition in temporal lobe epilepsy: a diffusion tensor imaging study. *Neurol. India* 58:891-899.
- Wang YX, Zhu XL, Deng M, Siu DY, Leung JC, Chan Q, Chan DT, Mak CH, Poon WS (2010b) The use of diffusion tensor tractography to measure the distance between the anterior tip of the Meyer loop and the temporal pole in a cohort from Southern China. *J. Neurosurg.* 113:1144-1151.

Warach S, Gaa J, Siewert B, Wielopolski P, Edelman RR (1995) Acute human stroke studied by whole brain echo planar diffusion-weighted magnetic resonance imaging. *Ann. Neurol.* 37:231-241.

Wechsler D (1997) *Manual for the Wechsler Adult Intelligence Scale-III*. The Psychological Corporation, San Antonio.

Wedeen VJ, Hagmann P, Tseng WY, Reese TG, Weisskoff RM (2005) Mapping complex tissue architecture with diffusion spectrum magnetic resonance imaging. *Magn Reson. Med.* 54:1377-1386.

Wehner T, LaPresto E, Tkach J, Liu P, Bingaman W, Prayson RA, Ruggieri P, Diehl B (2007) The value of interictal diffusion-weighted imaging in lateralizing temporal lobe epilepsy. *Neurology* 68:122-127.

Wendland JP, Nerenberg S (1960) Visual field studies after temporal lobectomy for epilepsy. *Arch. Ophthalmol.* 64:195-200.

Werring DJ, Toosy AT, Clark CA, Parker GJ, Barker GJ, Miller DH, Thompson AJ (2000) Diffusion tensor imaging can detect and quantify corticospinal tract degeneration after stroke. *J. Neurol. Neurosurg. Psychiatry* 69:269-272.

Wheeler-Kingshott CA, Cercignani M (2009) About "axial" and "radial" diffusivities. *Magn Reson. Med.* 61:1255-1260.

Wheeler-Kingshott CA, Hickman SJ, Parker GJ, Ciccarelli O, Symms MR, Miller DH, Barker GJ (2002) Investigating cervical spinal cord structure using axial diffusion tensor imaging. *Neuroimage.* 16:93-102.

White ML, Zhang Y (2010) Three-tesla diffusion tensor imaging of Meyer's loop by tractography, color-coded fractional anisotropy maps, and eigenvectors. *Clin. Imaging* 34:413-417.

Wiebe S, Blume WT, Girvin JP, Eliasziw M (2001) A randomized, controlled trial of surgery for temporal-lobe epilepsy. *N. Engl. J. Med.* 345:311-318.

Wieser HG (1986) Selective amygdalohippocampectomy: indications, investigative technique and results. *Adv. Tech. Stand. Neurosurg.* 13:39-133.

Wieser HG, Blume WT, Fish D, Goldensohn E, Hufnagel A, King D, Sperling MR, Luders H, Pedley TA (2001) ILAE Commission Report. Proposal for a new classification of outcome with respect to epileptic seizures following epilepsy surgery. *Epilepsia* 42:282-286.

Wieser HG, Yasargil MG (1982) Selective amygdalohippocampectomy as a surgical treatment of mesiobasal limbic epilepsy. *Surg. Neurol.* 17:445-457.

Wieshmann UC, Symms MR, Clark CA, Lemieux L, Franconi F, Parker GJ, Barker GJ, Shorvon SD (1999) Wallerian degeneration in the optic radiation after temporal lobectomy demonstrated in vivo with diffusion tensor imaging. *Epilepsia* 40:1155-1158.

Wilde EA, Newsome MR, Bigler ED, Pertab J, Merkley TL, Hanten G, Scheibel RS, Li X, Chu Z, Yallampalli R, Hunter JV, Levin HS (2011) Brain imaging correlates of verbal working memory in children following traumatic brain injury. *Int J. Psychophysiol.* 82:86-96.

Wirtz CR, Bonsanto MM, Knauth M, Tronnier VM, Albert FK, Staubert A, Kunze S (1997) Intraoperative magnetic resonance imaging to update interactive navigation in neurosurgery: method and preliminary experience. *Comput. Aided Surg.* 2:172-179.

Woermann FG, Barker GJ, Birnie KD, Meencke HJ, Duncan JS (1998) Regional changes in hippocampal T2 relaxation and volume: a quantitative magnetic resonance imaging study of hippocampal sclerosis. *J. Neurol. Neurosurg. Psychiatry* 65:656-664.

Woermann FG, Jokeit H, Luerding R, Freitag H, Schulz R, Guertler S, Okujava M, Wolf P, Tuxhorn I, Ebner A (2003) Language lateralization by Wada test and fMRI in 100 patients with epilepsy. *Neurology* 61:699-701.

Wu W, Rigolo L, O'Donnell LJ, Norton I, Shriver S, Golby AJ (2012) Visual pathway study using in vivo diffusion tensor imaging tractography to complement classic anatomy. *Neurosurgery* 70:145-156.

Wyler AR, Hermann BP, Richey ET (1989) Results of reoperation for failed epilepsy surgery. *J. Neurosurg.* 71:815-819.

Wyler AR, Hermann BP, Somes G (1995) Extent of medial temporal resection on outcome from anterior temporal lobectomy: a randomized prospective study. *Neurosurgery* 37:982-990.

- Yamamoto A, Miki Y, Urayama S, Fushimi Y, Okada T, Hanakawa T, Fukuyama H, Togashi K (2007) Diffusion tensor fiber tractography of the optic radiation: analysis with 6-, 12-, 40-, and 81-directional motion-probing gradients, a preliminary study. *AJNR Am. J. Neuroradiol.* 28:92-96.
- Yamamoto T, Yamada K, Nishimura T, Kinoshita S (2005) Tractography to depict three layers of visual field trajectories to the calcarine gyri. *Am. J. Ophthalmol.* 140:781-785.
- Yasargil MG, Ture U, Yasargil DC (2004) Impact of temporal lobe surgery. *J. Neurosurg.* 101:725-738.
- Yeni SN, Tanriover N, Uyanik O, Ulu MO, Ozkara C, Karaagac N, Ozyurt E, Uzan M (2008) Visual field defects in selective amygdalohippocampectomy for hippocampal sclerosis: the fate of Meyer's loop during the transsylvian approach to the temporal horn. *Neurosurgery* 63:507-513.
- Yogarajah M, Focke NK, Bonelli S, Cercignani M, Acheson J, Parker GJ, Alexander DC, McEvoy AW, Symms MR, Koepp MJ, Duncan JS (2009) Defining Meyer's loop-temporal lobe resections, visual field deficits and diffusion tensor tractography. *Brain* 132:1656-1668.
- Yogarajah M, Focke NK, Bonelli SB, Thompson P, Vollmar C, McEvoy AW, Alexander DC, Symms MR, Koepp MJ, Duncan JS (2010) The structural plasticity of white matter networks following anterior temporal lobe resection. *Brain* 133:2348-2364.
- Yogarajah M, Powell HW, Parker GJ, Alexander DC, Thompson PJ, Symms MR, Boulby P, Wheeler-Kingshott CA, Barker GJ, Koepp MJ, Duncan JS (2008) Tractography of the parahippocampal gyrus and material specific memory impairment in unilateral temporal lobe epilepsy. *Neuroimage.* 40:1755-1764.
- Yoo SY, Chang KH, Song IC, Han MH, Kwon BJ, Lee SH, Yu IK, Chun CK (2002) Apparent diffusion coefficient value of the hippocampus in patients with hippocampal sclerosis and in healthy volunteers. *AJNR Am. J. Neuroradiol.* 23:809-812.
- Yu AH, Li KC, Yu CS, Wang YP, Xue SF (2006) Diffusion tensor imaging in medial temporal lobe epilepsy. *Chin Med. J. (Engl.)* 119:1237-1241.
- Yu CS, Li KC, Xuan Y, Ji XM, Qin W (2005) Diffusion tensor tractography in patients with cerebral tumors: a helpful technique for neurosurgical planning and postoperative assessment. *Eur. J. Radiol.* 56:197-204.

Yu HJ, Christodoulou C, Bhise V, Greenblatt D, Patel Y, Serafin D, Maletic-Savatic M, Krupp LB, Wagshul ME (2012) Multiple white matter tract abnormalities underlie cognitive impairment in RRMS. *Neuroimage*. 59:3713-3722.

Zahr NM, Rohlfing T, Pfefferbaum A, Sullivan EV (2009) Problem solving, working memory, and motor correlates of association and commissural fiber bundles in normal aging: a quantitative fiber tracking study. *Neuroimage*. 44:1050-1062.

Zhang H, Schneider T, Wheeler-Kingshott CA, Alexander DC (2012) NODDI: Practical in vivo neurite orientation dispersion and density imaging of the human brain. *Neuroimage*. 61:1000-1016.

Zhao Y, Chen X, Wang F, Sun G, Wang Y, Song Z, Xu B (2012) Integration of diffusion tensor-based arcuate fasciculus fibre navigation and intraoperative MRI into glioma surgery. *J. Clin. Neurosci*. 19:255-261.

Zhong J, Petroff OA, Prichard JW, Gore JC (1993) Changes in water diffusion and relaxation properties of rat cerebrum during status epilepticus. *Magn Reson. Med*. 30:241-246.